

**TECHNISCHE UNIVERSITÄT MÜNCHEN**  
**Lehrstuhl für Physikalische Chemie**

**Optical properties of size-selected  
supported metal clusters measured by  
cavity ring-down spectroscopy**

**Aras Kartouzian**

Vollständiger Abdruck der von der Fakultät für Chemie der Technische Universität  
München zur Erlangung des akademischen Grades eines

**Doktors der Naturwissenschaften**

genehmigten Dissertation.

Vorsitzender: Univ.-Prof. Dr. W. Domcke

Prüfer der Dissertation:

1. Univ.-Prof. Dr. U. K. Heiz
2. Univ.-Prof. Dr. K.- O. Hinrichsen
3. Univ.-Prof. Dr. J. Barth

Die Dissertation wurde am 25.02.2010 bei der Technischen Universität München  
eingereicht und durch die Fakultät für Chemie am 12.04.2010 angenommen.



---

## Table of contents

<b>TABLE OF CONTENTS.....</b>	<b>I</b>
<b>ABSTRACT.....</b>	<b>1</b>
<b>1. INTRODUCTION.....</b>	<b>3</b>
<b>2. THE APPARATUS .....</b>	<b>7</b>
2.1. GENERAL ASPECTS.....	7
2.1.1. <i>The sample</i> .....	7
2.1.2. <i>Spectroscopic requirements</i> .....	9
2.1.3. <i>Ultra high vacuum</i> .....	9
2.2. SPECTROSCOPIC METHOD .....	10
2.2.1. <i>A short summary of some suitable spectroscopic methods</i> .....	10
2.2.1.1. Laser induced fluorescence (LIF).....	11
2.2.1.2. Resonance enhanced multiphoton ionisation (REMPI) .....	11
2.2.1.3. Photoacoustic spectroscopy .....	11
2.2.1.4. Degenerate four-wave mixing (DFWM).....	12
2.2.1.5. Second harmonic generation spectroscopy (SHGS).....	12
2.2.1.6. Intracavity laser absorption spectroscopy (ICLAS).....	13
2.2.2. <i>Cavity ring-down spectroscopy</i> .....	13
2.2.2.1. History .....	14
2.2.2.2. Theory.....	14
2.2.2.3. Sensitivity .....	18
2.2.2.4. Laser bandwidth and multi-exponential decays .....	21
2.2.2.5. Cavity ring-down mirrors .....	21
2.2.2.6. Cavity modes and mode matching .....	23
2.2.3. <i>CRDS under UHV conditions</i> .....	31
2.2.4. <i>Laser system</i> .....	32
2.2.5. <i>Detection unit</i> .....	33
2.2.6. <i>Application of CRDS to solid samples</i> .....	35
2.2.6.1. Reflection mode condensed phase CRDS .....	35
2.2.6.2. Transmission mode condensed phase CRDS.....	36
2.2.7. <i>The optical setup</i> .....	39
2.3. PRODUCTION OF SMALL METAL CLUSTERS.....	42
2.3.1. <i>Cluster sources</i> .....	43
2.3.1.1. Seeded supersonic nozzle source .....	43
2.3.1.2. Gas aggregation cluster source.....	43
2.3.1.3. Ion sputtering source.....	43
2.3.1.4. Liquid-metal ion source .....	43
2.3.1.5. Laser vaporisation cluster source.....	44

---

2.3.1.6. Pulsed arc cluster ion source .....	47
2.4. ION OPTICS AND MASS SELECTION UNIT .....	47
2.5. DEPOSITION .....	49
2.5.1. Neutralisation and electron source .....	49
2.5.2. Temperature of the sample .....	50
2.5.3. Sample holder and the second cooling shield .....	52
2.6. THE OVERVIEW OF THE SETUP .....	54
<b>3. PUBLICATIONS.....</b>	<b>57</b>
3.1. PAPER 1 .....	58
3.2. PAPER 2 .....	68
3.3. PAPER 3 .....	74
<b>4. OUTLOOKS .....</b>	<b>81</b>
4.1. NORMAL INCIDENCE CONFIGURATION CRDS .....	81
4.2. SECOND HARMONIC GENERATION SPECTROSCOPY .....	81
4.3. IR-CAVITY RING-DOWN SPECTROSCOPY .....	82
4.4. CONTROLLED SURFACE CHEMISTRY ON ISOLATED SIZE-SELECTED METAL CLUSTERS: A RESEARCH PROPOSAL .....	83
4.4.1. Introduction .....	83
4.4.2. Research Project .....	84
4.4.3. Methodology .....	84
<b>5. SUMMARY.....</b>	<b>87</b>
5.1. EXPERIMENTAL ACHIEVEMENTS.....	87
5.2. SCIENTIFIC ACHIEVEMENTS .....	89
5.3. SCIENTIFIC PROSPECTIVE.....	90
<b>APPENDIX A: CONSTRUCTIONS.....</b>	<b>93</b>
A1. MIRROR HOLDER.....	93
A2. CLUSTER SOURCE.....	104
A3. ELECTRON SOURCE .....	128
A4. SAMPLE HOLDER.....	134
A5. SECOND COOLING SHIELD .....	140
<b>APPENDIX B: CALCULATIONS .....</b>	<b>143</b>
B1. RAY TRANSFER MATRIX ANALYSIS.....	143
B2. COOLING OF THE SUBSTRATE .....	144
<b>ACKNOWLEDGEMENTS .....</b>	<b>147</b>
<b>REFERENCES .....</b>	<b>149</b>

## **Abstract**

Supported size-selected metal clusters have attracted considerable interest due to their special catalytic properties. Optical spectroscopy is a powerful method to characterise the electronic and geometrical properties of such systems. However, observing the optical properties of these small clusters is not trivial and highly sensitive techniques such as cavity ring-down spectroscopy (CRDS), a method previously used to study gas phase samples, are required. An experimental apparatus capable of studying the optical properties of support size-selected metal clusters is presented here for the first time. The metal clusters were prepared using a state-of-the-art laser ablation source, and size selected prior to deposition onto an optically transparent support material. CRDS was adapted for the study of solid samples over an extended wavelength range and used to investigate the size dependent optical properties of supported metal clusters.

## **Zusammenfassung**

Wegen ihrer besonderen katalytischen Eigenschaften stehen massenselektierte Metallcluster im Fokus intensiver Forschungsarbeiten. Für ihre Charakterisierung eignen sich spektroskopische Methoden im sichtbaren Bereich, da dadurch Rückschlüsse auf die elektronische Struktur gewonnen werden können. Eine experimentelle Herausforderung ist dabei die geringe Absorption. Dies erfordert die Anwendung hoch empfindlicher Methoden wie z.B. die "Cavity Ring-Down Spectroscopy" (CRDS). Hierbei handelt es sich um eine Methode, die vorwiegend in der Gasphase verwendet wurde. In dieser Arbeit wird ein neuer experimenteller Ansatz vorgestellt, mit dem die optischen Eigenschaften getragener Cluster untersucht werden können. Die Herstellung der Cluster erfolgt mittels einer Laserverdampfungs-Clusterquelle. Die verwendete spektroskopische Methode ist die UHV-kompatible CRD-Spektroskopie, die die in-situ Messung über einen großen spektralen Bereich erlaubt.



## 1. Introduction

*"What would the properties of materials be if we could really arrange the atoms the way we want them? They would be very interesting to investigate theoretically. I can't see exactly what would happen, but I can hardly doubt that when we have some control of the arrangement of things on a small scale we will get an enormously greater range of possible properties that substances can have, and of different things that we can do."*

**Richard Feynman, 1959**

Richard Feynman was surely one of the most visionary scientists in the 20<sup>th</sup> century. His ideas have driven many researchers in various fields. The above mentioned paragraph is an example of his intriguing ideas which has partly become true. The main message behind his famous speech *"There's Plenty of Room at the Bottom"* was, let's investigate the properties of materials at smaller and smaller length-scale, since these would be different to what we know from the bulk and atoms. He was actually asking the scientific community to create and develop new devices, which needed to go beyond the limits of that time.

Several changes in properties occur as atoms combine to form dimers, trimers, larger clusters and so on, until finally a size is reached at which the collection is identifiable as the bulk. An obvious example is made by any metal; a single atom of any material has no metallic property! There are a number of fundamentally important questions concerning the nature of the evolution of bulk metallic properties, for instance. Over what size range are properties intermediate between those of the atomic and metallic states? Is the transition abrupt or gradual, monotonic or discontinuous? Do all properties change in parallel fashion? Is the nature of the evolution the same for all metals, or does each have its own pattern? These questions have been the topic of many research activities over the past decades. Currently, a vast collection of experimental and theoretical data is available which delivers quite satisfying answers to some of these questions<sup>1-10</sup>. It is known that dimensional confinement is one of the reasons for the so called "size effect", and that depending on the property under consideration, the characteristic length at which the confinement sets in can vary. These changes of property can be divided into two regimes; the non-scalable regime for small clusters where the properties change drastically by adding a single atom, and the scalable regime where the properties monotonically converge toward bulk values. Theory has been quite successful in both, determining and predicting the material properties in the scalable range where an extrapolation of bulk values through solid state considerations result in good agreement between experiment and calculation. In the non-scalable range, however, theory becomes more and more dependant on various assumptions, and its success is only justified by agreement with the experimental results.

The optical properties of metal clusters have been the subject of continuously growing interest, mainly due to the information on the electronic structure which can be gained. A variety of samples have been studied e.g. clusters in the gas phase<sup>11-16</sup>, clusters embedded in matrices<sup>17-26</sup>, clusters in solutions<sup>27-31</sup> and clusters at surfaces<sup>32-34</sup>. Among the aforementioned samples, supported clusters are of high importance since they deliver the most practical way of technological implementation. However, much less is known about the evolution of the optical properties of metal clusters with size. Furthermore, it has been shown that the interaction between clusters and the support material strongly influences the observed optical properties<sup>35</sup> by manipulating the electronic structure of the clusters through e.g. charge transfer. The medium surrounding the clusters affects the properties of cluster/medium system. Therefore, this system as a whole should be studied. The common shortcoming among the investigations undertaken on supported metal clusters to date is that the size range of the clusters under study is relatively broad, and size specific information is not available. This becomes more dramatic in the non-scalable regime for clusters containing up to 50 atoms, where a drastic change is expected by the addition of each atom.

Optical absorption spectroscopy is a powerful method to characterise electronic transitions in very small clusters supported on surfaces, and not only delivers an insight into their electronic structure, but also when compared to theoretical predictions, into their geometric structure and interaction with support material. The low particle concentration of monodispersed materials is an experimental challenge that has drastically slowed the investigations on size specific properties of supported species. The subject of the current work is to tackle this problem by designing a novel experimental apparatus capable of producing and characterising appropriate samples and measuring the optical properties of size-selected supported metal clusters. In the context of the present work, clusters are defined as a number of atoms ( $N$ ) bound together, where  $1 < N < 20$ .

In the following, the general aspects of an experimental apparatus suitable for measuring the optical properties of size-selected supported clusters are first reviewed. The capabilities that the spectroscopic method should possess and the specifications of the samples are then given. Following on, the spectroscopic method of choice is introduced and discussed in detail. The technical difficulties are outlined and in each case a practical solution is provided. Production of metal clusters through laser vapourisation cluster source is explained and further details of the cluster source used in this work are included followed by an overview of the apparatus as a whole. In Chapter 3 the publications which resulted from this work are presented accompanied by a short description. Finally, future outlooks are presented in chapter 4. The development of a unique experimental setup



## 1. Introduction

---

requires many custom parts to be designed and constructed. The drawings of these parts, as used in the presented work are attached in Appendix A.



## 2. The apparatus

Generally speaking any experimental equipment designed with the purpose of measuring the optical properties of supported size-selected metal clusters is composed of three main parts: 1) A cluster source to produce a beam of metal clusters of different sizes; 2) Ion optics and size selection unit to guide the beam to the support material where the clusters are deposited after selection of a specific cluster size from the beam; 3) An analysis unit where the optical properties are investigated. In the following section, the general prerequisites of different parts are first presented, and then details of each are given.

### 2.1. General aspects

Metal nanoclusters are as old as the beautiful metal-containing stained glasses of the Middle Ages. The very first investigations are perhaps those of Rayleigh, who recognised that the scattering of light by small metal clusters embedded in the glass was the source of its colour. Gustav Mie followed Rayleigh's work with an extensive electrodynamic treatment which is relevant even today. As might be expected from either a molecular or a solid-state point of view, atomic clusters have properties different from the bulk. Since then, there has been great interest in the physics and chemistry of small clusters arising from their size dependent electronic<sup>36</sup>, thermodynamic<sup>37, 38</sup> chemical<sup>39</sup>, and magnetic<sup>40</sup> properties.

#### 2.1.1. The sample

An exploration of the optical properties of supported size-selected clusters requires an appropriate cluster/support system. It is of central importance to create a sample consisting of a single (monodispersed) cluster size. A schematic of such a sample is shown in Figure 1. In order to fulfil this prerequisite it is required that a specific cluster size is deposited onto the substrate so that firstly, no agglomeration occurs and secondly, no fragmentation takes place. Fragmentation may be avoided by keeping the kinetic energy of the cluster below a certain limit. To avoid agglomeration, however, the surface coverage (number of

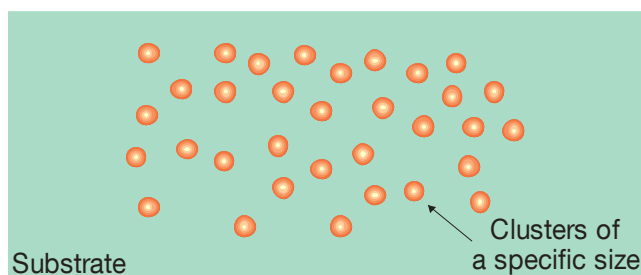


**Figure 1** Schematic view of a sample which fulfils the main criterion. It consists of clusters of a single size which are well separated.

clusters per unit of surface area) must be less than a certain limit. Assuming a random distribution of the clusters on the surface, the relevant parameter to be controlled is the nearest neighbour (NN) distribution function which can be calculated for a given density (coverage) according to equation (1) <sup>41, 42</sup> where  $H(r)$ ,  $r$ ,  $\rho$  and,  $v_D$  are the distribution function, the distance between the clusters, the cluster coverage and the dimension dependent volume of the clusters (in case of surface coverage  $v_D = \pi r^2$ ), respectively.

$$H(r) = \rho \frac{dv_D(r)}{dr} e^{(-\rho v_D(r))} \quad (1)$$

Figure 2 shows the calculated NN distribution function for various cluster coverages. As is seen in Figure 2A, the most probable value of the NN distance diminishes for higher coverages. Furthermore, the amount of clusters which have NNs in distances below a threshold increases as well, as shown in Figure 2B. This enforces an upper limit on the allowed coverage, which in turn depends on the size of the clusters. For larger clusters, the NN distance should be larger in order to have well separated clusters compared to the case of smaller clusters. However, a certain coverage is necessary in order for the optical properties of the clusters to be observed. This minimum coverage is mainly predefined by the detection limit of the measurement method. In the next section, the required capabilities of the spectroscopic method are discussed.

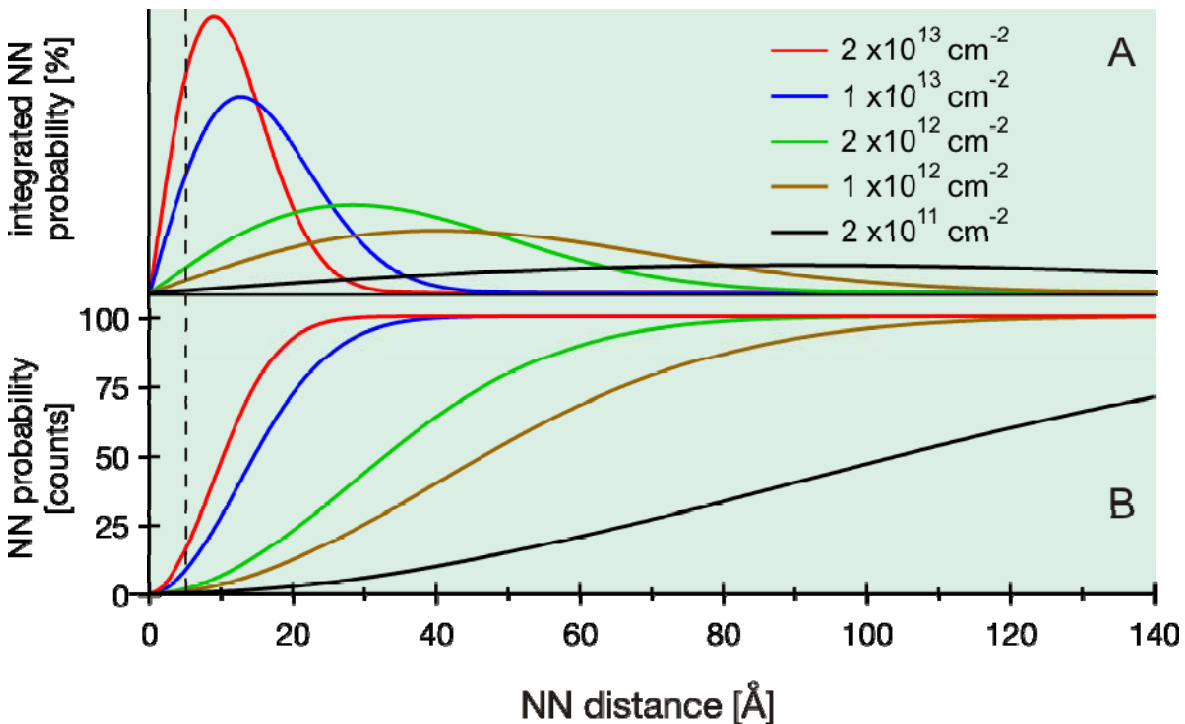


**Figure 2 A)** The nearest neighbour distribution functions for different cluster coverages. **B)** The integrated NN probability in percent. The vertical broken line at  $r = 5 \text{ Å}$  is drawn for easier comparison.

In order to have a sample of monodispersed clusters, the correct coverage of the clusters is only a “necessary” condition. Another issue is to avoid agglomeration of the clusters via their diffusion across the surface. It is, therefore, required that either the temperature of the sample stays low enough to freeze the clusters at their initial positions or to anchor them locally.

A final important requirement for a suitable sample is its purity. A pure sample consists of clusters and the substrate and no contamination. This may be fulfilled to some extent by working under ultra high vacuum conditions as will be discussed in section 2.1.3.

### 2.1.2. Spectroscopic requirements

The first criterion mentioned in section 2.1.1 may be fulfilled by keeping the cluster coverage below  $10^{12}$  cm<sup>-2</sup> (the brown curve in Figure 2) for all clusters. Since small cluster of up to 50 atoms in size will have a radius smaller than 1 nm (Au<sub>55</sub> has a diameter of ~1.5 nm), the majority of the clusters will be far enough from each other and agglomeration will be avoided. Considering the small absorption cross section of transition metal clusters in the visible range of the spectrum ( $\sigma \approx 0.1$  Å<sup>2</sup>, it gets larger in the UV), one can conclude that the spectroscopic method should be able to measure absorption losses ( $L$ ) in the order of 10 parts per million ( $L = \rho \cdot \sigma$ ). Among the methods which are capable of measuring such low optical losses, the linear optical methods are preferred since it is easier to interpret the acquired spectra.

### 2.1.3. Ultra high vacuum

As already mentioned, the cleanliness of the sample is an important issue, since the presence of contamination may manipulate the electronic structure of the system and so the measured optical properties will not be that of the system of interest. Hence, to avoid the interaction of the cluster/substrate system with foreign molecules, it is preferred to perform the measurement under vacuum where the amount of contaminating molecules is reduced. The quality of the vacuum should allow for a measurement taking about 5 hours to be performed with negligible contamination. To this end, the mean free path of the molecules present in the vacuum is the relevant quantity. It can be shown that for pressures higher than  $1 \times 10^{-9}$  mbar, it takes less than one hour for the whole surface, to be covered by residual water molecules<sup>43</sup>, assuming a sticking coefficient of 1. Thus, it is necessary to have a vacuum of high enough quality ( $1 \times 10^{-10}$  mbar) in order to have clean samples over a relatively extended time.

Since the formation of clusters is accompanied by introducing pressures in the range of  $1 \times 10^{-3}$  mbar, a differentially pumped vacuum system should be employed. Here the cluster source (where the clusters are produced) is separated

from the analysis chamber (where the sample is investigated) through a number of vacuum chambers which are separately pumped, and connected only via small openings. The cluster beam should be guided to the substrate where deposition takes place. Common to all cluster sources, is that they produce neutral as well as negatively and positively charged clusters. It is therefore possible to guide the charged clusters using electrical fields and separate them according to their mass to charge ratio.

### **2.2. Spectroscopic method**

The basic capabilities of the suitable spectroscopic method were briefly mentioned in section 2.1.2. Direct absorption spectroscopy of atoms and molecules in the gas phase yields both quantitative absolute concentrations as well as absolute frequency-dependent cross-sections, and is a very powerful tool in analytical chemistry and physical chemistry. This absoluteness is the reason why sensitive absorption spectroscopy techniques have gained renewed interest, even in research fields where more sophisticated laser-based diagnostic techniques are commonly applied. Among the various direct absorption techniques, the cavity ring-down (CRD) spectroscopy has proven to be a valuable addition, since it combines a good sensitivity with a rather simple and straightforward experimental set-up. In a 'conventional' absorption experiment, one measures the amount of light that is transmitted through a sample. If the light source is monochromatic (e.g. a laser), one can obtain an absorption spectrum of the sample by recording the transmitted intensity as a function of the frequency. Alternatively, a broad light source can be used when the incident light or the transmitted light is spectrally dispersed. A drawback of direct absorption might be its limited sensitivity because a small attenuation in transmitted beam has to be measured on top of a large background. High sensitivity is obtained by using modulation schemes and by increasing the absorption path length. Alternatively, other experimental spectroscopy techniques can be used which are based on the detection of phenomena that are induced by absorption of light, such as pressure changes in photoacoustic spectroscopy, fluorescence in laser-induced fluorescence (LIF), or ions in resonant enhanced multiphoton ionization (REMPI). The great advantage of these techniques is that they are background free. A disadvantage is the sometimes difficult calibration procedure which is needed to make these techniques absolute (i.e. these techniques are not self-calibrating).

#### **2.2.1. A short summary of some suitable spectroscopic methods**

The main problem associated with laser absorption spectroscopy when detecting inherently weak absorption (e.g. that of small metal clusters) is that the change in intensity is very small compared to the initial laser intensity. Therefore the sensitivity is generally limited by fluctuations in laser intensity. However, several other laser-based methods of obtaining absorption-related spectra exist

which rely upon some subsequent side effects of the excitation process such as above-mentioned methods. Examples of such methods are briefly outlined below.

### **2.2.1.1. Laser induced fluorescence (LIF)**

Following the absorption of a photon, an electronically excited molecule may decay to its ground state by emission of radiation, a process known as fluorescence. By monitoring this fluorescence (generally at 90° to the laser beam), molecular absorption can be detected while the input laser wavelength is scanned. LIF is, at least in theory, a zero-background technique, but some sources of noise are inevitable, the principal one usually being scattered laser light from the surfaces. LIF is thus, a highly sensitive absorption technique: for example, for detection of tropospheric OH, a sensitivity of  $1.8 \times 10^6$  molecules per  $\text{cm}^3$  was demonstrated and further improvements have since been made<sup>44</sup>. Detection of fluorescence is ultimately constrained by the quantum efficiency of the photomultiplier tube (PMT). A primary limitation of LIF is the requirement that the excited state must have a large fluorescence quantum yield. Many excited electronic states decay via other competing pathways, such as predissociation or collisional quenching, and thus show little or no fluorescence. Examples of small molecules and radicals commonly probed by LIF include  $\text{I}_2$ , NO, OH, CH, CN,  $\text{NO}_2$  and CO.

### **2.2.1.2. Resonance enhanced multiphoton ionisation (REMPI)**

A molecule can be induced to absorb two or more photons simultaneously, provided the intensity of light is sufficiently high to compensate for the very small cross-sections for such processes. Typically, small molecules composed of light atoms will have ionisation energies around 10-15 eV, corresponding to the absorption of three UV photons from the ground state of the neutral molecule. The cross-section of this ionisation process is greatly enhanced if there is a real excited state resonant at the energy of one or two absorbed photons. By monitoring the photoionisation yield as the laser wavelength is scanned, a spectrum corresponding to absorption to the resonant state is obtained<sup>45-47</sup>. REMPI has certain advantages over single photon spectroscopy; in particular, different selection rules for multiphoton transitions allow many previously unobservable transitions to be seen (e.g. for the two-photon absorption, g-g and u-u transitions in a centrosymmetric molecule), and it can be mass selective if used in combination with time of flight (TOF) detection. If the resonant state is heavily predissociated, however, little or no ion formation will occur. Key species detected by REMPI include  $\text{H}_2$ , HCl, NO and,  $\text{CH}_3$ .

### **2.2.1.3. Photoacoustic spectroscopy**

Absorption of electromagnetic radiation raises the internal energy of the molecules in a sample. This energy can be dissipated to a bath gas via collisions

that cause internal (e.g. electronic or vibrational) to translational (E-T or V-T) energy transfer, resulting in a local, thermally induced pressure increase. A pulsed laser or modulated continuous wave (CW) laser will thus, generate pressure waves when tuned to be resonant with an absorption feature of the sample gas, and these pressure waves may be monitored by a piezoelectric detector or a microphone placed within the sample cell. The intensity of the sound detected depends on the degree of heating, which, in turn, is related to the strength of the absorption: hence, plotting sound level versus laser frequency yields an absorption spectrum<sup>48</sup>. Photoacoustic spectroscopy is a highly sensitive form of laser absorption spectroscopy: for example, Davidson et al.<sup>49</sup> specified a limiting absorption coefficient of  $4 \times 10^{-10} \text{ cm}^{-1}$ . The technique has thus found extensive applications in the study of high vibrational overtones of small hydride molecules and in analytical chemistry.

### 2.2.1.4. Degenerate four-wave mixing (DFWM)

DFWM involves the interaction of three coherent laser beams of identical frequencies with a medium to produce a fourth, coherent signal beam<sup>50, 51</sup>. A simple, qualitative description of the process is as follows: two laser beams cross at a small angle to produce an optical fringe pattern, which, in an absorbing medium, will give rise to a spatial modulation of ground and excited state populations. The third laser beam can then be scattered by Bragg diffraction from the population grating to produce a signal beam. This process happens when the medium absorbs; therefore, detection of the signal beam gives an absorption spectrum. DFWM has the advantage over LIF and REMPI that it can be used to detect rapidly predissociating species without resultant loss of signal. Because of its coherent nature, the signal beam may be detected remotely, making DFWM a useful probe of hostile environments such as flames and plasmas. In practice, however, DFWM is a difficult technique to implement and the extraction of quantum-state population distributions from the resultant spectra is complicated by the non-linear nature of the interaction of light and matter in the DFWM process. DFWM signal intensities scale with the square of the concentration of the detected species, making detection of trace species very difficult, and DFWM cannot generally be regarded as possessing the sensitivity of either LIF or REMPI. Nevertheless, it has been used for the successful detection of, for example, HCO from the photolysis of acetaldehyde<sup>52</sup>, CH in a flame<sup>53</sup> and both C2 and CH in a diamond-growth reactor<sup>54</sup>.

### 2.2.1.5. Second harmonic generation spectroscopy (SHGS)

Optical second harmonic generation (SHG) is the nonlinear conversion of two photons of frequency  $\omega$  to a single photon of frequency  $2\omega$  which, in the electric dipole approximation, requires a non-centrosymmetric medium. This phenomenon is used in laser technology for frequency doubling through non-



centrosymmetric crystals. SHG may also be obtained at the interface between two centrosymmetric media, where the symmetry is broken. Since only the few atomic or molecular monolayers on either side of the interface participate in the symmetry breaking, the SHG process can be employed as a highly surface sensitive optical probe of interfacial phenomena<sup>55</sup>. The sensitivity of the SHG technique has led to its application in the study of surface chemistry for a large number of interfacial systems<sup>56</sup>.

### **2.2.1.6. Intracavity laser absorption spectroscopy (ICLAS)**

An absorber placed within a laser cavity can alter the gain and hence, the output of the laser. Therefore, by placing a narrow band absorber into the cavity of a laser and determining the gain at different wavelengths, an absorption spectrum can be obtained. The wavelength-dependent gain can be determined either by tuning the (narrow-band) laser or by using a broad-band multimode laser and dispersing the output light with a high resolution spectrograph. Quantitative intensity measurements may be extracted from these spectra, allowing concentrations or oscillator strengths to be determined. ICLAS is a very sensitive technique, which may be performed in the visible range using a dye laser or in the IR using a colour-centre laser, and has been applied to a number of species to measure high overtone spectra<sup>57</sup>.

### **2.2.2. Cavity ring-down spectroscopy**

CRD spectroscopy is a sensitive absorption technique in which the rate of absorption rather than the magnitude of the absorption of a light pulse confined in an optical cavity is measured<sup>58</sup>. The sample is placed inside a high-finesse optical cavity consisting of two highly reflective mirrors. A short laser pulse is coupled into the cavity, the light is reflected back and forth inside the cavity and, every time that the light is reflected, a small fraction of it leaks out of the cavity. Instead of measuring the total intensity of the light exiting the cavity, one determines the decay time by measuring the time dependence of the light leaking out of the cavity. In this way the rate of absorption can be obtained; the more the sample absorbs, the shorter the measured decay time is. There are several advantages to this approach. Since the absorption is determined from the time behaviour of the signal, it is independent of any pulse-to-pulse fluctuations of the laser. Furthermore, the effective absorption path-length, which depends on the reflectivity of the cavity mirrors, can be very long (up to several kilometres), while the sample volume can be kept rather small. Compared with other sensitive absorption techniques, especially those using modulation schemes, CRD spectroscopy has the additional advantage that the absorption is measured on an absolute scale since CRDS is a direct technique. Another attractive property is its simplicity, a CRD setup may be constructed using relatively few components.

### 2.2.2.1. History

The work reported by Herbelin *et al.*<sup>59</sup> and Anderson *et al.*<sup>60</sup> can be regarded as precursors to the CRD technique, although the transmission of a light pulse through an optical cavity had already been studied for a long time<sup>61</sup>. Herbelin *et al.* were the first to propose the use of an optical cavity for measuring the reflectance of mirror coatings. By intensity modulating a CW light beam and measuring the phase shift introduced by the optical cavity, they were able to determine accurately the high reflectance of their mirrors. In 1984, Anderson *et al.* demonstrated that the reflectance could be measured even more accurately by abruptly switching off the CW light source when the intra-cavity field exceeded a certain threshold value, followed by the recording of the subsequent intensity decay of the light in the optical cavity. In both techniques, injection of light into the cavity occurred via accidental coincidences of the (narrow-bandwidth) laser frequency with the frequency of one of the narrow cavity modes. In 1988 O'Keefe and Deacon showed that problems associated with mode coincidences could be circumvented by using a pulsed laser<sup>62</sup>. Additionally, owing to the pulsed character, no electronics were needed for monitoring the intra-cavity power or for switching off the laser, before observing the decay transient, thus providing a simple experimental design for measuring the cavity loss. O'Keefe and Deacon realized that this method was suitable for measuring the absorption spectrum of molecules present in the cavity. They demonstrated the sensitivity by recording the CRD absorption spectrum of the weak  $b^1\Sigma_g^- \rightarrow X^3\Sigma_g^-$  bands of molecular oxygen<sup>62</sup>. Since then, it has been shown by many groups that this technique is powerful in gas-phase spectroscopy for measurements of either strong absorptions of species present in trace amounts or weak absorptions of abundant species and developments in this technique are still continuing today.

### 2.2.2.2. Theory

The principle behind CRD spectroscopy is very simple and was already introduced at the beginning of section 2.2.2. A light pulse trapped inside a stable optical cavity travels back and forth and at each reflection from the mirrors a portion of it leaks out of the cavity due to the imperfect reflectivity of the cavity mirrors. This is illustrated schematically for an empty cavity in Figure 3. Here, the intensity of the laser before the cavity is  $I_i$ , the intensity of the light travelling to the right inside the cavity (leaving the front mirror) is labelled  $I_f$ , and that of the light leaving the back mirror outside the cavity is labelled  $I_{b_n}$ , where  $n$  is the number of round-trips inside the cavity. For a cavity built from two identical mirrors with reflectivity  $R$ ,  $I_{b_n}$  can be calculated using equation (2).

## 2. The apparatus

$$\begin{aligned}
 I_{f_0} &= I_i(1 - R) \\
 I_{f_n} &= I_{f_{n-1}} \cdot R^2 \\
 I_{b_n} &= I_{f_n}(1 - R) \\
 I_{b_n} &= I_i(1 - R)^2 \cdot R^{2n} = I_i(1 - R)^2 \cdot e^{2n \ln(R)}
 \end{aligned} \tag{2}$$

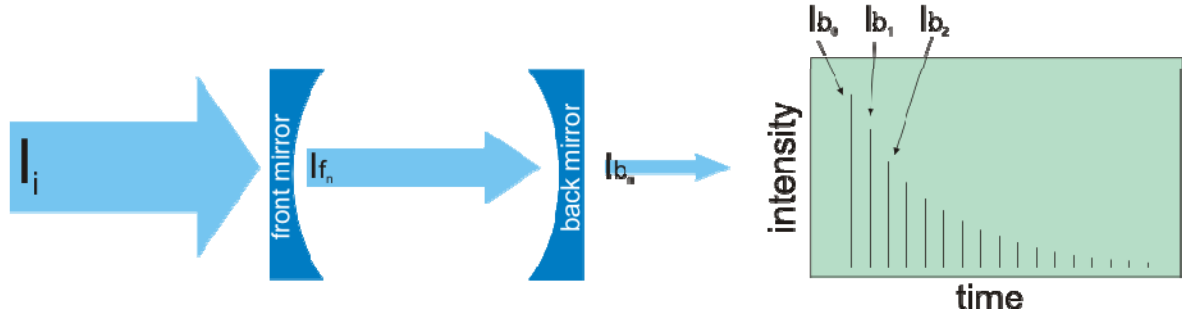


**Figure 3** The schematic view of cavity ring-down concept. A laser pulse with intensity  $I_i$  is coupled to the cavity made of two identical highly reflective mirrors. The light leaking out of the cavity at the back mirror is detected.

The elapsed time between two successive lines at the detector is the round-trip time (the time it takes for the light to make a complete detour inside the cavity) and is given by equation (3), where  $c$  is the speed of light and  $d$  is the spacing between the cavity mirrors.

$$t_r = \frac{2d}{c} \tag{3}$$

The number of round-trips can be calculated at each time according to:

$$n = \frac{t}{t_r} \tag{4}$$

Using equation (4) and rewriting equation (2) one obtains the behaviour of the intensity of light, which leaks out of the cavity from the back mirror as a function of time.

$$I(t) = I_i(1 - R)^2 \cdot e^{\frac{tc}{d} \ln(R)} \tag{5}$$

It should be noted that since the reflection losses only occur at the mirrors, for very short laser pulses, this function is essentially discrete and should be handled with extra care. During the time between successive reflections the intensity of light inside the cavity is not changing. Figure 4 shows the evolution of the light intensity inside the cavity for an empty cavity. As for practically used cavities ( $d <$

## 2. The apparatus

2m) the round-trip time is quite short ( $t_r < 14\text{ns}$ ) and usual detectors cannot resolve the signal temporary. Therefore, a smooth exponentially decaying curve is usually observed.

The ring-down time is defined as the time constant of the decaying signal and in the case of an empty cavity is given by equation (6). Here, we made use of the limit equality that for  $R \rightarrow 1$ ,  $\ln(R) \rightarrow R - 1$ .

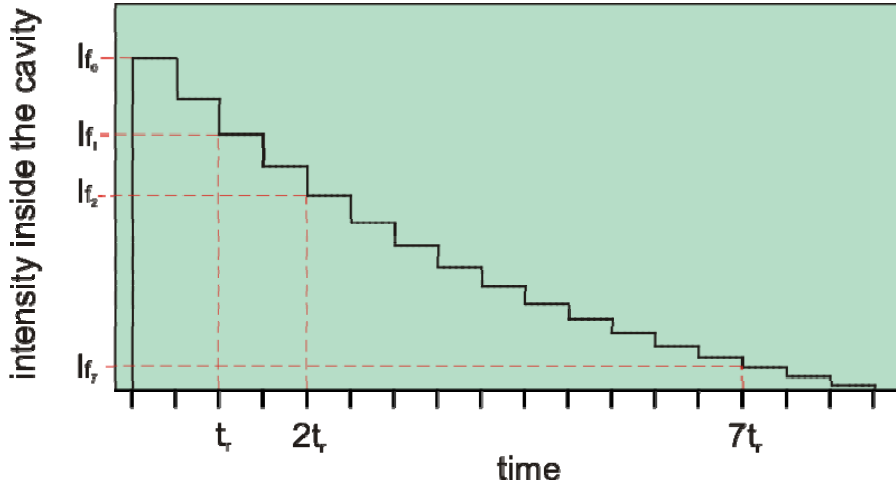


**Figure 4** Evolution of the light intensity inside an empty cavity with time.

$$I(\tau) = \frac{I(0)}{e}$$

$$\tau = \frac{-d}{c \ln(R)} = \frac{d}{c(1-R)} \quad (6)$$

The optical loss (intensity loss of the light) is determined by the unit-less value,  $L$ , and can be calculated according to equation (7).

$$L(\Delta t) = \frac{I(t) - I(t + \Delta t)}{I(t)} \quad (7)$$

For an empty cavity, where the losses have their origin only in imperfect reflectivity of the mirrors (or equivalently their non-zero transmission), the loss for each single pass is given by equation (8).

$$\Delta t = \frac{d}{c}$$

$$L = 1 - e^{\ln(R)} = 1 - R \quad (8)$$

## 2. The apparatus

---

By comparing equations (8) and (6) it becomes clear that the ring-down time,  $\tau$ , and,  $L$ , are connected. Equation (9) manifests this relation.

$$\tau = \frac{d}{cL} \Rightarrow L = \frac{d}{c\tau} \quad (9)$$

Introducing a sample into the cavity will cause additional optical losses. Obviously, the ring-down time becomes shorter. It can be shown that the ring-down signal will keep its exponential form. The light intensity undergoes a change by passing through the sample due to absorption and scattering. This attenuation for each round-trip can be determined from equations (10a) and (10b). Here,  $L_A$ , denotes absorption loss where,  $L_S$ , stands for scattering loss and,  $n$ , is the number of round-trips.

$$I_n = I_{n-1} \cdot e^{-L_A} \quad (10a)$$

$$I_n = I_{n-1} \cdot e^{-L_S} \quad (10b)$$

Similarly to equations (5) and (6), the following overall expression is derived for the ring-down time.

$$\tau = \frac{d}{c (-\ln(R) + L_S + L_A)} \quad (11)$$

Since both,  $L_A$ , and,  $L_S$ , have positive values, the ring-down time gets smaller due to introduction of a sample into the cavity. The resulting optical losses, which originate from the sample, can be put together in a single loss term,  $L_T = L_A + L_S$ , presenting the total loss of the sample. In Figure 5 the schematic ring-down signal is reproduced for comparison between the above mentioned cases.

A CRDS measurement is about determination of the initial ring-down time of the cavity without the sample of interest at the first step, and then the measurement of the ring-down time including the sample, as a function of wavelength. The optical losses arising from the sample can be then calculated according to equation (12).

$$L_T = \frac{d}{c} \left( \frac{1}{\tau} - \frac{1}{\tau_0} \right) \quad (12)$$

Alternatively and equally valid, one could determine each loss term by measuring the ring-down time once with and without the specific loss term included in the total loss. For example, in the case of supported clusters, the two measurements would be one with the bare substrate before deposition of metal

clusters and another after deposition. Inserting the recorded ring-down times into equation (12) the optical losses caused by the clusters can be found.

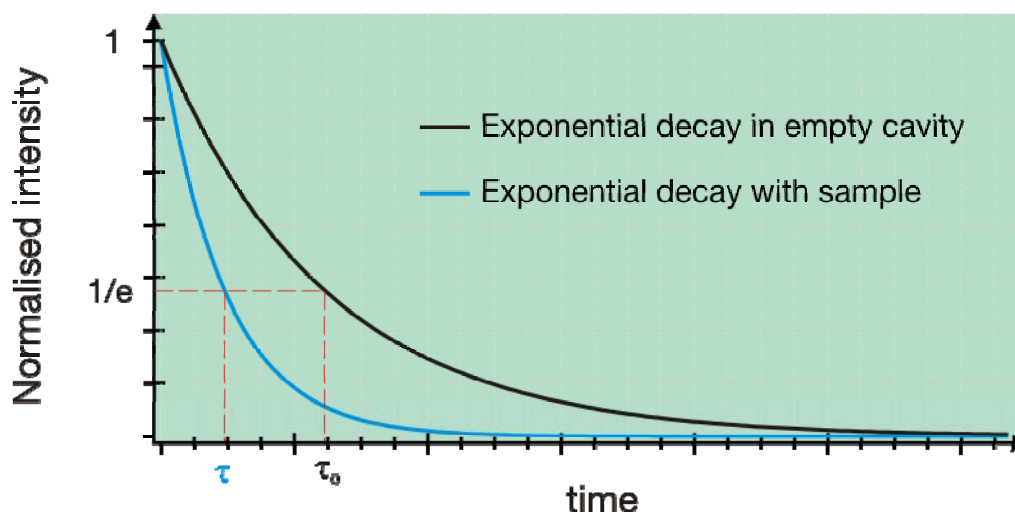


**Figure 5** The exponential decay for an empty cavity and a sample-containing cavity. The intensity scale is normalised for easier comparison. The ring-down time for an empty cavity is termed  $\tau_0$ .

### 2.2.2.3. Sensitivity

In this section the variables that influence the attainable sensitivity in CRDS are addressed. Examples are presented that highlight the fundamental limitations associated with a given experimental configuration. Unlike techniques that are typically limited by simple photon or ion-counting statistics, the sensitivity in CRDS can be dictated by a complex interplay of many variables.

In CRDS, as with other absorption methods, sensitivity is most generally discussed in terms of the minimum detectable fractional absorption *per pass*  $L_{\min}$ , since this allows an unambiguous definition for a specified number density and absorption cross section. For CRDS this is primarily given by equation (13).

$$L_{\min} = \Delta L = \Delta \left( \frac{d}{c \tau} \right) = \frac{d}{c \tau^2} \Delta \tau = L \frac{\Delta \tau}{\tau} \quad (13)$$

The use of effective absorption path length values are explicitly avoided (derived from the number of passes in the decay time) so are sensitivity limits in terms of inverse path length. In the former this value changes with the strength of the absorber and in the latter it is specific only for a given molecule with a fixed number density and absorption cross section. The fundamental limitation of the sensitivity of CRDS is determined by the accuracy of the ring-down time measurement. As mirror reflectivity increases, the fractional uncertainty in the decay time will generally decrease, which subsequently, leads to a higher sensitivity limit. This fact makes it essential to specify mirror reflectivities to

assess the sensitivity limit of a CRDS experiment. Although the theoretical limit is typically not achieved in most experiments, higher mirror reflectivities offer the simplest means of routinely achieving ppm (part per million) sensitivity levels without a great deal of effort. This point underscores the desirability and high priority of obtaining mirrors with the highest possible  $R$  value. For a given set of mirrors, cavity length, laser properties, and detectors are the primary variables that dictate the experimentally achievable sensitivity.

A convenient starting point for the discussion of CRDS sensitivity is the ideal model used in the derivation of the first-order exponential expression for the cavity decay time as introduced in section 2.2.2.2. In this model, the spatial length of the laser pulse injected into the cavity is assumed to be much shorter than the cavity round-trip length, leading to discrete pulses being transmitted through the exit mirror of the cavity with each round-trip. Consequently, interference effects are not important, and the intensity measured at the detector (usually a photomultiplier tube) will be a series of pulses of regularly decreasing intensity spaced in time by  $2d/c$  (see also Figure 3). In this picture, the ultimate sensitivity will depend explicitly on the ratio of the uncertainty in the number of round-trips of the light pulse to the total number of round-trips that occur during the actual *measurement* of the ring-down time. As an example, consider a cavity comprised of mirrors having equal reflectivities  $R = 99.995\%$  that are spaced 0.52 m apart. Then, one measures a decay time of about 34.7  $\mu\text{s}$ , during which time the light pulse makes more than 9000 round-trips. Here determination of the ring-down time to within a single round-trip (1 part in 9000) translates into a spectrometer absorption sensitivity of about 5.5 parts per billion (see equation (13)). If the individual pulses are well separated and it is possible to resolve the individual features of each pulse, the cavity decay time can be determined with a precision greater than the transit time of the light pulse across the cavity, that subsequently leads to increased sensitivity. This may most easily be achieved by assuring the length of the laser pulse ( $\sim 30$  cm/ns) is less than the round-trip length of the cavity; otherwise, the ability to discriminate individual light pulses is likely lost. For example, a laser pulse with 15 ns pulse-length would undergo ca. 5 round-trips in the same 0.52 m resonator in the duration of the laser pulse. In this case, the ring-down decay would at best exhibit periodic fluctuations on the round-trip time. While points on the decay spaced in time by  $2d/c$  still fit to a simple exponential, and the envelope of these fluctuations should decay exponentially. When averaged over the round-trip time, these fluctuations will produce steps rather than a smooth decay. This may hinder the precise determination of the decay time and so decrease the sensitivity.

In the discussion of absorption sensitivity, it is important to realize that in CRDS, as the absorption strength increases, the associated precision of the decay time measurement is reduced. A cavity with a base-line loss (empty cavity loss for gas phase measurements or alternatively the loss of the cavity plus that

of the substrate in the case of supported clusters) of 100 ppm with a 10 ppm absorber (total loss 110 ppm) is capable of determining the absorption to a precision of 1 ppm for a decay time precision of 1%, while a 400 ppm absorber in the same cavity (total loss 500 ppm) is only accurate to within 5 ppm for the same 1% decay time precision. In essence, the CRDS method becomes less accurate as the absorption intensity increases, since the decay time is shorter for larger absorption. This effect is demonstrated in Figure (6). In this regard, CRDS possesses a somewhat limited dynamic range, which is severely reduced as mirror reflectivity decreases. Typically, CRDS is unsuitable for measuring fractional absorption of greater than a few percent and is therefore complimentary to other methods, such as Fourier transform spectroscopy, that are capable of accurately measuring absorption that approaches 100%.

From this discussion, it is clear that extremely high levels of sensitivity can in theory be reached with the CRDS technique. In practice, however, there are many factors that limit the experimentally achievable sensitivity. Although CRD spectroscopy is significantly more sensitive than ‘conventional’ absorption spectroscopy, in general, it cannot compete with background-free detection techniques such as LIF, REMPI, and SHG. The CRD technique, however, can still be applied with success when the molecule’s excited state does not fluoresce (a prerequisite for LIF) or cannot be ionized (a prerequisite for REMPI). In high-pressure samples, such as flames and plasmas, CRDS can be successfully used to extract quantitative absolute concentration data, which is nearly impossible using either LIF (because of difficulties associated with collisional quenching of the fluorescing state) or REMPI (owing to difficulties in extracting the charged particles).

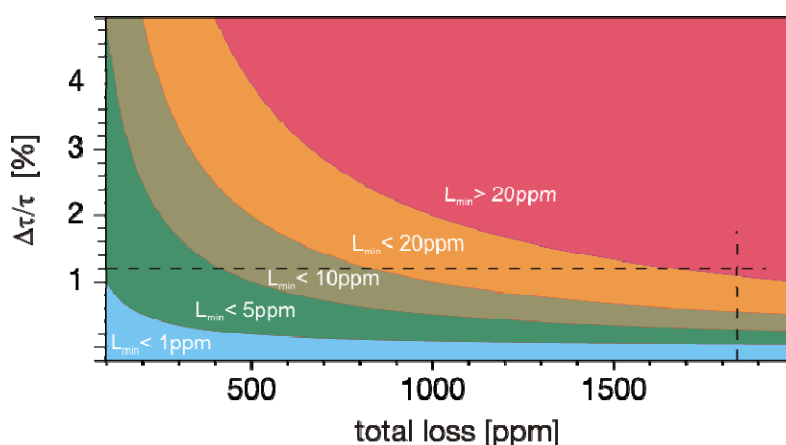


**Figure 6** The loss dependent sensitivity of CRDS. Regions of various  $L_{\min}$  values (the smaller the better) are differently coloured. The vertical broken line shows that for system of a specific loss, higher sensitivity can be achieved by higher precision in time measurement. The horizontal broken line shows that for a certain relative error of time measurement, the sensitivity is better for systems with lower loss.



### **2.2.2.4. Laser bandwidth and multi-exponential decays**

Here the frequency spectrum of the laser light trapped in the cavity is considered. In the event that CRDS is implemented for quantitative analysis of spectral intensities, the laser bandwidth with respect to the absorption line width must be taken into account, as is the case in conventional absorption spectroscopy (i.e., applicability of Beer's law). However, several phenomena, unique to CRDS, may occur that result in non-exponential cavity decays and subsequent distortion of the spectral intensities.

In the case of an empty cavity, the ring-down time is dictated by the frequency-dependent reflectivity of the mirror coatings, and there will always exist, a range of decay times for a given bandwidth. The more broadband the laser light, the larger this range of decay times, and hence, the lower the ultimate sensitivity. If each frequency of the input bandwidth is not equally attenuated with each pass, accurate values for the cavity loss are not obtained from fits to a single exponential. Similarly, when a sample is placed into the cavity, accurate absorption intensities are not obtained.

In the case of molecular absorption, one must consider the specific interaction of the input laser spectral content with the absorbing species. In the case of molecular absorption, where the line width of the molecule is less than that of the laser light that is coupled into the cavity, only frequency components resonant with the molecular transition are absorbed as the laser pulse circulates in the cavity. This effect leads to decays that can deviate significantly from a single exponential and results in the under calculation of the absorption intensity. If the light exiting the cavity were dispersed into its various frequency components, different decay times would be measured for the resonant and non-resonant components, with subsequent increased absorption for the resonant components. Hodges et al.<sup>63</sup> have demonstrated experimentally that in cases where the laser light consists of multiple modes and is broader than the line width of the absorber, its frequency spectrum must be explicitly included to extract accurate absolute absorption intensities.

### **2.2.2.5. Cavity ring-down mirrors**

The reflectivity of the mirrors, which form the cavity, is of high importance as was discussed in section 2.2.2.3. The required reflectivity of 99.995% or more, is much higher than that achieved with normal metallic mirrors, due to absorption losses. Therefore, dielectric mirrors must be used. The function of dielectric mirrors is based on the interference of light reflected from the different layers of a dielectric stack. This is the same principle used in multi-layer anti-reflection coatings, which are dielectric stacks designed to minimise rather than maximise reflectivity. Simple dielectric mirrors consist of a stack of layers with a high refractive index interleaved with layers of a low refractive index. The thicknesses

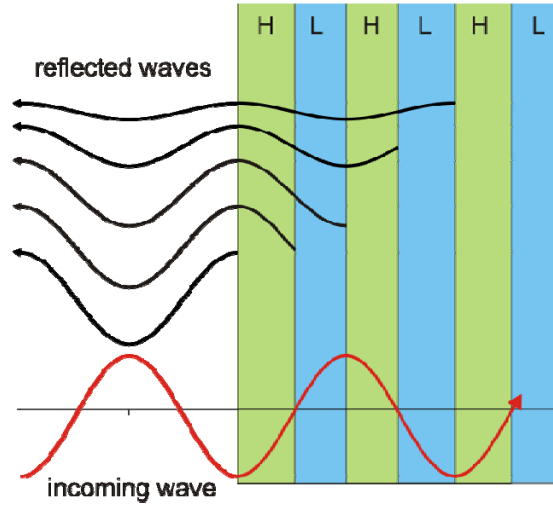


**Figure 7** The schematic view of a dielectric mirror. Layers of high (H) and low (L) refractive index are differently coloured. The thickness of each layer is equal to the quarter of the desired wavelength.

of the layers are chosen such that the path-length differences for reflections from different high-index layers are integer multiples of the wavelength for which the mirror is designed. The reflections from the low-index layers have exactly half a wavelength in path length difference. There is a 180-degree phase shift at a low-to-high index boundary, compared to a high-to-low index boundary, which means that these reflections are also in phase. In the case of a mirror at normal incidence, the layers have a thickness of a quarter wavelength<sup>48</sup>. This concept can be demonstrated analytically by taking a linearly polarised light wave and determining the wave equations of the reflected waves. The incoming light wave can be described by its electrical field as in equation (14) where  $k$  is the wave vector and  $\omega$  is the radial frequency of the light.

$$\vec{E} = \vec{A} \cdot \cos(\omega t - kx) \quad (14)$$

It is important to consider that reflection from an optically denser medium changes the phase of the wave by  $\pi$ . Figure 7 shows the schematic view of a multilayer dielectric mirror for normal incidence. Taking the interface between the first layer and air (or vacuum) as the origin of the  $x$  axis ( $x = 0$ ), the reflected wave at this point will be described by equation (15).

$$\vec{E}_1 = \vec{A}_1 \cdot \cos(\omega t + \pi) \quad (15)$$

At the next interface the portion of the light which was transmitted through the first layer is reflected. The wave reflected from this interface keeps its phase and at the interface to air ( $x=0$ ) it has travelled a distance of,  $2 \times \lambda/4$ . At the next interface the reflected wave undergoes a 180 degrees phase change and should

put back a distance of a full wavelength to get to  $x=0$  position. Note that the amplitude of the reflected waves is smaller for deeper layers. The reflected waves from each interface can be described as follows:

$$\overline{E}_n = \overline{A}_n \cdot \cos\left(\omega t + n\pi - (n-1)k\frac{\lambda}{2}\right) \quad (16)$$

Since,  $k = 2\pi/\lambda$ , equation (16) can be rewritten to equation (17) and it can be seen that all the reflected waves are in phase and consequently their interference is fully constructive.

$$\overline{E}_n = \overline{A}_n \cdot \cos(\omega t + n\pi - (n-1)\pi) = \overline{A}_n \cdot \cos(\omega t + \pi) \quad (17)$$

Because the thickness of the dielectric layers is tuned for a specific wavelength, these mirrors have a narrow range of high reflectivity which is about  $\pm 5\%$  of the central wavelength<sup>48, 64</sup>. It is not possible to cover an extended range of light wavelengths with a single mirror. A list of the dielectric mirrors (cavity ring-down mirrors) which are used in this work is presented in table 1.

central wavelength	430	480	520	570	610	640	nm
available range	410-457	451-515	495-559	539-605	589-669	625-690	nm

**Table 1** The list of the cavity ring-down mirrors used in this work. The central wavelengths and the available wavelength ranges are given. Note that all adjacent mirrors have an overlap range. For some of the mirrors the full available range could not be used due to other practical difficulties.

### 2.2.2.6. Cavity modes and mode matching

Cavity modes are field distributions which reproduce themselves (apart from a possible loss of power) after one round-trip. They can exist whether or not the resonator is stable, but the mode properties of unstable resonators are fairly sophisticated. In the following, only modes of stable resonators are considered. For optical cavities comprised of two identical spherical mirrors, the cavity modes (resonator modes) are Laguerre–Gaussian modes. The simplest of those are the Gaussian modes, where the field distribution is defined by a Gaussian function. The evolution of the beam radius and the radius of curvature of the wave-fronts is determined by the details of the cavity, which dictates the boundary conditions. A collection of some Laguerre–Gaussian profiles is presented in Figure 8.

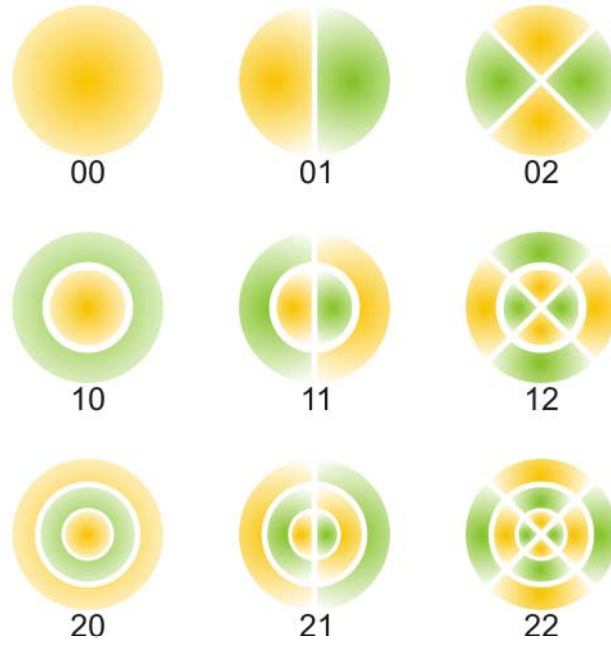


**Figure 8** Some Laugerre-Gaussian profiles. The indices,  $(mn)$ , stand for the number of radial ( $m$ ) and angular ( $n$ ) nodes. Change of colour indicates  $180^\circ$  rotation of the electric field vector.

The fundamental (or longitudinal) mode spacing  $\nu_0$  (the frequency difference between adjacent standing waves within the cavity), of the cavity is given by  $c/2d$ , where  $d$  is the mirror spacing. Frequencies for the higher order transverse modes are calculated using equation (18) where  $q$  is the longitudinal mode index,  $m$  and  $n$ , are the transverse mode indices, and,  $r$ , is the mirror radius of curvature <sup>65</sup>.

$$\nu_{qmn} = \nu_0 \left[ q + \frac{2}{\pi} (m + n + 1) \tan^{-1} \left( \left[ \sqrt{\frac{2r}{d}} - 1 \right]^{-1} \right) \right] \quad (18)$$

For several compelling reasons, the lowest order transverse mode,  $TEM_{00}$ , is the most widely used. The flux density is ideally Gaussian over the beam's cross-section for  $TEM_{00}$ . In addition there are no phase shifts in the electric field across the beam in contrast to the other modes (see Figure 8), and so, spatial coherency is close to complete. Furthermore, the beam's angular divergence is the smallest and it can be focussed down to the smallest-sized spot <sup>64</sup>. In the following a more detailed description of Gaussian beams and there properties is given.

The spatial extension of a Gaussian beam with wavelength  $\lambda$  propagating along  $z$ -axis is given by equation (19). Here  $\omega_0$  is the radius of the beam at the origin of the axis ( $z=0$ ). At this point the beam has its smallest size, called "beam waist".

$$\omega(z) = \omega_0 \sqrt{1 + \left( \frac{z\lambda}{\pi\omega_0^2} \right)^2} \quad (19)$$

A simple plot of  $\omega(z)$  against  $z$ , is shown in Figure 9 where the relevant parameters are introduced and will be explained. At each plane, perpendicular to the propagation axis, the beam has a Gaussian profile. The width reaches its minimum at the waist and then expands again. The same amount of energy needs to be distributed in each plane (no energy loss while propagating). As a consequence, the maximum irradiance is achieved at the beam waist. The distance at which the width of the beam spreads,  $\sqrt{2}$  times the beam waist, is known as the Rayleigh range, and can be shown using equation (19) that:

$$z_R = \frac{\pi\omega_0^2}{\lambda} \quad (20)$$

The divergence of the beam is shown in Figure 9 by  $\theta$ . In the paraxial approach, where the beam's transversal dimension is small (which means that the angular spectrum of the amplitude distribution is located around the axis of propagation), the divergence is given by equation (21).

$$\theta \cong \tan(\theta) = \frac{\lambda}{\pi\omega_0} \quad (21)$$

From equation (21), it is seen that the divergence and the beam waist are reciprocal parameters. This means, that large values of the beam waist results in lower divergence, and vice versa.

Another important parameter, concerning Gaussian beams, is the radius of curvature of the wavefront. Its dependence with,  $z$ , is given through equation (22).

$$R(z) = z \left[ 1 + \left( \frac{\pi\omega_0^2}{z\lambda} \right)^2 \right] \quad (22)$$

Equation (22) suggests that when  $z$  tends to infinity, a linear variation with,  $z$ , is achieved, which is typical for a spherical wavefront originated at  $z=0$ , e.g. coming from a point source. However, the radius of curvature is infinity at the beam waist. This means, that at this position, (beam waist) the wavefront is plane. Figure 10 illustrates this dependency.

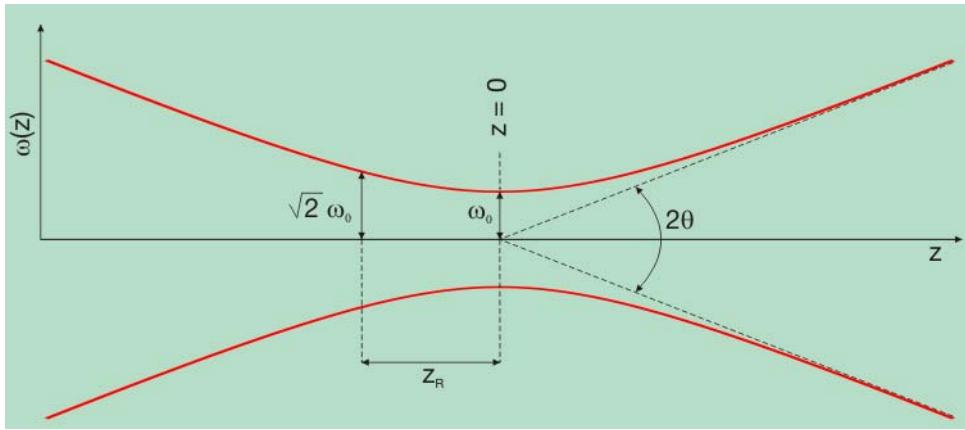


**Figure 9** Gaussian beam with  $\omega(z)$  as a function of propagation distance  $z$ . indicated are: Rayleigh range  $z_R$  and beam divergence  $\theta$ .

Again from equation (22), the position of the minimum radius of curvature with regard to the beam waist, can be derived as in equation (23). Note that, the unfortunate similar notation of  $z_{R_{\min}}$  (the  $z$  value at which the minimum radius of curvature occurs) and  $z_R$  (Rayleigh range) may cause confusion.

$$z_{R_{\min}} = \pm \frac{\pi \omega_0^2}{\lambda} = \pm z_R \quad (23)$$

As already mentioned at the beginning of this sub-section, there are many reasons why it is desired to work with Gaussian laser beams ( $TEM_{00}$ ). The case of CRDS is no exception. However, more care should be taken, since the laser beam has some properties dependent on the laser system, and the beam parameters do not necessarily match those of the ring-down cavity. In the following, the behaviour of a Gaussian beam inside the cavity is first described and the process of mode matching is then introduced.

Being confined to an optical cavity, a Gaussian beam can only be stable if its parameters match those dictated by the cavity. For example, the radius of curvature of the beam should match that of the cavity mirrors at the mirror position and so, the position of the beam waist inside the cavity as well as its size, and consequently the divergence of the beam are predefined by the cavity. For an optical resonator which is built out of two identical spherical mirrors with radius of curvature,  $R_M$ , and spacing,  $d$ , the beam waist of the stable Gaussian beam, called “cavity waist”, can be calculated using equation (24).

$$\omega_{0c} = \sqrt[4]{\frac{d \lambda^2}{4 \pi^2} (2 R_M - d)} \quad (24)$$

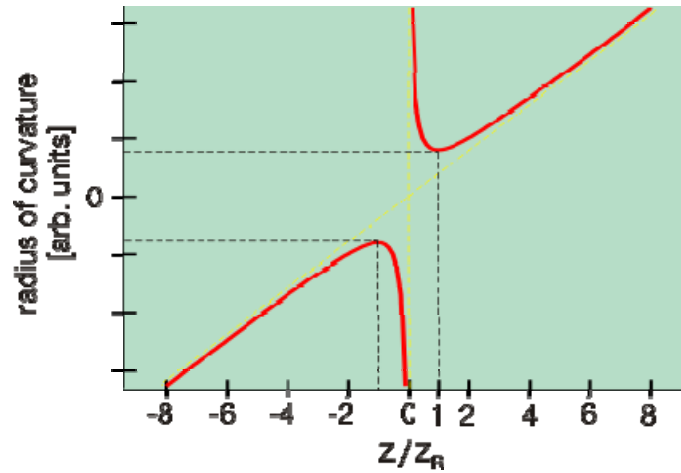


**Figure 10** Radius of curvature of a Gaussian beam around the beam waist. The beam reaches a minimum of the radius of curvature at distances  $+z_R$  and  $-z_R$  from the beam waist.

Knowing the cavity waist, all the other parameters are easily calculated from equations (19-23). In order to excite only the  $TEM_{00}$  mode of the cavity, it is required that the laser beam, which is coupled into the cavity has the same beam parameters. This is generally not the case and hence, a process of mode matching is required, where the laser beam is modified prior to the cavity, so that the beam parameters match.

It is possible to condense the properties of a Gaussian beam in a single complex value, which is called the complex beam parameter and is termed,  $q$ . As expected, this value varies with  $z$  and is given through equation (25).

$$\frac{1}{q(z)} = \frac{1}{R(z)} - \frac{i\lambda}{\pi\omega(z)^2} \quad (25)$$

For a mode matched system, the complex beam parameter of the incoming laser beam should be equal to that of the Gaussian beam, stable in the cavity. When the beam is propagating through air or vacuum, it is trivial to follow the evolution of  $q(z)$ . However, a beam passing through various optical elements is manipulated in a more complex manner. Matrix optics has been well established a long time ago <sup>66, 67</sup>. Within the paraxial approach, it provides a strong tool by describing the effect of an optical system as the cascade operation of its components. In the so called ray transfer matrix analysis, each optical component is represented by a matrix and the evolution of the beam through the whole system, is achieved by transformation of the initial parameters of the beam by the resultant matrix product. In paraxial optics, the light is presented by its height and its angle with respect to the optical axis of the system. These two parameters can be arranged as a column vector. The simplest mathematical object relating two vectors (beside the multiplication by a scalar quantity) is a matrix. In this case the

## 2. The apparatus

---

transfer matrix is a 2x2 matrix, that is usually called *ABCD* matrix because its elements are labelled as *A*, *B*, *C*, and *D*. The relation can be written as:

$$\begin{pmatrix} h_2 \\ a_2 \end{pmatrix} = \begin{pmatrix} A & B \\ C & D \end{pmatrix} \begin{pmatrix} h_1 \\ a_1 \end{pmatrix} \quad (26)$$

In equation (26), the column vector with index 1 stands for the input ray, and index 2 stands for the output ray. An interesting result of equation (26) is obtained by definition of a new variable as the ratio between height and angle. From Figure 11, this parameter coincides with the distance between the ray-optical axis interception, and the position of reference for the description of the ray. This distance is interpreted as the radius of curvature of a wavefront, departing from that intersection point and arriving to the plane of interest, where the column vector is described. When this radius of curvature is obtained by using the matrix relation, the following result is found:

$$R_2 = \frac{AR_1 + B}{CR_1 + D} \quad (27)$$

This expression is known as the *ABCD* law for the radius of curvature. It relates the input and output radii of curvatures for an optical system described by the corresponding *ABCD* matrix.

The complex beam parameter of a Gaussian beam is the complex equivalent of the radius of curvature and is sometimes called the complex radius of curvature. The so called *ABCD* law for Gaussian beams is the result of applying the *ABCD* law for the radius of curvature, to the complex radius of curvature, and is given by equation (28).

$$q_2 = \frac{Aq_1 + B}{Cq_1 + D} \quad (28)$$

The results of the application of the *ABCD* law can be written in terms of the complex radius of curvature and the Gaussian width by properly taking the real and imaginary parts of the resulting complex radius of curvature.

When a Gaussian beam propagates along an *ABCD* optical system, its complex radius of curvature is changed according to the *ABCD* law. However, there exists an invariant parameter that remains the same throughout the whole optical system. This parameter is defined as:

$$\theta\omega_0 = \frac{\lambda}{\pi} \quad (29)$$



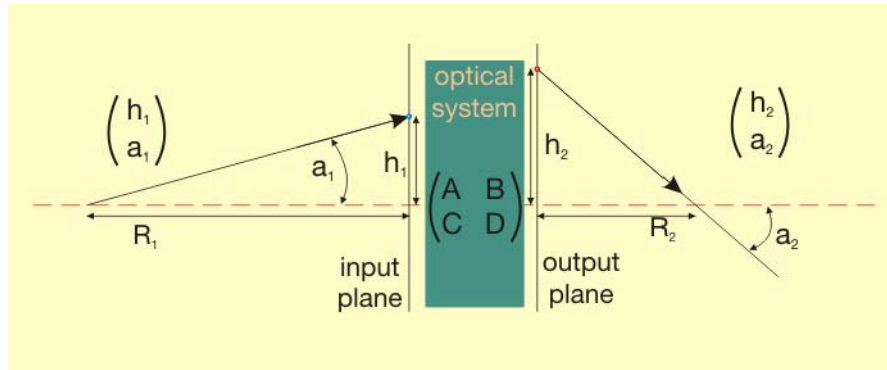


**Figure 11** The optical system is represented by the  $ABCD$  matrix. The input (blue spot) and the output (red spot) rays are characterised by their height and their slope with respect to the optical axis. The radius of curvature is related to the distance between the intersection of the ray with the optical axis and the input or the output planes.

A list of transfer matrices for various optical elements is presented in table 2. For some transfer matrices, extra care is required, e.g. the radius of curvature of a mirror can be either positive or negative, depending from which side the ray is approaching. The necessary hints are included in the right column of table 2.

The process of mode matching has two main steps. First, the input and output complex beam parameters (complex radius of curvatures)  $q_{in}$  and  $q_{out}$  should be determined. In the case of CRDS, this would translate in knowing the complex parameter of the beam prior to the ring-down cavity ( $q_{in}$ ), and the complex beam parameter of the  $TEM_{00}$  mode of the ring-down cavity ( $q_{out}$ ). The next step is about choosing the right  $ABCD$  matrix, which makes the suitable transformation. Usually a limited number of optical elements are available, like a set of lenses with fixed focal length, and mirrors of given radius of curvature. Therefore, the single  $ABCD$  matrices for the elements are fixed and known beforehand. The only transfer matrix, which has an available variable, is the free space propagation. Hence, the main challenge is to find the proper distances that the beam needs to travel between the elements. However, it is not always possible to find a solution and one may need to replace some of the optics (e.g. lenses with different focal length and so on).

A hidden assumption in the discussion of mode matching, as introduced previously, is that the laser beam is a Gaussian beam. This, however, is quite often not true and there are not many laser systems which deliver the  $TEM_{00}$  mode. Fortunately, it is possible to clean the beam from all the non-Gaussian components, through spatial filtering, so that only the fundamental mode is remaining.

Spatial filtering is based on Fourier optics and is commonly used to clean up the laser beam profile, in order to obtain a beam, which contains only a single

## 2. The apparatus

Optical action	ABCD matrix	Notes
Propagation in free space or in a medium with constant refractive index	$\begin{pmatrix} 1 & l \\ 0 & 1 \end{pmatrix}$	$l = \text{distance}$
Reflection from a flat mirror	$\begin{pmatrix} 1 & 0 \\ 0 & 1 \end{pmatrix}$	identity matrix
Refraction at a flat interface	$\begin{pmatrix} 1 & 0 \\ 0 & \frac{n_1}{n_2} \end{pmatrix}$	$n_1 = \text{initial refractive index}$ $n_2 = \text{final refractive index}$
Reflection from a curved mirror	$\begin{pmatrix} 1 & 0 \\ -\frac{2}{R} & 1 \end{pmatrix}$	$R = \text{radius of curvature, } R > 0 \text{ for concave}$
Passing through a thin lens	$\begin{pmatrix} 1 & 0 \\ -\frac{1}{f} & 1 \end{pmatrix}$	$f = \text{focal length of lens where } f > 0 \text{ for convex/positive (converging) lens. Valid if and only if the focal length is much greater than the thickness of the lens.}$
Refraction at a curved interface	$\begin{pmatrix} 1 & 0 \\ \frac{n_1 - n_2}{R \cdot n_2} & \frac{n_1}{n_2} \end{pmatrix}$	$R = \text{radius of curvature, } R > 0 \text{ for convex (centre of curvature after interface)}$ $n_1 = \text{initial refractive index}$ $n_2 = \text{final refractive index.}$

**Table 2** Ray transfer (ABCD) matrices for common optical processes. The right column includes some hints about the matrices which need extra care while being applied.

transverse mode of the laser's resonator. To achieve this aim, the beam is focussed through a lens. At the focal plane of the lens the two-dimensional Fourier transform of the transverse intensity distribution of the beam is formed. In this context, the focal plane is called the transform plane. The light at the very centre of the transform pattern corresponds to a perfect, wide plane wave. Other light correspond to the structure of the beam, with light further from the central spot corresponding to more complex structures. It is possible to manipulate this pattern at the focal plane and by back transformation of the beam (letting it through another lens), reform a collimated beam with a new transverse profile. The most common way of doing this, is to place a pinhole at the focal plane that allows the desired light (in the centre) to pass, while blocking the rest. This way an almost perfect Gaussian beam can be achieved<sup>64</sup>.

Both, mode matching and spatial filtering have been performed in this work. The details of the elements are presented in section 2.2.7., where the schematic view of the optical setup is introduced. Before, some information on the ring-down cavity and the laser system are given in the next sections.

### 2.2.3. CRDS under UHV conditions

As already mentioned in section 2.1.3, it is necessary that the samples stay in ultra-high vacuum (UHV). In this section the implementation of CRDS in UHV conditions is discussed.

Principally, there are no problems concerning applicability of the method under UHV conditions. However, a few technical difficulties need to be overcome. One issue is that the laser source cannot be located inside the vacuum, while at least the inner side of the cavity ring-down mirrors needs to be in vacuum. This is required, since introducing any component other than the sample of interest, into the ring-down cavity, will increase the overall optical loss, and so diminish sensitivity (see Figure 6). There are two possible approaches to this issue. One possibility is to use the mirrors as vacuum windows, where one side is inside the vacuum chamber and the other side is outside. The main disadvantage of this approach is the problem with the vacuum sealing. Here the mirror coating may be damaged by sealing components, which are in direct contact with the mirror's surface. The other possibility is to have the cavity ring-down mirrors completely inside the vacuum. The main challenge concerning this approach is the accessibility of the mirrors for alignment, once in vacuum.

Another issue is concerning the samples. Performing CRDS under vacuum, using a single cavity at a time is less attractive. In this case, for every cavity set, the vacuum chamber should be vented, regardless which of the two above-

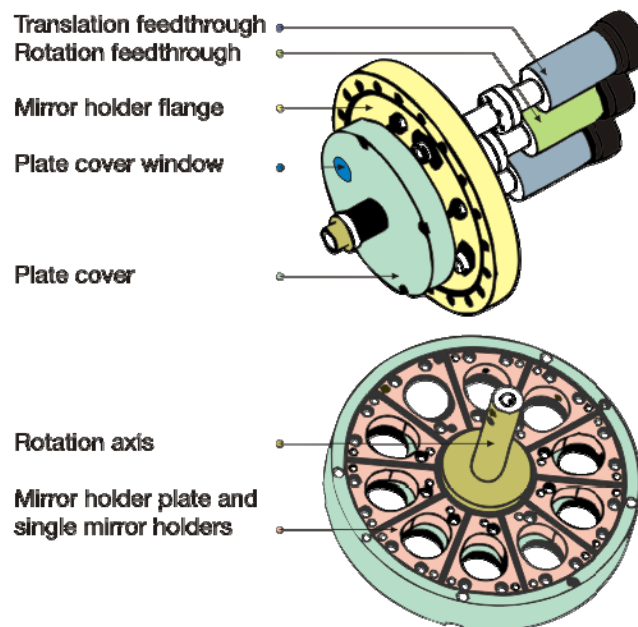


**Figure 12** The UHV compatible mirror holder. Individual parts are differently coloured and labelled. With this mirror holder it is possible to install up to ten cavities into vacuum and align them from outside.

mentioned approaches are taken. Consequently, the sample is contaminated while the mirrors are being replaced. This problem would be overcome by simply replacing the sample with a new one as well, however, by doing so the direct comparison between data set is not unambiguously possible. From this discussion it becomes clear that the best solution would be to have all the cavities available in vacuum. In the following a UHV compatible mirror holder is introduced as the solution to these problems.

A schematic view of the mirror holder is illustrated in Figure 12. The function of the mirror holder can be explained as the following. A plate, which contains ten single mirror holders, is pressed against a plate cover using a spring. The plate cover, has a window (a hole), which is slightly bigger than the aperture of the mirrors. The plate and the plate cover, are mounted on a vacuum flange (mirror holder flange), upon which three vacuum feedthroughs and a vacuum window ( $\text{CaF}_2$  window) are mounted. The flange window and the window of the plate cover are on the same optical axis. The central feedthrough is a rotation feedthrough and is used to rotate the mirror plate from outside of the vacuum. This can be used to bring any of the ten single mirror holders in front of the window of the plate cover. The other two feedthroughs are translation feedthroughs and serve as alignment screws, to tilt the whole mirror holder plate. Using a pair of this mirror holder, it is possible to mount up to ten cavity ring-down mirrors on each and once in vacuum, also align them to form a high-finesse cavity, for each pair. As a result, it is possible to measure a sample over the range of ten different cavities without venting the chamber, leading to more reliable and faster measurements. The detailed plans of the mirror holder are included in Appendix A.

### 2.2.4. Laser system

An important part of any spectroscopic setup is the light source. In CRDS, a tuneable laser source is required. Optical parametric oscillator (OPO) lasers are a good choice, since they deliver a broad range of wavelengths. In this work an OPO laser has been used for spectroscopic studies, of which a brief description is included here.

The optical parametric oscillator makes use of nonlinear optical effects, in order to obtain tuneable emission. Here the parametric interaction involves three waves. A high frequency wave, called the pump, with a frequency,  $\omega_p$ , interacts via the nonlinear response of a medium with a pair of lower frequency electromagnetic waves, called the signal and idler, at frequencies,  $\omega_s$  and  $\omega_i$  respectively, to produce amplification at these two frequencies. By varying parameters associated with the interaction, the signal and idler frequencies can be changed, resulting in a tuneable source of radiation. The three frequencies are connected by the relation given in equation (30).

$$\omega_p = \omega_s + \omega_i \quad (30)$$

Equation (30) implies energy conservation. For the interaction of the three waves to be effective, it is required that the momentum is conserved as well. This can be mathematically expressed through equation (31), where  $k_p$ ,  $k_s$  and  $k_i$  stand for the wave vectors of the pump, signal, and idler wave, respectively.

$$k_p = k_s + k_i \quad (31)$$

When equation (31) is satisfied, the three waves are said to be *phase matched*. This effect is responsible for the tunability of the OPO. By varying the angle between the three waves for a nonlinear interaction, the frequencies of the signal and idler wave satisfying the conservation equation can be varied. A complete treatment of the OPO process can be found for example in the laser handbook, edited by Arecchi and Schulz-Dubois<sup>68</sup>. Compared to dye lasers, OPO lasers are more convenient to operate because the time consuming dye solution changing is avoided.

In this work a midband OPO (GWU VisIR2/400 ULD), pumped with the third harmonic of a Nd:YAG laser (Innolas Spitlight-1200), with a bandwidth below 10 cm<sup>-1</sup>, and a pulse duration between 3-7 ns, and a repetition rate of 20 Hz is used. The output energy varies between 10 and 20 mJ per pulse, depending on the wavelength. The profile of the beam is nearly rectangular and has a size of about 8x8 mm<sup>2</sup>, and is linearly polarised.

### 2.2.5. Detection unit

The light leaking out of the ring-down cavity has a much lower intensity, compared to the light which approaches the cavity, therefore, a sensitive light detector should be employed. In addition, the detector needs to be fast, compared to the ring-down time, in order to avoid the manipulation of the exponential decay of the cavity via the time constant of the detector. Photomultiplier tubes (PMT) are sensitive photon detection devices, which can be quite fast. These detectors multiply the current produced by incident light, by as much as 100 million times in multiple dynode stages, enabling individual photons to be detected, when the incident flux of light is very low. A schematic over-view of a PMT is shown in Figure 13. The function of the PMT can be explained as the following. Photomultipliers are constructed from a glass envelope with a high vacuum inside, which houses a photocathode, several dynodes, and an anode. Incident photons strike the photocathode material, which is present as a thin deposit on the entry window of the device. Free electrons are produced as a consequence of the photoelectric effect. These electrons are directed, by the focusing electrode, toward the electron multiplier, where electrons are multiplied

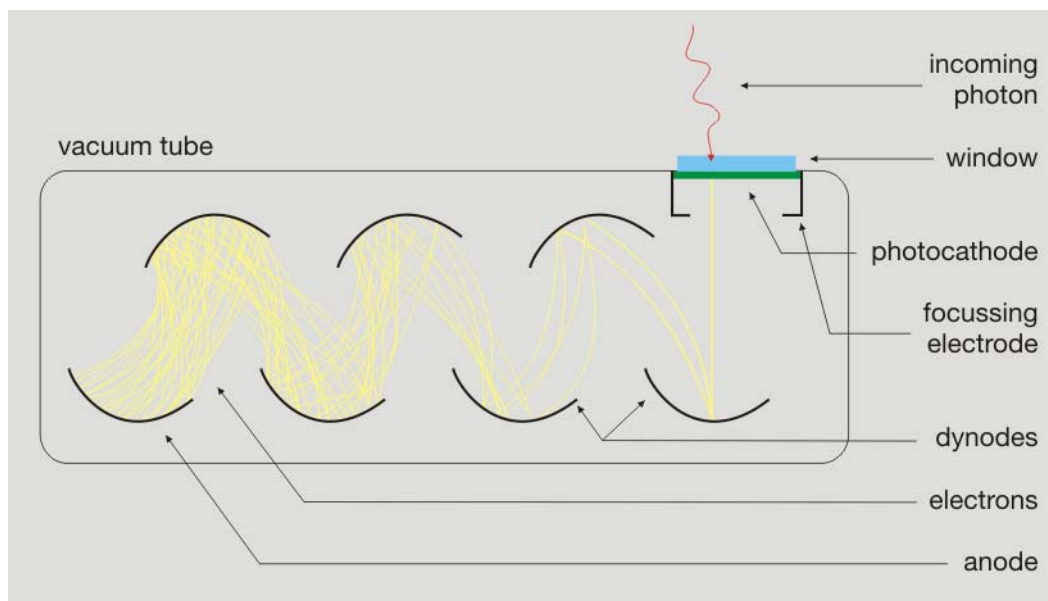


**Figure 13** The operation principle of photomultiplier tube is shown. A photo-electron which is produced at the photocathode as the photon strikes on it is focussed towards the first dynode. There further electrons are ejected through secondary emission and are accelerated towards the next dynode and so on. At the anode a measureable current of electrons is achieved. The whole process takes place in the vacuum tube.

by the process of secondary emission. The electron multiplier consists of a number of electrodes called, *dynodes* (see Figure 13). Each dynode is held at a more positive voltage than the previous. The electrons leave the photocathode, having the energy of the incoming photon (minus the work function of the photocathode). As the electrons move toward the first dynode, they are accelerated by the electric field and arrive with much greater energy. Upon striking the first dynode, more low energy electrons are emitted, and these electrons in turn are accelerated toward the second dynode. The geometry of the dynode chain is such, that a cascade occurs with an ever-increasing number of electrons being produced at each stage. Finally, the electrons reach the anode, where the accumulation of charge results in a sharp current pulse, indicating the arrival of a photon at the photocathode.

In this work a photomultiplier tube is used (Hamamatsu 7732-10), which has a broad range of operation, from 190 nm up to 900 nm. The light leaking out of the back mirror is guided by a pair of silver mirrors, and then focussed on to the PMT. The output of the PMT is fed into an 8 bit digital storage oscilloscope (LeCroy Waverunner 6051), which can save the data on the internal hard drive. Online monitoring of the signal quality is performed through a self-developed *LabView* program. The recorded data are then transferred to a desktop, where the final treatment takes place using self-developed procedures in *IgorPro*.

### 2.2.6. Application of CRDS to solid samples

CRDS has been mainly applied to investigate gas phase samples. Its application to solid samples is underdeveloped due to the fact that a solid sample generally introduces high optical losses through reflection and scattering. This increased loss affects the sensitivity of the method as discussed in section 2.2.2.3. (see Figure 6). In spite of this challenge, some solid phase approaches have been reported. There are two main methods for application of CRDS to a solid sample, namely the transmission and the reflection mode. In transmission mode, the sample is placed inside the cavity and the light passes through it, as in the gas phase CRDS. Here, however, special care should be taken to minimise the reflection losses. This can be achieved by aligning the sample either perpendicular to the optical axis, so that the reflected light stays inside the cavity, or at the Brewster's angle to the optical axis, where the reflection of the p-polarised light is theoretically zero. In reflection mode, the sample is usually located inside the cavity and the light reflected from the surface of interest, is kept in the cavity. Here, folded cavities are usually used, where the optical axis is folded. Since in this case the reflectivity of the sample should be high, either dielectric mirrors are used as the substrate, on which the sample of interest is directly deposited (an expensive method), or the total internal reflection in a prism is used. In the latter case, the sample of interest is brought on to the surface of the prism, where the total internal reflection takes place and the attenuation in the beam intensity is caused by absorption of the evanescent wave. A short summary of these methods is given here.

#### 2.2.6.1. Reflection mode condensed phase CRDS

Here, only evanescent wave CRDS is considered, since this is the most widely (perhaps the only) applied method. Pipino *et al.* were the first group who made use of total internal reflection (TIR) and evanescent wave (EW) absorption in cavity ring-down spectroscopy<sup>69</sup>. The very concept of the technique can be described according to Figure 14. A folded cavity is arranged with the inclusion a high quality prism, so that the two sides of the prism are normal to the light propagation axis. This way, the reflected light is maintained inside the cavity. At the third face of the prism, where the total internal reflection occurs, an evanescent wave is formed which may be absorbed by the molecules and/or thin film which are deposited at this surface. Due to the limited penetration depth of the EW this technique is highly surface sensitive. There are other alternative configurations to this method. For example, it is possible to coat the two prism sides with multilayer films and form a dielectric mirror<sup>70</sup>. Here, the cavity consists of the prism itself, and the problem with the reflection at these surfaces is circumvented completely. Another possibility is to use a Pellin-Broca prism and align it in a way that the light reaches the prism surface at the Brewster's angle<sup>71</sup>.

The main disadvantage of this technique lays in the fact, that for each new sample the prism needs to be either cleaned, which not always is trivial ( e.g. in

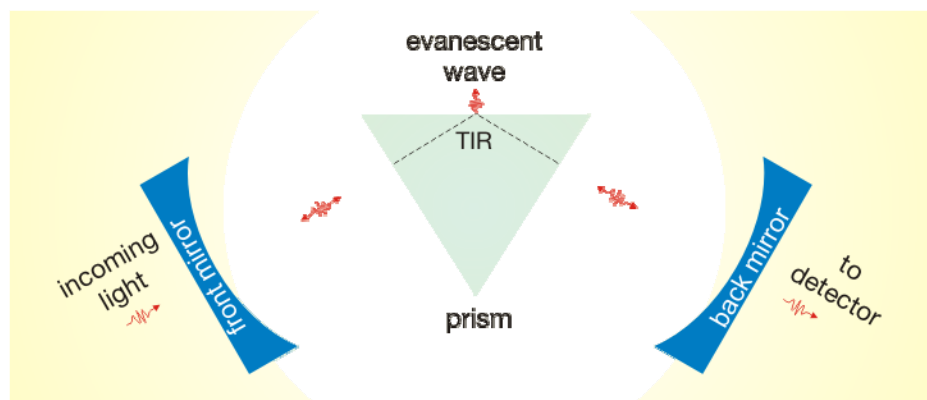


**Figure 14** Schematic over-view of an EW-CRDS configuration. The total internal reflection at the surface of a high quality prism and the formation of evanescent wave is used to investigate the optical properties of molecules and/or films on the surface of the prism. Photons are shown by wavy arrows. The light path inside the prism is indicated by the broken line.

the case of size-selected clusters) and is usually costly, or replaced. However, there have been developments in order to clean the prisms reliably e.g. by plasma ashing<sup>72</sup>, and to reuse them several times .

### 2.2.6.2. Transmission mode condensed phase CRDS

The first report about application of CRDS to condensed phase samples, in reflection mode, is that of Engeln *et al.* where the absorption spectrum of a 20-30 nm thick  $C_{60}$  film deposited on a 3 mm thick ZnSe substrate<sup>73</sup> was measured. They inserted the substrate into the cavity, perpendicular to the optical axis of the linear cavity. This configuration has been used by other groups as well<sup>74-77</sup>. In this case the cavity is actually divided in three cavities; one formed by the front mirror and the substrate's surface, one formed by the two surfaces of the substrate and the third one formed by the substrate's surface and the back mirror<sup>58</sup>. In order to minimise the losses in this configuration, it is required that the two surfaces of the substrate are parallel and of high quality. Alternatively the substrate can be brought to the cavity at Brewster's angle, which can be calculated according to Snell's law using equation (32). Here,  $\theta_B$  is the Brewster's angle and  $n_1$  and  $n_2$  are the refractive indices of vacuum and the substrate respectively.

$$\theta_B = \tan^{-1} \left( \frac{n_2}{n_1} \right) \quad (32)$$

In this case, the light reflected from the substrate leaves the cavity and is encountered as optical loss. At Brewster's angle, however, the reflection curve of the p-polarised light reaches the minimum value of zero. This property can be used to reduce the reflection losses to a great extent. Expectedly, the surface quality of the substrate is as important as in the normal configuration, however,



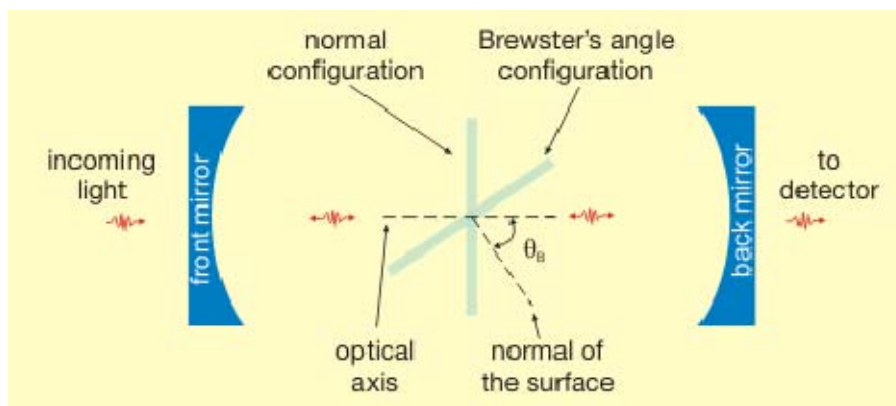


**Figure 15** Schematic view of the two possible configurations for application of CRDS to condensed phase samples in transmission mode. The angle of incidence is equal to zero in the perpendicular (normal) configuration and is equal to Brewster's angle in the case of Brewster's angle configuration.

the parallelism of the two surfaces is less critical, since the angle dependence of the reflection loss is much smoother for the Brewster's angle compared to the normal angle<sup>78</sup>. The main disadvantage of the Brewster's angle configuration is that only p-polarised light can be utilised. The other challenge in using the Brewster's angle arrangement is that, for a heterogeneous sample (e.g. a substrate covered with clusters), the Brewster's angle is not unambiguously defined. Figure 15 depicts these two configurations.

For measurement of size-selected supported clusters, the choice of substrate material is critical. Since the main topic of interest is the optical properties of the clusters and the substrate actually plays the role of the support, it is preferred that the optical losses due to the substrate are as low as possible. In terms of substrate properties, this translates in being transparent and having surfaces of high optical quality (low roughness, to minimise scattering losses), which are parallel. As already mentioned, the Brewster's angle configuration is less sensitive to the parallelism of the surfaces and therefore, such substrates are easier to get. On the other hand the thickness of the substrate plays a minor role in normal incidence, in contrast to Brewster's angle incidence, if the material is not absorbing. In the latter, the beam displacement, as the light passes through the substrate, gets larger for thicker samples. This makes no complication to CRDS under ambient conditions (e.g. on an optical table in the lab), since the back mirror can be positioned accordingly to compensate for the effect. For CRDS to be performed under UHV conditions this requires an extra degree of freedom to position the mirrors. There is, however, another criterion which is only relevant for the Brewster's angle arrangement. The substrate material should not possess birefringence, since this would cause the rotation of the polarisation. The rotated portion of the light will be reflected out of the cavity by the substrate in the next pass. This will increase the optical losses and as a consequence, the sensitivity will be reduced (see section 2.2.2.3.). Here, only materials which are either cubic

in structure (these are isotropic) or amorphous (having no long term crystalline order), may be employed. All other materials show, to a lower or higher extent, birefringence effects and are therefore, not suitable. A list of some suitable materials is presented in table 3. In this work a transmission mode arrangement has been chosen, because it is easier to implement in to vacuum. From the two possible configurations presented in Figure 15, the Brewster's angle layout is chosen. The main argument here is the availability of suitable substrates.

The cleanliness of the support material plays an important role. On one side the purity of the sample (cluster/substrate), is crucial for the reliability of the optical measurements. On the other side, the optical loss of the system, which affects the sensitivity of the method, will be higher in presence of contaminations. Therefore, the substrates are cleaned by spectroscopy grade acetone, through sweeping by a lens cleaning tissue, prior to use. This is done before the substrates are mounted into the vacuum. Once in vacuum, another cleaning step may be performed via sputtering by  $\text{Ar}^+$  ions generated by a commercial sputter gun (EX03 Ion Gun System-Thermo VG Scientific).

material	structure	transparent window [nm]
MgO	cubic	250-8000
KBr	cubic	300-20000
LiF	cubic	150-9000
$\text{BaF}_2$	cubic	150-15000
$\text{CaF}_2$	cubic	300-7000
BK7	glass	350-1700
$\text{SiO}_2$	glass	200-2100
YSZ	cubic	400-6000

**Table 3** A list of materials which are suitable for Brewster's angle configuration CRDS. BK7 is a borosilicate glass. YSZ stands for yttria-stabilised zirconia.

### 2.2.7. The optical setup

At this point almost all the optical components which are used in the spectroscopic part have been introduced. In this chapter all the parts are combined to give a complete overview of the optical setup. A schematic view is illustrated in Figure 16. Since the laser output is not necessarily at the same level as that of the optical axis of the cavity, some level-adjustment is required. This is easily done by a combination of at least two mirrors. Here, a three-mirror combination is used in order to keep all the reflections at 90 degrees and consequently, preserve the polarisation of the beam.

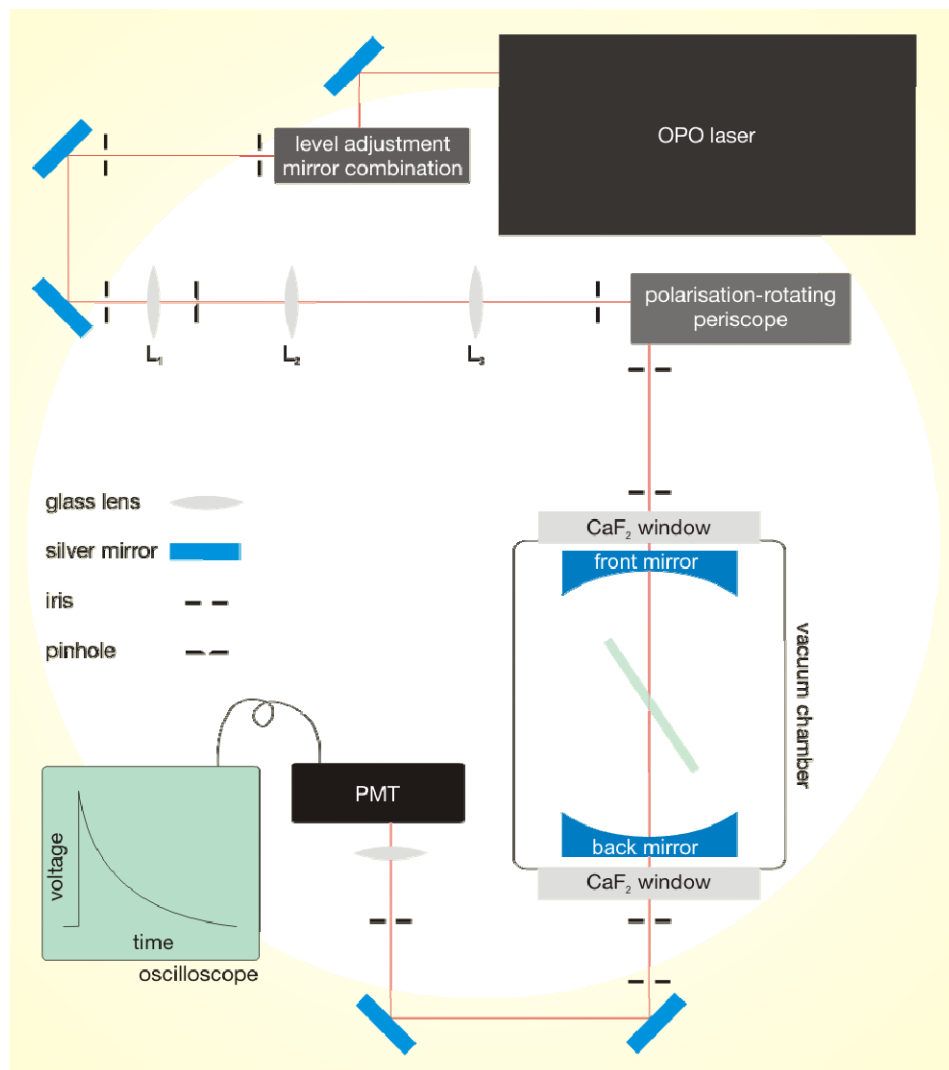


**Figure 16** Schematic overview of the optical setup. The output of the OPO laser is brought to the desired height through a set of three mirrors (level adjustment mirror combination). The beam is then spatially filtered by focussing it through a  $35\ \mu\text{m}$  pinhole using a glass lens  $L_1$  ( $f = 40\ \text{mm}$ ). Mode matching is performed by the means of two glass lenses  $L_2$  ( $f = 100\ \text{mm}$ ) and  $L_3$  ( $f = 500\ \text{mm}$ ). The position of the lenses with respect to the cavity was calculated through ray transfer matrix analysis. The polarisation of the beam (originally s-polarised) is rotated via a periscope (polarisation-rotating periscope) prior to the cavity. A number of silver mirrors and irises are used to guide the beam and to keep trace of its path way respectively. The cavity mirror spacing is 52 cm.

## 2. The apparatus

As already mentioned in section 2.2.4., the beam profile of the OPO system, needs to be cleaned. Consequently, a spatial filter is used which consists of a glass lens with a focal length of 40 mm and a high power pinhole 35  $\mu\text{m}$  in diameter. The result is an almost perfect Gaussian beam. Mode matching of this beam with regards to the cavity is performed using a pair of glass lenses ( $L_2$  and  $L_3$  in Figure 16). For mode matching calculations, the complex beam parameter at the pinhole position and at the middle of the ring-down cavity, are taken as the initial and final states, respectively. The full transfer matrix of the whole system is the product of the transfer matrices of each element including the free space travels. The full matrix  $\overrightarrow{A}_F$  can be divided into three smaller matrices  $\overrightarrow{A}_M$  (the matrix describing the path from the outer surface of the cavity mirror to the middle of the cavity),  $\overrightarrow{A}_V$  (the matrix describing the path from the outer surface of the vacuum window to the outer surface of the cavity mirror), and  $\overrightarrow{A}_L$  (the matrix describing the path from the pinhole to the outer surface of the vacuum window). The mathematical description of each path is given in the equation (33), for the special case presented here.

$$\overrightarrow{A}_F = \overrightarrow{A}_M \cdot \overrightarrow{A}_V \cdot \overrightarrow{A}_L \quad (33a)$$

from the outer surface of the cavity mirror to the middle of the cavity

$$\overbrace{\begin{pmatrix} 1 & 26 \\ 0 & 1 \end{pmatrix} \begin{pmatrix} 1 & 0 \\ \frac{0.515}{600 \cdot 1} & \frac{1.515}{1} \end{pmatrix} \begin{pmatrix} 1 & 0.66 \\ 0 & 1 \end{pmatrix} \begin{pmatrix} 1 & 0 \\ 0 & \frac{1}{1.515} \end{pmatrix}} = \overrightarrow{A}_M \quad (33b)$$

traveling half of the cavity
refraction at the inner surface of the mirror ( $n_1 = 1.515$ )
traveling through the thickness of the mirror
refraction at the outer surface of the mirror ( $n_1 = 1$ )

from the outer surface of the window to the outer surface of the cavity mirror

$$\overbrace{\begin{pmatrix} 1 & 2 \\ 0 & 1 \end{pmatrix} \begin{pmatrix} 1 & 0 \\ 0 & \frac{1.433}{1} \end{pmatrix} \begin{pmatrix} 1 & 0.5 \\ 0 & 1 \end{pmatrix} \begin{pmatrix} 1 & 0 \\ 0 & \frac{1}{1.433} \end{pmatrix}} = \overrightarrow{A}_V \quad (33c)$$

traveling from the vacuum window to the cavity mirror
refraction at the inner surface of the window ( $n_1 = 1.433$ )
traveling through the thickness of the window
refraction at the outer surface of the window

from the pinhole to the outer surface of the vacuum window

$$\overbrace{\begin{pmatrix} 1 & d_3 \\ 0 & 1 \end{pmatrix} \begin{pmatrix} 1 & 0 \\ -\frac{1}{50} & 1 \end{pmatrix} \begin{pmatrix} 1 & d_2 \\ 0 & 1 \end{pmatrix} \begin{pmatrix} 1 & 0 \\ -\frac{1}{10} & 1 \end{pmatrix} \begin{pmatrix} 1 & d_1 \\ 0 & 1 \end{pmatrix}} = \overrightarrow{A}_L \quad (33d)$$

traveling from the lens ( $L_3$ ) to the vacuum window
passing through  $L_3$ 
traveling from  $L_2$  to  $L_3$ 
passing through  $L_2$ 
traveling from the pinhole to  $L_2$

The numerical values, which are used in equation (33), are depicted in Figure 17. The reflection from the flat silver mirrors is not included in the calculation, since these are represented by the unity matrix. The complex beam parameters at the middle of the cavity,  $q_c$ , and at the pinhole,  $q_p$ , are given through equations (24-25). At both of these positions, the radius of curvature is infinity, so that the beam parameter is purely imaginary. The beam waist at the pinhole can be considered as that of a Gaussian beam which keeps its full power after traversing the pinhole. Considering the Gaussian profile of the beam, at a radius of  $\frac{\pi}{2}\omega_p$ , ( $\omega_p$  is the waist of the beam) from the centre of the beam, more than 99% of the total power is contained. The values of the beam parameters at the pinhole and at the middle of the cavity are given in equations (34) and (35), respectively, for a laser wavelength of 520 nm.

$$\frac{1}{q_p} = \frac{1}{\infty} - \frac{i\lambda}{\pi\omega_p^2} = \frac{-i\lambda}{\pi\left(\frac{2r_p}{\pi}\right)^2} = i\frac{-\pi\lambda}{4r_p^2} = -13.33574i \text{ cm}^{-1} \quad (34)$$

$$\frac{1}{q_c} = \frac{1}{\infty} - \frac{i\lambda}{\pi\omega_c^2} = \frac{-i\lambda}{\pi\sqrt{\frac{d\lambda^2}{4\pi^2}(2R_M - d)}} = -0.008186i \text{ cm}^{-1} \quad (35)$$

It can be seen from equation (35), that the beam parameter in the middle of the cavity, is not wavelength dependent. Starting from these values the free parameters in equation (33) ( $d_1$ ,  $d_2$  and  $d_3$ ), should be found so that the resulting ABCD matrix transfers the beam parameter of the pinhole to that of the ring-down cavity. This is about solving a set of two equations (one for real part and one for the imaginary part of the beam parameter), with three unknowns. This can only be done by guessing an initial value for one, and search for the answers for the other two. Doing so, the distances between the elements are found for the case of only one single wavelength. In principle this procedure should be repeated for all the wavelengths. Here, however, the values calculated for 520 nm are taken and starting from those values the position of the lenses with regard to the cavity mirror are adjusted (through micrometer stages), for the best mode matching by monitoring the quality of the CRDS signal. A solution was found for  $d_1 = 8.3$  cm,  $d_2 = 18.33$  cm and  $d_3 = 164.82$  cm. The Mathematica code of the calculation is included in Appendix B1.

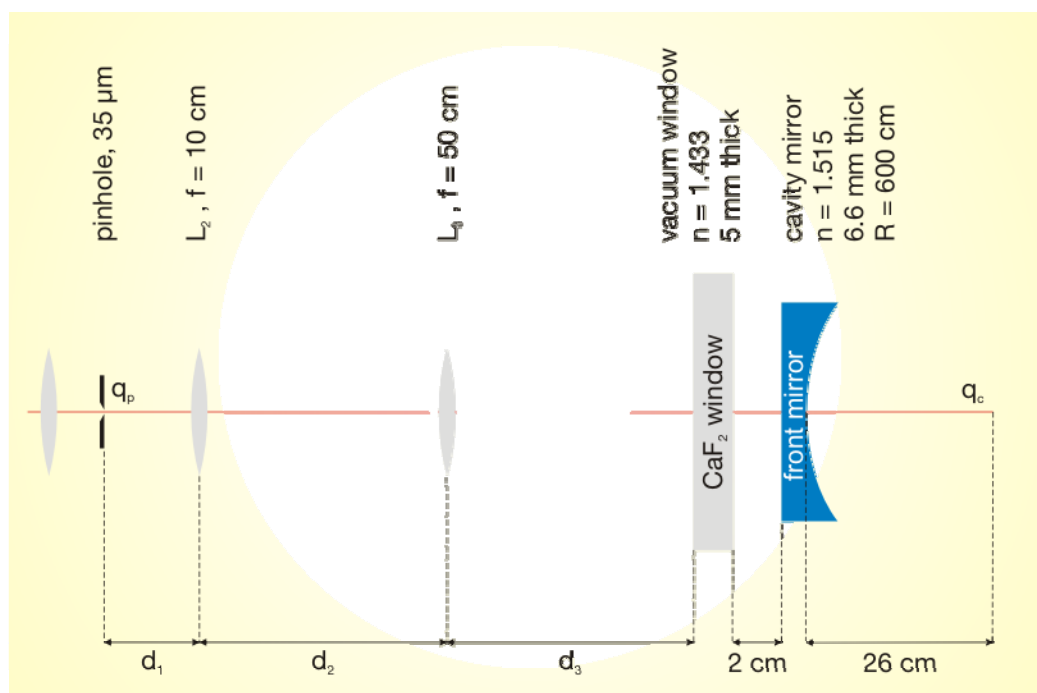


**Figure 17** Mode matching optical layout is schematically presented. The beam parameter at the pinhole is to be matched to the beam parameter at the middle of the cavity. The data which are required for the calculation of the transfer (ABCD) matrix are included.

### 2.3. Production of small metal clusters

The development of cluster sources and subsequently the investigation of cluster properties started back in the 1960s<sup>79-81</sup>. The breakthrough was the idea of utilising the non-equilibrium conditions of an adiabatically expanding vapour. Clusters formation is believed to be due to the supersaturating of the rapidly cooled vapour flow which stimulated homogenous nucleation in the beam<sup>81</sup>. Cluster ion beams are efficient tools for manipulating agglomerates of atoms providing control over the synthesis of structures on the nanometer scale, in particular, control of cluster size and interaction energy with the substrate<sup>82-84</sup>. Cluster beams can also be utilized for formation of ordered arrays on patterned or functionalised surfaces<sup>85, 86</sup>. One of the main advantages of the cluster ion beam technique, compared to some other methods such as chemical preparation<sup>87, 88</sup> or the atomic vapour growth of nanoparticles<sup>89</sup>, is the precise control of the cluster impact energy, high cluster size resolution, and easy fabrication of very small clusters consisting of just a few or few tens of atoms, having sizes below or in the region of 1 nm.

### **2.3.1. Cluster sources**

There are various possibilities to produce atomic clusters from bulk material. Common to almost all methods is that atoms are first extracted from the bulk material and then single atoms are brought together to form atomic clusters. An exception to this general picture is the liquid-metal ion source, which is briefly introduced in section 2.3.1.4. A short summary of the most commonly used cluster sources is presented here.

#### **2.3.1.1. Seeded supersonic nozzle source**

In this source, metal is vaporised in a hot oven. The metal vapour is seeded in an inert carrier gas by pressurising the oven with the inert gas. The mixture is ejected into vacuum through a small hole, producing a supersonic molecular beam<sup>90</sup>. This source is perhaps the most intense cluster source and is capable of producing clusters with up to several hundreds of atoms. The molecular beam is continuous and possesses a reasonably narrow velocity distribution. The main disadvantage of this source is its limitation to low-boiling-point metals.

#### **2.3.1.2. Gas aggregation cluster source**

This source is particularly efficient in the production of large clusters with more than 10000 atoms per cluster. The intensities are generally much lower than seeded supersonic nozzle sources. Here metal is vaporised and introduced in a flow of cold inert gas. Due to the low temperature of the inert gas the vapour becomes highly supersaturated and clusters are primarily produced by successive single-atom addition. Since the reverse process (re-evaporation) is negligible, thermodynamic stability of the clusters plays a vanishing role in the cluster abundances and the size distribution is a relatively smooth<sup>91, 92</sup>.

#### **2.3.1.3. Ion sputtering source**

Cluster ion beams are produced by bombarding a metal surface with high energy inert gas ions. The cluster intensities are typically exponentially decreasing functions of the cluster size<sup>93</sup>. High intensities for mass selected clusters (on the order of 10 nA) have been reported<sup>19</sup> for smaller sizes. The initial cluster ion temperatures are very high. The clusters typically cool by in-flight evaporation and therefore, the abundance spectra reflect the thermodynamic stabilities related to the clusters binding energies. This source delivers a continuous molecular beam of cluster ions with temperatures close to the evaporation limit.

#### **2.3.1.4. Liquid-metal ion source**

These sources are mainly used to produce multiply charged clusters of low-melting point metals. In this kind of source a needle is wetted with the metal and is heated above the melting point of the metal. Then a potential is applied which causes a high electric field at the tip of the needle. Subsequently, a spray of very

small droplets of hot metal is emitted from the tip. The formed droplets undergo evaporative cooling and fission and form smaller clusters<sup>94, 95</sup>.

### 2.3.1.5. Laser vaporisation cluster source

The first version of the laser vaporisation cluster source (LVC) was reported back in early 1980s, at Rice University in the group of R. E. Smalley<sup>96</sup>. They combined the laser vaporisation technique with the pulsed supersonic nozzle technology, which was in heavy use in their group. The use of lasers to vaporise material is very important as it allows the production of metal vapours of even the most refractory metals such as W and Mo without heating any part of the apparatus up to extremely high temperatures. The supersonic expansion is the other important phenomenon employed in LVC sources. A schematic view of a LVC source is shown in Figure 18.

Laser vaporisation cluster sources produce clusters in the size range from the single atom to several hundreds of atoms per cluster. These sources are pulsed and, although the time-averaged flux is low compared to the other sources, intensities within a pulse are typically higher. Since in this source, metal vapour is generated by the pulsed-laser ablation of the metal, clusters of any metal can be produced<sup>97-99</sup>. Similar to seeded supersonic nozzle sources, the vaporised material is cooled by collisions with inert gas molecules. Here, however, the gas is pulsed. The inert gas/cluster mixture is then ejected out of the nozzle and so the cluster beam is formed. The clusters formed in this source are generally cold, due to higher instantaneous pressures in the source, which are possible because the gas is pulsed and the time-averaged pressure remains below pumping limits. The observation of neutral iron clusters with an argon atom attached to them is a direct evidence of the low temperature of clusters formed in this kind of source<sup>100</sup>. The clusters can be cooled even further by reducing the temperature of the nozzle or of the entire source. The other advantage of these sources is the low material consumption. For the laser vaporization source to function, the following three major technical details are of importance: 1) the movement of the target to

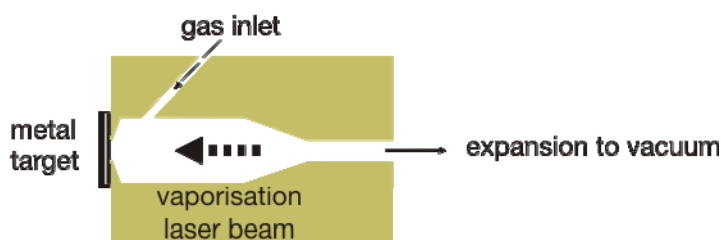


**Figure 18** A schematic over-view of the laser vaporisation cluster source is illustrated. A laser beam is focussed on to a metal target in the presence of a buffer gas to produce plasma. The plume is mixed with the gas and is expanded through vacuum.



prevent the laser pulses from burning holes and grooves into the target, which is important to obtain stable cluster beams; 2) the design of the source cavity and expansion zone, which determine cluster size distributions, temperatures, and flux; 3) the pulsed inert gas assembly and the tightness of the source, in order to obtain reproducible He pulses, and stable cluster beams.

In this work a laser vaporisation cluster source similar to that of Heiz *et al.*<sup>97</sup> is used to produce small metal clusters. The third harmonic (355 nm) of a 50 Hz Nd:YAG laser (Innolas Spitlight 600, ~80 mJ/pulse, <10 ns pulse-width) is focused onto the rotating metal disk. Pure He (He 6.0, Air Liquid) is used as buffer gas, and is pulsed with the same frequency as the laser using a homemade piezovalve. The gas pulse is delayed with respect to the laser pulse by means of a delay generator (Berkeley Nucleonic Corps, 500 Pulse Generator) which in turn is triggered by the laser. The mixture of the buffer gas and the plasma is expanded through a nozzle which is 67 mm long and 2 mm in diameter. This expansion cools the plasma and causes the formation of clusters (neutral as well as charged both negatively and positively). To move the target disk we use a slightly modified principle introduced by Gangopadhyay and Lisy<sup>101</sup>. The disk is integrated in a motor driven hypocycloidal planetary gear assembly. It consists of the target disk with a diameter of 45 mm, which is fixed to an inner gear (diameter 50 mm). This disk turns inside an outer gear which is screwed on a mirror polished stainless steel disk serving as the ground plate. The laser hole is drilled off-axis into the ground plate. With this mechanism the laser beam burns a hypocycloid pattern into the disk which covers more than 90% of the target area. The usable surface is therefore almost 15 cm<sup>2</sup> and about a factor of 10 larger than in conventional sources using rods as targets<sup>102-104</sup>. During operation the disk turns with a frequency of 0.5-2 Hz. It is pushed against the ground plate by a spring mechanism. The sealing between the disk and the ground plate is done by a flat Teflon ring. Unlike other sources the expansion nozzle is coaxial with respect to the incoming vaporisation laser beam. This reduces the total volume of the thermalisation cavity and therefore higher pressures may be achieved with the same He back pressure. A 3-dimensional view of the source chamber is presented in Figure 19 and the detailed plans of the source are included in Appendix A2.

The relevant parameters for the operation of the source are the energy of the laser, the pressure of the buffer gas, the delay between the gas and laser pulse, the voltage which is applied to the piezovalve and the gas pulse duration. The energy of the ablation laser needs to be over a threshold value. No systematic study on this parameter has been performed, however, for laser energies below 70 mJ the stability of the source is drastically reduced. The pressure of the He gas varies between 3 and 10 bar with higher pressure suitable for formation of larger clusters. The delay of the gas pulse should be tuned so that at the moment of the plasma formation the optimum gas pressure is achieved. This value varies

## 2. The apparatus

depending on material and the desired cluster size. The opening of the piezovalue is controlled through a high voltage (between 300 and 600 V) and is another method of changing the actual pressure in the source.

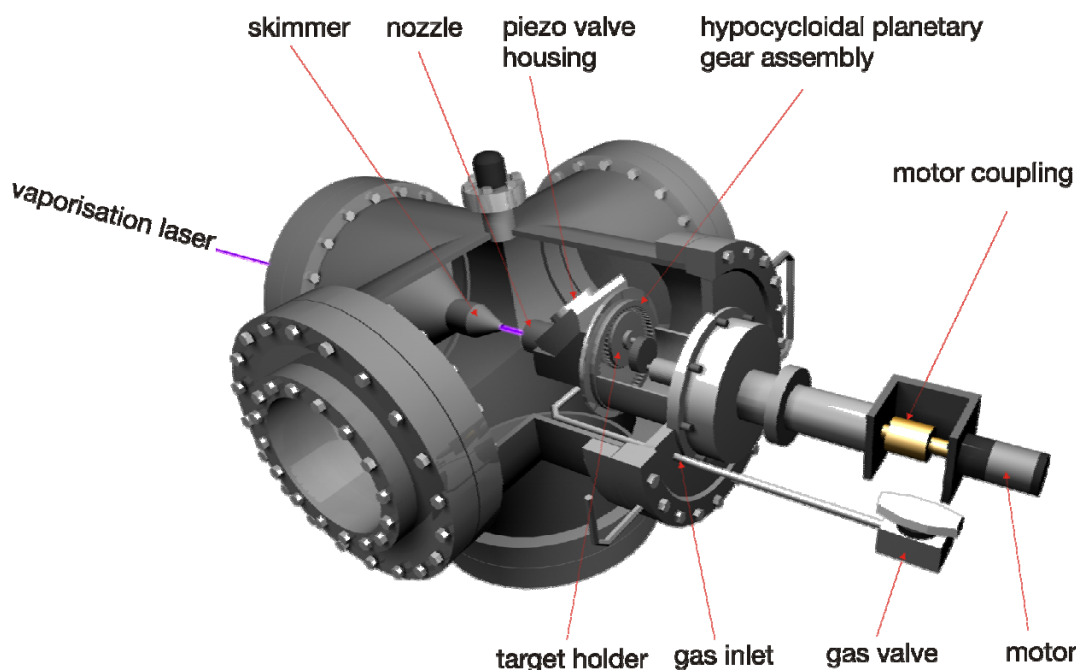


**Figure 19** A 3D view of the cluster source used in this work is presented. Individual parts are labelled in the figure.

Clusters of different materials (Cu, Ag, Au, Pd, Co, Fe, Pt, Ni and Nb) and of all masses up to 4000 amu could be produced. A mass spectrum for  $\text{Pt}_n^+$  clusters ( $n=1-20$ ) is shown in Figure 20. Cluster currents of about 100 pA are easily achieved.

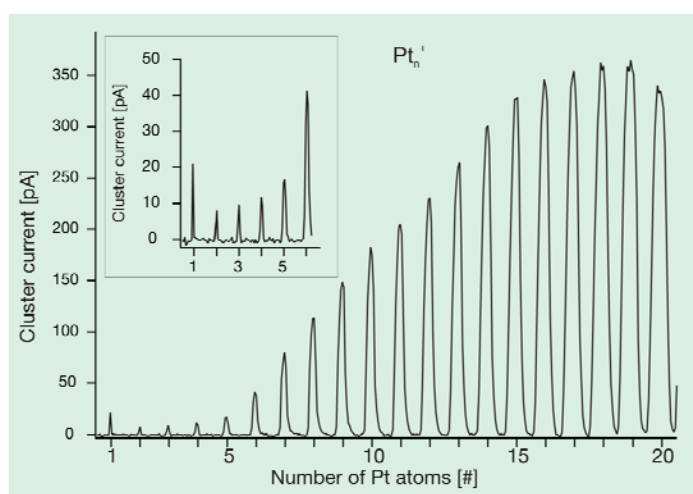


**Figure 20** Mass spectrum of Pt clusters produced by the cluster source used in this work is shown. The inset shows the peaks for Pt atom up to  $\text{Pt}_6$ . The source has been optimised for production of  $\text{Pt}_{19}$  clusters.

### 2.3.1.6. Pulsed arc cluster ion source

Quite similar to the laser vaporisation cluster sources are the pulsed arc cluster ion sources, where the metal is vaporised not by a laser but by an intense electrical discharge. The main advantages over the laser vaporisation source are the lower price, because it does not require a laser, and the higher cluster intensities<sup>105</sup>. In general the clusters are not cold, however, under suitable conditions Van der Waals complexes with Ar atoms have been reported<sup>106</sup>.

### 2.4. Ion optics and mass selection unit

As mentioned in section 2.1.3., the cluster beam needs to be guided through a differentially pumped vacuum system. In this case ion optics are used to control the path of the ions through each pumping stage. A 3-dimensional view of the employed system is presented in Figure (21). In the following the cluster beam path is described starting from the skimmer down to the focussing octopole, including a short description of each element.

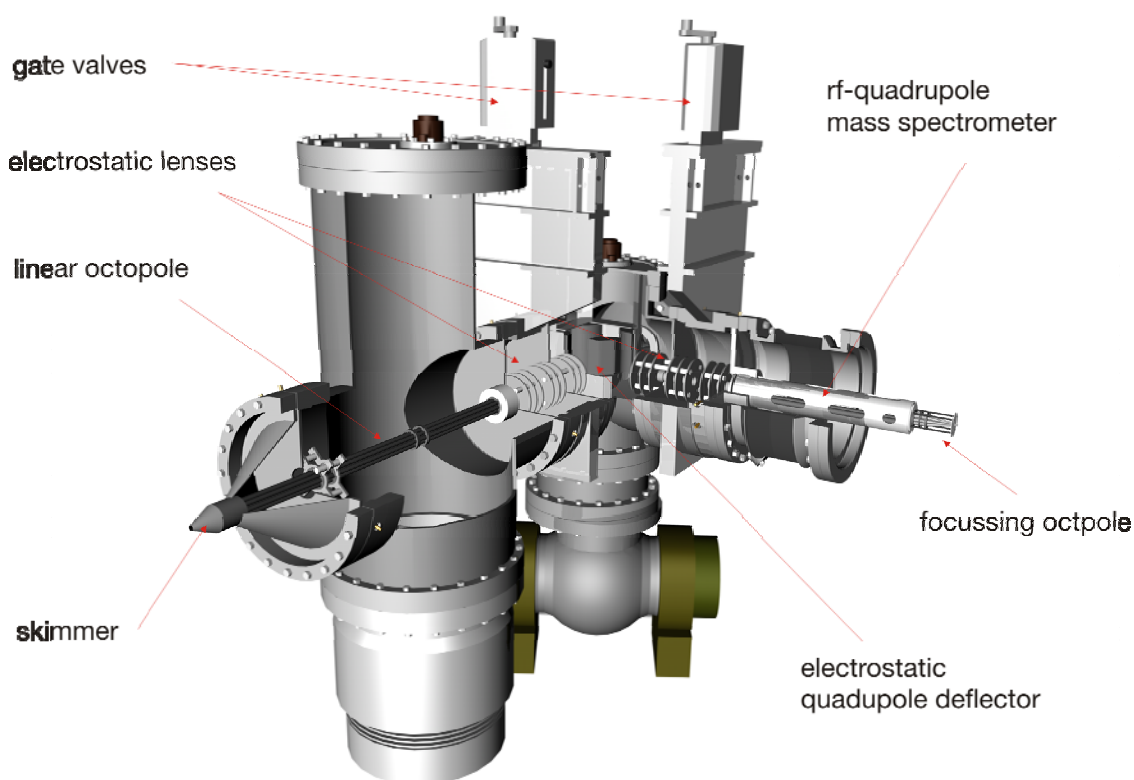


**Figure 21** 3D view of the cluster beam path through the differentially pumped vacuum system, including the ion optics, is illustrated. Individual components are labelled.

Leaving the nozzle, the clusters traverse a skimmer with an opening of 5 mm in diameter. The main functions of the skimmer are to collimate the expanded gas mixture into a beam<sup>107</sup> and to separate the source chamber from the octopole chamber (see Figure 21). The skimmer is electrically separated from the chamber

and its potential can be controlled to perform a kind of high pass filtering of the cluster ion energies. The neutral gas flow which leaves the nozzle (mainly He atoms) has a conical shape. The distance between the skimmer and the nozzle can be varied. As the distance between the skimmer and the nozzle increases, the part of this cone which gets through the skimmer, and therefore contributes to the pressure in the octopole chamber, decreases.

Immediately behind the skimmer, a radio-frequency (rf) driven octopole is located to guide the ions. The frequency and the power of the octopole are controlled by an amateur rf transceiver (Kenwood TS-570S). A direct current (DC) voltage is applied on top of the rf field to increase the transmission of the octopole. For the purpose of controlling the rf signal and the floating of the octopole by the DC voltage, both voltages are applied via an interposed homemade amplifier-transformer circuit <sup>108</sup>.

After the octopole ion-guide, the cluster beam travels through a small orifice (5 mm in diameter) before it enters a set of three electrostatic immersion lenses (each consisting of three cylindrical electrodes). If the potentials on the first and the last element of an immersion lens are equal it is called unipotential or Einzel lens. Either of the two can be used to focus an ion beam <sup>109</sup>. In the present work the potentials were controlled separately.

The electrostatic lenses focus the ion beam into an electrostatic quadrupole deflector, where the positively charged ions undergo a 90° deflection. At this point, the negatively charged ions are separated and neutral species are abandoned. This separation is crucial, since the neutrals cannot be mass selected and if they make it to the surface of the support material, where the clusters are deposited, the size selectivity of the measurement is lost. The deflector is composed of four quarter-cylindrical electrodes approximating the hyperbolic shape suggested by Zeman <sup>110</sup>.

After exiting the deflector, a set of three electrostatic immersion lenses are again employed to focus the beam, which now consists of only positively charged clusters, into a commercial quadrupole mass spectrometer (Extrel 5500 series, mass range up to 4000 amu). The quadrupole mass spectrometer (QMS) can be used either in mass filter or ion guide mode. In the ion guide mode (rf only) all the masses are transmitted through the QMS. In the mass filter mode, a specific mass to charge ratio is transmitted and a cluster beam consisting of cluster cations of only one single mass leaves the QMS.

The mass selected beam traverses through an rf-driven conical octopole (focussing octopole) <sup>108</sup>, which is controlled by a separate amateur rf transceiver. Here, similarly to the guiding octopole, a DC voltage is applied on top of the rf

field to increase the transmission. The focussing octopole is used to control the size of the cluster spot which is deposited on the surface.

The energy of the cluster ions can be monitored by applying a retarding voltage to a metal plate downstream the focussing octopole. This metal plate is mounted on a translation feedthrough and can be removed out of the cluster beam for deposition. A typical energy analysis of  $\text{Ni}_{20}^+$  clusters is depicted in Figure (22).

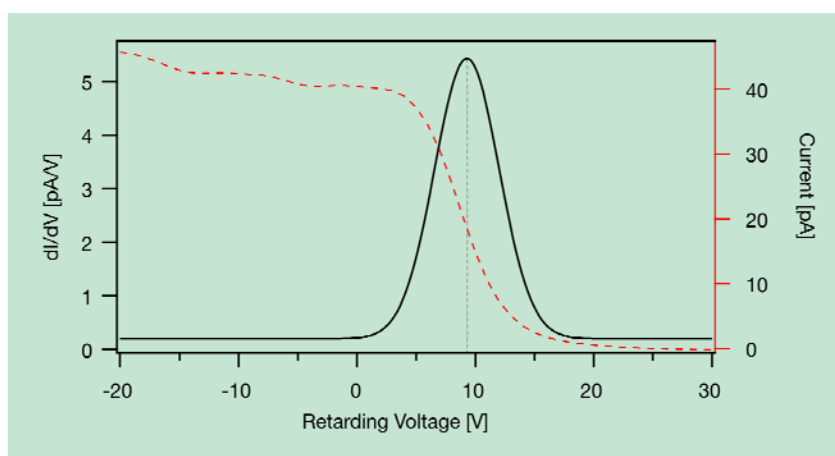


**Figure 22** Retarding field analysis of  $\text{Ni}_{20}^+$  clusters produced by the cluster source used in this work. Here, the cluster current is measured on a faraday plate while the retarding voltage is scanned from -20 V up to +30 V. The mean kinetic energy of the clusters is  $\sim 9$  eV (the vertical broken line) with a FWHM of  $\sim 7.5$  eV. This indicates an energy-per-atom value of 0.2-0.9 eV.

## 2.5. Deposition

### 2.5.1. Neutralisation and electron source

The mass selected cluster cations are deposited onto the support material. Due to the fact that the support material (for a list look at table 3) is an insulator, it is therefore, necessary to neutralise the cluster ions, so that deposition is not interrupted by the electrostatic field created at the substrate, which deflects the cluster ions coming next. Consequently, an electron source of home design (Figure 23) is used. The electron source is composed of a body, a filament which is wiggled over a ceramic tube and two independently controllable metal grids. By placing the filament into the housing, the possible contamination of the support through the atoms or cations, which are vaporised from the filament, is completely avoided. Furthermore, the energy and the amount of electrons are separately controllable by altering the voltages at the two grids and the body and the potential of the filament. The body of the source is biased to a negative potential so that the electrons are deflected away. The positive potential at the

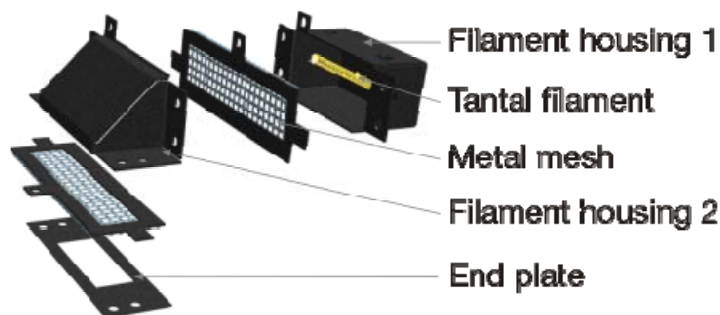


**Figure 23** A 3D view of the electron source is presented. A tantalum filament is used as the source of thermal electrons. The filament is placed inside a metal housing which can be biased to a potential. Two metal mesh grids are used to accelerate the electrons.

first grid accelerates towards the second cage where the electrons are again deflected from the body and pulled by the second grid. The current flowing through the filament can be controlled to vary the amount of the emitted thermal electrons. Electron currents of up to  $2\mu\text{A}$  are achieved. Detailed plans of the electron source are included in Appendix A3.

The process of neutralisation happens almost exclusively at the surface, since the clusters are too fast (1-2 km/s, as a result of supersonic expansion) and the probability of capturing an electron in flight is too small. This means that the cluster ions arrive at the surface where they can take up an electron and become neutral. The electron current should be high enough, so that the positive charge of the cluster cations is fully compensated. This can be achieved with a continuous supply of electron current, which is about 20 times higher than the cluster current, since the clusters are produced at a repletion rate of 50 Hz. For a typical cluster current of  $+100\text{ pA}$ , an electron current of  $-2\text{ nA}$  is sufficient.

### 2.5.2. Temperature of the sample

Altering the temperature of the substrate provides the possibility to render the behaviour of the sample at different temperatures for example to study in inset of the surface diffusion or desorption of the clusters on the surface. To this end a broad range of available temperature is advantageous.

Considering the size and the thermal properties of the substrate and the geometrical arrangement, the temperature profile of the substrate as a function of time can be calculated according to the heat transfer differential equation given in equation (36) <sup>111</sup>, where  $T = T(x, y, t)$  [K] is the temperature of the substrate,  $a$  [ $\text{m}^2\text{s}^{-1}$ ] is the temperature conductivity,  $A$  [ $\text{m}^2$ ] is the surface area of the substrate,  $V$  [ $\text{m}^3$ ] is the volume of the substrate,  $\sigma$  [ $\text{Js}^{-1}\text{m}^{-2}\text{K}^{-4}$ ] is the Stefan-Boltzmann constant,  $c$  [ $\text{Jkg}^{-1}\text{K}^{-1}$ ] is the specific heat capacity,  $\rho$  [ $\text{kgm}^{-3}$ ] is the

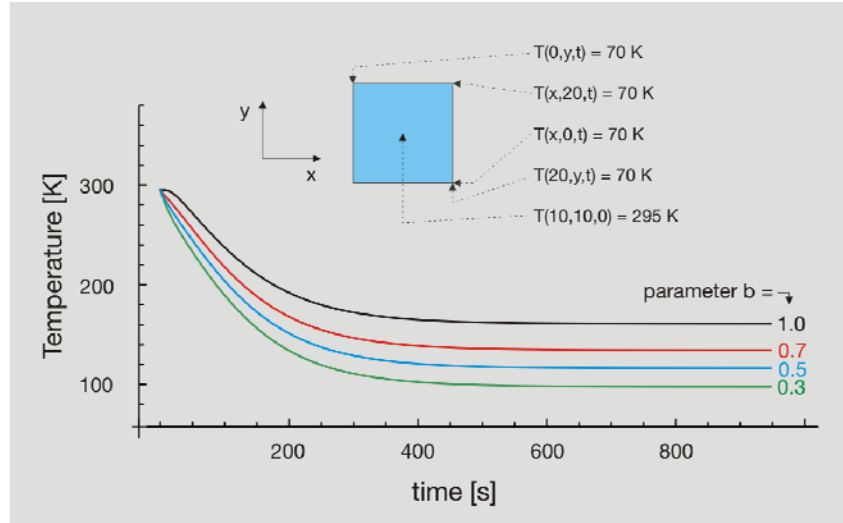


**Figure 24** Boundary conditions and results of time dependent heat transfer equation given in equation (36) for a quartz substrate (20 x 20 mm<sup>2</sup> and 0.13 mm thick) for different values of parameter b, solved for the middle point of the substrate (x = 10mm, y = 10mm).

density,  $\theta [K]$  is the temperature of the radiative heater surrounding the substrate,  $\varepsilon$  is the unit-less emissivity and,  $b$  is a unit-less factor determining the effectivity of the radiative heat transfer being 1 for a closed body. The first term on the right hand side of the equation explains the heat transfer and distribution inside the material, where the second term treats the radiative absorption and emission. In Vacuum heat transfer by convection is neglected.

$$\frac{\partial T}{\partial t} = a \left( \frac{\partial^2 T}{\partial x^2} + \frac{\partial^2 T}{\partial y^2} + \frac{\partial^2 T}{\partial z^2} \right) + \frac{2A\sigma\varepsilon(b\theta^4 - T^4)}{V c\rho} \quad (36)$$

Since the substrate is very thin, the temperature gradient through the thickness of the substrate can be neglected and the problem can be reduced to two dimensions. In the general case that the temperature profile at the surface is position dependent, the surface area in the nominator of the very right term in equation (36) should be replaced by a two dimensional integral over the coordinates. Accounting for the above mentioned issues, equation (36) can be rewritten as in equation (37), where  $x'$  and  $y'$  represent the side length of the substrate in  $x$  and  $y$  directions respectively.

$$\frac{\partial T}{\partial t} = a \left( \frac{\partial^2 T}{\partial x^2} + \frac{\partial^2 T}{\partial y^2} \right) + \frac{2\sigma\varepsilon}{V c\rho} \int_0^{x'} \int_0^{y'} (b\theta^4 - T^4) dy dx \quad (37)$$

Equation (37) can be solved numerically for a given set of boundary conditions. This equation was solved for a quartz glass substrate ( $A = 20 \times 20 \text{ mm}^2$ ,  $d = 150 \mu$  thick,  $\rho = 2210 \text{ kgm}^{-3}$ ,  $c = 730 \text{ Jkg}^{-1}\text{K}^{-1}$ ,  $a = 0.87 \times 10^{-6} \text{ m}^2\text{s}^{-1}$  and  $\varepsilon = 0.8$ ) which is held at a constant temperature from all the edges and is located inside a

## 2. The apparatus

---

closed cage which is at the constant temperature  $\theta = 295K$  (to simulate the walls of the vacuum chamber). The effectivity factor is varied from its maximum value  $b = 1$  down to  $b = 0.3$  which corresponds to a shielding of 70%. Figure (24) shows the boundary conditions and results for the time evolution of the temperature at the centre of a substrate which is held on all edges at liquid nitrogen (LN) temperature (70 K). It is seen from Figure (24) that when starting with a substrate at room temperature, even by cooling the substrate (in the given geometry) down to LN temperature, the LN temperature cannot be achieved. This is due the radiation which comes from the vacuum walls (In our example the cage walls). First after blocking this radiation, lower temperatures may be achieved. The Mathematica code of the calculation is included in Appendix B2.

### 2.5.3. Sample holder and the second cooling shield

As shown in Figure (24) the temperature of the sample can only be reduced to low temperatures by shielding the radiation of the vacuum walls. In order to shield the radiation it is required that the radiation is absorbed at some place other than the substrate and is not subsequently reemitted. This can be done by surrounding the substrate through a cooled metal surface, which is kept at a lower or same temperature than the desired temperature of the substrate. This heat sink can be realised in our case by a suitable design of a sample holder as is presented in Figure (25). The sample holder is mounted on a cryogenic manipulator (Vacuum Generators, xyz + 360° rotation) and can be cooled down to LN temperature. Using the sample holder presented in Figure (25) about a third of the radiation

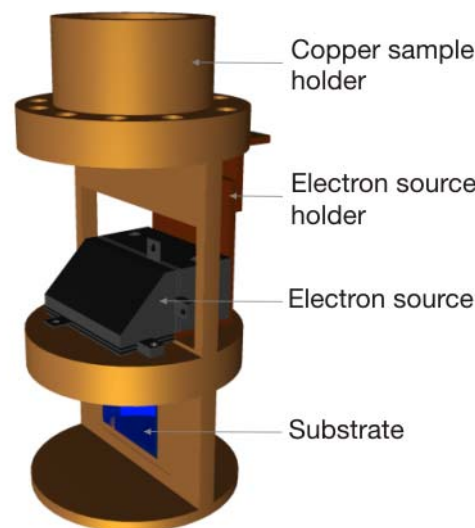


**Figure 25** A 3D view of the sample holder is shown including the electron source. The sample holder is cooled down to liquid nitrogen temperatures and shields the substrate from  $\sim 30\%$  of the surrounding radiations.



from the vacuum walls is blocked. This corresponds roughly to the red curve ( $b = 0.7$ ) in Figure (24). It should be noted that the electron source gets warm and radiates heat when in function and serves as an additional heat source for the substrate. It is therefore preferred to shield the electron source to be able to reduce the temperature as calculated in Figure (24). The sample holder presented in Figure (25) blocks the radiation of the electron source almost completely. The detailed plans of the sample holder construction are included in Appendix A4.

Due to the fact that the Brewster's angle configuration is used for CRDS measurements, further shielding cannot be realised by the sample holder. However it is possible to surround the sample holder with cylindrical double walled tube which is held at LN temperature. A view of this second shield with the sample holder is depicted in Figure (26). It should be mentioned that the second shield not only blocks the radiation from the walls and so stops the warming of the substrate, but also cools the substrate. Since, it is kept at a lower temperature and heat is transferred through radiation now from the substrate to the second shield. The detailed plans of the second cooling shield are presented in Appendix A5.

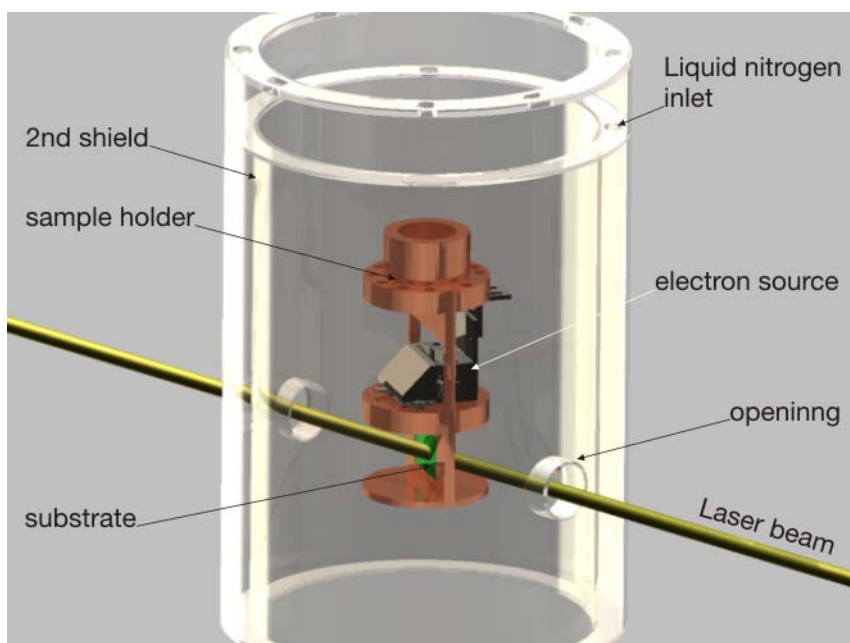


**Figure 26** A schematic view of the double-walled second cooling shield is shown including the sample holder and electron source. The volume between the two walls of the shield is filled with liquid nitrogen for cooling purposes. The laser path is indicated. The second shield is made of stainless steel. Here, a transparent view is presented for convenience.

## 2.6. The overview of the setup

Here a summary of the setup as a whole is presented. A 3 dimensional view of the vacuum chamber together with the optical setup is shown in Figure (27) . The apparatus can be divided in four main parts: 1) cluster source; 2) ion optics and mass selection unit; 3) analysis unit and 4) the optical setup. These parts are labelled in Figure (27).

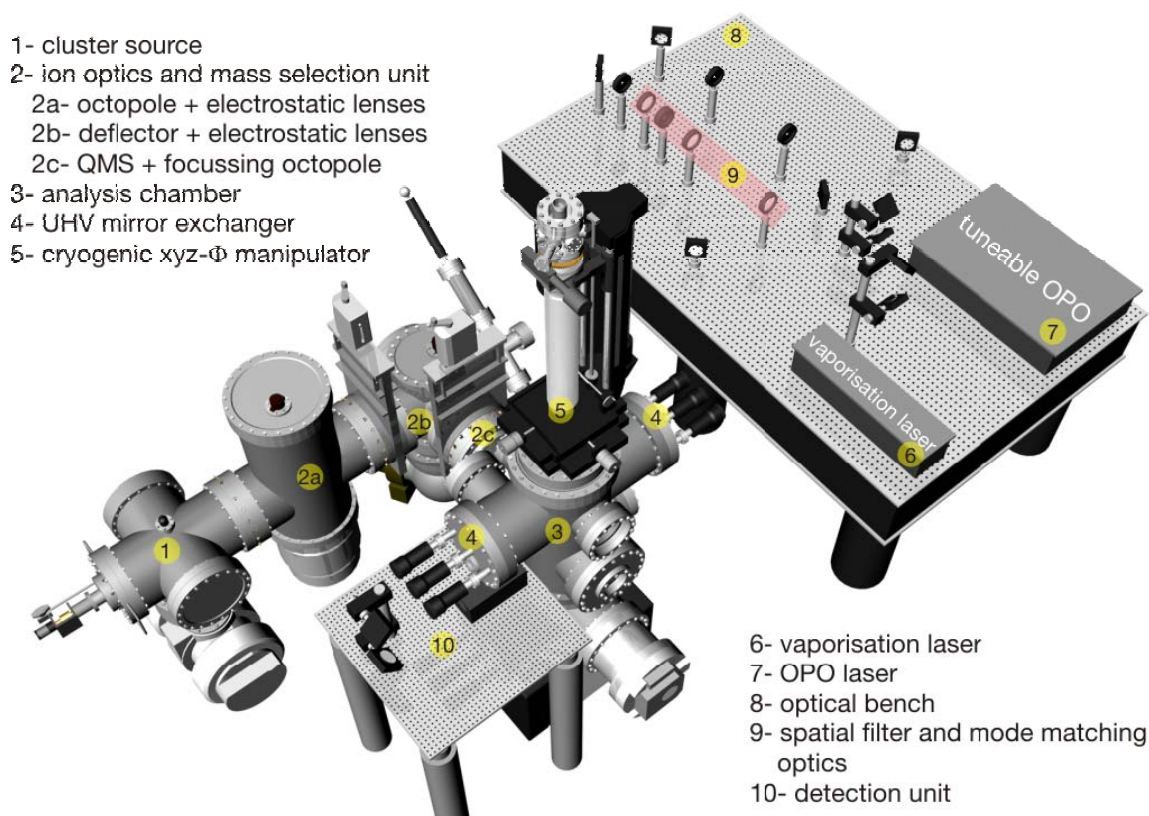


**Figure 27** A 3D overview of the apparatus built in the course of this work is presented. Individual parts are labelled. The apparatus may be observed as consisting of four main parts: a cluster source (1, and 6), ion optics an mass selection unit (2a, 2b and 2c), analysis chamber (3- including 4 and 5) and optical setup (4, 7, 8, 9 and 10).

A newly built laser vaporisation cluster source is utilised for the production of metal clusters. The resultant cluster beam is guided through electrostatic ion optics and rf-multipoles toward the support material whereon they are deposited after size selection. Since the substrate materials suitable for CRDS measurements presented here are insulators, the cluster cations should be neutralised in order to avoid interruptions in deposition process. To this end, a novel electron source is designed, to supply a controllable amount of electrons with a specified energy, and block the vaporised material. This means that the

substrate and cluster cations are only exposed to the electrons, and are not contaminated, in contrast to the commonly used bare hot filaments.

A cryogenic sample holder is designed, which allows deposition and spectroscopic measurements at low temperatures. In UHV conditions, heat is mainly transferred through radiation. This effect is fully considered in the development of the sample holder, based on theoretical calculations for the special case presented here.

The highly sensitive technique of cavity ring-down spectroscopy is adopted to measure the optical properties of supported size selected clusters. The vulnerability of the clusters and their electronic structure, against any contamination limits the measurements to ultra high vacuum conditions. The cavity ring-down spectrometer is therefore designed to be compatible with these conditions. To this aim a unique UHV-compatible mirror exchanger is proposed and constructed, which completely circumvents the aforementioned practical difficulties.



## 3. Publications

In the course of this work, three peer reviewed journal articles have been published about the feasibility, characterisation, and application of cavity ring-down spectroscopy to study size-selected supported metal clusters. In this section, each article is presented after a short description of its context. The order in which these articles are presented follows their topics relative importance, and relevance to the context of this work.

The successful application of the CRDS technique to study condensed phase samples is demonstrated in paper 3, however, for relatively large gold nanoparticles, which have been produced wet chemically, dip-coated on to thin SiO<sub>2</sub> substrates. These measurements are performed under ambient conditions and present a proof of principle.

In paper 1, the details of the new experimental apparatus including the laser vaporisation cluster source, the ion optics including mass selection unit, and the CRD spectrometer are given. The performances of each of the compartments are discussed. The preliminary results on a model system are used to pronounce the high sensitivity of the technique and to explain the measurement procedure. Details of data treatment are given and justified. In addition the first experimental findings on optical properties of Ni clusters are presented. The spectra are interpreted according to simple Mie-Drude model and partial oscillator strength.

Paper 2 treats the practical issues concerning the experimental setup introduced in paper 1. The criteria for support material are discussed and commercially available substrates are compared. The high sensitivity of CRDS is utilised to characterise the quality of the materials and it is shown that trace amounts of impurity are unambiguously detectable. The structural deformation of some samples is observed to increase the optical losses drastically, which leads to a limited measurement temperature range. Furthermore, a low damage method for in-situ cleaning of the support material is introduced, and again characterised through CRDS. The successful removal of clusters from surfaces is demonstrated, which allows multiple reuse of the substrates.

### 3.1. Paper 1

#### **Cavity ring-down spectrometer for measuring the optical response of supported size-selected clusters and surface defects in ultrahigh vacuum**

In the following article the experimental apparatus is introduced and all the details concerning the hardware of the setup are included. This paper serves as the reference for the coming experiments which will be performed using the CRDS experimental setup.

The cluster source, ion optics and mass selection unit, and analysis chamber are explained. The vacuum compatible cavity ring-down mirror exchanger is introduced to the scientific community for the first time, and its function is described. The optical setup, including the laser system and detection unit, is presented.

The performance of various parts of the apparatus is presented. The capability of the cluster source to produce clusters of transition metals is mentioned in the case of gold and nickel. The process of deposition is characterised through analytical methods such as atomic absorption spectrometry (AAS) and total reflection x-ray fluorescence (TXRF). It is shown that, more than 70% of the nominally deposited gold clusters are detected at the surface. This indicates the successful neutralisation of clusters by the electron source. The possibility to control the size of the cluster spot at the surface of the support material by the means of the focussing octopole is demonstrated, and the recorded cluster spot size as a function of the distance between the substrate and the focussing octopole is presented.

The high sensitivity of the CRD spectrometer is inferred, by comparison of recorded spectra by CRDS and a commercial UV-Vis spectrometer, for a model system of laser dye mixture. The presented spectra are used to outline the measurement procedure and provide details of the data treatment.

The application of the CRD spectrometer to study supported metal clusters is indicated by measuring the optical loss spectra of size-selected Nickel clusters ( $\text{Ni}_n$ ,  $n= 7, 10, \text{ and } 20$ ) on the wavelength range between 417 and 669 nm. The spectra are discussed based on simple Mie theory calculations. The oscillator strength sum rule is applied to give further insight into the quality of the recorded spectra.

Finally the evidence of detection of surface defects through CRDS is mentioned and its relevance and importance is emphasised.

## Cavity ring-down spectrometer for measuring the optical response of supported size-selected clusters and surface defects in ultrahigh vacuum

A. Kartouzian,<sup>a)</sup> M. Thämer, T. Soini, J. Peter, P. Pitschi, S. Gilb, and U. Heiz

*Technische Universität München, Lehrstuhl für Physikalische Chemie Lichtenbergstr. 4, 85748 Garching, Germany*

(Received 27 June 2008; accepted 9 November 2008; published online 23 December 2008)

A cavity ring-down spectrometer designed to investigate optical properties of size-selected clusters on surfaces under ultrahigh vacuum (UHV) conditions is presented. Clusters are produced using a laser vaporization cluster source with typical size-selected cluster currents of about 100 pA. The size of the deposition area can be controlled by means of a focusing octopole. Using the UHV compatible mirror exchanger, it is possible to have up to ten ring-down cavities and to adjust them while in vacuum. With ten cavities it is possible to cover a continuous spectral range as broad as 600 nm. The sensitivity of the method is shown to be about 5 ppm, which is two orders of magnitude better than commercial techniques. The optical spectra of small Ni<sub>N</sub> clusters ( $N=7, 10, \text{ and } 20$ ) supported at amorphous SiO<sub>2</sub> in the range between 417 and 669 nm are presented. Simple Mie theory calculations and oscillator-strength sum rule are in good agreement with the experimental data. The method proved to be sensitive enough for detection of defect sites and therefore makes it possible to study the interaction between the clusters and different surface defects. Furthermore the cryogenic sample holder can be used to perform cavity ring-down spectroscopy at low temperatures. © 2008 American Institute of Physics. [DOI: 10.1063/1.3053179]

### I. INTRODUCTION

In the past decades, optical properties of metal clusters have been extensively studied, theoretically as well as experimentally.<sup>1–8</sup> One of the motivations is the information expected to be gained on the electronic structure of clusters and particularly the evolution of the optical response with cluster size and shape, which is important for the design of optical materials. In this respect, supported metal clusters are especially relevant as any technical application of metal clusters definitely requires any kind of support. Compared to the gas phase, there are not many studies reported on optical properties of supported clusters; this is a direct result of experimental and theoretical difficulties. Relatively low absorption cross-sections of the coinage metal clusters make it necessary to increase the number of clusters under investigation in order to obtain measurable responses. On planar surfaces, high cluster densities would lead to cluster aggregation and thus the obtained results become ambiguous and cannot be attributed to a single cluster size. This becomes particularly important in the nonscaleable size regime for clusters with up to about 50 atoms where the cluster properties vary drastically with addition of each single atom.<sup>9–12</sup>

Electron and optical spectroscopy techniques such as photoelectron spectroscopy and electron energy loss spectroscopy,<sup>13</sup> absorption, fluorescence, and excitation spectroscopies<sup>14</sup> have been commonly used to explore the electronic structure of supported clusters. Another interesting possibility to study occupied electronic state densities is provided by the surface sensitive metastable He\* impact electron spectroscopy.<sup>15</sup> The above mentioned prerequisite for the in-

vestigation of mass-selected supported metal clusters, namely, the need to avoid aggregation, is also valid when applying these techniques. Therefore it is necessary to keep the particle density as low as 1% of a monolayer or less ( $<2 \times 10^{13}$  cluster cm<sup>-2</sup>).<sup>16</sup> This, together with the low absorption cross-sections of metal clusters especially in the visible range of the spectrum, pushes the conventional methods to their sensitivity limits and beyond. In ultraviolet (UV) and x-ray, the absorption cross-sections usually increase and some important results have been achieved with the required low cluster coverage,<sup>17</sup> however, in the visible range a more sensitive technique must be employed. Cavity ring-down spectroscopy (CRDS) is an extremely sensitive technique, which has been applied in the gas phase, e.g., for trace material detection<sup>18–20</sup> and can be adopted to be used as a suitable tool to study the photoabsorption properties of supported metal clusters.<sup>21–24</sup> The high sensitivity of the method makes it possible to detect absorption losses as low as 10 ppm.<sup>22</sup>

An experimental setup consisting of a high frequency laser vaporization cluster source, ion optics to guide the clusters onto the substrate and mass filter a single cluster size, as well as a dedicated analysis chamber to perform the CRDS measurements is presented. The practical difficulties of performing CRDS under ultrahigh vacuum (UHV) conditions and its application to mass-selected supported clusters are described. The sensitivity of the technique is discussed and the performance of the whole setup and its components is summarized. The performance of the method is illustrated by reporting on the optical spectra of small Ni clusters supported on amorphous SiO<sub>2</sub> surfaces. Finally the results are discussed and conclusions of the work are given.

<sup>a)</sup>Electronic mail: aras.kartouzian@mytum.de.



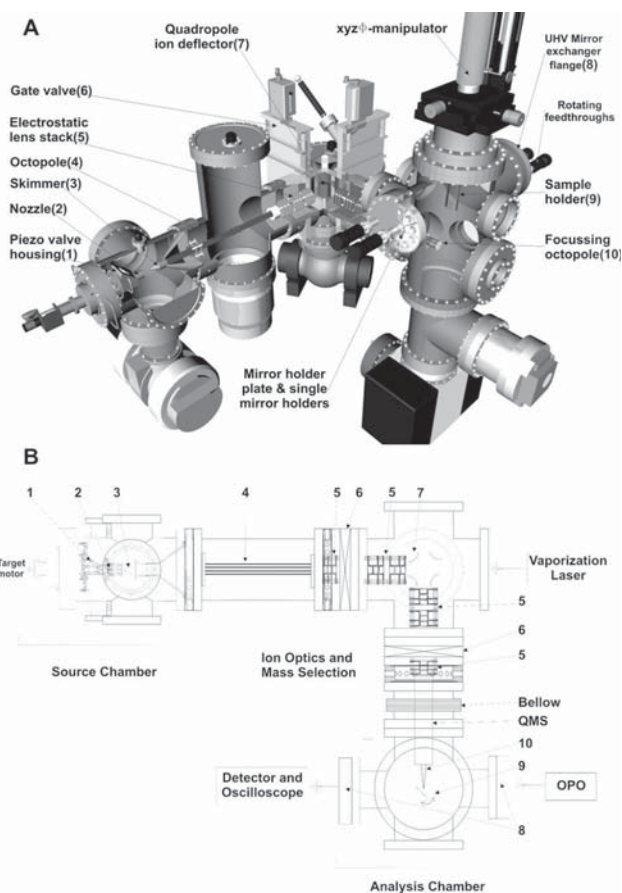


FIG. 1. (a) Three-dimensional view of the setup. Different parts are depicted and labeled. Ion optics including guiding octopole, Einzel lenses, and focusing octopole are shown, as well as mirror exchanger component. Also indicated are the pumping units. The numbers in parentheses refer to the part numbers used in schematic view. (b) Schematic view of the setup. Here the laser entrance for vaporization laser and probe laser (OPO) are better observed. A convex lens ( $f=1000$  mm, not shown here) is used to focus the vaporization laser on the target surface. Setup is divided in three main parts: source chamber, ion optics, and mass selection and analysis chamber.

## II. EXPERIMENTAL DESIGN

The experimental setup is composed of two main parts: (I) the cluster deposition unit including laser vaporization cluster source, ion optics, and mass selection device (for brief details see Sec. II A) and (II) the CRDS UHV analysis chamber. The latter is specifically designed to carry out cavity ring-down (CRD) measurements and will be discussed in more detail in Sec. II B. The vacuum system is divided into four differentially pumped chambers. This is required in order to maintain UHV conditions ( $10^{-10}$ – $10^{-11}$  mbar) in the analysis chamber while having rough vacuum ( $10^{-1}$  mbar) in the expansion zone of the cluster source. An overview of the setup is shown in Fig. 1. The source chamber is pumped by a  $139$   $\text{l s}^{-1}$  Roots pump (Balzers WKP-500A) backed with a rotary pump (Balzers UNO 060A). The base pressure is about  $10^{-2}$  mbar. During cluster formation the partial pressure of the carrier gas (He) inside the source chamber increases up to  $10^{-1}$  mbar. The second chamber (octopole chamber) is pumped by a  $1250$   $\text{l s}^{-1}$  turbo pump (Pfeiffer TPU 1201 P) backed with a rotary pump (Leybold–Heraeus D65BCS); the base pressure is  $10^{-6}$  mbar. Following the

skimmer, there are several sets of Einzel lenses and a quadrupole deflector. This part of the vacuum chamber can be separated from the octopole and analysis chambers with two gate valves. The deflector chamber is pumped by a  $500$   $\text{l s}^{-1}$  turbo pump (Pfeiffer TPU510) backed with a rotary pump (Balzers DUO 016B) and pressures down to  $2 \times 10^{-7}$  mbar are reached. Finally the analysis chamber is equipped with a  $500$   $\text{l s}^{-1}$  turbo pump (Pfeiffer TMU 521P) backed with a dual membrane pump (Pfeiffer XtraDry 150–2), an ion pump and a titanium sublimation pump (Varian VacIon plus 300 Combination Pump 919–2641). After bake out a base pressure of  $1 \times 10^{-10}$  mbar is achieved.

### A. Cluster source, ion optics, and mass selection

The cluster source is similar to the one introduced by Heiz *et al.*<sup>25</sup> The third harmonic of a 50 Hz Nd-doped yttrium aluminum garnet (Nd:YAG) laser (Innolas Spotlight 600) is focused onto the rotating metal disk. Pure He (He 6.0, air liquid) is used as carrier gas. The gas is pulsed into the source chamber using a homemade piezovalve. The gas-pulse delay (with respect to the laser pulse) and duration is controlled by a homemade piezopulsar. For optimum cluster current, it is found that opening the piezovalve slightly earlier than the laser pulse is required in order to obtain the highest gas pressures before plasma formation. The piezovalve and the expansion nozzle (67 mm long and 2 mm in diameter) are not cooled. The clusters (cations, anions, and neutrals) are formed in the nozzle and traverse a skimmer with an opening of 5 mm in diameter. The skimmer separates the source chamber and the octopole chamber having working pressures of  $10^{-2}$  and  $10^{-3}$  mbar, respectively. The 50 cm long octopole serves as an ion guide. The frequency and the power of the octopole are controlled by an amateur rf transceiver (Kenwood TS-570S). The octopole chamber is connected to the deflector chamber via an orifice of 5 mm in diameter. In the deflector chamber, the clusters are further guided through a series of Einzel lenses until they reach the electrostatic quadrupole deflector of in-house design. Deflection of the cluster beam is essential in order to separate neutral clusters from the ions and thus to prevent deposition of mass-unselected neutral clusters on the support. The deflector is a two-dimensional (2D) quadrupole composed of four cylindrical electrodes approximating the hyperbolic shape suggested by Zeman.<sup>26</sup> After exiting the deflector, charged clusters are focused into a commercial quadrupole mass spectrometer (Extrel 5500 series, mass range up to 4000 amu) by another set of electrostatic lenses. After mass-selection, the cluster ions immediately enter a focusing octopole,<sup>27</sup> which is controlled by another amateur rf transceiver. The clusters are then deposited onto the substrate (in this work: amorphous  $\text{SiO}_2$ ), which is fixed to a cryogenic sample holder mounted on a UHV manipulator with four degrees of freedom ( $x, y, z, \phi$ ). Depending on the distance of the focusing octopole from the sample, the former either works as a focusing or defocusing element. In this way, the spot area of the deposited clusters can be controlled. The focusing octopole can be replaced by a channeltron amplifier in order to record mass spectra. The cluster source produces



both positively and negatively charged clusters. Ion optics and the cluster source can be optimized for the deposition of both types of ions. In this work, cations are used as they can easily be neutralized by an electron beam upon deposition onto an isolating substrate. This is necessary because otherwise the support will become charged and the ions consequently deflected by the generated electrostatic field. A hot tantalum (Ta) filament (0.1 mm thick and 60 mm long) is used as an electron source. The filament is heated by a typical current of 0.75 A, supplied by a high precision dc power supply (Votcraft PPS-3502). A metal plate is mounted onto a separate translational feedthrough and is connected to an electrometer (Keithley 6517A). This is used as a Faraday cup to measure either cluster currents or the emitted electrons from the hot filament. The energy distribution of the clusters is obtained by applying a retarding voltage on the metal plate and recording the cluster current as a function of the applied voltage.

## B. Analysis chamber and detection unit

The analysis chamber has been optimized for CRDS measurements, and additionally surface preparation techniques (sputter gun, gas inlet system) are available. The main parts are an  $xyz$  manipulator with a  $360^\circ$ -rotation stage (Vacuum generators), a cryogenic sample holder where the substrate and the Ta filament are mounted and the UHV compatible mirror exchanger of in-house design. The manipulator is used for moving the substrate from measurement position  $P_M$  to deposition position  $P_D$ .

To carry out CRDS on supported clusters, the sample can be inserted into the cavity either at Brewster's angle or perpendicularly to the optical axis of the cavity. In the latter configuration, the substrate must be plan parallel and reveal optically flat surfaces in order to minimize losses due to reflection and thus optimizing sensitivity. The drawback of samples, which fulfill these conditions are the high price and the fact that the angular dependence is very sharp.<sup>28</sup> In contrast, for the Brewster's angle configuration, the reflection loss varies relatively smoothly<sup>28</sup> with the angle and therefore roughness of the substrate surface and the angle mismatch of two sides are not as critical. The main disadvantage of the Brewster's angle configuration is that only  $p$ -polarized light (with respect to the substrate) can be used. In both configurations the angle of the substrate with respect to the optical axis of the cavity is crucial. In this work the Brewster's angle configuration is used. In order to analyze the sample surface and to obtain a two dimensional image (surface map) of the cluster density (see below), the sample is moved at Brewster's angle and at the center of the cavity in the  $x$  and  $z$  direction.

A schematic view of the optical setup is illustrated in Fig. 2(a). The output of a Nd-YAG pumped optical parametric oscillator (OPO) laser (Innolas *integra*, 20 Hz,  $\sim 3\text{--}7$  ns pulses,  $10\text{ cm}^{-1}$ ) is injected into the stable cavity without mode matching optics. The light leaking from the cavity is then guided through a polarizer where the light intensity can be controlled to avoid saturation of the detector. A convex lens is used to focus the light onto a diffuser so that the mode structure of the laser is lost. After the diffuser, the light is focused by another convex lens onto the photomultiplier tube (Hamamatsu H7732-10). The signals are recorded and processed *in situ* with an oscilloscope (Lecroy Waverunner 6051). Data acquisition and scanning of the laser are fully automated by a self-written LABVIEW program. Since the reflectivity of the mirrors depends on the wavelength as does the intensity of the light leaking out of the ring-down cavity, the sensitivity of the detector must be adjusted in order to avoid saturation of the detector while still achieving maximum resolution of the oscilloscope for all wavelengths. This is done by applying a variable sensitivity voltage to the detector. To this purpose, the sensitivity of the detector is controlled from a calibration table using the auxiliary output of the oscilloscope. The sensitivity voltage is optimized for

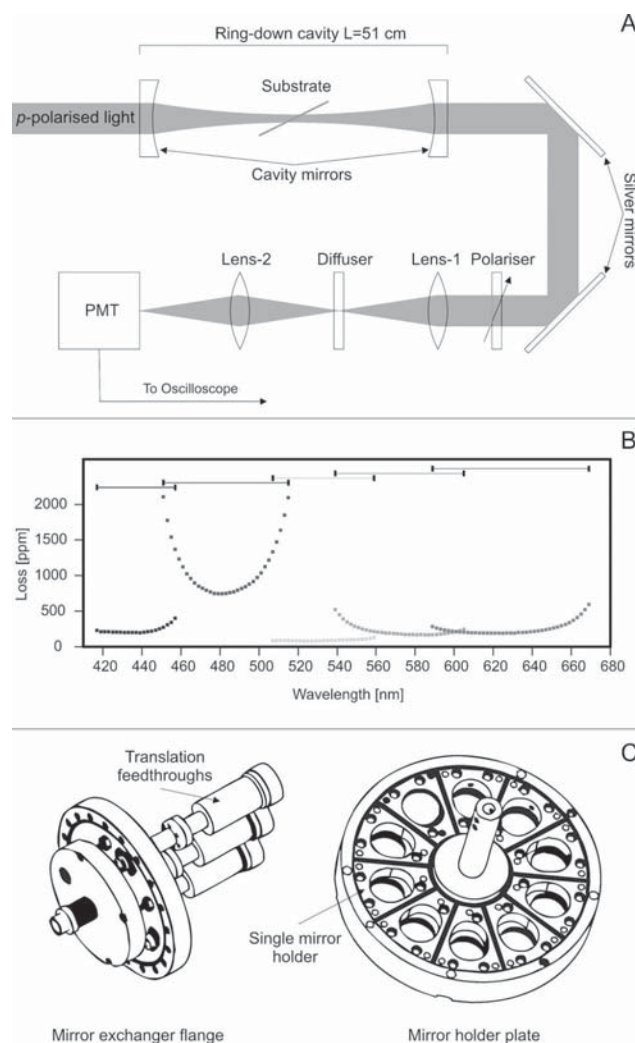


FIG. 2. (a) Schematic view of the optical setup used for the CRDS measurements. The output of an OPO laser is injected into the stable cavity without mode matching optics. The light leaking from the cavity is then guided through a polarizer where the light intensity can be controlled to avoid saturation of the detector. A convex lens is used to focus the light onto a diffuser so that the mode structure of the laser is lost. After the diffuser, the light is focused by another convex lens onto the photomultiplier tube. (b) The wavelength dependence loss of the cavity mirrors is depicted. Note the limited range and the overlap between the used cavities. The wavelength range of each cavity is indicated. (c) The construction of the UHV compatible mirror exchanger.

structure of the laser is lost. After the diffuser, the light is focused by another convex lens onto the photomultiplier tube (Hamamatsu H7732-10). The signals are recorded and processed *in situ* with an oscilloscope (Lecroy Waverunner 6051). Data acquisition and scanning of the laser are fully automated by a self-written LABVIEW program. Since the reflectivity of the mirrors depends on the wavelength as does the intensity of the light leaking out of the ring-down cavity, the sensitivity of the detector must be adjusted in order to avoid saturation of the detector while still achieving maximum resolution of the oscilloscope for all wavelengths. This is done by applying a variable sensitivity voltage to the detector. To this purpose, the sensitivity of the detector is controlled from a calibration table using the auxiliary output of the oscilloscope. The sensitivity voltage is optimized for

each mirror set for various wavelengths in an interval of 5 nm. During measurements, the calibration data are interpolated for the wavelengths in between. The most essential part of the analysis chamber is the UHV compatible mirror exchanger with up to 10 mirrors. Since the highly reflective CRD mirrors have a narrow bandwidth of about 60 nm, several mirrors must be used to cover the visible and near UV range. In the experiments presented here, five different cavities are employed for the range between 420–670 nm, which consists of two highly reflective mirrors ( $R > 99.99\%$ , Los Gatos Research). The length of the cavities is 51 cm [see Fig. 2(b)]. For this purpose we designed a UHV compatible mirror exchanger [Fig. 2(c)] allowing the use of up to ten different cavities. It is designed in such a way that the cavities can be adjusted from the outside without venting the analysis chamber and realigning the probe laser. The mirror exchanger consists of a rotatable disk plate, the plane of which can be adjusted by two linear feedthroughs. This disk plate contains ten single mirror holders, which can be adjusted separately. The disk plate is mounted onto a conflat flange (CF-150). A small viewport is used for the probe laser. By rotating the two disk plates, one of the cavities can be used for the CRD measurements. The alignment of the cavities is carried out as follows: before pumping, the UHV chamber coarse alignment of each cavity is done separately by means of the individual mirror holders. At UHV conditions, each cavity is optimized by aligning the disk plate with the linear feedthroughs.

### III. CHARACTERIZATION OF THE SETUP

Prior to the investigation of the optical properties of size-selected clusters on surfaces, the performance of the cluster source and the focusing octopole as well as the efficiency of the neutralization is tested. The mass spectra of gold and nickel reveal well-resolved cluster sizes over the whole mass range of the quadrupole mass spectrometer (for gold,  $\text{Au}_N^+$ ,  $N=1-20$ ). Typical cluster currents vary between 1 nA for  $\text{Au}_1^+$  and 120 pA for  $\text{Au}_{20}^+$  clusters. Upon deposition, the cluster ions are neutralized by electrons from a hot filament. Successful deposition of the clusters is verified by atomic absorption spectrometry<sup>29</sup> (AAS) and total reflection x-ray fluorescence (TXRF).<sup>30</sup> After deposition of approximately 14.7 ng  $\text{Au}_{20}$  clusters, more than 10 ng gold is detected. Thus the efficiency is at least 70%. The deviation is attributed to uncertainties in cluster current measurements and the material loss during dissolving gold in aqua regia [ $\text{HNO}_3 + 3\text{HCl}(\text{aq})$ ] from the substrate surface.

The performance of the focusing octopole is characterized by evaluating the size of the cluster spots measured by CRDS. Spot sizes as function of the distance between the focusing octopole and the substrate are illustrated in Fig. 3 and show nonlinear dependency. The spot sizes are obtained by mapping the optical losses with CRDS at a fixed wavelength in an area around cluster deposition. The obtained map is fitted by a 2D Gaussian, the full width at half maximum of which defines the spot size. Transmission of the focusing octopole is obtained from the ratio of the cluster

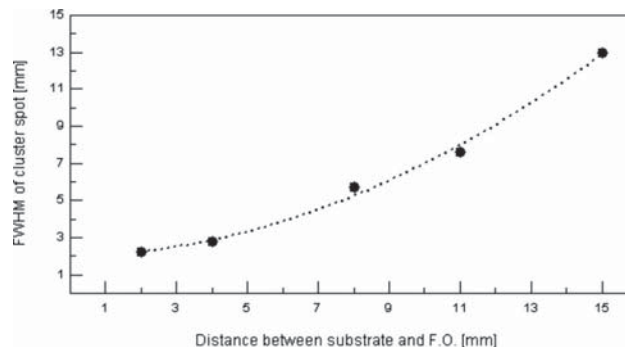


FIG. 3. Dependence of cluster spot size on the distance from focusing octopole. As the distance is increased, a nonlinear increase in the cluster spot size is observed.

current measured at the entrance plate of the focusing octopole to that at the sample; a typical value is  $\sim 60\%$ .

The sensitivity of the CRD spectroscopy is determined by the minimal loss detection limit  $L_{\min}$ .  $L_{\min}$  is generally calculated as the product of the intrinsic loss of the cavity and the relative error in the measurement of the ring-down time  $\tau(\omega)$ . Equation (1) gives the relation between ring-down time  $\tau(\omega)$ , the roundtrip losses  $L_i(\omega)$  generated in the cavity, and round trip time  $t_r$ .

$$\tau(\omega) = \frac{t_r}{\sum_i L_i(\omega)} = \frac{t_r}{L_{\text{cavity}}(\omega) + L_{\text{substrate}}(\omega) + L_{\text{cluster}}(\omega)}. \quad (1)$$

The total intrinsic losses of the cavity include the losses of cavity mirrors and the losses due to the substrate  $L_0 = L_{\text{cavity}} + L_{\text{substrate}}$ . From Eq. (1), it follows that by measuring  $\tau(\omega)$  the individual losses can directly be calculated by performing experiments with and without substrate and/or clusters. Typical values of  $L_{\min}$  are  $\sim 25$  ppm after investigating 75 000 CRD traces measured at 570 nm for a  $\text{SiO}_2$  sample of 0.13 mm thickness. The detection limit can be substantially improved by averaging. Using the same raw data and averaging 100 traces, a detection limit of  $\sim 2.4$  ppm is achieved. Care should be taken when considering this value since the absolute number of the detection limit varies with the intrinsic loss of the cavity at different wavelengths:  $L_{\min}$  increases as the intrinsic losses increase. This is the reason for the lower sensitivity of CRDS for supported clusters; due to the presence of the substrate, the loss of the cavity is increased. The relative error of  $\tau(\omega)$  when averaging 100 traces is 0.3%. This leads to a maximum detection limit of 10 ppm over the whole wavelength range since the intrinsic loss of the cavity including the substrate has never been observed to be higher than 3300 ppm. In the majority of the investigated wavelength range,  $\tau(\omega)$  is better than 5 ppm.

### IV. EXPERIMENTAL PROCEDURE

All measurements are performed at room temperature. Thin amorphous  $\text{SiO}_2$  plates are used as substrate (Marienfeld BK7, 0.13 mm thick), cleaned with the highest purity acetone (Merck spectroscopy grade) and mounted in the

analysis chamber. The surface of the substrate is mapped using CRDS at a single wavelength by scanning the substrate in the  $x$  and  $z$  direction in increments of 0.5 mm. Subsequently the clusters are deposited at the substrate position with the highest surface quality (an area with small and constant loss). The exact position of the cluster spot ( $P_{\text{sample}}$ ) is then determined with respect to the horizontal and vertical edges of the substrate. The position of the substrate edges can easily be determined by the high scattering losses observed in the CRDS measurement. In fact, the ring-down signal almost vanishes when the edge of the glass is brought into the cavity. Due to the finite size of the laser spot inside the cavity, this measurement has an uncertainty of about 0.1 mm. A second position is chosen as reference point ( $P_{\text{reference}}$ ). The clusters are deposited at  $P_{\text{sample}}$ . The cluster current is optimized for the corresponding cluster size. After deposition, CRD spectra are recorded at both positions,  $P_{\text{sample}}$  and  $P_{\text{reference}}$ , and for the empty cavity. For each mirror pair, the cavity is readjusted and the positions of substrate edges are measured to determine the exact positions  $P_{\text{sample}}$  and  $P_{\text{reference}}$ . This reduces a possible position mismatch. At each wavelength, 100 CRD signals are averaged to improve the signal-to-noise ratio. The resulting spectrum over a given wavelength range is composed of the recorded data from the different cavities. Figure 4 illustrates the data treatment procedure for a model system. To demonstrate the performance of the CRD spectrometer, a solution containing Coumarin 334®, Rhodamine B®, and Oxazine 1® laser dyes dissolved in methanol was chosen (1.5 mg l<sup>-1</sup> for Rhodamine B®, concentration of Coumarin 334® and Oxazine 1® were adjusted to get 0.2 and 1 as peak height ratio in solution, respectively). The substrate was dip coated with the solution and then measured. The number density of dye molecules at the surface could be calculated from the known absorption cross-sections of the dyes. In the case of Rhodamine B®  $\sim 3.3 \times 10^{11}$  cm<sup>-2</sup> was determined. In a first step, the empty cavity loss is subtracted from spectra measured at  $P_{\text{sample}}$  and  $P_{\text{reference}}$ . The result is depicted in Fig. 4(a). Figure 4(b) shows the difference between the two spectra, which is the spectrum of the sample only. The mirrors used in this work are chosen in a way that an overlap of at least 8 nm is available. This allows adjustments (scaling and/or shifting) of the spectra from the different cavities, as in the overlap region identical absolute absorption cross-sections must be measured. Simple shifting is justified because the substrate surface is not homogeneous. The error in the position (0.1 mm) results in variations in the absolute loss, which in turn causes a shift upon the subtraction of the sample spectra. Scaling is justified when taking variations in the surface coverage into account. Typically cluster coverages reveal Gaussian distributions and a mismatch of 0.1 mm for  $P_{\text{sample}}$  for the different cavities can result in variations in absolute loss values, which scale linearly with the deviation in the total number of probed molecules or clusters. In this work, a combination of scaling and shifting is used in order to compensate for both uncertainties. Typical scaling factors lie between 0.98 and 1.02 and absolute shifts are smaller than 150 ppm. In addition, a surface map is measured at an arbitrary wavelength around  $P_{\text{sample}}$ . From the map, the absolute loss at the

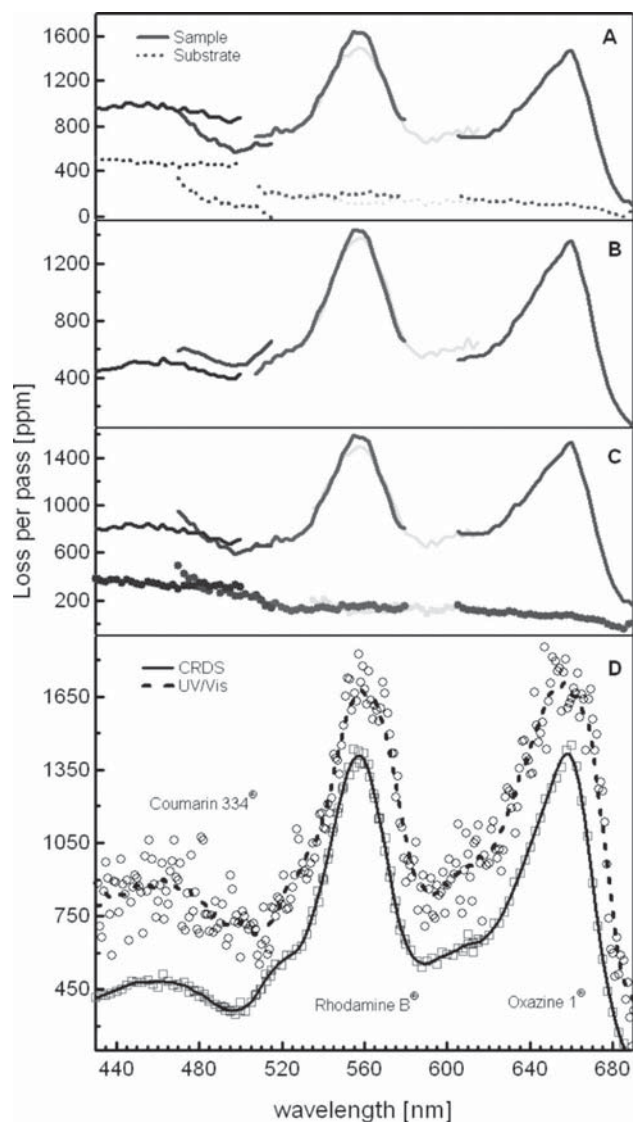


FIG. 4. Absorption spectrum of a dye mixture solution (1.5 mg l<sup>-1</sup> for Rhodamine B®, concentration of Coumarin 334®, and Oxazine 1® were adjusted to get 0.2 and 1 as peak height ratio in solution, respectively) recorded by CRDS. Different colors indicate different cavity mirrors. (a) The loss of the uncoated substrate and coated substrate (labeled as substrate and sample, respectively) are shown. Intrinsic loss of the cavity without substrate is subtracted already. (b) The difference between “sample” and “substrate” losses is shown. Note the shift at overlap regions. (c) The scaled version of part A. (d) The scaled version of part B and the UV/visible measurement of the same sample (labeled as CRDS and UV/visible, respectively). The UV/visible spectrum is upshifted by 300 ppm for better illustration. In both cases, the measured data and a smooth line to guide the eyes are shown.

specific wavelength is extracted. The corrected spectrum is then shifted as a whole so that the loss value at that specific wavelength is consistent with the one observed in the surface map. Note that the correction procedure does not add or remove any features to or from the measured spectrum. The corrected version of Fig. 4(a) is depicted in Fig. 4(c). It is crucial to consider this information while interpreting the spectra because they deliver the information, whether or not the structures in the spectra are originating from the background. At the end, Fig. 4(d) (solid line) presents the final result of the measurement, which is the corrected version of



Fig. 4(b). The dashed line in Fig. 4(d) shows the absorption spectrum of dye mixture measured by commercial UV/visible (analytic-Jena Specord 40) in step mode with 2 s integration time as a reference (max integration time of 10 s did not reduce the noise level). The peak positions and relative intensities are in perfect agreement with the spectrum measured by CRDS and shown in Fig. 4(d) by the solid line. The UV/visible data at shorter wavelengths have, however, a much larger noise level compared to the spectrum obtained by CRDS. The CRD spectrum has a relative error of 2% and is much more accurate than UV/visible with an error of up to 50% [see Fig. 4(d) in the range of 430–500 nm]. Both spectra depict all the spectral features of the dyes found in reference data from the dye producers. This comparison clearly reveals the procedure for measuring CRD spectra, which leads to reliable data and shows CRDS to be superior in sensitivity by almost 2 orders of magnitude as verified by concentration dependent measurements.

## V. RESULTS AND DISCUSSION

The results on CRDS spectra in the visible range of size-selected Ni clusters supported on amorphous silica are reported. Upon deposition on the insulating substrate, the clusters are neutralized by electrons from a hot filament, furthermore the cluster current could not be measured continuously but only at a given interval with the movable Faraday cup. Assuming a neutralization efficiency of unity and stable cluster currents between measuring intervals the coverages  $\rho$  have been determined to be  $10^{12} \text{ cm}^{-2}$ . In the following, we express the optical results in loss per pass  $\Lambda$  and not in cross-section  $\sigma$  ( $\sigma = \Lambda/\rho$ ) in order to exclude any systematic errors in cluster coverages. The spectra obtained between 417 and 669 nm are represented in Fig. 5 for  $\text{Ni}_7$ ,  $\text{Ni}_{10}$ , and  $\text{Ni}_{20}$ . The spectrum of the uncoated substrate is subtracted. For all three cluster sizes, a structureless increase in the loss is observed for increasing photon energies. Two steps at  $\sim 480$  and  $600$  nm are observed in all spectra. It may be that all three cluster sizes reveal such features and that they are indeed intrinsic to the three cluster sizes. Note, however, that the spectra of amorphous silica reveal small absorption bands at these two wavelengths (bottom of Fig. 5—marked with two arrows; also shown as comparison is the spectrum of  $\text{Ni}_{20}$ ), which can be attributed to defect sites.<sup>31</sup> The clusters are likely to be trapped at these sites and as the spectrum of the silica substrate is taken as background (see Sec. IV) the two absorption bands related to defects are manifested in the spectra of the clusters as negative absorptions (e.g., steps). The intensity of the absorption bands varies from substrate to substrate and this is the reason why the negative absorptions are differently pronounced for different measurements.

The optical response of free nickel spheres with diameters much smaller than the wavelength of the probing light can be predicted by using the classical Mie theory, where the wavelength dependent absorption cross-section  $\sigma_{\text{Mie}}(\lambda)$  of a nickel sphere with volume  $V$  and the dielectric function  $\epsilon = \epsilon_1 + i\epsilon_2$  can be written as

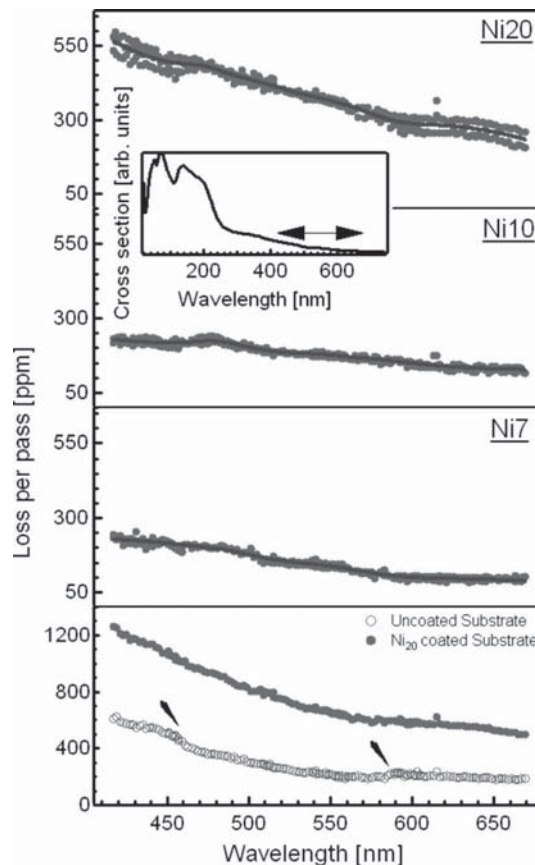


FIG. 5. Experimentally measured spectra of  $\text{Ni}_n$  ( $n=7, 10$ , and  $20$ ) clusters supported on silica surface (three upper panels). The spectra show almost no structure and are in good agreement with simple Mie calculation for free Ni clusters (inset). Oscillator strength scales with cluster size almost perfectly showing two and three times higher losses for  $\text{Ni}_{20}$  compared to  $\text{Ni}_{10}$  and  $\text{Ni}_7$ , respectively. There are two steps in all spectra at around 480 and 600 nm. These are originating from uncoated substrate spectrum, which shows two features (arrows in bottom graph) at 460 and 585 nm. For comparison, the spectrum recorded at cluster coated substrate is shown as well. This on the other hand is smooth and monotonous. Note that it is not possible to fit a  $\lambda^{-4}$  function to the spectra. This indicates that the scattering losses are not the main part of the measured optical losses for the clusters inside the cavity, however, their contribution cannot be excluded.

$$\sigma_{\text{Mie}}(\lambda) = \frac{18\pi}{\lambda} \frac{\epsilon_2}{(\epsilon_1 + 2)^2 + \epsilon_2^2} V. \quad (2)$$

$V$  is the volume of the  $\text{Ni}_n$  clusters and is calculated from the bulk density; note that this is the only size dependent parameter in this model. For the dielectric function, the bulk value of nickel<sup>32</sup> is used. The calculated spectrum is depicted as inset of Fig. 5, from which it is evident that small free Ni clusters reveal a smooth absorption spectrum at wavelengths above 350 nm, which is consistent with the CRD spectra. A small band is observed at  $\sim 340$  nm (3.65 eV) and distinct absorption bands only at higher energies. Furthermore, our data are consistent with photodissociation spectra of  $\text{Ni}_n\text{Ar}_m$  clusters in the gas phase from Knickelbein *et al.*<sup>33</sup> These measurements were also interpreted by the simple Mie approximation. Nour *et al.*<sup>34</sup> studied the electronic spectra of small nickel clusters trapped in argon matrices at 12 K and found a band centered at 415 nm (3 eV). The maximum of this band is not covered by the range measured in this work.

At a temperature of 12 K, they could clearly resolve three vibronic bands of Ni<sub>2</sub> and Ni<sub>3</sub> clusters. The vibronic bands of Ni<sub>7</sub> and larger clusters could not be resolved in an experiment performed at 300 K. In experiments presented here, the transitions are additionally broadened due to the interaction with the substrate. The CRD spectra of Ni atoms and dimers on SiO<sub>2</sub> substrate have been recorded as well (not shown here). Interestingly, no sharp absorption peaks could be observed in the measured range neither for Ni atoms nor for Ni dimers. Strong interactions between Ni atoms and dimers with the substrate indeed shift the expected peaks to wavelengths out of the range investigated here (to either lower or higher wavelengths). The band of nickel clusters in argon matrices at 415 nm is redshifted by 75 nm when comparing to the band at 340 nm predicted by simple Mie calculations. A similar shift has been observed by Knickelbein *et al.*<sup>33</sup> for Ni<sub>n</sub>Ar<sub>m</sub> clusters. For nickel clusters on surfaces shifts in both directions are possible<sup>35</sup> our results suggest, however, that the peak is redshifted by less than 75 nm or even blueshifted when comparing absolute peak positions.

According to classical and quantum theories, the sum of oscillator strengths from all electronic transitions over the whole spectral range scales with the total number of electrons in the molecule.<sup>36</sup> Thus the partial oscillator strength for each cluster size can be obtained by integrating the absorption cross-sections over the wavelength range of the experiment

$$f_n = \int_{\lambda=417 \text{ nm}}^{669 \text{ nm}} \frac{\sigma_n(\lambda)d\lambda}{\lambda^2} = \frac{1}{\rho} \int_{\lambda=417 \text{ nm}}^{669 \text{ nm}} \frac{\Lambda_n(\lambda)d\lambda}{\lambda^2}. \quad (3)$$

The ratio of the partial oscillator strength for each pair of clusters ( $f_{10}/f_7, f_{20}/f_7, f_{20}/f_{10}$ ) can be extracted and so the following values are obtained from the recorded spectra:  $f_{10}/f_7=1.37, f_{20}/f_7=2.78$ , and  $f_{20}/f_{10}=2.04$ . Despite the fact that the measured range covers only a small portion of the oscillator strength, these values fit almost perfectly to the expected theoretical data.

## VI. CONCLUSION

In this paper the design of an experimental setup dedicated to the measurements of the optical properties of size-selected clusters on various support materials by CRDS under UHV conditions is presented. A UHV compatible mirror exchanger allows for carrying out experiments in the whole visible range efficiently and the setup is robust enough to be used on a daily basis. The sensitivity of CRDS is better than 10 ppm over the whole spectral range, improved performance can be obtained for selected support materials and cavities. The sensitivity ( $\sim 2.5$  ppm) is at least two orders of magnitude better than that obtained with commercial techniques ( $\sim 500$  ppm). Only with this superior sensitivity it is possible to study optical properties of size-selected clusters on surfaces, although experiments could be carried out on any optically transparent substrate materials. Results on size-selected Ni clusters fit well to simple Mie calculations. The ratios of the partial oscillator strength for each pair of clusters are consistent with the oscillator strength sum rule. The agreement of the general shape of the obtained spectra with

Mie theory suggests that the electronic states involved in the optical transition are not to be perturbed considerably by the interaction with the amorphous silica substrate.

The sensitivity of the setup is also sufficient for the characterization of defect sites on various support materials. Combining optical data of defect sites and of size selected clusters will allow a complete picture of the trapping sites for the clusters on the substrate to be obtained. Further temperature dependent measurements will further reveal thermal stabilities of size-selected clusters on various support materials.

## ACKNOWLEDGMENTS

This research is supported by the Deutsche Forschungsgemeinschaft within the Priority Program No. SPP1153. The authors want to thank M. Maier for AAS and TXRF measurements and K. Hartl for her contribution to model system measurements.

<sup>1</sup>W. A. DeHeer, *Rev. Mod. Phys.* **65**, 611 (1993).

<sup>2</sup>M. Brack, *Rev. Mod. Phys.* **65**, 677 (1993).

<sup>3</sup>J. Lermé, B. Palpant, B. Prevel, E. Cottancin, M. Pellarin, M. Treilleux, J. L. Vialle, A. Perez, and M. Broyer, *Eur. Phys. J. D* **4**, 95 (1998).

<sup>4</sup>W. Harbich, S. Fedrigo, and J. Buttet, *Chem. Phys. Lett.* **195**, 613 (1992).

<sup>5</sup>W. Harbich, S. Fedrigo, and J. Buttet, *Z. Phys. D: At., Mol. Clust.* **26**, 138 (1993).

<sup>6</sup>W. Harbich, S. Fedrigo, J. Buttet, and D. M. Lindsay, *Z. Phys. D: At., Mol. Clust.* **19**, 157 (1991).

<sup>7</sup>B. Palpant, E. Cottancin, M. Pellarin, J. Lermé, J. L. Vialle, M. Broyer, B. Prevel, M. Treilleux, and A. Perez, *Ann. Phys. (Paris)* **23**, 167 (1998).

<sup>8</sup>B. Palpant, B. Prevel, J. Lermé, E. Cottancin, M. Pellarin, M. Treilleux, A. Perez, J. L. Vialle, and M. Broyer, *Phys. Rev. B* **57**, 1963 (1998).

<sup>9</sup>U. Heiz, A. Sanchez, S. Abbet, and W. D. Schneider, *J. Am. Chem. Soc.* **121**, 3214 (1999).

<sup>10</sup>A. Sanchez, S. Abbet, U. Heiz, W. D. Schneider, H. Häkkinen, R. N. Barnett, and U. Landman, *J. Phys. Chem. A* **103**, 9573 (1999).

<sup>11</sup>M. A. Röttgen, S. Abbet, K. Judai, J. M. Antonietti, A. S. Wörz, M. Arenz, C. R. Henry, and U. Heiz, *J. Am. Chem. Soc.* **129**, 9635 (2007).

<sup>12</sup>H. Häkkinen, W. Abbet, A. Sanchez, U. Heiz, and U. Landman, *Angew. Chem., Int. Ed.* **42**, 1297 (2003).

<sup>13</sup>P. Fayet, F. Patthey, H. V. Roy, T. Detzel, and W. D. Schneider, *Surf. Sci.* **269–270**, 1101 (1992).

<sup>14</sup>S. Fedrigo, W. Harbich, and J. Buttet, *J. Chem. Phys.* **99**, 5712 (1993).

<sup>15</sup>P. Stracker, S. Krischok, and V. Kempter, *Surf. Sci.* **473**, 86 (2001).

<sup>16</sup>S. Abbet, K. Judai, L. Klinger, and U. Heiz, *Pure Appl. Chem.* **74**, 1527 (2002).

<sup>17</sup>W. Eberhardt, P. Fayet, D. M. Cox, Z. Fu, A. Kaldor, R. Sherwood, and D. Sondericker, *Phys. Rev. Lett.* **64**, 780 (1990).

<sup>18</sup>G. Berden, R. Peeters, and G. Meijer, *Int. Rev. Phys. Chem.* **19**, 565 (2000).

<sup>19</sup>M. D. Wheeler, S. M. Newman, A. J. Orr-Ewing, and M. N. R. Ashfold, *J. Chem. Soc., Faraday Trans.* **94**, 337 (1998).

<sup>20</sup>J. J. Scherer, J. B. Paul, A. O'Keefe, and R. J. Saykally, *Chem. Rev.* **97**, 25 (1997).

<sup>21</sup>A. C. R. Pipino, J. P. M. Hoefnagels, and N. Watanabe, *J. Chem. Phys.* **120**, 2879 (2004).

<sup>22</sup>J. M. Antonietti, M. Michalski, U. Heiz, H. Jones, K. H. Lim, N. Röscher, A. Del Vitto, and G. Pacchioni, *Phys. Rev. Lett.* **94**, 213402 (2005).

<sup>23</sup>R. Engeln, G. von Helden, A. J. A. van Roij, and G. Meijer, *J. Chem. Phys.* **110**, 2732 (1999).

<sup>24</sup>S. Gilb, K. Hartl, A. Kartouzian, J. Peter, U. Heiz, H. G. Boyen, and P. Ziemann, *Eur. Phys. J. D* **45**, 501 (2007).

<sup>25</sup>U. Heiz, F. Vanolli, L. Trento, and W. D. Schneider, *Rev. Sci. Instrum.* **68**, 1986 (1997).

<sup>26</sup>H. D. Zeman, *Rev. Sci. Instrum.* **48**, 1079 (1977).

<sup>27</sup>M. A. Röttgen, K. Judai, J. M. Antonietti, U. Heiz, S. Rauschenbach, and K. Kern, *Rev. Sci. Instrum.* **77**, 013302 (2006).

<sup>28</sup>S. E. Fiedler, A. Hese, and A. A. Ruth, *Rev. Sci. Instrum.* **76**, 023107-1 (2005).

- <sup>29</sup>B. Welz and M. Sperling, *Atomic Absorption Spectroscopy*, 3rd ed. (Wiley, New York, 1999).
- <sup>30</sup>A. Prange, *Spectrochim. Acta, Part B* **44**, 437 (1989).
- <sup>31</sup>A. Kartouzian, M. Thämer, and U. Heiz (unpublished).
- <sup>32</sup>J. H. Weaver, C. Krafka, D. W. Lynch, and E.-E. Koch, *Optical Properties of Metals Part I* (Fachinformationszentrum Energie Physik Mathematik, Karlsruhe, 1981).
- <sup>33</sup>M. B. Knickelbein, *J. Chem. Phys.* **99**, 2377 (1993).
- <sup>34</sup>E. M. Nour, C. Alfaro-franco, K. A. Gingerich, and J. Laane, *J. Chem. Phys.* **86**, 4779 (1987).
- <sup>35</sup>U. Kreibig, G. Bour, A. Hilger, and M. Gartz, *Phys. Status Solidi A* **175**, 351 (1999).
- <sup>36</sup>J. Berkowitz, *Photoabsorption, Photoionization and Photoelectron Spectroscopy* (Academic, New York, 1979).



## 3.2. Paper 2

### **Characterisation and cleaning of oxide support materials for cavity ring-down spectroscopy**

The importance of the choice of support material for CRDS measurements on size-selected supported metal clusters is discussed thoroughly in previous sections. In the following contribution some of the commercially available substrates are tested for their compatibility and quality. Sputtering with low energy  $\text{Ar}^+$  ions produced by a commercial ion source is introduced as a non-destructive method to clean substrates and remove previously deposited clusters from their surface. Characterisation is performed using the cavity ring-down spectrometer introduced in paper 1.

In the experimental part the measurement apparatus is described briefly. The concepts of spatial filtering and mode matching are given and their application in the case of the used laser system is justified. It is shown that an improved beam profile is achieved through spatial filtering, and that the relative error of the measurement is reduced by about 50% with mode matching.

From the materials suitable for Brewster's angle configuration CRDS, amorphous silica, borosilicate, and yttria stabilised zirconia (YSZ) are tested and compared based on their optical losses. It is shown that the commercially available borosilicate substrates provide the highest optical quality. The high sensitivity of the apparatus is again demonstrated by the detection of trace amounts of Nd ions in YSZ samples.

It is observed that the optical quality of the borosilicate samples is degraded after common bake-out procedures. X-ray diffraction measurements reveal that the structure of the borosilicate glass undergoes a deformation after being exposed to slightly elevated temperatures ( $\sim 140^\circ\text{C}$ ) for over five days.

The high optical quality of the substrates which is required for CRDS measurements, together with the low thickness makes their manufacturing both difficult and costly. This triggers a motivation to develop a method for cleaning substrates from deposited clusters so that they may be reused more often. In this paper, the successful application of low energy ion sputtering for substrate cleaning is demonstrated, and it is indicated that the method causes marginal damages to the support material as characterised by the cavity ring-down spectrometer. The removal of gold clusters from the surface is confirmed through analytical methods including atomic absorption spectrometry and total reflection x-ray fluorescence.



# Characterisation and cleaning of oxide support materials for cavity ring-down spectroscopy

Aras Kartouzian\*, Martin Thämer, and Ulrich Heiz

Lehrstuhl für Physikalische Chemie, Technische Universität München, Lichtenbergstr. 4, 85748 Garching, Germany

Received 16 October 2009, revised 30 November 2009, accepted 22 December 2009

Published online 29 January 2010

PACS 36.40.Mr, 42.62.Fi, 78.40.Pg, 78.40.Ha, 78.66.Jg, 78.68.+m

\* Corresponding author: e-mail [Aras.kartouzian@mytum.de](mailto:Aras.kartouzian@mytum.de), Phone: +49 89 289 13414, Fax: +49 89 289 13389

Cavity ring-down spectroscopy (CRDS) has been applied to characterise different oxide materials (amorphous silica, borosilicate and yttria stabilised zirconia YSZ) which are suitable to be used as support material for size-selected metal clusters. The sensitivity of the spectroscopic method was improved by means of transversal mode matching and spatial filtering of the laser beam profile, reducing the relative error by 50%. The high sensitivity of CRDS allows the detection of trace amounts of impurities and defect sites in the samples, based on their absorption properties. In YSZ, traces of Nd have been

detected. The optical quality of the substrates was determined qualitatively according to the measured optical losses. CRDS surface maps have been used to monitor the homogeneity of the support materials, and the influence of ion bombardment on the surface has been studied. It is shown that in the case of BK7<sup>®</sup> substrates, sputtering with low energy Ar<sup>+</sup> ions could remove deposited gold clusters almost completely causing very low damage to the surface. These results were confirmed analytically.

© 2010 WILEY-VCH Verlag GmbH & Co. KGaA, Weinheim

**1 Introduction** Supported metal nanoclusters play an important role in modern chemical catalysis, as novel catalytic properties may evolve in the nanoscale size regime [1]. The evolution of the electronic properties of metal clusters with size is accompanied by dramatic changes in the optical, chemical and magnetic behaviour of small clusters and nanoparticles with respect to bulk materials. Optical characteristics of metal clusters and their variation with size, shape and environment are of fundamental interest, both theoretically and experimentally [2–6]. Understanding the link between the electronic structure and catalytic activity of metal nanoparticles is key for future material design and efficiency optimisation. A powerful method to investigate the electronic structure of matter is optical spectroscopy. In the study of supported size-selected metal clusters, it is necessary to employ a highly sensitive spectroscopic method because of their (i) small absorption cross-section, and (ii) low surface coverage (to hinder agglomeration).

Cavity ring-down spectroscopy (CRDS) is an extremely sensitive technique, which has been widely used in gas phase studies, e.g. for trace material detection with sensitivities in ppb range [7–9]. When applied to solid samples, it is capable of measuring optical losses with sensitivities lower than

5 ppm [10–23]. The lower sensitivity of CRDS in the case of solid samples is caused by additional losses originating from scattering, reflection at the interfaces and absorption of the substrate material, which are not present in gas phase measurements. Therefore, the choice of support material and its quality is of great importance for the desired performance of CRDS.

Beside the intrinsic properties of oxide support materials, the geometry of the setup plays a decisive role in reducing losses. The substrate can be inserted into the cavity either perpendicularly or at the Brewster's angle to the optical axis of the cavity. In the former configuration, the substrate must be perfectly plane parallel and optically flat due to the sharp angular dependency of reflection losses [24]. The limited availability of such substrates is their main drawback. In contrast, for the Brewster's angle configuration, the reflection loss varies relatively smoothly with the angle [24] and therefore, the roughness of the substrate's surface and the angle mismatch between two sides are not as critical. The main disadvantage of the Brewster's angle configuration, however, is that only p-polarised light can be used. Furthermore, to avoid birefringence, the oxide materials must have either an amorphous structure or possess

**Table 1** A list of some optical materials suitable for CRDS in Brewster's angle configuration.

material	structure	transparent window (nm)
SiO <sub>2</sub>	glass	200–2100
BK7 <sup>®</sup>	glass	360–1700
YSZ	cubic	400–6000
MgO	cubic	300–6000

a cubic lattice. Birefringence causes the increase of optical losses by rotating the polarisation. A list of selected materials that fulfil the criteria mentioned above is presented in Table 1. It is obvious that the substrate should be transparent in the measurement range.

The current work presents a spectroscopic comparison among some of the oxide support materials for Brewster's angle configuration (SiO<sub>2</sub> glass, BK7<sup>®</sup> glass and yttria stabilised zirconia (YSZ)). Additionally, a low damage method is introduced for cleaning the substrates after being coated with metal clusters. In the experimental section, the UHV apparatus and the spectroscopy are described briefly and the measurements are explained. The results are then discussed followed by the conclusions of the work.

**2 Experimental** The experimental setup was introduced in a previous paper [13] and hence only a brief description is included here. Metal clusters were produced using a laser vaporisation cluster source. The metal atoms from a target were evaporated by the third harmonic of a Nd-doped yttrium aluminium garnet (Nd:YAG) laser to form a plasma. Clusters were formed upon collision with carrier gas molecules and the following supersonic expansion through a nozzle. Positively charged cluster ions were guided by a set of ion optics and focused into a quadrupole mass-selecting unit by a set of Einzel lenses. Following a path through a focusing octopole, the mass-selected clusters were soft-landed onto the support, upon which they are neutralised by thermal electrons

from a hot filament. The sample was then transferred into the optical cavity, where the CRDS measurements were carried out under ultra-high vacuum conditions using a tuneable laser source. A midband OPO laser (Innolas) was used for spectroscopic studies (repetition rate: 20 Hz, energy per pulse: 10–35 mJ, pulse duration: 7 ns and line width: 0.1 nm).

Spatial filtering and mode matching were performed to reduce the noise level. Many reports have manifested the application of CRDS to different samples without mode matching optics [9–13, 25–27]. In order to achieve the highest possible sensitivity, however, mode matching is necessary. In an optical cavity, different transverse electromagnetic (TEM) modes hit the mirrors at different profiles and positions, and in addition possess a different profile and size inside the cavity. Each TEM mode travels therefore effectively through a different cavity. The ring-down signal is consequently a multi-exponential function [28–31] with random fluctuations due to variations in the mode structure of the laser. In the case of an inhomogeneous solid sample this problem is magnified. Having different spot sizes and profiles inside the cavity implies that different TEM modes go through the sample at different positions, covering different areas and so averaging over various regions. For best results, the TEM<sub>00</sub> mode of the laser should be coupled into the cavity such that the TEM<sub>00</sub> mode is the only excited mode of the cavity [28, 29]. To this end, the output of the laser was focused through a pinhole in order to pick out the TEM<sub>00</sub> mode. The resulting single mode laser beam was then guided through two spherical lenses before it entered the ring-down cavity. The position and focal length of the lenses were calculated based on ray transfer matrix analysis (RTMA) [32] to match the TEM<sub>00</sub> mode of the cavity. Figure 1A demonstrates the schematic view of the mode matching optics used in this work. The relative errors for loss measurements with and without mode matching are shown in Fig. 1B. The histograms are based on single shot measurements recorded at 570 nm for BK7<sup>®</sup> substrates. An improvement of about 50% was observed. Averaging 100

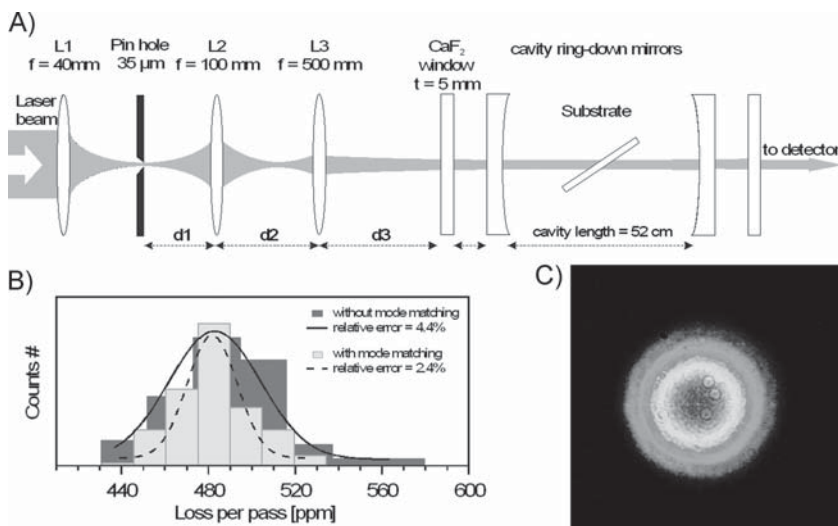


**Figure 1** (A) The schematic view of the mode matching optics used in this work. The distances  $d_1$ ,  $d_2$  and  $d_3$  are calculated based on the RTMA method. (B) The histograms of 100 ring-down signals at 570 nm for BK7<sup>®</sup> substrates with and without mode matching. The relative error of the measured losses is two times better for the mode matched case. (C) A snap shot of the laser beam profile after spatial filtering. A round Gaussian intensity distribution corresponding to TEM<sub>00</sub> mode is observed.

shots will further reduce the error by a factor of  $\sim 10$  as shown in a previous contribution [13].

Surface map images were taken before and after deposition of clusters by scanning an  $11 \times 11$  mesh ( $10 \times 10 \text{ mm}^2$ ) of the substrate's surface while recording 100 CRD signals at each point at a fixed wavelength. These surface images contain information about the sample's surface with the sensitivity of CRDS. The effect of any treatment of the samples could be monitored using the surface maps, e.g. the damage caused by low energy ion bombardment could be determined quantitatively.

A method to remove the clusters from the substrate without damaging its surface will make it possible to use the same substrate for different measurements. This will not only reduce the time demanding venting/pumping/bake-out steps, but also economically justify the use of support materials with higher quality. Heating and ion bombardment are commonly used in surface science for cleaning purposes. However, heating can only be applied as long as no structural change in substrate, e.g. crystallisation, phase transformation or dopant segregation takes place. A commercial sputter gun (EX03 Ion Gun System-Thermo VG Scientific) was used to remove the clusters from oxide surfaces by  $\text{Ar}^+$  ions. The effect of sputtering on the optical losses of the substrate and the efficiency of cluster desorption are discussed.

**3 Results and discussion** The optical spectrum of an YSZ substrate ( $500 \mu\text{m}$  thick, Crystal GmbH) measured by CRDS is shown in Fig. 2. According to literature YSZ is a transparent material [33] in the visible and infrared range of the spectrum, however, the spectrum shows distinct sharp peaks. These absorption peaks are not intrinsic to pure YSZ and indicate the presence of one or more rare earth metal impurities [33, 34]. The absorption peaks observed in Fig. 2 are mainly attributed to the presence of trace amounts of Nd. Many studies show similar absorption peaks for  $\text{Nd}^{3+}$  ions in different media [35–37]. The intense peak at  $588.3 \text{ nm}$  corresponds to the transition from  $^4\text{I}_{9/2}$  to  $^4\text{G}_{5/2}$  and has been used to determine the concentration of Nd in YAG crystals [38]. The substrate presented here apparently cannot be used

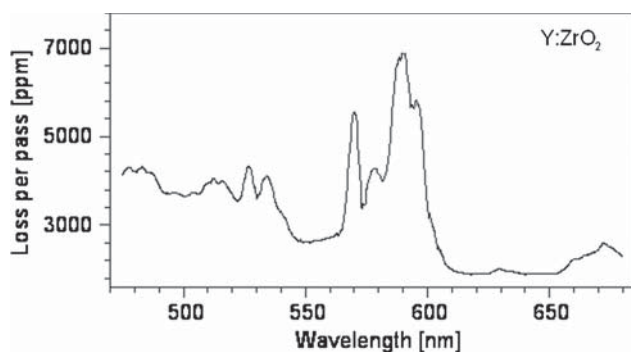


**Figure 2** The optical loss spectrum of a  $500 \mu\text{m}$  thick YSZ sample with Nd content recorded by CRDS. Note the high absorption losses (up to 7000 ppm). The sharp absorption bands are common among rare earth metals due to their f–f transitions.

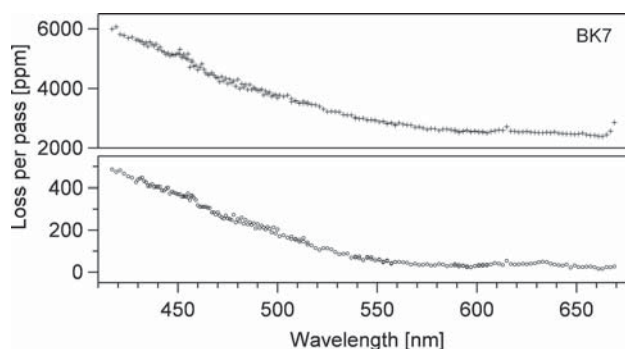
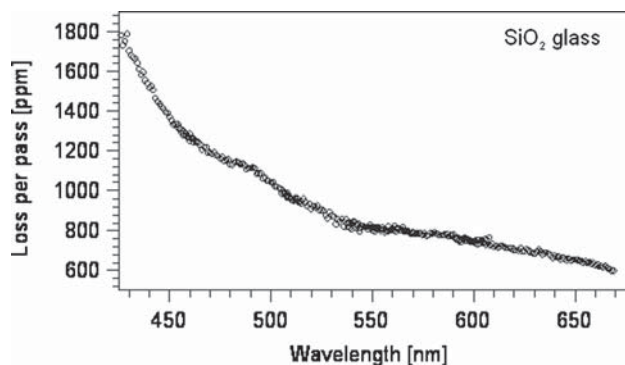


**Figure 3** The optical losses of BK7 substrates recorded by CRDS. Low optical losses between 50 and 450 ppm are measured for an untreated sample (marked with circles). After being heated at  $140 \text{ }^\circ\text{C}$  for over 5 days, optical quality of the substrate has degraded drastically (marked with +).

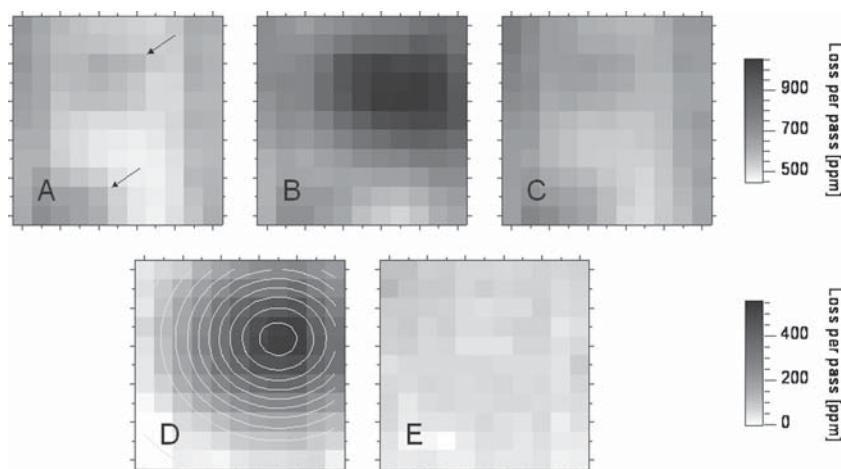
as a support material for size-selected clusters in CRDS measurements, where an optical loss of 10–500 ppm is expected [13].

Figure 3 shows the spectra of  $130 \mu\text{m}$  thick BK7<sup>®</sup> substrates. The presence of borates and other oxides ( $\text{Na}_2\text{O}$ ,  $\text{K}_2\text{O}$ , etc.) in BK7<sup>®</sup> may play an important role in CRDS measurements. On the one hand, they may increase the binding probability of metal clusters to the surface compared to pure silicates [10, 39–41]. On the other hand, they limit the treatment possibilities like heating, due to the low melting point of borosilicate glasses ( $\sim 650 \text{ }^\circ\text{C}$ ). Under elevated temperatures, substituent atoms become mobile and substrate deformation occurs. XRD measurements reveal slight structural deformation in samples after being heated at  $140 \text{ }^\circ\text{C}$  over 5 days during a bake-out process. This affects the optical losses of the substrates as shown in Fig. 3, e.g. by introducing higher scattering losses. This indicates that the substrate is not thermally stable and cannot be used for high temperature measurements. However, at slightly increased temperature of about  $70 \text{ }^\circ\text{C}$  no changes in the optical properties have been observed.

The optical loss spectrum of a  $150 \mu\text{m}$  thick glassy silica sample is illustrated in Fig. 4. Amorphous silica is



**Figure 4** The optical loss spectrum of amorphous silica recorded by CRDS.



**Figure 5** Surface images of a BK7<sup>®</sup> substrate at 520 nm ( $10 \times 10 \text{ mm}^2$ ). (A) Before any treatment. Optical losses of the substrate vary with position. (B) After deposition of unselected gold clusters. Local increase of the optical loss is observed. (C) After sputtering the surface with low energy argon ions. The image is quiet similar to that of an untreated substrate. (D) Image A is subtracted from image B. Counters indicate a round two-dimensional Gaussian distribution of clusters. (E) Image A is subtracted from image C. The surface profile of the substrate is practically unchanged. An average increase in measured loss of less than 50 ppm is observed.

transparent from 200 to 2100 nm (Table 1). Compared to borosilicate glass the optical losses are about 500 ppm higher in the case of  $\alpha\text{-SiO}_2$ . Similar to BK7<sup>®</sup> samples, glassy silica supplies a featureless optical background, suitable for CRDS measurements on supported size-selected clusters. The monotonous loss increase toward shorter wavelengths in the case of Silica glass and BK7<sup>®</sup> has its origin in the fact that for these materials the optical losses in the measured range are dominated by the scattering losses which increase for shorter wavelengths.

Surface maps of a BK7<sup>®</sup> substrate before and after deposition of unselected gold clusters, and after sputtering for 10 min with low energy  $\text{Ar}^+$  ions (300 eV) are illustrated in Fig. 5. The first image (Fig. 5A) demonstrates the optical loss profile of the sample prior to cluster deposition. The inhomogeneous character of the substrate is clearly seen. The optical losses of the substrate vary between 450 and 700 ppm. After deposition of gold clusters ( $\sim 2\%$  of a monolayer), a loss enhancement on the coated area is observed (Fig. 5B). Figure 5C shows the influence of the subsequent sputtering on the substrate. At first glance, it is clear that the cluster spot has disappeared. Subtracting the map before deposition from the one after deposition shows the spatial distribution of the clusters at the surface and the increased loss due to the clusters, only (Fig. 5D). The round shape of this spot is caused by the focusing octopole which has a round opening [13, 42]. It should be mentioned here that the surface maps have been recorded by moving the substrate in two directions both perpendicular to the optical axis. The step sizes have been chosen to be 1 mm in the direction parallel to the rotation axis of the manipulator and  $\cos(\theta_B)$  mm ( $\theta_B = \text{Brewster's angle}$ ) for the other direction. This way the steps are equal with respect to the substrate surface, for both dimensions and a symmetric shape is expected. The presence of gold is confirmed by additional analytical investigations (atomic absorption spectroscopy (AAS) and total reflection X-ray fluorescence (TXRF)) of the sample after sputtering, revealing the presence of less than

1% of the total amount of deposited gold. Note that, the optical loss profile of the surface shows a similar pattern as before deposition. Direct comparison between the images recorded before deposition and after sputtering (Fig. 5E) indicates a slight increase in optical losses. The cluster spot, however, has totally vanished. Apparently sputtering has not changed the measured optical loss profile. Nevertheless, a slight overall increase of the optical loss of the sample ( $\sim 50$  ppm) is observed. The high optical quality of the substrate has not been affected, suggesting that surface roughening has occurred homogeneously. Regions marked by arrows in Fig. 5A have not been influenced by sputtering at all. One possible explanation would be the presence of scattering centres inside the material including gas bubbles, segregates, unreleased stress, etc. It should be mentioned here that the size of the features in surface maps measured by CRDS is affected by the size of the laser spot. The observed shape and size is a convolution of the laser spot and the feature. Increasing the energy of  $\text{Ar}^+$  ions did not show a better cleaning efficiency but increased the optical losses of the substrate. Therefore, the optical losses of the substrate caused by sputtering can be attributed to surface roughening.

**4 Conclusions** Different oxide materials were characterised using a cavity ring-down spectrometer. The sensitivity of the spectrometer was improved by using mode matching optics and spatial filtering. YSZ is theoretically an appropriate material to be used as a support for metal clusters in CRDS studies; however, high purity is required. Trace amounts of Nd in YSZ were clearly detected by CRDS. Considering the optical losses, the BK7<sup>®</sup> samples are the most appropriate substrates for CRDS measurements. The low optical loss and availability of this material are its major advantages over other substrates. The main disadvantage of borosilicate glass is its low melting point. Heating up to  $140^\circ\text{C}$  over 5 days caused deformation in glass structure which increased the optical losses drastically. Silica glass



shows higher optical losses compared to the borosilicate samples. This material is a proper alternative substrate for optical measurements on size-selected clusters. A low optical damage cleaning method was introduced to remove the metal clusters from the support material using low energy Ar<sup>+</sup> ions sputtering.

**Acknowledgements** This research is supported by the Deutsche Forschungsgemeinschaft within the Priority Program no. SPP1153. The authors want to thank M. Maier for AAS and TXRF measurements, and F. Esch and V. Habibpour for constructive discussions.

## References

- [1] U. Heiz and U. Landman, *Nanocatalysis, Nanoscience and Technology* (Springer Verlag, Berlin, 2007).
- [2] W. Harbich, S. Fedrigo, and J. Buttet, *Chem. Phys. Lett.* **195**, 613 (1992).
- [3] W. Harbich, S. Fedrigo, and J. Buttet, *Z. Phys. D* **26**, 138 (1993).
- [4] W. Harbich, S. Fedrigo, J. Buttet, and D. M. Lindsay, *Z. Phys. D* **19**, 157 (1991).
- [5] U. Kreibitz, G. Bour, A. Hilger, and M. Gartz, *Phys. Status Solidi A* **175**, 351 (1999).
- [6] J. H. Weaver, C. Krafka, D. W. Lynch, and E.-E. Koch, *Optical Properties of Metals Part I, Physics Data Series No. 18-1* (Fachinformationszentrum Energie Physik Mathematik, Karlsruhe, 1981).
- [7] J. J. Scherer, J. B. Paul, A. Okeefe, and R. J. Saykally, *Chem. Rev.* **97**, 25 (1997).
- [8] M. D. Wheeler, S. M. Newman, A. J. Orr-Ewing, and M. N. R. Ashfold, *J. Chem. Soc. Faraday Trans.* **94**, 337 (1998).
- [9] G. Berden, R. Peeters, and G. Meijer, *Int. Rev. Phys. Chem.* **19**, 565 (2000).
- [10] J. M. Antonietti, M. Michalski, U. Heiz, H. Jones, K. H. Lim, N. Rösch, A. Del Vitto, and G. Pacchioni, *Phys. Rev. Lett.* **94**, 213402 (2005).
- [11] R. Engeln, G. von Helden, A. J. A. van Roij, and G. Meijer, *J. Chem. Phys.* **110**, 2732 (1999).
- [12] S. Gilb, K. Hartl, A. Kartouzian, J. Peter, U. Heiz, H. G. Boyen, and P. Ziemann, *Eur. Phys. J. D* **45**, 501 (2007).
- [13] A. Kartouzian, M. Thämer, T. Soini, J. Peter, P. Pitschi, S. Gilb, and U. Heiz, *J. Appl. Phys.* **104**, 124313 (2008).
- [14] A. C. R. Pipino, J. P. M. Hoefnagels, and N. Watanabe, *J. Chem. Phys.* **120**, 2879 (2004).
- [15] I. M. P. Aarts, B. Hoex, A. H. M. Smets, R. Engeln, W. M. M. Kessels, and M. C. M. van de Sanden, *Appl. Phys. Lett.* **84**, 3079 (2004).
- [16] K. Egashira, A. Terasaki, and T. Kondow, *J. Chem. Phys.* **126**, 221102 (2007).
- [17] M. A. Everest, V. M. Black, A. S. Haehlen, G. A. Haveman, C. J. Kliewer, and H. A. Neill, *J. Phys. Chem. B* **110**, 19461 (2006).
- [18] J. M. Herbelin and J. A. McKay, *Appl. Opt.* **20**, 3341 (1981).
- [19] F. Li and R. N. Zare, *J. Phys. Chem. B* **109**, 3330 (2005).
- [20] S. L. Logunov, *Appl. Opt.* **40**, 1570 (2001).
- [21] G. A. Marcus and H. A. Schwettman, *Appl. Opt.* **41**, 5167 (2002).
- [22] R. N. Muir and A. J. Alexander, *Phys. Chem. Chem. Phys.* **5**, 1279 (2003).
- [23] A. Terasaki, T. Kondow, and K. Egashira, *J. Opt. Soc. Am. B* **22**, 675 (2005).
- [24] S. E. Fiedler, A. Hese, and A. A. Ruth, *Rev. Sci. Instrum.* **76**, 023107 (2005).
- [25] B. D. Bean, A. K. Mollner, S. A. Nizkorodov, G. Nair, M. Okumura, S. P. Sander, K. A. Peterson, and J. S. Francisco, *J. Phys. Chem. A* **107**, 6974 (2003).
- [26] M. G. H. Boogaarts, P. J. Bocker, W. M. M. Kessels, D. C. Schram, and M. C. M. van de Sanden, *Chem. Phys. Lett.* **326**, 400 (2000).
- [27] R. Engeln, G. vonHelden, G. Berden, and G. Meijer, *Chem. Phys. Lett.* **262**, 105 (1996).
- [28] D. H. Lee, Y. Yoon, B. Kim, J. Y. Lee, Y. S. Yoo, and J. W. Hahn, *Appl. Phys. B* **74**, 435 (2002).
- [29] K. K. Lehmann and D. Romanini, *J. Chem. Phys.* **105**, 10263 (1996).
- [30] R. D. van Zee, J. T. Hodges, and J. P. Looney, *Appl. Opt.* **38**, 3951 (1999).
- [31] P. Zalicki and R. N. Zare, *J. Chem. Phys.* **102**, 2708 (1995).
- [32] H. Kogelnik and T. Li, *Appl. Opt.* **5**, 1550 (1966).
- [33] S. Gutzov and W. Assmus, *J. Mater. Sci. Lett.* **19**, 275 (2000).
- [34] R. I. Merino, V. M. Orera, R. Cases, and M. A. Chamorro, *J. Phys.: Condens. Matter* **3**, 8491 (1991).
- [35] G. A. Kumar, J. R. Lu, A. A. Kaminskii, K. I. Ueda, H. Yagi, T. Yanagitani, and N. V. Unnikrishnan, *IEEE J. Quantum Electron.* **40**, 747 (2004).
- [36] K. Kuriki, S. Nishihara, Y. Nishizawa, A. Tagaya, Y. Koike, and Y. Okamoto, *J. Opt. Soc. Am. B* **19**, 1844 (2002).
- [37] K. Terashima, S. Tamura, S. H. Kim, and T. Yoko, *J. Am. Ceram. Soc.* **80**, 2903 (1997).
- [38] M. L. Meil'man, A. I. Kolomitset, I. S. Volodina, A. G. Smagin, K. S. Bagdasarov, and A. M. Kevorkov, *Zh. Prikl. Spektrosk.* **38**, 755 (1983).
- [39] L. Giordano, A. Del Vitto, and G. Pacchioni, *J. Chem. Phys.* **124**, 034701 (2006).
- [40] H. Iddir, S. Ogut, N. D. Browning, and M. M. Disko, *Phys. Rev. B* **72**, 081407 (2005).
- [41] U. Martinez, J. F. Jerratsch, N. Nilius, L. Giordano, G. Pacchioni, and H. J. Freund, *Phys. Rev. Lett.* **103**, 056801 (2009).
- [42] M. A. Röttgen, K. Judai, J. M. Antonietti, U. Heiz, S. Rauschenbach, and K. Kern, *Rev. Sci. Instrum.* **77**, (2006).

### 3.3. Paper 3

#### **Cavity ring-down spectroscopy of metallic gold nanoparticles**

The following paper addresses the application of cavity ring-down spectroscopy to study the optical properties of supported gold nano-particles of various sizes.

In the experimental section, the preparation of the nano-particles is first described briefly. Here the nano-particles are produced wet chemically by loading block co-polymer reverse micelles (block-poly (2-vinylpyridine)-polystyrene) with a metal salt ( $\text{AuHCl}_4$ ). At equilibrium the micelles are homogeneously loaded and so the amount of the metal salt inside each micelle is the same. The spectroscopic samples are produced by dip-coating the support material with the loaded micelles, before plasma etching to remove the organic polymers and reduce the salt to metallic gold. It is exhibited that the particles are in an oxidised state after plasma etching through x-ray photoelectron spectroscopy experiments. The unstable gold oxide is then reduced to metallic gold either by annealing or alternatively storing at ambient conditions for several days. The size distribution of the samples is characterised by atomic force microscopy experiments.

The cavity ring-down setup used to perform the spectroscopic measurements is introduced. In contrast to the measurements in paper 1 and 2, here the experiments were performed under ambient conditions. The principles of the CRDS are reviewed and some details on data acquisition and treatment are given. The challenges regarding the application of CRDS to the condensed phase are explained and various aspects of the quality of the substrate materials are pointed out.

Surface Plasmon resonance is observed for the nano-particles investigated in this work. However the peak is not as distinct as it is for matrix isolated silver or larger gold nano-particles. The experimental findings are compared to Mie-Drude calculations considering both the peak positions and broadenings. Good agreement between the experimental results and theoretical calculations are found. The details of the findings are discussed based on the contribution of a skin region with decreased polarisability, in order to explain the deviation from the red-shift in the peak position for decreasing particle size which is predicted by the Mie calculations and has been observed for free alkali clusters.

# Cavity ring-down spectroscopy of metallic gold nanoparticles

S. Gilb<sup>1,a</sup>, K. Hartl<sup>1</sup>, A. Kartouzian<sup>1</sup>, J. Peter<sup>1</sup>, U. Heiz<sup>1</sup>, H.-G. Boyen<sup>2</sup>, and P. Ziemann<sup>2</sup>

<sup>1</sup> Lehrstuhl für Physikalische Chemie I, Technische Universität München, 85747 Garching, Germany

<sup>2</sup> Abteilung Festkörperphysik, Universität Ulm, 89069 Ulm, Germany

Received 27 April 2007

Published online 27 June 2007 – © EDP Sciences, Società Italiana di Fisica, Springer-Verlag 2007

**Abstract.** The optical properties of supported gold nanoparticles with sizes of 1.3 nm, 1.6 nm, 2.5 nm, and 2.9 nm have been studied by using cavity ring-down spectroscopy in the photon energy range between 1.8 eV and 3.0 eV. The obtained results show the possibility to obtain optical information of nanoassembled materials with high sensitivity. The experimental findings are compared to calculations using Mie-Drude theory. Whereas the broadening of the surface plasmon resonance with decreasing size is well described by this model, the observed blue-shift of the surface plasmon resonance contradicts the predictions of the Mie-Drude theory. The latter effect can be explained by the presence of a skin region with decreased polarizability typical for coinage metal particles. Furthermore, it is found that the supported gold nanoparticles are robust under ambient conditions, an important issue when using these materials for optical applications.

**PACS.** 61.46.Df Nanoparticles

## 1 Introduction

Progress in nanoscience made new materials, consisting of monodispersed nanoclusters or nanoparticles with narrow size distributions, available [1–3]. Such materials can for instance be synthesized by cluster deposition from pre-formed molecular beams [1], the deposition of molecular precursors [3] or by self-assembly on surfaces [2]. The interest in such nanostructured materials, comes in part from their fascinating optical properties, which can be tuned in a sophisticated way by varying size or the chemical composition of the nanoparticles [4–6]. The unique optical properties of metal nanoparticles have their origin in the surface plasmon, which strongly depends on size, shape and surrounding of the particle [7–11]. Experimental studies of optical properties of nanoparticles on surfaces is not trivial, as the surface density of the particles has to be low, in order to keep the particles well separated. These, together with the relatively low absorption cross sections of small metal particles, prevent the use of regular spectroscopic methods to obtain optical information of such nanoassembled materials.

Cavity ring-down spectroscopy (CRDS) has been proven to be very sensitive and it has been applied successfully in the gas phase for studying transitions of molecules with low absorption cross sections at low densities [12–14]. A few studies demonstrated the feasibility to use cavity ring-down spectroscopy (CRDS) for the optical characterization of thin films or particles supported on transparent samples with high sensitivity [15–18]. CRDS is based

on an optical cavity built of two highly reflective mirrors ( $R > 99.99$ ), in which a short light pulse of a given wavelength is introduced. By measuring the lifetime of the light pulse inside the cavity (called ring-down time), one is able to determine the intrinsic loss of the cavity due to transmission through the mirrors, scattering losses and in the present case losses from the support material inside the cavity. This intrinsic loss of the support material can be compared to the one obtained after nanoparticle preparation on the support material, resulting in the loss due to the nanoparticles. The losses of the nanoparticles as function of wavelength correspond to the absorption spectrum of the respective nanoparticles. In this work we apply CRDS for studying two dimensional arrays of gold nanoparticles with sizes ranging from  $\sim 1$  nm up to  $\sim 3$  nm on amorphous  $\text{SiO}_2$  and discuss the experimental findings with the aid of classical Mie-Drude theory.

## 2 Experimental

### 2.1 Preparation of the particles

The preparation of the nanoparticles is described in detail elsewhere and will be only briefly discussed here [2,19]. It is based on a two step process. First, spherical reverse micelles are formed by dissolving polystyrene (PS)-*block*-poly(2-vinylpyridine) in an apolar solvent such as toluene. A metal salt, in this case  $\text{HAuCl}_4$  is added to the solution and the salt slowly migrates into the core of the micelles while carefully stirring the micelle solution. At equilibrium, all micelles are loaded with an equal

<sup>a</sup> e-mail: [Stefan.Gilb@mytum.de](mailto:Stefan.Gilb@mytum.de)

amount of metal salt, resulting in a small size dispersion of the final metal particles. The loaded micelles are transferred onto the substrate by dip coating. At this stage, the loaded micelles are distributed on the substrate in a hexagonal arrangement. Removing the ligand polymer and reducing the metal precursor salt to pure metal are done by exposing the “monomicellar” layer to an oxygen plasma. X-ray photoelectron spectroscopy experiments revealed that after the oxygen plasma treatment gold oxides are formed. After an annealing step, or alternatively after storing at ambient conditions for several days, the  $\text{Au}_2\text{O}_3$  is completely reduced to Au [20]. It has been observed previously that the original order of the micellar arrangement is conserved, and a two dimensional array of hexagonally arranged nanoparticles is obtained [20]. Typical size distributions were measured by AFM to be e.g.  $2.9 \text{ nm} \pm 0.5 \text{ nm}$ , or  $1.3 \pm 0.3 \text{ nm}$  [2]. It has also been shown that on sapphire and silicon supports the particles have a nearly spherical shape, and it is assumed that this is also true on the silica substrates used in this work [19].

For the CRDS experiments a transparent substrate is required to perform the measurements; for this reason microscopy coverslip plates with a thickness of 0.13–0.16 mm were used as substrate materials. The dip coating was done for half of the glass substrate, resulting in substrates, which are half covered on both sides with micelles. The investigated samples were the result of two different batches. The first batch includes the nanoparticles with an average diameter of 2.9 nm, 1.6 nm, and 1.3 nm, respectively and was stored for more than 9 months before the experiments were carried out. A second batch was used to produce samples with an average diameter of 2.9 nm and was measured about one month after preparation. The samples were stored under ambient conditions between preparation and measurement. The measurements also were done under ambient condition.

## 2.2 CRD setup

The optical setup is illustrated in Figure 1. A stable ring-down cavity is formed by 2 confocal mirrors (Los Gatos Research Inc.) with a focal length of 6 m and a cavity length of 1.38 m. The pulsed radiation is produced by a Nd:YAG-laser-pumped midband optical parametric oscillator (OPO) (Innolas SpitLight-1200, GWU VisIR2/400 ULD) with a bandwidth below  $7 \text{ cm}^{-1}$  and a pulse length of  $\approx 7 \text{ ns}$ . The output energy varies between  $\approx 10 \text{ mJ}$  and  $20 \text{ mJ}$  per pulse depending on the wavelength. No special mode matching optics are used to adapt the laser profile to the cavity modes, but pinholes along the laser path are used to simplify the day to day alignment and select a homogeneous part of the otherwise rather large, nearly rectangular laser beam of the OPO-laser. The light is linearly polarized by a Glan-laser-polarizer directly in front of the cavity. The laser pulse injected into the cavity remains in the cavity for several microseconds. Its intensity is reduced after every round trip by the losses at the mirrors (scattering, transmission), and absorption and scattering losses of the sample. The light leaking out of the second cavity

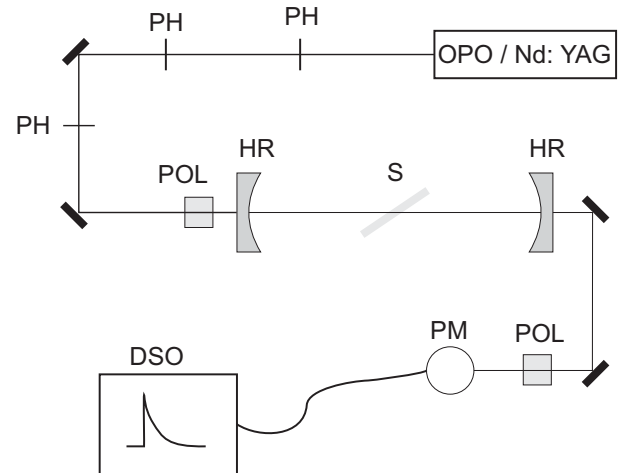


**Fig. 1.** Schematic illustration of the optical setup used in the experiment. PH: pinholes, HR: high reflective mirrors, POL: polarizers, PM: photomultiplier, DSO: digital oscilloscope, S: sample at Brewster’s angle.

mirror is detected and amplified with a photomultiplier (Hamamatsu 7732-10). A rotatable polarizer in front of the photomultiplier serves as variable intensity attenuator and prevents saturation of the photomultiplier tube. The signal from the photomultiplier is fed into an 8 bit digital storage oscilloscope (LeCroy Waverunner 6051), which measures single traces and saves them to the internal hard drive.

The wavelength scans are fully automated. The wavelength dependent output power of the OPO as well as the strongly wavelength dependent reflectivity of the cavity mirrors, require a change of the photomultiplier sensitivity to use the full dynamic range of the photomultiplier and the oscilloscope. This is done automatically by a home written LabView program for every measured wavelength by means of a lookup table. The LabView program runs on the internal computer of the oscilloscope, and also controls the wavelength settings of the OPO-laser. The used cavity mirrors cover only 30 to 70 nm around a center wavelength. To cover the entire wavelength range from 420 nm to 700 nm, we use 6 cavities centered at wavelengths of 430 nm, 480 nm, 520 nm, 570 nm, 610 nm and 640 nm, respectively. The cavity mirrors are chosen to have a minimum of 6 nm spectral overlap between the different cavities. However, typically an overlap between the cavities of more than 15 nm is achieved.

To determine the ring-down time at each measured point, 80 single ring-down traces were acquired. To each trace a single exponential decay according to the function

$$I(t) = I_0 + I_1 \exp\left(-\frac{t}{\tau}\right) \quad (1)$$

is fitted using the nonlinear Levenberg-Marquardt method.  $I_0$  and  $I_1$  are the offset and a scaling factor, respectively;  $\tau$  is the ring-down time. Due to instabilities of the laser system, about 1–4% of the laser shots have intensities close to zero, resulting in meaningless negative or



unrealistically large ring-down times in the order of ms. To prevent a corruption of the mean ring-down time by these single events, only ring-down times in a range of  $\pm 100\%$  of the median ring-down time were averaged to obtain a final value for a given wavelength point. The outlier percentage was in no case above 4% (e.g. 3 out of 80 measurements). From the averaged ring-down time  $\tau$ , the cavity length  $L$ , and the speed of light  $c$ , the loss can be calculated by:

$$A = 1 - \exp\left(-\frac{L}{c\tau}\right). \quad (2)$$

While the shot to shot standard deviation is in the order of 5%, the overall noise can be estimated directly from the scatter between adjacent data points in the obtained spectra and is typically  $\approx \pm 140$  ppm (see e.g. Fig. 3).

The main challenge in using solid samples in CRDS is the intrinsic loss due to scattering from the sample surfaces. One way to minimize these losses is to mount the glass slide perfectly perpendicular to the cavity axis, keeping reflection losses from the surfaces inside the cavity. The disadvantage of this method is the elaborate alignment that is required, since the slightest misalignment increases the loss by orders of magnitudes. The second method is the alignment of the sample at Brewster's angle, in which no reflections from the optical surfaces are to be expected. Due to the insensitivity of the reflectivity as a function of the angle around Brewster's angle ( $\approx 56^\circ$ ), the alignment is rather insensitive. Also, by putting the sample at Brewster's angle, the polarization of the light inside the cavity is fixed to p-polarization with respect to the sample. With the coverslip plates used in the preparation of the nanoparticles, the first method, with a perpendicular alignment of the sample was not only difficult to achieve, but also inferior in terms of losses compared to Brewster's angle configuration, which is rather easy to obtain. We attribute this to the imperfect planarity of the coverslip plates. In all measurements present here, the Brewster's angle configuration was used. The Brewster's angle of the sample was aligned prior to measurement for every one of the six cavities at the center wavelength of the corresponding cavity. We note that even in the case of the substrate to be well-aligned at Brewster's angle, losses of 1000–2000 ppm were observed, which is an order of magnitude higher than what is to be expected from absorption of a thin glass plate. This is partly due to the fact, that cleaning of the samples after preparation of the nanoparticles is not possible. But also in the case of freshly cleaned coverslip plates, we find high losses, which we attribute to the birefringence of the plates effectively creating small contributions of s-polarization at every pass through the sample. This polarization component is, due to reflection at the sample surface, not stable in the cavity.

### 3 Theory

The Mie-Drude theory is used to describe the spectra of nanoparticles in the size range considered here. The theory describes scattering and absorption of a plane wave

by a single sphere [21]. The derivation of the theory and application to nanoparticles can be found, for example, in reference [22]. We followed the method of implementation described in references [23,24] and only a brief description will be given here. The particle and the surrounding media are considered as homogeneous and are described by the bulk optical dielectric functions. Since the size of the particles is much smaller than the wavelength of the exciting radiation, the discussion can be restricted to the dipole term in the multipole expansion of the solution of the Maxwell equations. The cross section in the dipole approximation is then given by:

$$\sigma = 9\varepsilon_m^{3/2} V_0 \frac{\omega}{c} \frac{\varepsilon_2(\omega)}{[\varepsilon_1(\omega) + 2\varepsilon_m]^2 + \varepsilon_2^2(\omega)} \quad (3)$$

with  $\omega$  and  $c$  being the frequency and the speed of light, respectively,  $\varepsilon_m$  the dielectric constant of the media surrounding the nanoparticle, and  $V_0$  being the volume of the particle.  $\varepsilon_1(\omega)$  and  $\varepsilon_2(\omega)$  are the real and imaginary part of the dielectric constant of the absorbing solid. In the Mie-Drude model, the size effect is introduced by a size dependent scattering rate which alters the free electron contribution to the dielectric function. The scattering rate of the bulk,  $\Gamma_\infty$  is increased through a size dependent scattering rate. The latter can be interpreted as the average rate, with which the excited plasmon hits the outside of the particle. The total scattering rate  $\omega_s$  is thus equal to:

$$\omega_s = \Gamma_\infty + A \frac{v_F}{R}. \quad (4)$$

In this equation  $R$  is the radius of the particle and  $v_F$  is the Fermi velocity ( $v_F = 1.4 \times 10^8$  cm/s for gold) [25]. The proportional factor,  $A$ , is a model dependent parameter and his value depends on the type of scattering assumed. This parameter, essential a size scaling parameter, takes the value of unity for isotropic scattering or 3/4 if diffusive scattering is assumed. The value of 1, which corresponds to an isotropic scattering, is used throughout the calculations in this work. To incorporate the scattering into the dielectric function, the latter is separated into the free-electron (Drude) contribution ( $\varepsilon_{1D/2D}(\omega)$ ) from the s-electrons and the interband contribution ( $\varepsilon_{1B/2B}(\omega)$ ) originating from the d-electrons

$$\varepsilon_1(\omega) = \varepsilon_{1B}(\omega) + \varepsilon_{1D}(\omega), \quad \varepsilon_2(\omega) = \varepsilon_{2B}(\omega) + \varepsilon_{2D}(\omega). \quad (5)$$

The free electron part for the bulk can be calculated by:

$$\varepsilon_{1D}(\omega) = 1 - \frac{\omega_P^2}{\omega^2 + \Gamma_o^2}, \quad \varepsilon_{2D}(\omega) = \frac{\omega_P^2 \Gamma_o}{\omega(\omega^2 + \Gamma_o^2)}. \quad (6)$$

Here  $\omega_P$  is the plasma frequency corresponding to 8.89 eV for gold,  $\Gamma_\infty$  is the plasmon scattering rate in the bulk gold and corresponds to  $1.11 \times 10^{14}$  s<sup>-1</sup> for gold. The dielectric function from bulk can be found in [26]. From there  $\varepsilon_{1D/2D}(\omega)$  can be determined. In Figure 2 the size evolution of the spectrum predicted by this model is shown. For the case of a 2 nm particles it is shown how a size dispersion of  $\pm 0.5$  nm affects the spectral response of the nanoparticle in the framework of the Mie-Drude theory.

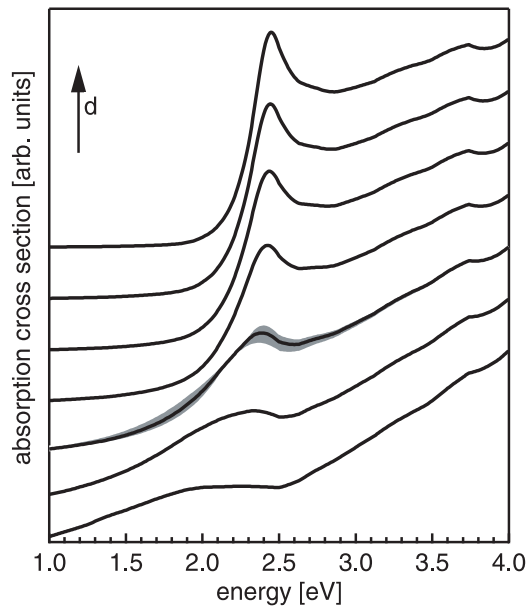


**Fig. 2.** Absorption cross sections calculated by the Mie-Drude theory as explained in the text. The spectra were normalized to an equal absorption at 4 eV and vertically shifted. The diameters used in the simulation are: 0.5, 1, 2, 5, 10, 20 nm and bulk.

## 4 Results and discussion

To acquire the whole spectrum from 1.78 eV to 2.95 photon energy we used 6 different cavity mirror sets, centered at different wavelengths. We denoted the range of the used cavities in Figure 3. Each individual run obtained by using a single cavity was scaled by a factor,  $S$ , to achieve reasonable overlap of the measured losses between adjacent cavities. The values of  $S$  were between 0.85 and 1.15. This uncertainty is caused by day to day variation of the measured losses and it is attributed to changes of the area on the sample probed by the laser beam. In fact, we found that the measured loss shows a dependence on the substrate position. Since this is true also for the *reference*, e.g. the uncoated part of the substrate (see below), we attribute this effect to the oxygen plasma treatment. It may lead to a random modification of the substrate surface. Thus, the alignment of the laser beam and laser mode fluctuations are very important.

To obtain the absorption spectra of the nanoparticles, the contribution to the absorption from the  $\text{SiO}_2$  support has to be subtracted. To obtain a reference spectrum the following procedure was carried out. The samples were prepared in such a way that only half of the area was dip coated with nanoparticles. Thus, the region with the nanoparticles was used for *sample* measurement, whereas the uncoated area served as *reference*. To minimize errors due to inhomogeneities of the substrate, a *sample* and a *reference* point was picked prior to the measurement and kept identical throughout the measurement. Figure 3 shows measurements of the sample and reference spectra taken at an area with gold nanoparticles with mean diameters of 2.5 nm and an area of the clean  $\text{SiO}_2$  support,

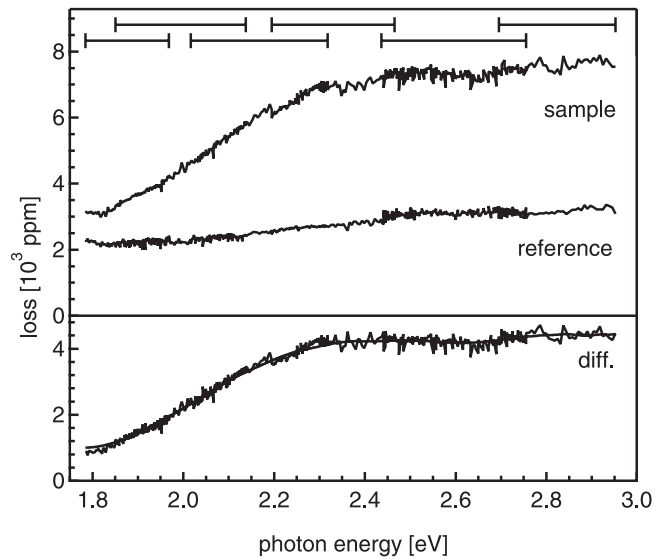


**Fig. 3.** Illustration of the reference method employed to disentangle the contribution from the support. Shown is the measured spectrum of the area with nanoparticles (*sample*) and the area without nanoparticles (*reference*). The difference of these two spectra is regarded as the absorption of the nanoparticles. Note, that the traces are not shifted and represent the real losses. The gold nanoparticles used in these studies have an average diameter of 2.5 nm. The solid line the difference spectrum represents moving averaged data to guide the eye. On the top of the graph the spectral ranges of the used cavities are illustrated by horizontal lines.

respectively. The difference spectrum is also shown in Figure 3 and it is attributed to the pure absorption spectrum of the respective nanoparticles. Despite the alignment of the substrate at Brewster's angle, the uncoated substrate shows a considerable extinction of light due to birefringence, absorption and scattering as mentioned above. More important, however, the reference spectrum is structureless and the loss increases linearly with the photon energy as shown in Figure 3. This characteristic behavior is typical for all  $\text{SiO}_2$  support materials used so far, whether they were treated by sputter-oxidation during sample preparation or whether they were new and untreated. Note, that for the lowest photon energy the loss in the difference spectrum shown in Figure 3 is not close to zero as one would expect for gold nanoparticles in the size range above 2 nm [22]. This indicates that in the present measurements there is an offset, which varies from sample to sample (cf. also Fig. 4). As described above and in contrast to the invariant spectral response of the substrate, the absolute losses measured at different positions of the substrate is inhomogeneous. This, however, results in an absolute shift of the loss in the difference spectra. It is important to note that the distinct spectral structure observed in the difference spectra can, however, unambiguously be attributed to the optical response of the nanoparticles alone and does not originate from spectral fluctuations in the reference measurements of the substrate. In Figures 3 and 4 no baseline correction was carried out in order to correct for this offset. The theoretical

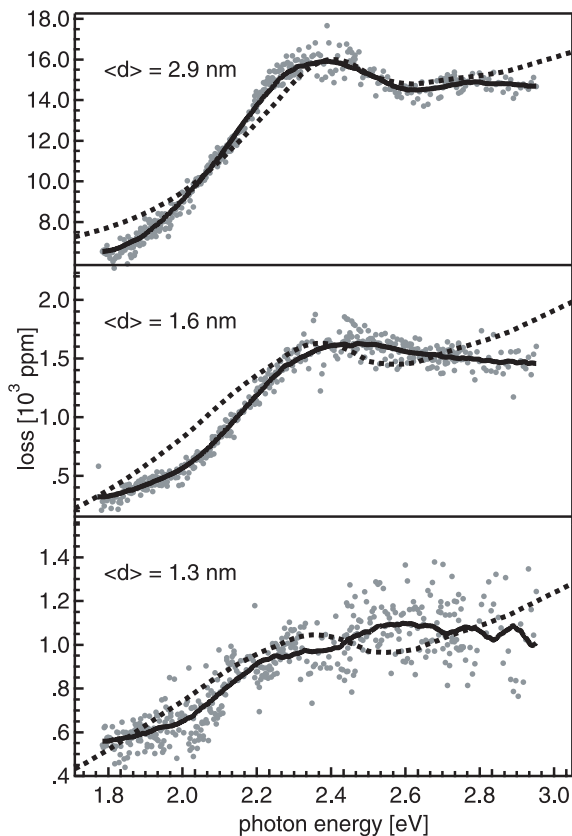


**Fig. 4.** Experimental data for supported nanoparticles of different mean diameters,  $\langle d \rangle$  ( $\langle d \rangle = 1.3 \text{ nm}, 1.6 \text{ nm}, 2.9 \text{ nm}$ ). The solid line is a moving average to guide the eye. The  $y$ -scaling is proportional to  $d$  [3] and chosen to reflect the volume dependence of the absorption cross section. We assume that the loss of the nanoparticles is close to zero at the lowest photon energy and set the offset of the  $y$ -axis for the theoretical spectra accordingly (see text). The theoretical spectra are obtained by using the Mie-Drude theory and are represented as dotted lines.

spectra shown in Figure 4, however, were shifted in order to account for the offset with respect to the measured loss found at 1.8 eV.

Figure 4 depicts the spectra of the nanoparticles obtained after subtraction of the reference spectrum. Whereas the average sizes of the nanoparticles were changed from 1.3 nm, 1.6 nm, and 2.9 nm, the average nearest neighbor distance was similar for all samples ( $\approx 35 \text{ nm}$ ), resulting in similar nanoparticle densities on the surface. The scaling factors of the three  $y$ -coordinates were chosen to be proportional to the volumes of the corresponding nanoparticles, in order to correct for the proportionality of the absorption cross section to the volume of the three nanoparticles as predicted by the Mie-Drude model (cf. Eq. (3)). Indeed, a first look at the spectra is in agreement with the prediction that the absolute absorption cross section scales with the particle's volume. Furthermore all spectra show an onset in the absorption above 1.8 eV. Maximal absorption cross sections are observed for energies around 2.4 eV, which corresponds to

the energy of the surface plasmon resonance (SPR) peak. For the nanoparticles studied here, the surface plasmon peak is not as distinct as it is for matrix isolated silver nanoparticles or larger gold nanoparticles [22, 27]. This behavior is well predicted by the Mie-Drude theory as displayed in Figures 3 and 4 [28]. The physical reason is the considerable lowering of the lifetime due to scattering at the particle boundaries, an effect which is enhanced for small particles. Smaller lifetimes result in a broadening of the SPR. As the onset of the interband transition in gold is below 2 eV these two contributions to the oscillator strength merge. Also this effect is well described by the Mie-Drude theory as shown by the simulated spectra in Figure 4 (dashed line). Similar effects have been observed for gold nanoparticles smaller than about 4 nm stabilized in various matrices like alumina or glass [6, 22, 24] and in solution [23].

While in the case of free alkali clusters a red shift of the SPR with decreasing cluster size has been measured [29], our data show a slight blue shift of the energy of maximal absorption when decreasing the mean particle diameter from 2.9 nm to 1.6 nm. This blue shift is in contradiction with the Mie-Drude theory, as it predicts a slight red-shift as shown in Figure 2. This observed blue shift, however, is in agreement with other experimental findings for coinage metal nanoparticles in the same size range [24]. For the coinage metals, the higher localization of the  $d$ -electrons compared to the  $s$ -electrons leads to an ineffective ion polarizability in the outer rim of the nanoparticles [24, 30]. This concept, introduced by Liebsch [31], predicts an alteration of the dielectric function. Lermé et. al integrated this alteration into semi-quantal theoretical calculation, and was able to explain the observed blue shift. The standard Mie-Drude model is indeed not able to describe this effect, since the bulk dielectric function is used throughout the nanoparticle. An extension of the Mie-Drude theory to take this surface effect into account is possible, but is beyond the scope of this experimental publication [32].

Further, we see no influence of the substrate, while in a former study on gold atoms and dimers a strong influence of surface defects has been observed [16, 33]. In that study we showed that the observed optical transitions involves electronic states, which are localized in the substrate-gold bond. This one electron transitions are orders of magnitude smaller than the collective electron excitations observed here.

## 5 Conclusion

In this work we measured for the first time the size evolution of two-dimensional hexagonally ordered arrays of gold nanoparticles in a size range of 1.3 nm up to 2.9 nm by using CRDS. This possibility clearly reveals the high sensitivity of CRDS in comparison with other optical methods. The measured spectra show typical characteristics of small gold particles, which proves the long term stability of these two dimensional nanostructures against complete oxidation even under ambient conditions. The experimental findings were discussed within the Mie-Drude theory

and we found a good description of the broadening of the SPR with decreasing size. The red-shift predicted by the Mie-Drude theory is not found in our experiments. This finding is in accordance with other experimental results on coinage metal nanoparticles, and can be explained by the presence of a skin region with decreased polarizability.

This research is supported by the Deutsche Forschungsgemeinschaft within the priority program SPP1153. We also acknowledge support from the European Project GSOMEN (contract No. 1549).

## References

1. S. Gilb, M. Arenz, U. Heiz, *Mat. Today* **9**, 49 (2006)
2. H.G. Boyen, G. Kastle, F. Weigl, B. Koslowski, C. Dietrich, P. Ziemann, J.P. Spatz, S. Riethmuller, C. Hartmann, M. Möller, G. Schmid, M.G. Garnier, P. Oelhafen, *Science* **297**, 1533 (2002)
3. T.M. Bernhardt, B. Kaiser, K. Rademann, *Phys. Chem. Chem. Phys.* **4**, 1192 (2002)
4. M. Bruchez, M. Moronne, P. Gin, S. Weiss, A.P. Alivisatos, *Science* **281**, 2013 (1998)
5. Y.G. Sun, Y.N. Xia, *Analyst* **128**, 686 (2003)
6. B. Palpant, B. Prevel, J. Lerme, E. Cottancin, M. Pellarin, M. Treilleux, A. Perez, J.L. Vialle, M. Broyer, *Phys. Rev. B* **57** 1963 (1998)
7. C.L. Haynes, R.P.V. Duyne, *J. Phys. Chem. B* **105**, 5599 (2001)
8. Y.Y. Yu, S.S. Chang, C.L. Lee, C.R.C. Wang, *J. Phys. Chem. B* **101**, 6661 (1997)
9. D. Sarkar, N.J. Halas, *Phys. Rev. E* **56**, 1102 (1997)
10. S. Underwood, P. Mulvaney, *Langmuir* **10**, 3427 (1994)
11. U. Kreibig, L. Genzel, *Surf. Sci.* **156**, 678 (1985)
12. G. Berden, R. Peeters, G. Meijer, *Inter. Rev. Phys. Chem.* **19**, 565 (2000)
13. M.D. Wheeler, S.M. Newman, A.J. Orr-Ewing, M.N.R. Ashfold, *J. Chem. Soc. Faraday Trans.* **94**, 337 (1998)
14. J.J. Scherer, J.B. Paul, A. Okeefe, R.J. Saykally, *Chem. Rev.* **97**, 25 (1997)
15. A.C.R. Pipino, J.T. Woodward, C.W. Meuse, V. Silin, *J. Chem. Phys.* **120**, 1585 (2004)
16. J.M. Antonietti, M. Michalski, U. Heiz, H. Jones, K.H. Lim, N. Rösch, A.D. Vitto, G. Pacchioni, *Phys. Rev. Lett.* **94**, (2005)
17. R. Engeln, G.V. Helden, A.J.A.V. Roij, G. Meijer, *J. Chem. Phys.* **110**, 2732 (1999)
18. R.N. Muir, A.J. Alexander, *Phys. Chem. Chem. Phys.* **5**, 1279 (2003)
19. H.G. Boyen, G. Kastle, K. Zurn, T. Herzog, F. Weigl, P. Ziemann, O. Mayer, C. Jerome, M. Möller, J.P. Spatz, M.G. Garnier, P. Oelhafen, *Adv. Funct. Mat.* **13**, 359 (2003)
20. G. Kastle, H.G. Boyen, F. Weigl, G. Lengl, T. Herzog, P. Ziemann, S. Riethmuller, O. Mayer, C. Hartmann, J.P. Spatz, M. Möller, M. Ozawa, F. Banhart, M.G. Garnier, P. Oelhafen, *Adv. Funct. Mat.* **13**, 853 (2003)
21. G. Mie, *Ann. Physik* **25**, 377 (1908)
22. U. Kreibig, M. Vollmer, *Optical Properties of Metal Clusters* (Springer, Berlin, 1995)
23. M.M. Alvarez, J.T. Houry, T.G. Schaaff, M.N. Shafiqullin, I. Vezmar, R.L. Whetten, *J. Phys. Chem. B* **101**, 3706 (1997)
24. E. Cottancin, G. Celep, J. Lerme, M. Pellarin, J.R. Huntzinger, J.L. Vialle, M. Broyer, *Theor. Chem. Acc.* **116**, 514 (2006)
25. U. Kreibig, C. Vonfrags, *Z. Phys.* **224**, 307 (1969)
26. P.B. Johnson, R.W. Christy, *Phys. Rev. B* **6**, 4370 (1972)
27. E. Cottancin, J. Lerme, M. Gaudry, M. Pellarin, J.L. Vialle, M. Broyer, B. Prevel, M. Treilleux, P. Melinon, *Phys. Rev. B* **62**, 5179 (2000)
28. H. Hovel, S. Fritz, A. Hilger, U. Kreibig, M. Vollmer, *Phys. Rev. B* **48**, 18178 (1993)
29. C. Brechignac, P. Cahuzac, N. Kebaili, J. Leygnier, A. Sarfati, *Phys. Rev. Lett.* **68**, 3916 (1992)
30. J. Lerme, B. Palpant, B. Prevel, E. Cottancin, M. Pellarin, M. Treilleux, J.L. Vialle, A. Perez, M. Broyer, *Eur. Phys. J. D* **4**, 95 (1998)
31. A. Liebsch, *Phys. Rev. B* **48**, 11317 (1993)
32. S. Fedrigo, W. Harbich, J. Buttet, *Phys. Rev. B* **47**, 10706 (1993)
33. A.D. Vitto, G. Pacchioni, K.H. Lim, N. Rösch, J.M. Antonietti, M. Michalski, U. Heiz, H. Jones, *J. Phys. Chem. B* **109**, 19876 (2005)

### 4. Outlooks

The experimental apparatus presented here can be used to measure the optical properties of supported metal clusters in the near-UV and visible range of the light spectrum. Here some improvements which may increase on one hand the generality of the setup, and on the other hand the available spectral range are proposed.

#### 4.1. Normal incidence configuration CRDS

In this apparatus the Brewster's angle configuration CRDS is used to study the extinction properties of size-selected supported clusters and therefore, only p-polarised light may be employed. Modifying the sample holder in a way that precise alignment for perpendicular arrangement becomes possible, will provide the opportunity to investigate the optical properties of the clusters as the polarisation of the light is varied. In this case it is not necessary to use linearly polarised light, and circularly polarised light may also be taken. This will provide a possibility to extend the optical investigations study chiral species.

For normal incidence CRDS the thickness of the substrate material plays a minor role if the absorption losses are negligibly small. In contrast to the Brewster's angle configuration no beam displacement occurs in normal incidence arrangement. The other advantage of the perpendicular layout is a larger choice of support materials, since here birefringent materials may be used as well. The relevant criteria are the high transparency and surface quality. The main challenge concerning the availability of the suitable substrates is that both surfaces need to be precisely parallel.

#### 4.2. Second harmonic generation spectroscopy

In the UV range there will generally be more optical transitions to be observed for metal clusters than in the visible range <sup>112</sup>. The main challenge concerning the present setup is the choice of the support materials which are transparent in the UV. In addition the contribution of scattering losses needs to be very small, since Rayleigh scattering increases with the fourth power of the reciprocal wavelength and is generally much higher in the UV. This issue may be circumvented by using SHG spectroscopy as will be addressed in the following.

Second harmonic generation spectroscopy was already introduced briefly in section 2.2.1.5. Application of this method to supported metal clusters has already been reported in the past, however, only at one or at most two single wavelengths <sup>113, 114</sup>. The application to large nano-particle arrays has also been reported for an extended range of wavelengths <sup>115</sup>. The great motivation to apply

SHG spectroscopy to supported metal clusters is that the support material doesn't need to be transparent to frequency doubled light, if this is created at the back side of the substrate (seen from the propagation direction). In this case it would be sufficient if the substrate is transparent to the fundamental light. Obviously the same substrates which are used for CRDS measurements can be used for SHG measurements. This allows for a better understanding of the same system.

The SHG signal is enhanced for frequencies resonant with transitions at both the fundamental and the doubled frequency (if the transitions are allowed). An important point about application of SHG to adsorbed molecules generally, is that the laser fluence should be kept below a certain threshold in order to avoid desorption of the molecules. Therefore it is usually more convenient to study the transitions resonant with the double frequency<sup>116</sup>. For transitions which are resonant with the fundamental beam, absorption of the intense fundamental radiation can easily trigger desorption of the molecules or cause structural deformation and thus remove or shift the transition. In this context the SHG spectroscopy would be complimentary to CRDS measurements from two points of view. Firstly the effective measurement range will be extended and transitions which are not available to CRDS may be studied. Secondly, since the selection rules for the two techniques are different (SHG is a nonlinear method where CRDS is linear) a different set of transition are observed by each method.

The application of SHG spectroscopy to size-selected supported metal clusters would be a novel development and a similar characterisation process need to be done starting from simple model systems of known absorption (laser dyes coated on substrates). As the next step the response of the unselected clusters may be studied for various metals before samples of mono-dispersed clusters at surfaces are investigated.

### 4.3. IR-cavity ring-down spectroscopy

One of the fundamental interests in the optical properties of supported metal clusters lies in the expected information to be gained on electronic structure of the clusters at surfaces. This in turn is mainly triggered by the observed size dependent catalytic reactivity of the supported clusters<sup>117</sup>. Extension of the measurement range of the current setup into the IR region will make it possible to study the binding of the adsorbates to the clusters and in combination with information from the UV-Vis range a complete picture of the system may be achieved.

IR-CRDS has been extensively used in gas phase studies. The Saykally group were the pioneers, applying this technique to the infrared study of water clusters,

polycyclic aromatic hydrocarbons, nucleotide base clusters, or ablated carbon clusters in the frequency range between  $\sim 2000\text{ cm}^{-1}$  and  $4000\text{ cm}^{-1}$  <sup>118-122</sup>. The application of CRDS to the condensed-phase is considerably more difficult than to the gas-phase as already discussed in section 2.2.6. The main issue about IR-CRDS is the availability of highly reflective mirrors. Mirrors are available for the IR range, however, the reflectivity of the mirrors is not as high as that of the mirrors in the visible range. This increases the total losses of the cavity and suppresses the sensitivity. On the other hand the IR mirrors have a broader band compared to visible mirrors. The choice of support material is another issue. Almost all of the materials listed in table 3 could be used for IR-CRDS as well.

Having a defined system (cluster/support investigated through CRDS), supplied with hydrocarbons will permit the study of their chemistry on small clusters. Relevant reactions are the hydrogenation of aliphatic, cyclic and aromatic alkenes, the selective dehydrogenation of hydrocarbons, the polymerization of acetylene, or the activation of methane. To this end the second cooling shield (see section 2.5.3.) is armed with two independent gas lines. The binding of the gas molecules to the bare surface may be studied through shifts in C-H vibrational frequencies. By repeating the same measurements in the presence of deposited clusters, information on the degree of activation of adsorbed molecules will be achieved.

### **4.4. Controlled surface chemistry on isolated size-selected metal clusters: A research proposal.**

Based on the knowledge and experiences obtained throughout the current work, a future postdoctoral research is proposed as the following.

#### **4.4.1. Introduction**

Small metal clusters have attracted considerable interest over the past two decades not only due to the fundamental scientific interest in the evolution of physico-chemical properties from the atomic to the bulk, but also because these properties are non-scalable.<sup>123</sup> The catalytic reactivity of small transition metal clusters (2-30 atoms), for example, has been shown to vary by orders of magnitude upon the addition of a single additional metal atom to a cluster.<sup>124</sup> The major goal of this research remains to better understand the often subtle role in which the electronic and geometrical structures of a cluster influence its reactivity.<sup>125</sup> To this end, a precise knowledge of the electronic structure and geometry from both sophisticated spectroscopic and theoretical studies must be considered alongside the observed reactivity of the clusters.

Here, a novel integrated spectroscopic / reactivity approach is proposed, supported by high level calculations, in which infra-red radiation is used both, to

interrogate spectroscopically, molecularly decorated metal clusters, *and* to initiate thermally driven cluster surface chemistry.

#### 4.4.2. Research Project

Temperature programmed desorption (TPD) and reaction (TPR) are widely used for determination of the reactivity and activation energy of desorption/reaction on surfaces. In an approach based on recent results from work involving the group of Dr. S. Mackenzie,<sup>126</sup> we propose to develop an analogous technique of IR-induced reactivity on the surface of size-selected gas-phase metal clusters.

The main objectives of the proposal are:

1. To develop a novel laser ablation cluster source for the generation of cryogenically cold metal clusters decorated with multiple molecularly adsorbed reactant precursors.
2. To characterise the structures of these decorated clusters by infra-red multiple photon dissociation spectroscopy.
3. To drive controlled cluster surface reactivity by heating the cluster using the adsorbed moieties as suitable chromophores.
4. To rationalize the experimental findings, including plausible reaction pathways, using DFT investigations

#### 4.4.3. Methodology

We propose to build a new instrument, permitting the generation, trapping and spectroscopic interrogation of small decorated metal clusters. Size-selected metal clusters will be generated by a state-of-the-art laser ablation cluster source equipped with multiple late mixing valves, through which it will be possible to decorate the clusters with molecularly-adsorbed reactant precursors and/or spectroscopic messengers (Ar, Ne). The cluster channel will be a cryogenically (LN<sub>2</sub>) cooled copper channel, to generate cold clusters, minimising direct reaction. Expansion into vacuum will generate a supersonic cluster beam and charged clusters within the beam will be guided using an *rf*-octopole ion guide to a commercial quadrupole ion trap (QIT), in which they will be stored for extended

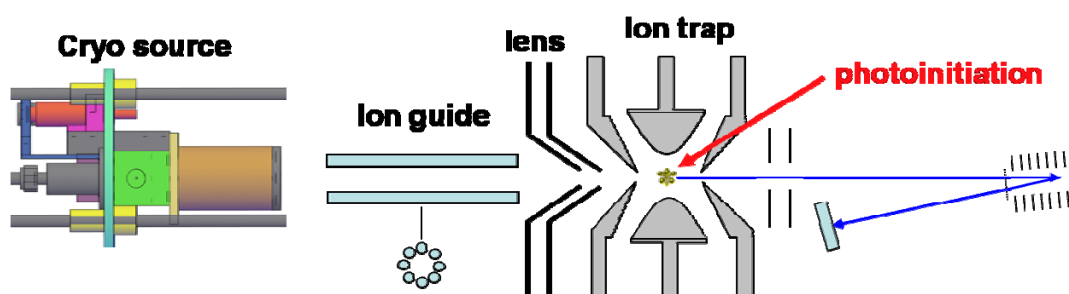


**Figure 28** The proposed experiment for the study of photoinitiated and infrared-driven chemistry on the surface of size-selected gas-phase transition metal clusters



periods. A schematic overview of the proposed setup is shown in Figure (28)

While stored within the trap, the clusters will be excited using a range of laser pulses. Laser systems operating from the far-infrared through the visible to the vacuum ultraviolet are available, almost without gap. The low number densities of clusters generated by laser ablation mean that only action spectroscopy, based on mass spectrometric detection is sufficiently sensitive to yield the required information. For example, the vibrational spectrum of the decorated metal clusters will be obtained through infrared multiple photon dissociation spectroscopy (IR-MPD), which relies on the loss of a weakly-bound adsorbate (e.g., a physisorbed Ar atom) to serve as a mass-spectrometric signature, that the photon has been absorbed. Monitoring either the depletion of the parent cluster signal or the enhancement of the fragment signal as a function of wavelength, provides a highly sensitive method to record the vibrational spectrum of naked and/or decorated metal clusters. Decorating the clusters with small molecules will allow us to investigate the binding of these molecules on the clusters, through the same technique.

Knowledge of the vibrational spectrum of decorated clusters will enable us to pump energy into the cluster using the adsorbate as an IR chromophore. This in turn will trigger a variety of interesting events on the surface, such as (trivially) desorption and (more interestingly) reaction. Since the total energy absorbed by the cluster may be controlled by the excitation laser fluence and the vibrational mode used, this will permit exquisite control over the surface processes excited.

On the evidence of previous work it will be essential to match depletion in one species channel with gains in other channels. For this purpose it will be important to detect all charged products. This rather precludes the traditional ejection of the trap contents into a linear trap for detection. Instead, following laser excitation, the contents of the ion trap will be detected by injecting all charges into a reflectron time of flight mass spectrometer. This is more challenging from an experimental perspective, but such systems are now commercially available. It will be important to detect all charged products to determine branching ratios for different processes.

By way of example system, we will mimic at the single cluster level, the type of chemistry which occurs within the automobile catalytic converter. For example, we will decorate rhodium clusters with molecularly adsorbed CO and N<sub>2</sub>O molecules and pump the cluster through both the CO stretch and the different N<sub>2</sub>O vibrational modes. Based on the recent work, we expect this to dissociate the surface bound N<sub>2</sub>O, desorbing N<sub>2</sub> and generating a surface mobile O-atom which may react with the CO generating CO<sub>2</sub>.  $\text{Rh}_n\text{CO}(\text{N}_2\text{O}) \Rightarrow \text{Rh}_n + \text{N}_2 + \text{CO}_2$ .

In addition to laboratory-based work the new instrument will be designed to be portable in order to allow it to be transported to national facilities such as the FELIX free-electron laser in the Netherlands, the ultra-fast ASTRA facility at the Rutherford Appleton Laboratory and the UK experimental free electron laser in Daresbury.

All of the experimental work will be supported by calculations based on density functional theory. These will be performed on the available computing cluster as well as the Supercomputing facilities of the University of Oxford and the National Service for Computational Chemistry Software.

### 5. Summary

The diverse field of cluster science is still very active in searching for a general description of the evolution of material properties with size, from a single atom toward the bulk. In the past decade, the optical properties of metal clusters have been extensively studied, both theoretically and experimentally. This growing interest is motivated by the fruitful information, expected to be gained, on the electronic structure and the dynamics of the delocalised conduction electrons. Oxide supported metal clusters are attracting an increasing interest for their potential impact in high-technological areas. Optical properties of small metal clusters have been studied vastly in gas phase, in correlation with cluster size. Corresponding measurements on supported clusters are, however, scarce. This is mainly due to the difficulties accompanying the production of suitable samples, and the extremely high sensitivity, which is required to detect the optical response of such samples.

It is necessary to systematically study the evolution of the optical properties of small metal clusters bounded to surfaces, as a whole system, since the interaction between the support material and the particles affects the aforementioned properties. This is the reason for the apparently random discrepancies observed between free and supported species, which are at least to date not fully understood. In the current work, a solution to this problem was proposed and realised by developing a novel experimental apparatus, capable of conducting these systematic investigations.

#### 5.1. Experimental achievements

For the first time, a cavity ring-down spectrometer was designed to investigate optical properties of size-selected metal clusters, supported on surfaces, under ultrahigh vacuum conditions. A number of experimental and technical challenges had to be overcome for this purpose.

**A) Cluster source:** Clusters of various metals (Au, Ag, Cu, Co, Ni, Nb, Pt, and Pd) were produced through a newly built pulsed laser vaporisation cluster source. This kind of source is used extensively in our group and naturally long standing experiences are available. The main issues concerning the cluster source are its stability, which is determined from the fluctuations in the measured cluster current (here positively charged cluster ions), and its effectivity in cluster formation, which is evaluated from the value of the cluster current. These in turn are affected by the stability of the vaporisation laser, carrier gas pressure, and voltages controlling the ion optics. In a pulsed laser vaporisation cluster source, collision with the carrier gas is used to form and cool metal clusters. Hence, the stability and reproducibility of the gas pulses are of great importance. Here, the

main concept of the source function was left unchanged, while some modifications were applied in order to improve its performance, and the convenience of its operation. For instance, the construction of the pulsed piezo valve housing was modified, so that its tuning and replacement became easier. Consequently, carrier gas pressure was stabilised. As a result, the life time of the piezo valve and hence, the stability of the source, were enhanced, and currents of  $\sim 100$  pA were easily achieved for positively charged size-selected cluster ions.

**B) UHV compatible cavity ring-down spectrometer:** The novelty of the apparatus arises from its spectroscopic capabilities, and the solutions provided to overcome specific challenges. Cavity ring-down spectroscopy (CRDS) is a highly sensitive direct absorption measurement technique, which has been originally developed for gas phase studies. This method was adapted to investigate the optical properties of supported metal clusters, in the near UV and visible range of the light spectrum. To achieve this a number of modifications regarding sample preparation and the spectrometer design were undertaken. From the two possible approaches concerning the geometrical configuration of the sample inside the cavity, the Brewster's angle layout was chosen due to the availability of appropriate substrates.

**C) UHV mirror exchanger:** Since small metal clusters and their properties are vulnerable to contamination, the measurements should be performed under controlled ultra high vacuum conditions. The narrow bandwidth of the dielectric mirrors employed in CRDS was compensated by using a collection of mirrors, centred at different wavelengths, in order to cover an extended spectroscopic range. Here, a UHV compatible multi-mirror holder was designed and constructed, which allows the simultaneous implementation of up to ten different mirror sets into the vacuum, and their in-situ alignment from outside the vacuum chamber. This piece plays an invaluable role in the presented apparatus, by drastically shortening the measurement time compared to other approaches (e.g. one mirror at a time etc.). Details of the mirror holder functioning mechanism and construction are included.

**D) Mode matching:** In order to take full advantage of the high sensitivity of CRDS, it is required that only the fundamental transverse electromagnetic mode ( $TEM_{00}$  mode) of the optical cavity is excited. To this end, the  $TEM_{00}$  mode of the laser beam was picked out through spatial filtering, and the beam parameters were modified, through an optical arrangement, to match to those of the cavity. As a result an enhancement of about 50%, in relative error of the recorded data was observed.

**E) Cryogenic sample holder:** A cryogenic sample holder was designed and constructed, to allow the possibility of temperature controlled measurements. In contrast to metallic samples, the substrates used in transmission mode CRDS,

are “heated” by the chamber walls, through radiation, because of their higher emissivity and lower heat conductivity. As the substrates are absorbing this radiation, it is not enough to simply cool the substrate. Low temperatures are only achieved after shielding the substrate against these radiations. This claim was supported based on calculations according to heat transfer equations. Full shielding was, however, not possible due to the limitations imposed by the laser path way and sample size. A second cooling shield, which surrounds the sample holder was proposed and realised for further cooling. Details of the calculations are included.

**F) Clean electron source:** In order to prepare monodispersed samples, it is necessary to extract a single cluster size, from the otherwise mixed cluster beam. Cluster ions are preferred in this case, since it is possible to distinguish them according to their mass to charge ratio, by the means of commercially available devices. In the case of CRDS, the support material is an insulator (a natural consequence of being transparent in the visible range). Hence, the surface charges up if the cluster ions are not neutralised. Cations are easily neutralised if exposed to electrons, and indeed thermal electrons, emitted from a hot filament, are commonly used for this purpose. In the case of CRDS, however, the vaporised material from the filament is not desired, and manipulates the system. In order to circumvent this contamination, a novel electron source was invented. The working principle of the e-source and the related drawings are presented in place. Since, in this source, the electrons are guided, the local electron currents are much higher than that of a naked filament, for the otherwise same operating conditions. Electron currents of  $\sim 2$  nA were generally used, however, it was also possible to obtain larger currents of up to  $2 \mu\text{A}$ .

**G) Removing metal clusters from substrate surface:** The high optical quality of the support material, and a strong motivation to avoid venting the vacuum, led us to develop a method for cleaning the substrates, in-situ, in order to be able to reuse them for the spectroscopic purposes. This was done by directing low energy  $\text{Ar}^+$  ions, produced by a commercial ion source, onto the substrate. CRDS surface maps in combination with analytical investigations indicated that metal clusters were almost completely removed (more than 99%), and the optical losses of the substrate were only slightly increased ( $\sim 50$  ppm) due to the resultant roughening.

## 5.2. Scientific achievements

The performance of the spectrometer was demonstrated by recording the optical absorption spectra of a model system, consisting of three laser dyes with known absorption properties. The solution was spin-coated onto the support material. Subsequent comparison of the results, acquired from CRDS, with those obtained through a commercially available spectrometer showed that the

presented spectrometer is superior in sensitivity, by more than two orders of magnitude. The detection limit was observed to be  $\sim 2.5$  ppm for the CRDS setup presented here.

The first results on optical spectra of supported size-selected metal clusters were recorded for  $\text{Ni}_n$  clusters ( $n = 7, 10, \text{ and } 20$ ), supported on  $\text{SiO}_2$  substrates. The results were discussed in the frame work of the Mie theory. In the investigated spectral range, no spectral features were observed, in accordance with Mie predictions. A comparison of partial oscillator strength among the samples indicated a scaling with the number of electrons in the clusters. This further demonstrated the high precision of the method.

Finally, it is proved that CRDS is a suitable approach for measuring the optical response of size-selected metal clusters supported on surfaces. The apparatus presented in this work is the first and only experimental device capable of performing such experiments. However, since cluster science is a very vivid area of research, there is of course still room for further improvements. Some suggestions were described in detail in the outlooks section.

### 5.3. Scientific prospective

Based on the experiences obtained during the course of the current thesis, a novel integrated spectroscopic / reactivity approach is proposed as a postdoctoral research topic, in which infra-red radiation will be used both, to interrogate spectroscopically, molecularly decorated metal clusters, and to initiate thermally driven cluster surface chemistry. A new instrument will be built, permitting the generation, trapping and spectroscopic investigation of small decorated metal clusters. Metal clusters will be produced by a state-of-the-art laser vaporisation cluster source, and decorated with molecularly-adsorbed reactant precursors and/or spectroscopic messengers. Charged clusters will be guided to a commercial quadrupole ion trap (QIT), in which they will be stored for extended periods.

The vibrational spectrum of the decorated metal clusters stored in the trap, will be obtained through infrared multiple photon dissociation spectroscopy (IR-MPD), which relies on the loss of a weakly-bound adsorbate (e.g., a physisorbed Ar atom) to serve as a mass-spectrometric signature, that the photon has been absorbed. Monitoring either the depletion of the parent cluster signal or the enhancement of the fragment signal as a function of wavelength, provides a highly sensitive method to record the vibrational spectrum of naked and/or decorated metal clusters.

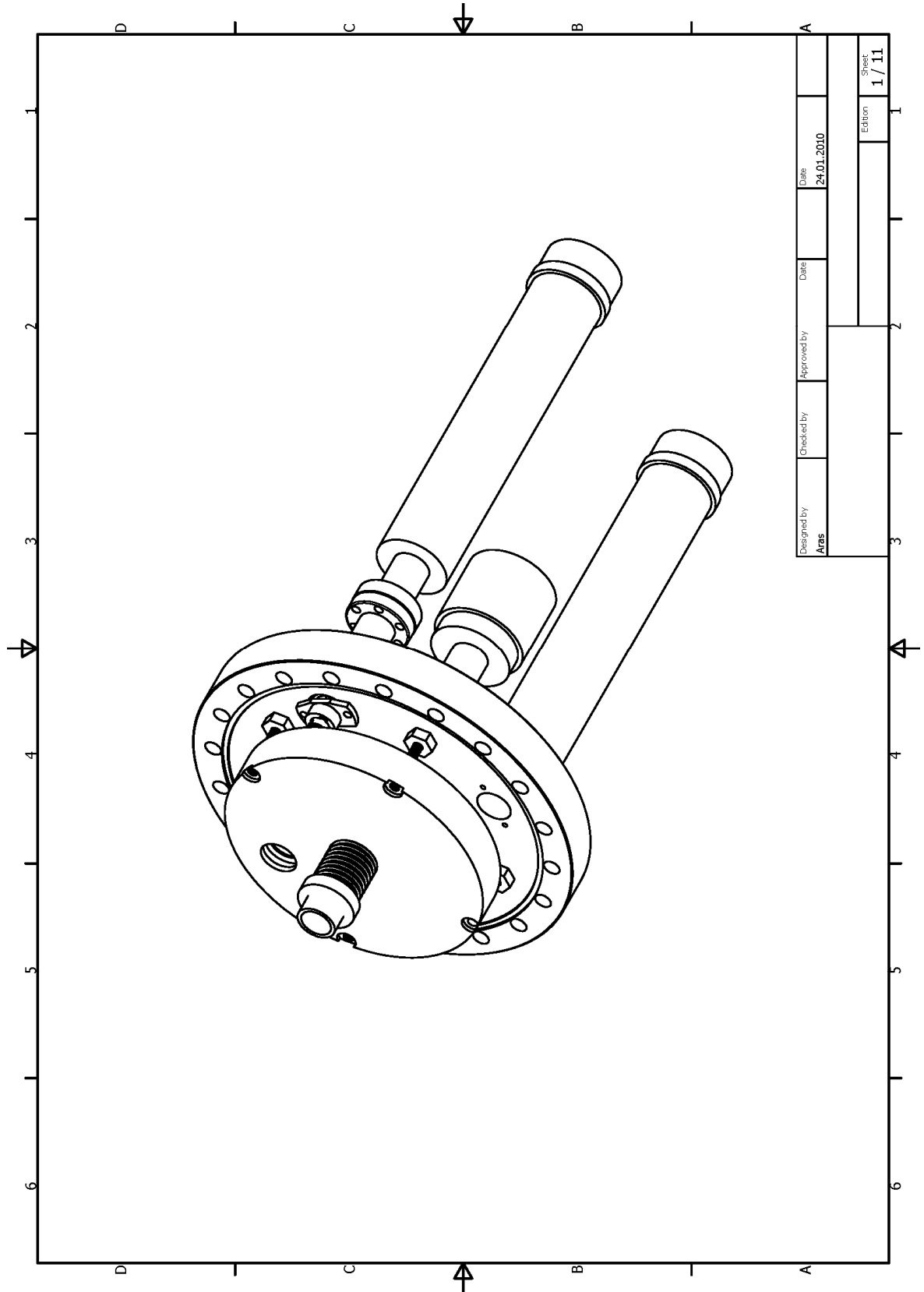
Knowledge of the vibrational spectrum of decorated clusters will enable us to pump energy into the cluster using the adsorbate as an IR chromophore. This in turn will trigger a variety of interesting events on the surface, such as desorption and reaction. Since the total energy absorbed by the cluster may be controlled by the excitation laser fluence and the vibrational mode used, this will permit exquisite control over the surface processes excited.

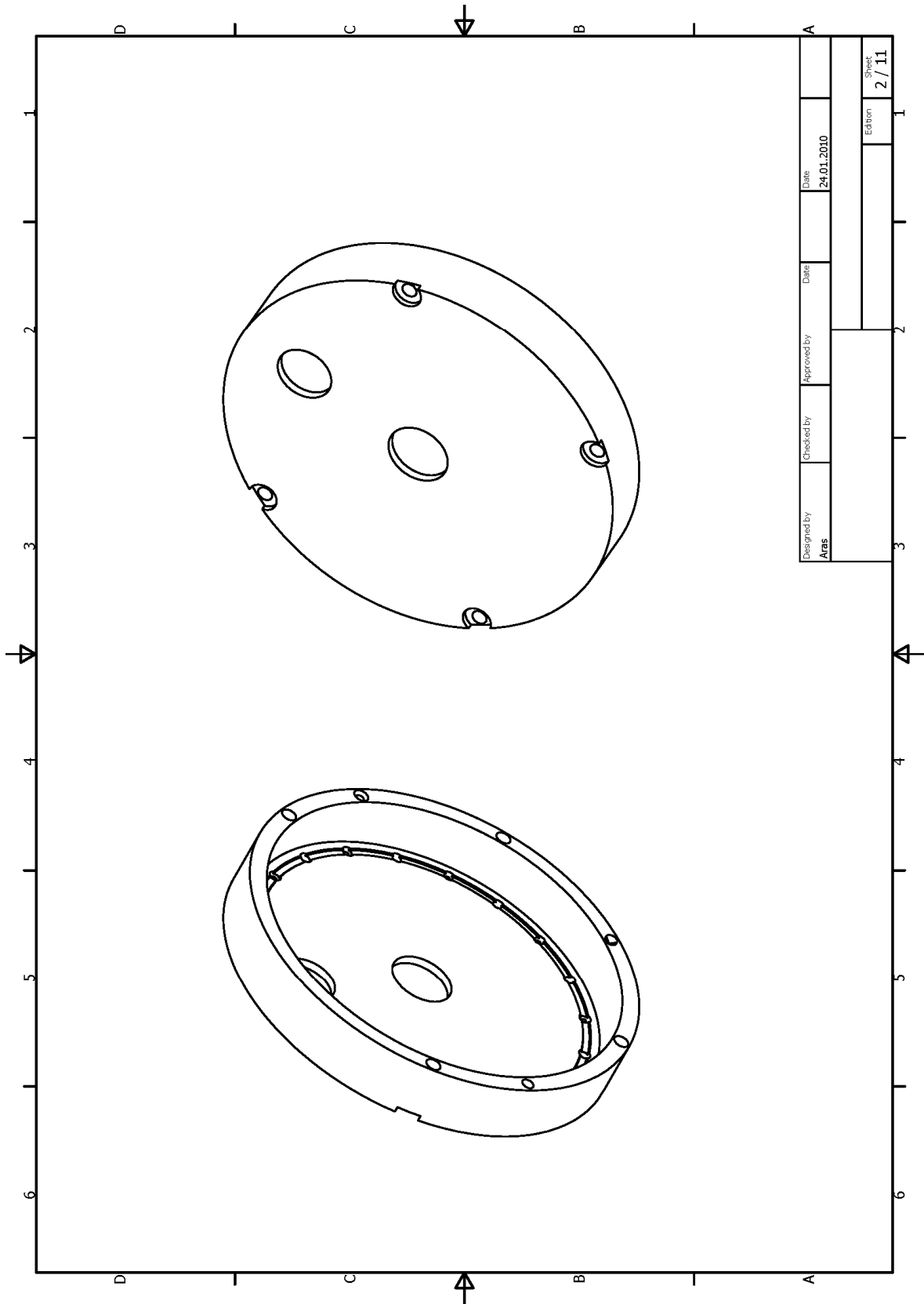


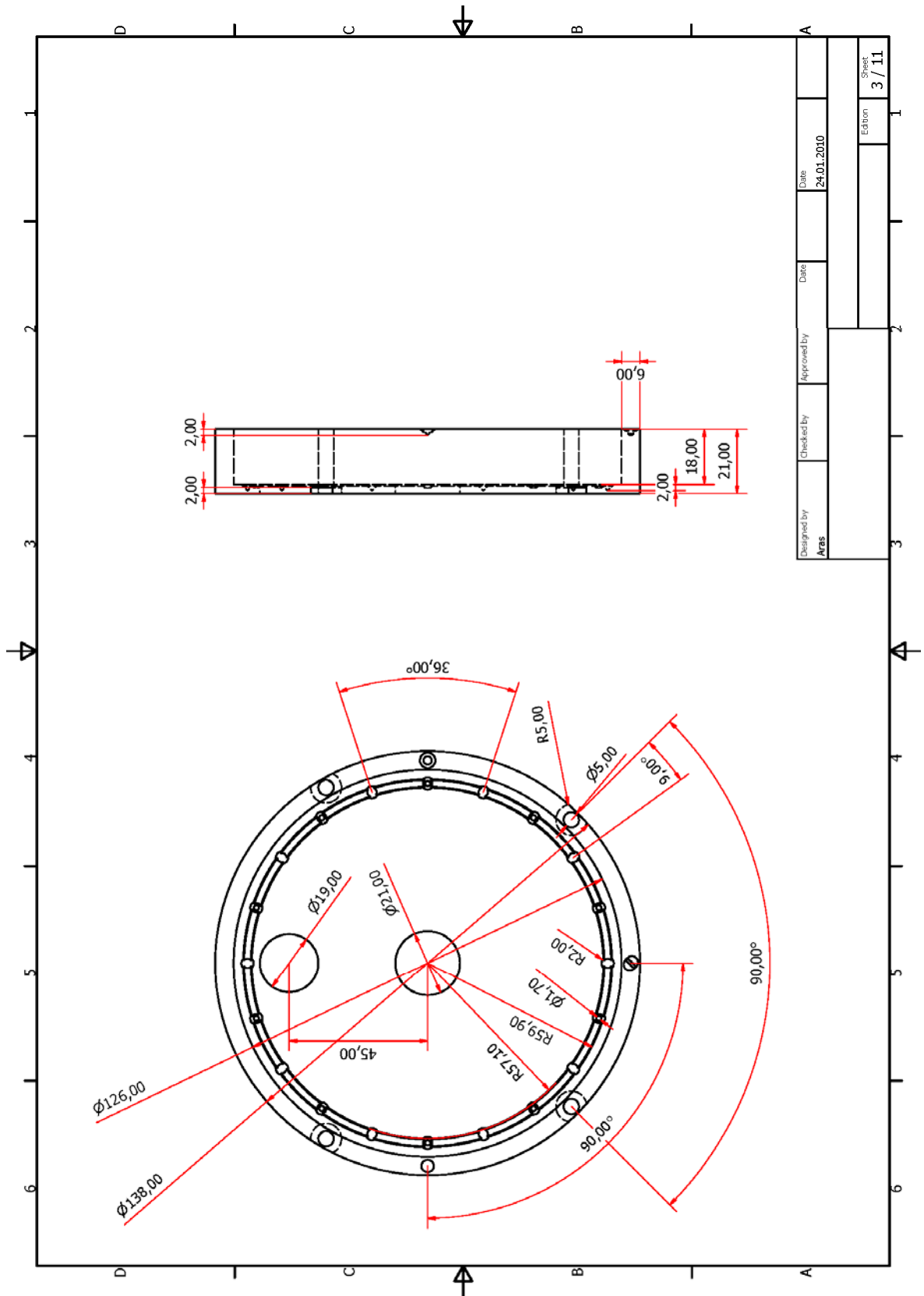


## Appendix A: Constructions

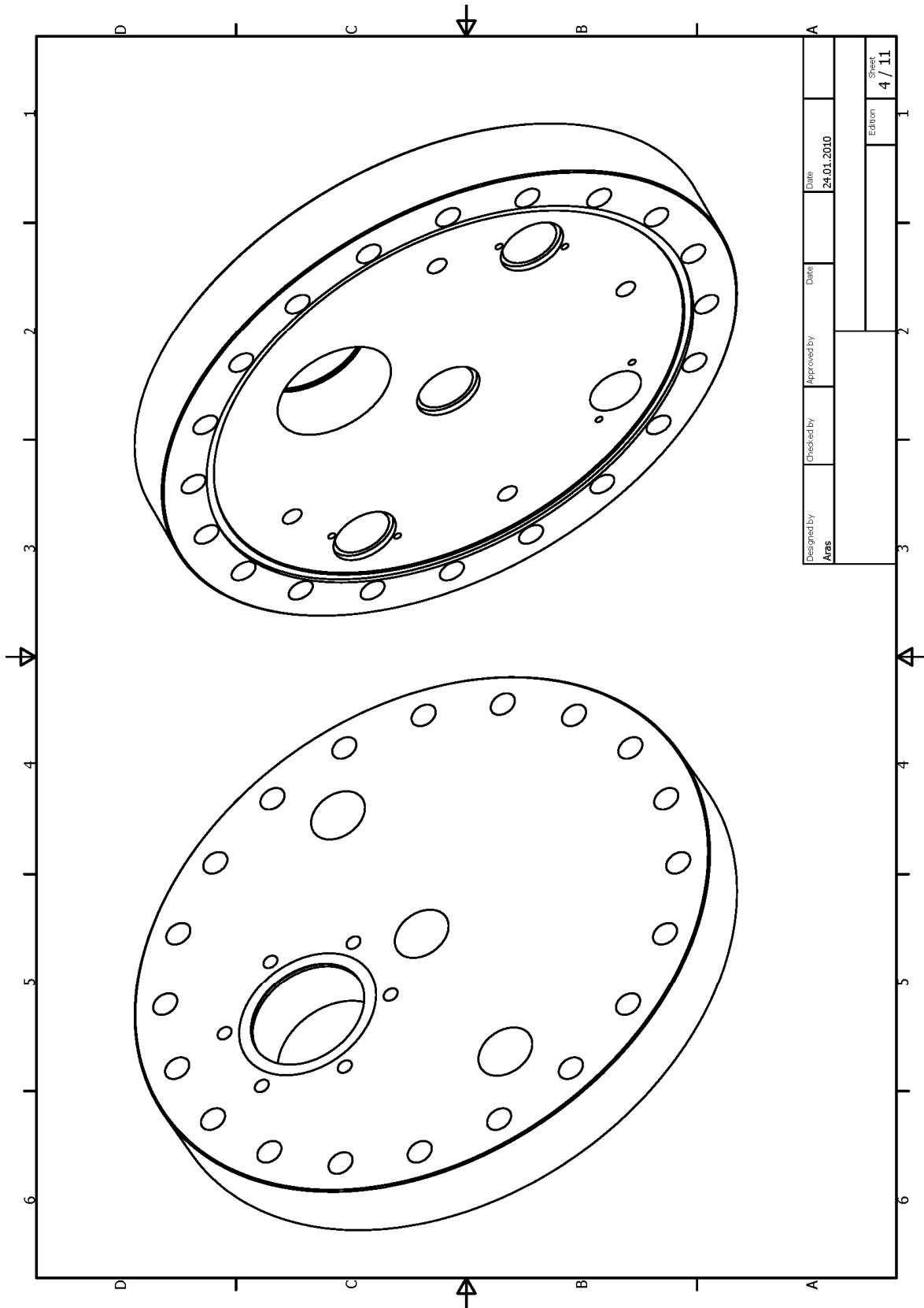
### A1. Mirror holder

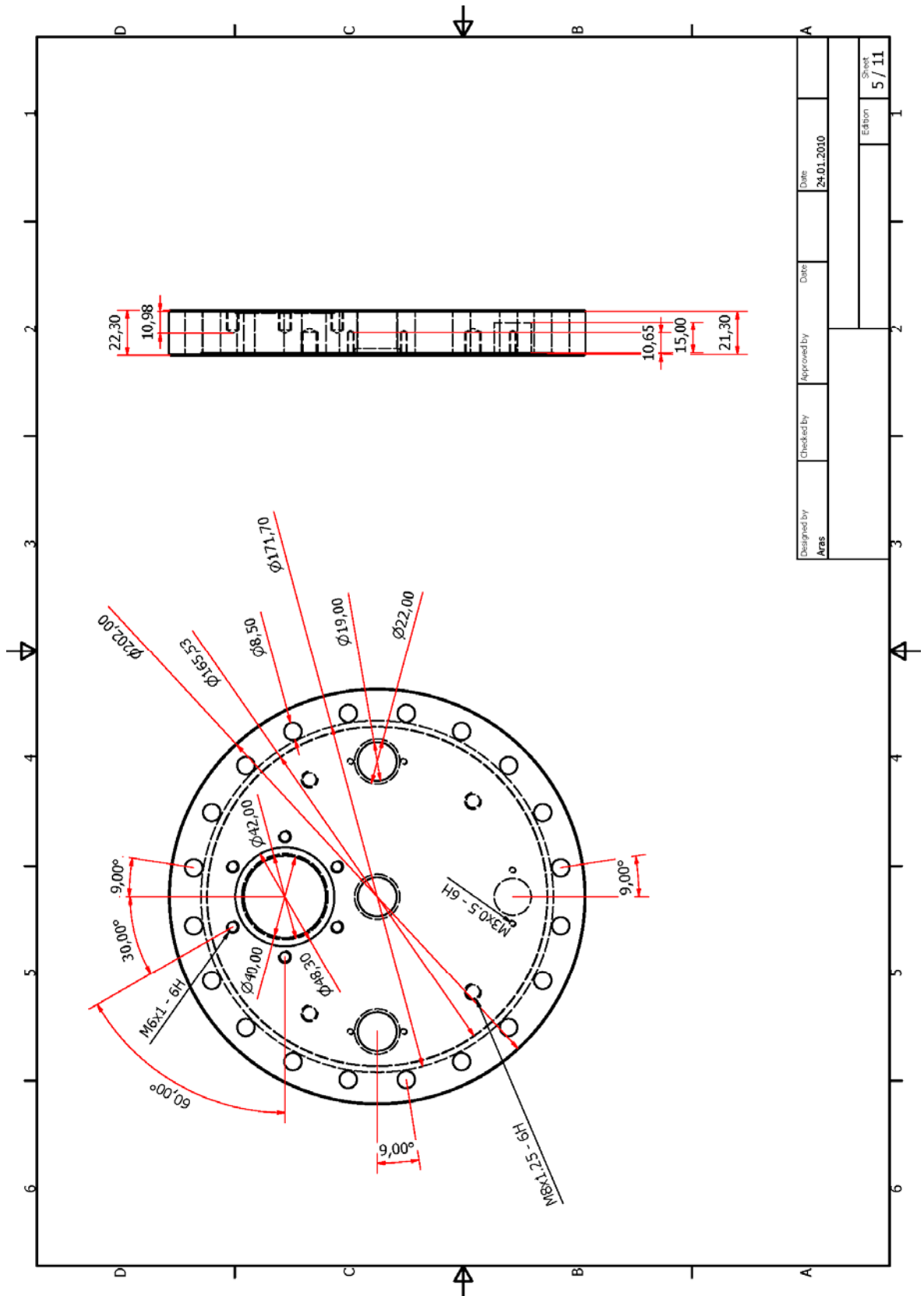




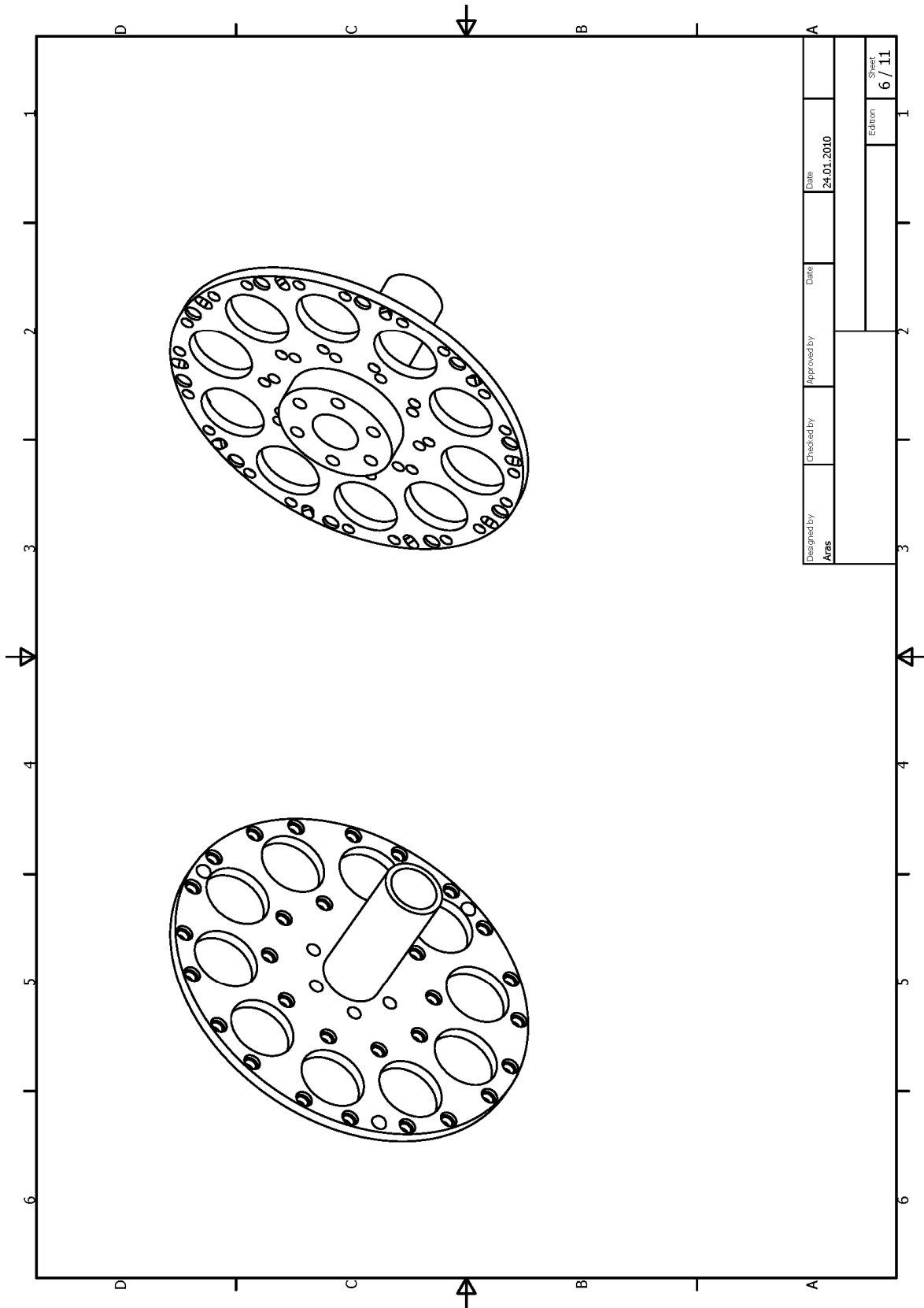


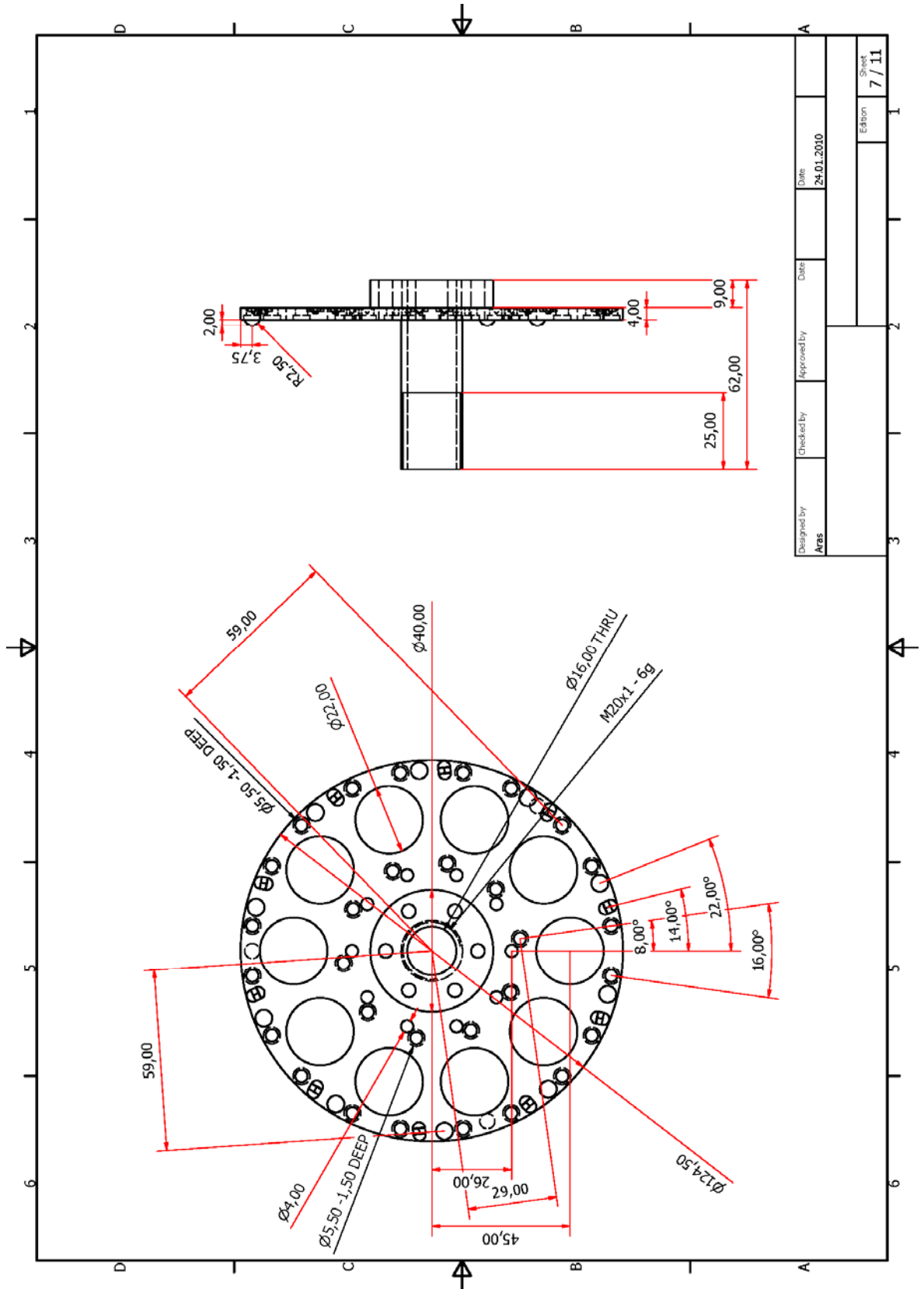
Designed by	Aras	Checked by		Approved by		Date	24.01.2010	
							Edition	3 / 11

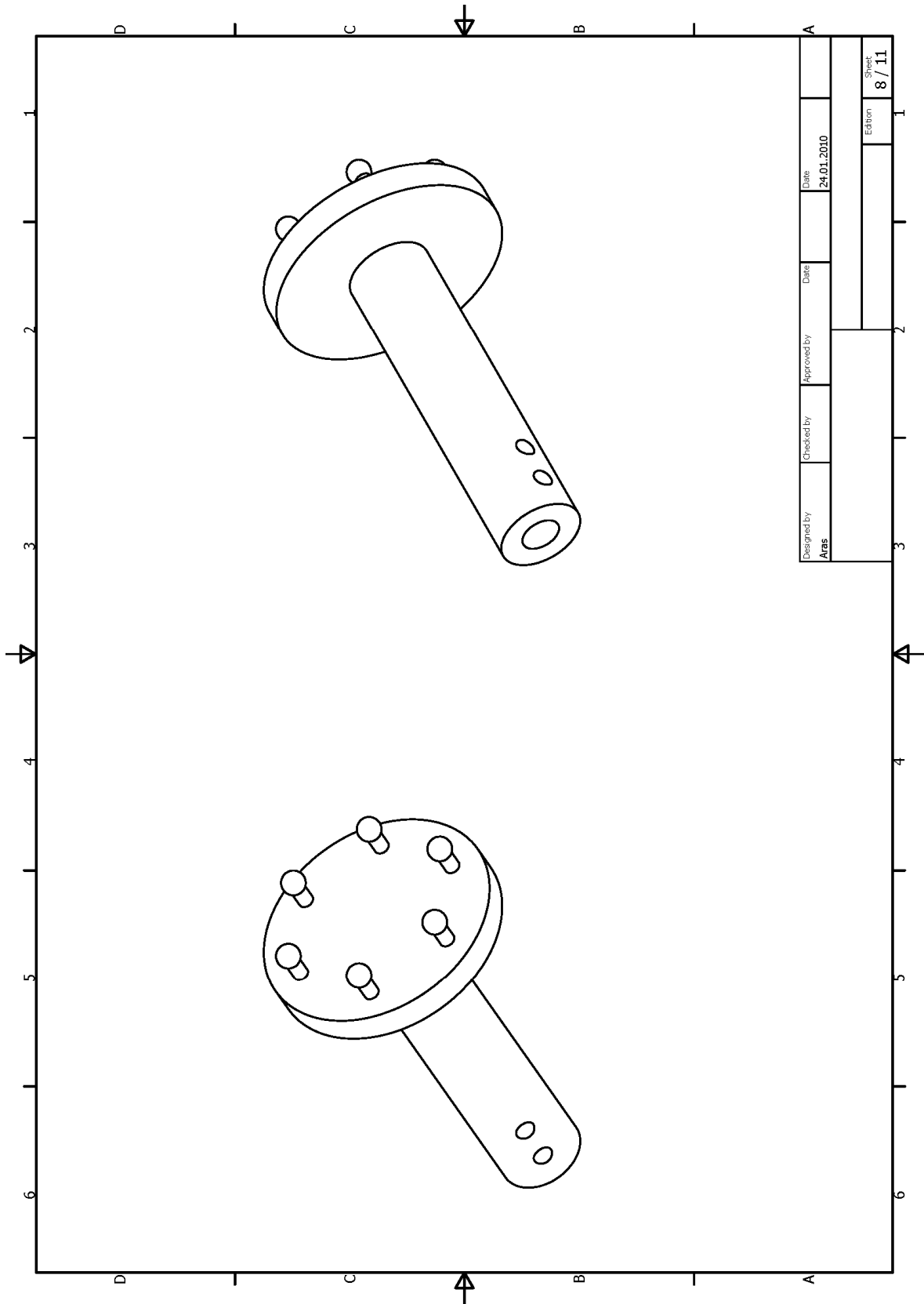




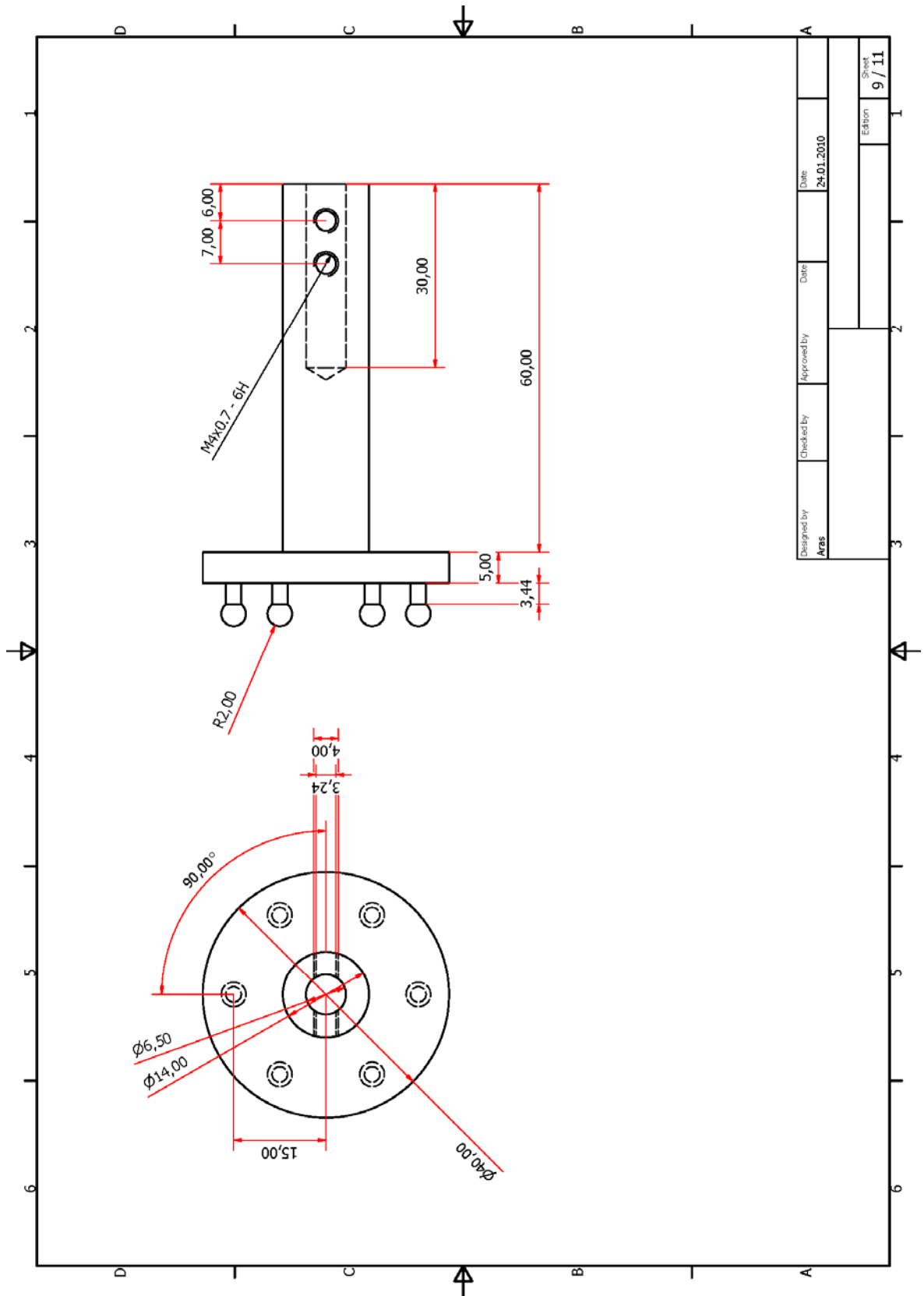
Designed by Aras	Checked by	Approved by	Date 24.01.2010
Edition			Sheet 5 / 11

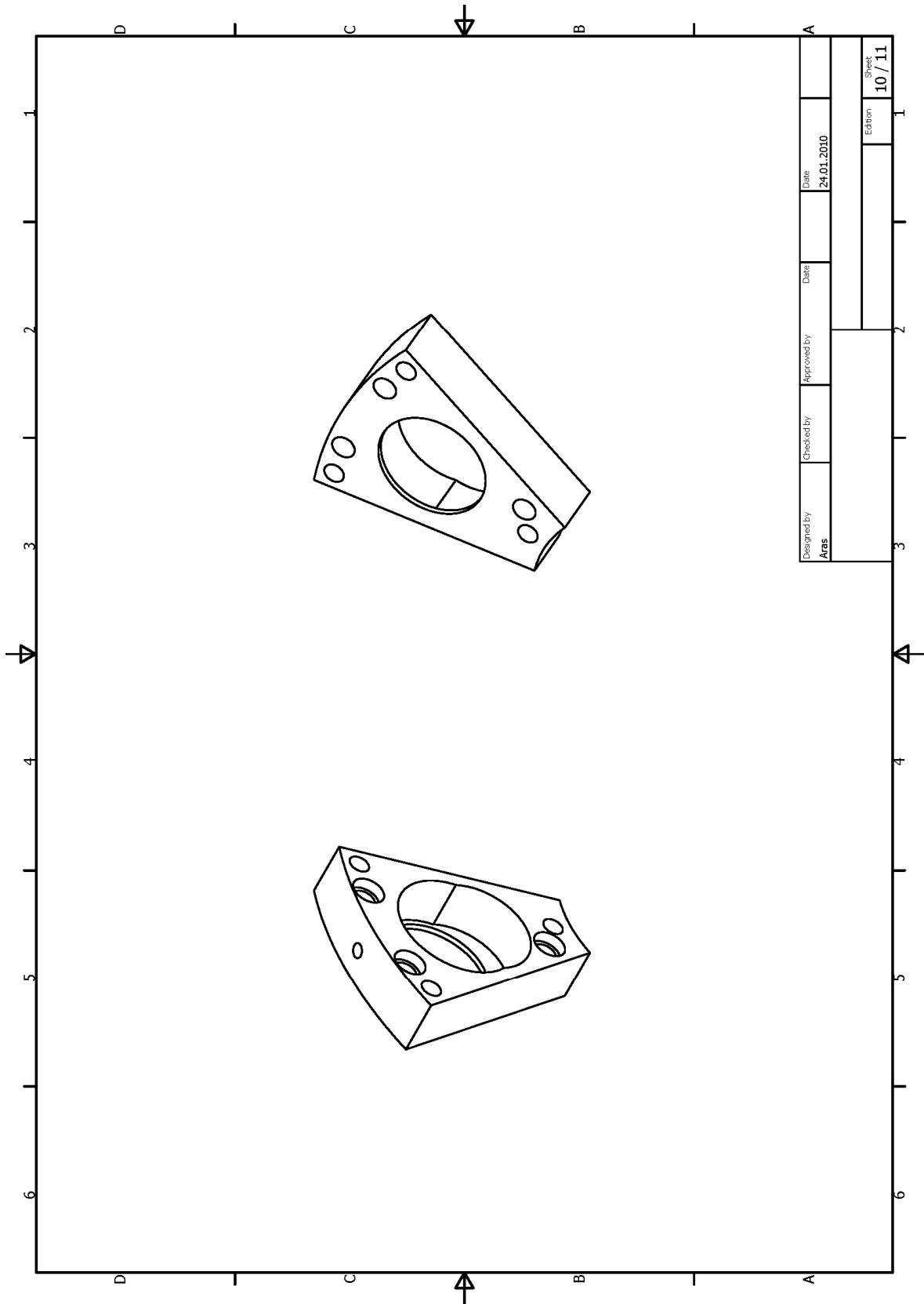


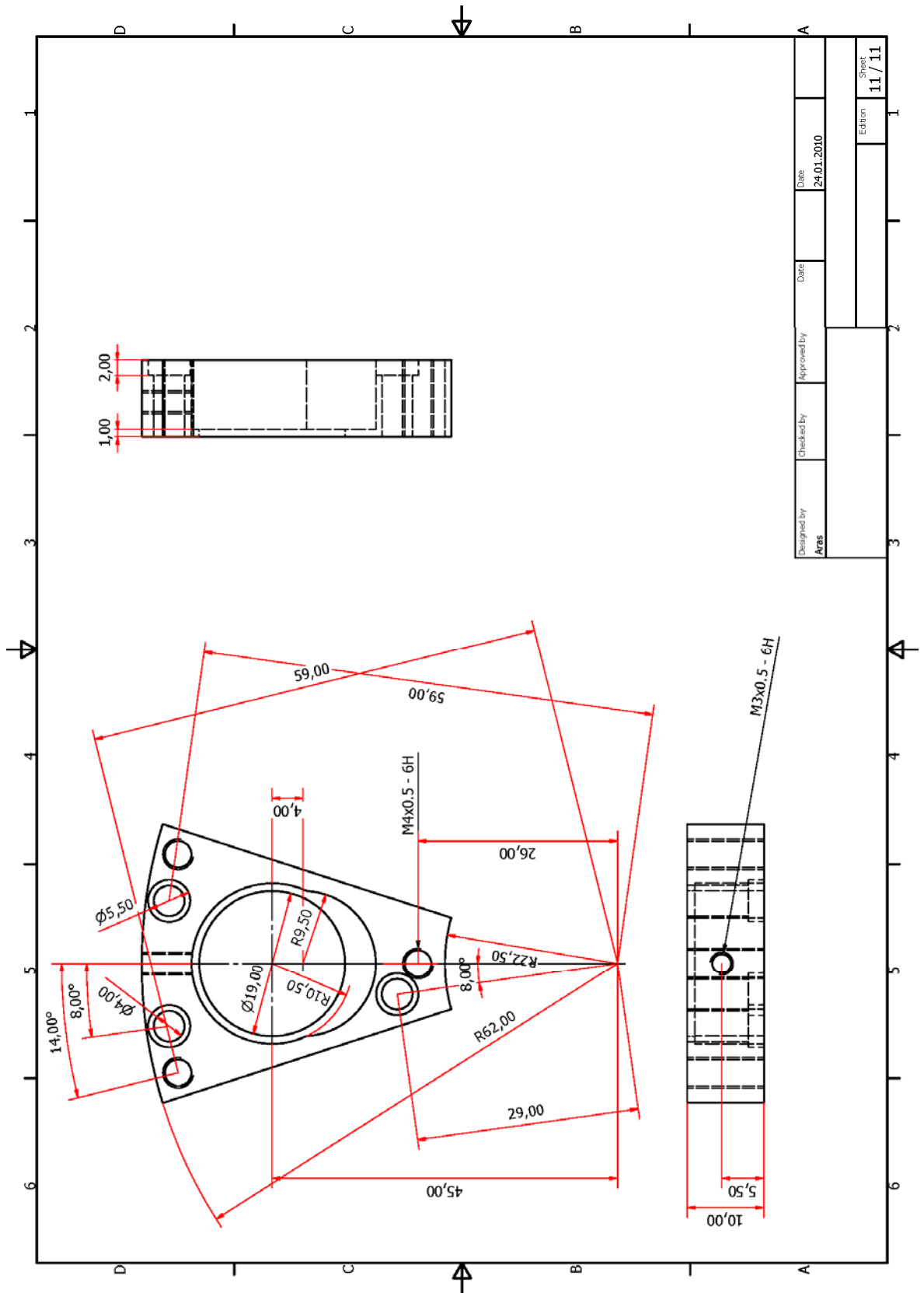






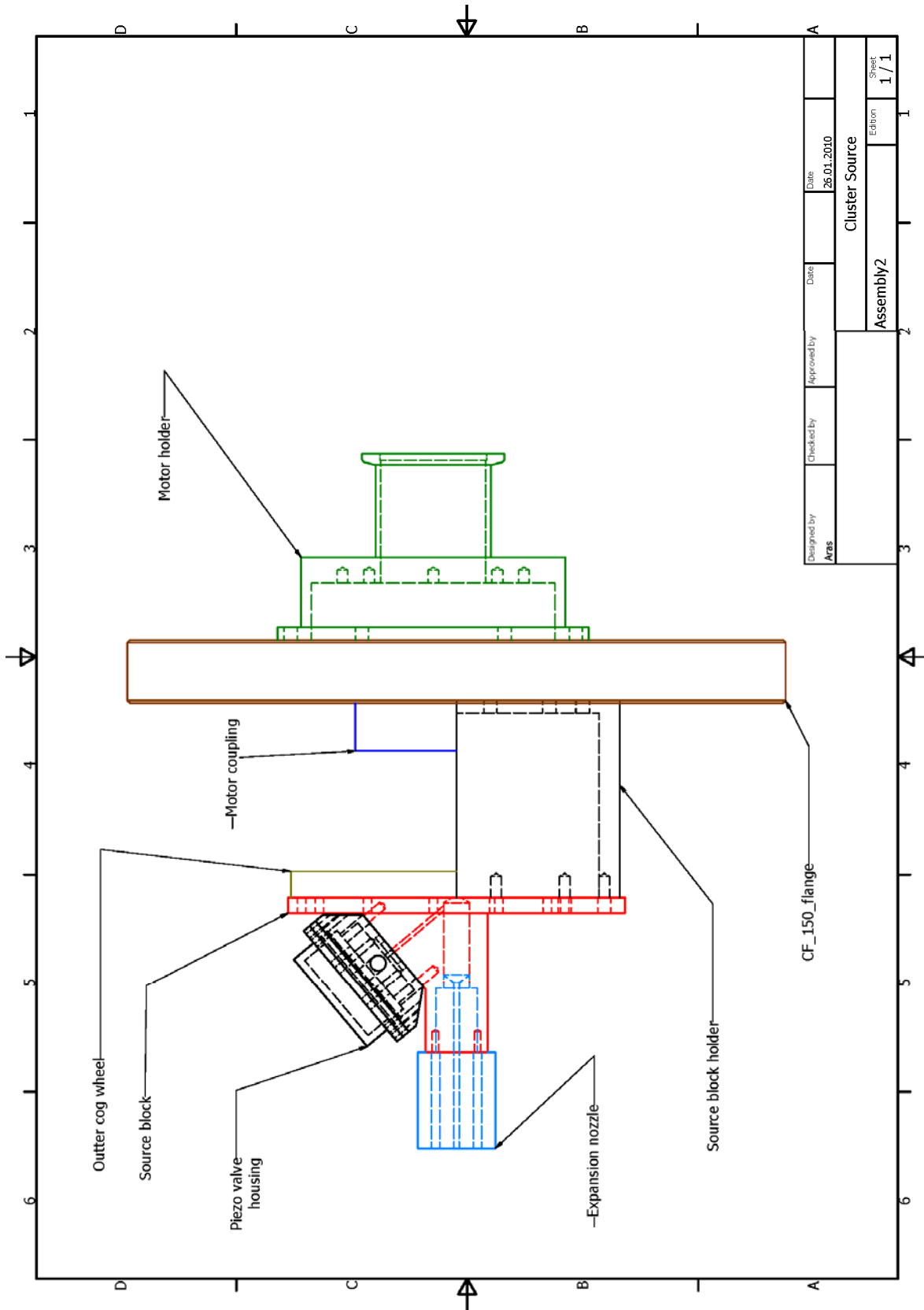


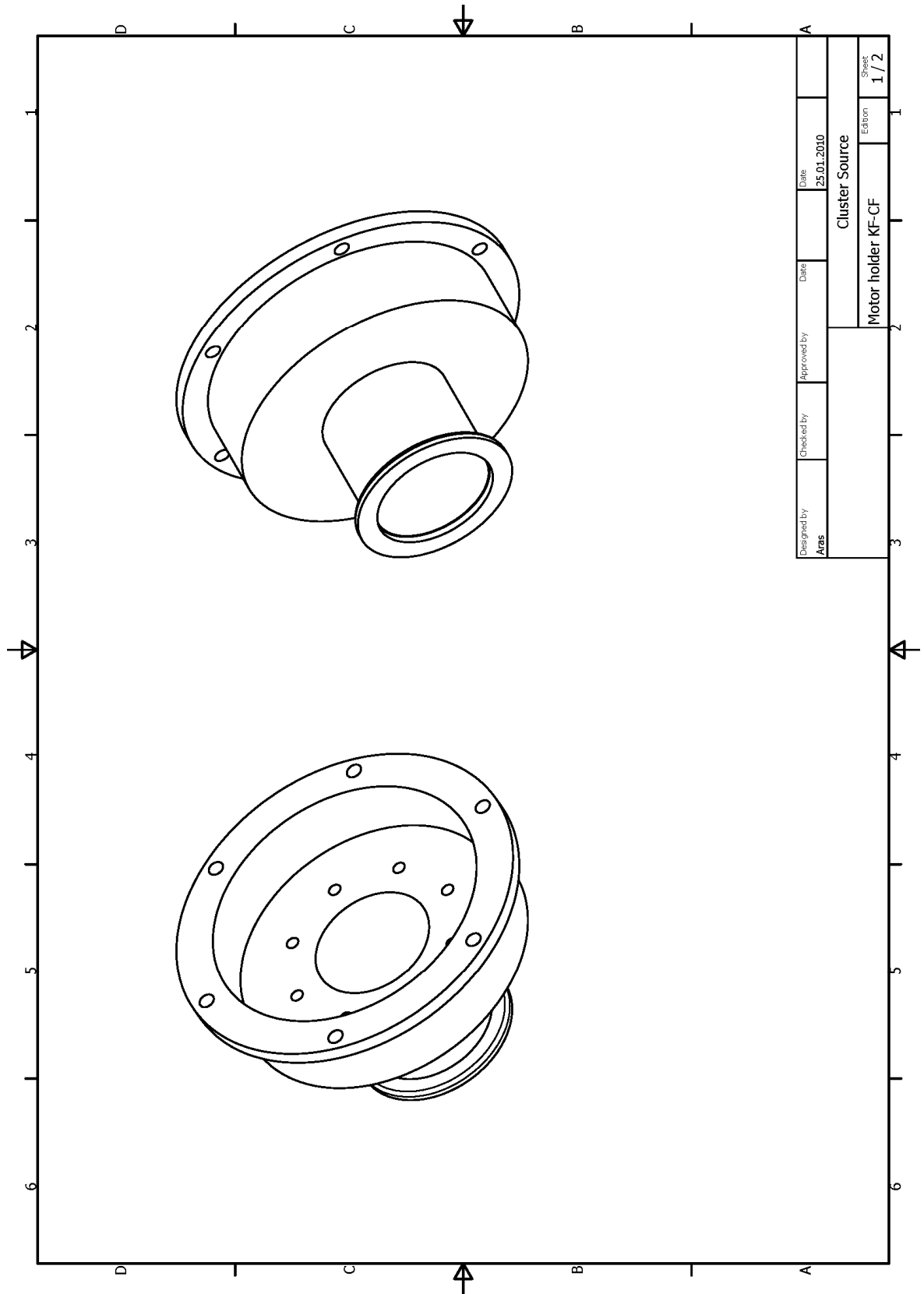


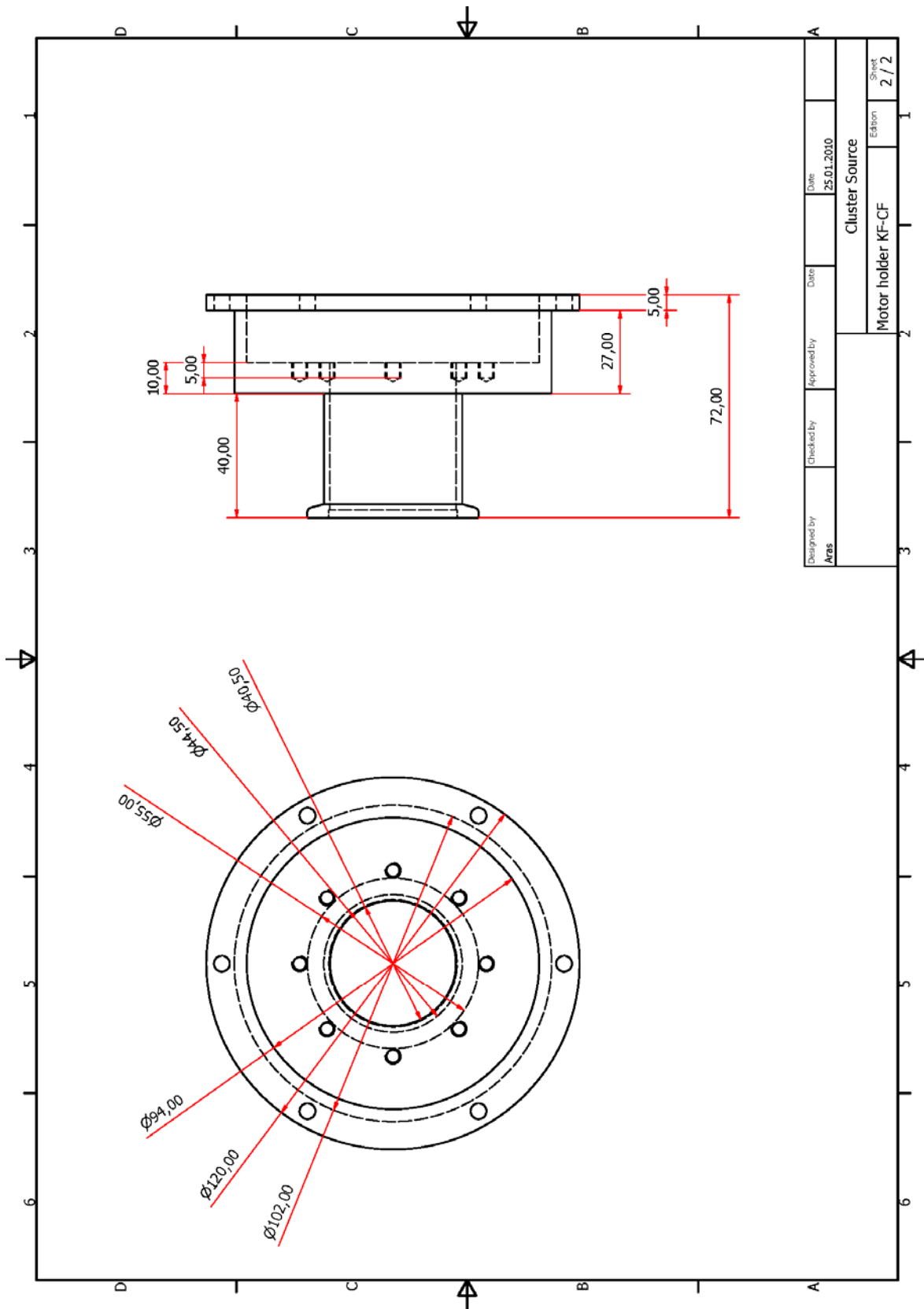


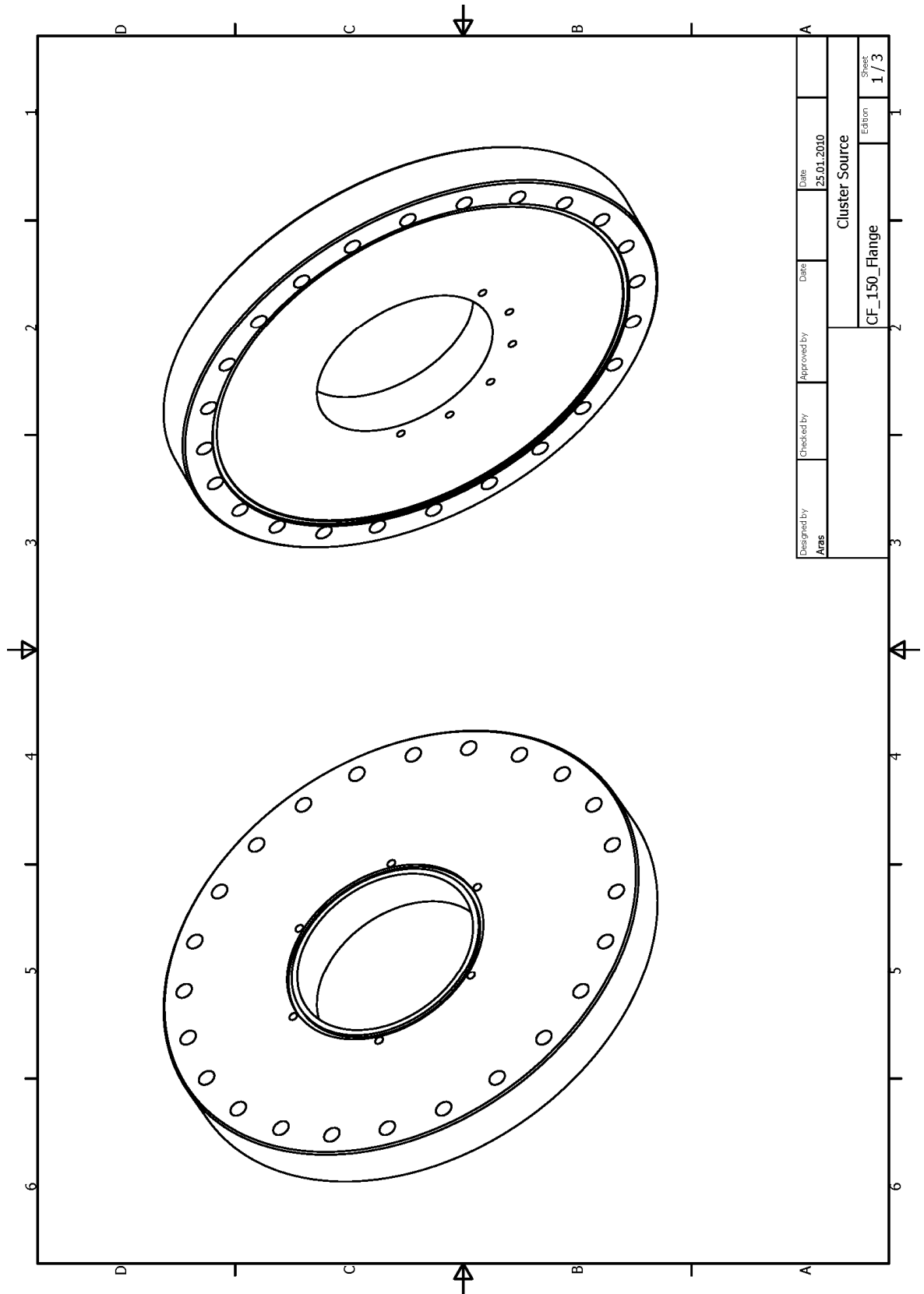
Designed by	Aras	Checked by		Approved by		Date	24.01.2010	
							Sheet	11 / 11
							Edition	1

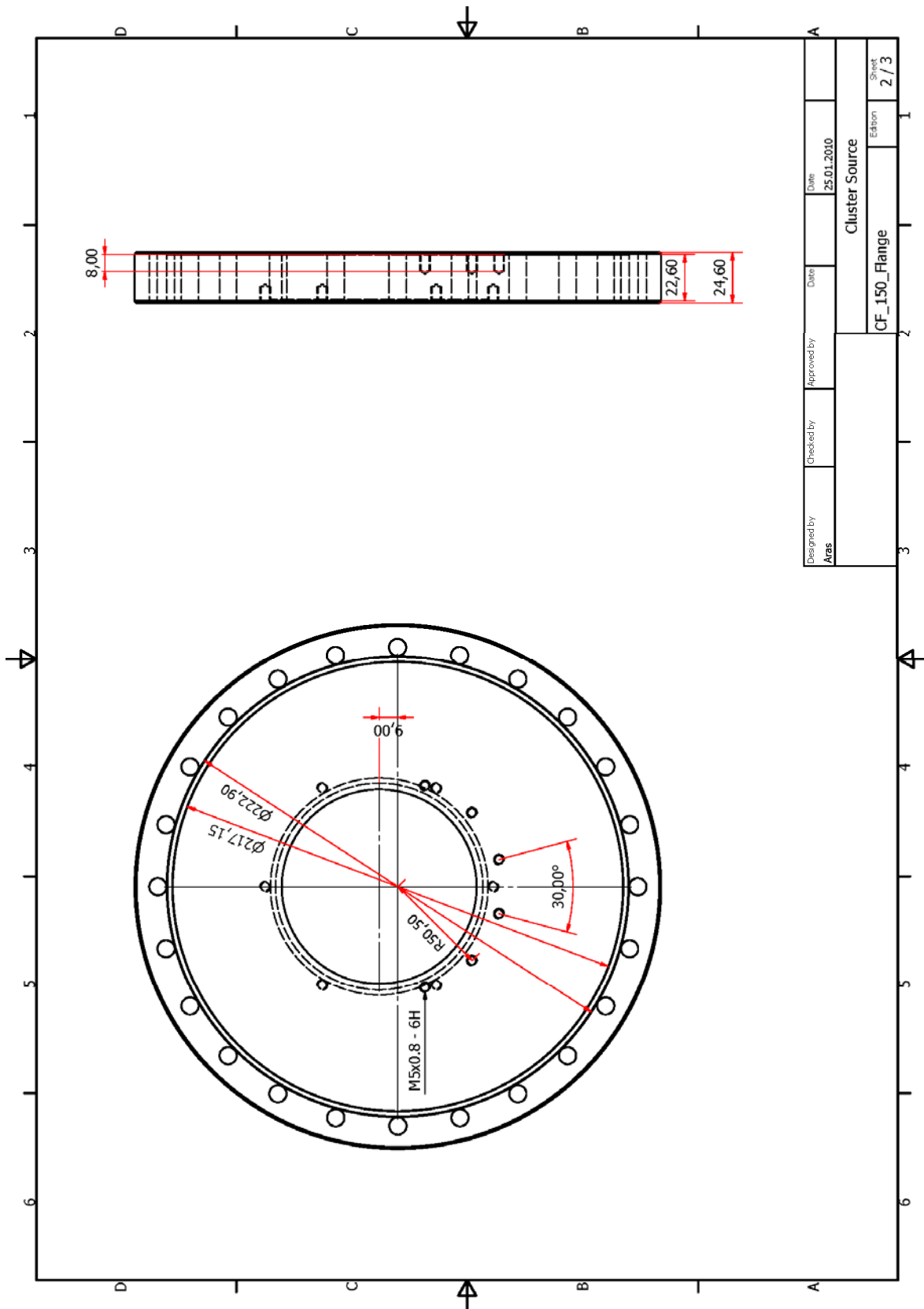
## A2. Cluster source



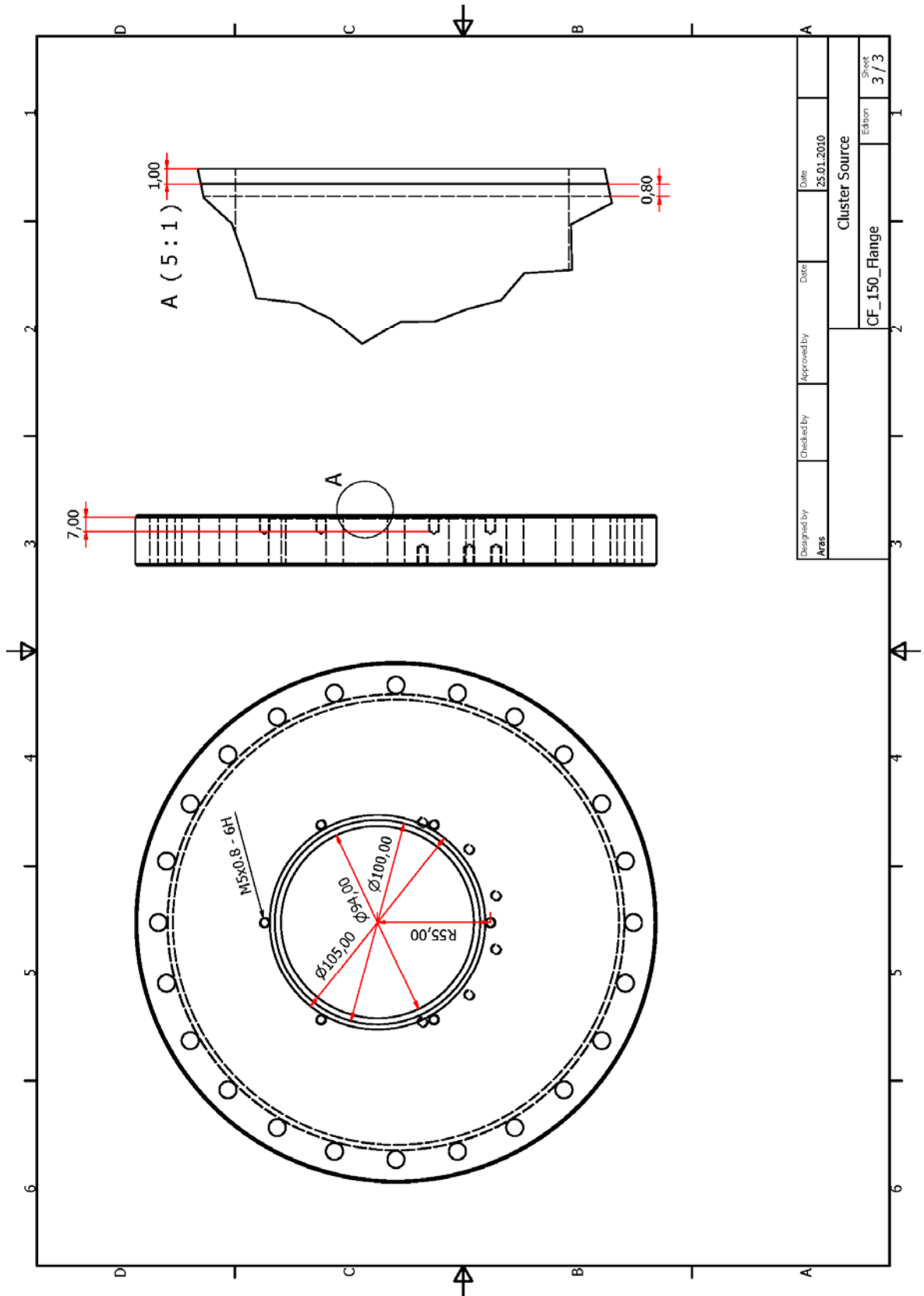




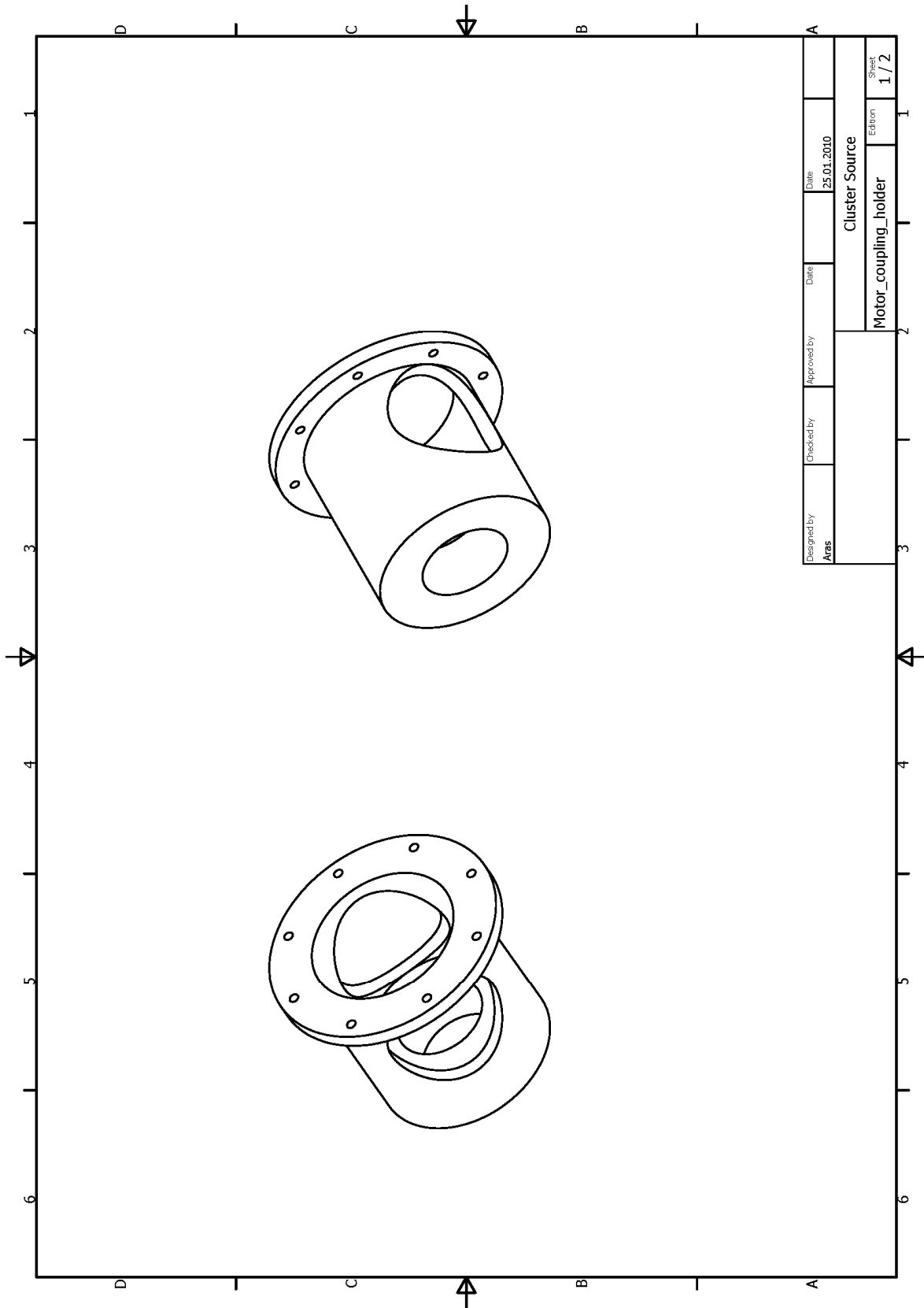




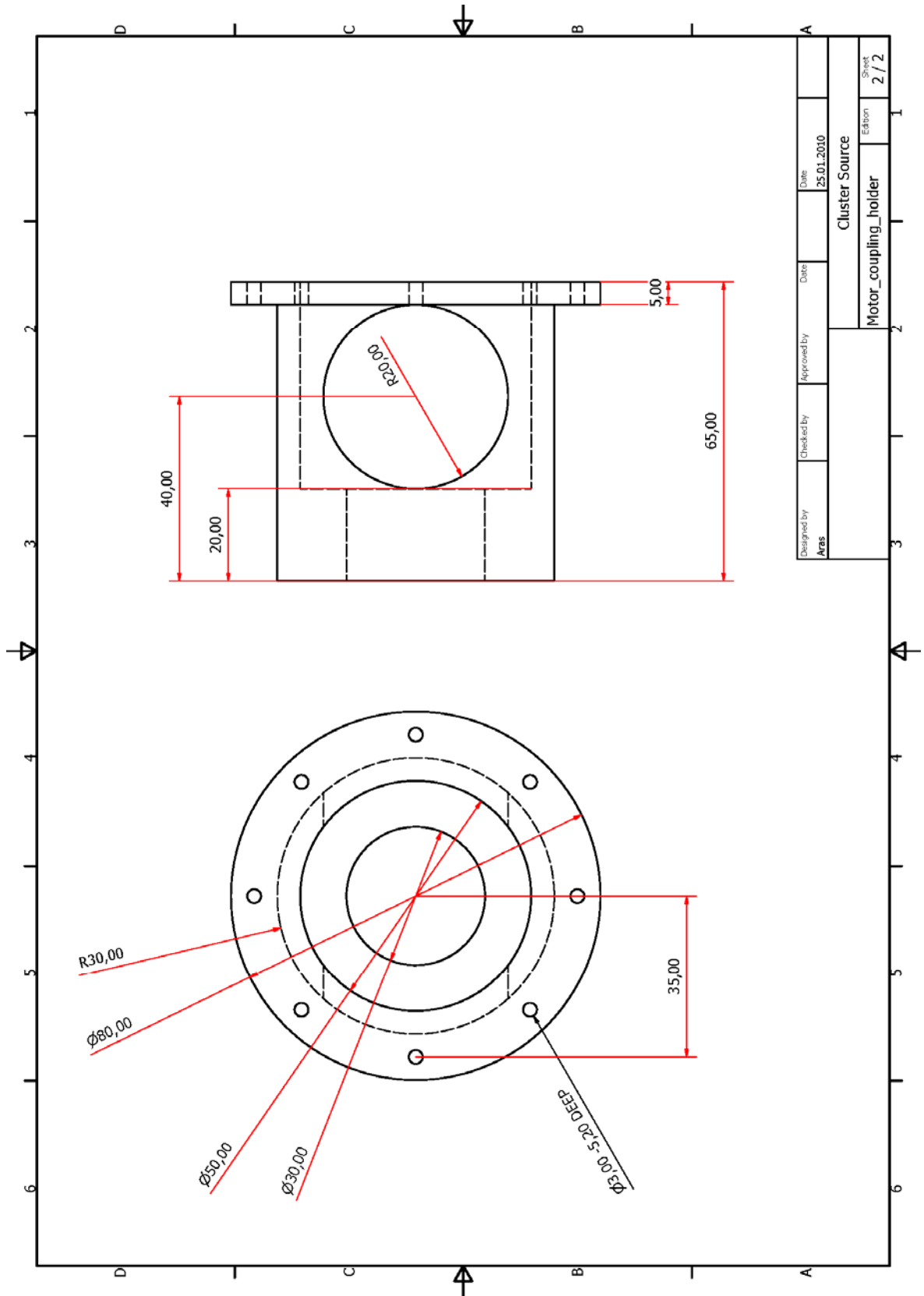


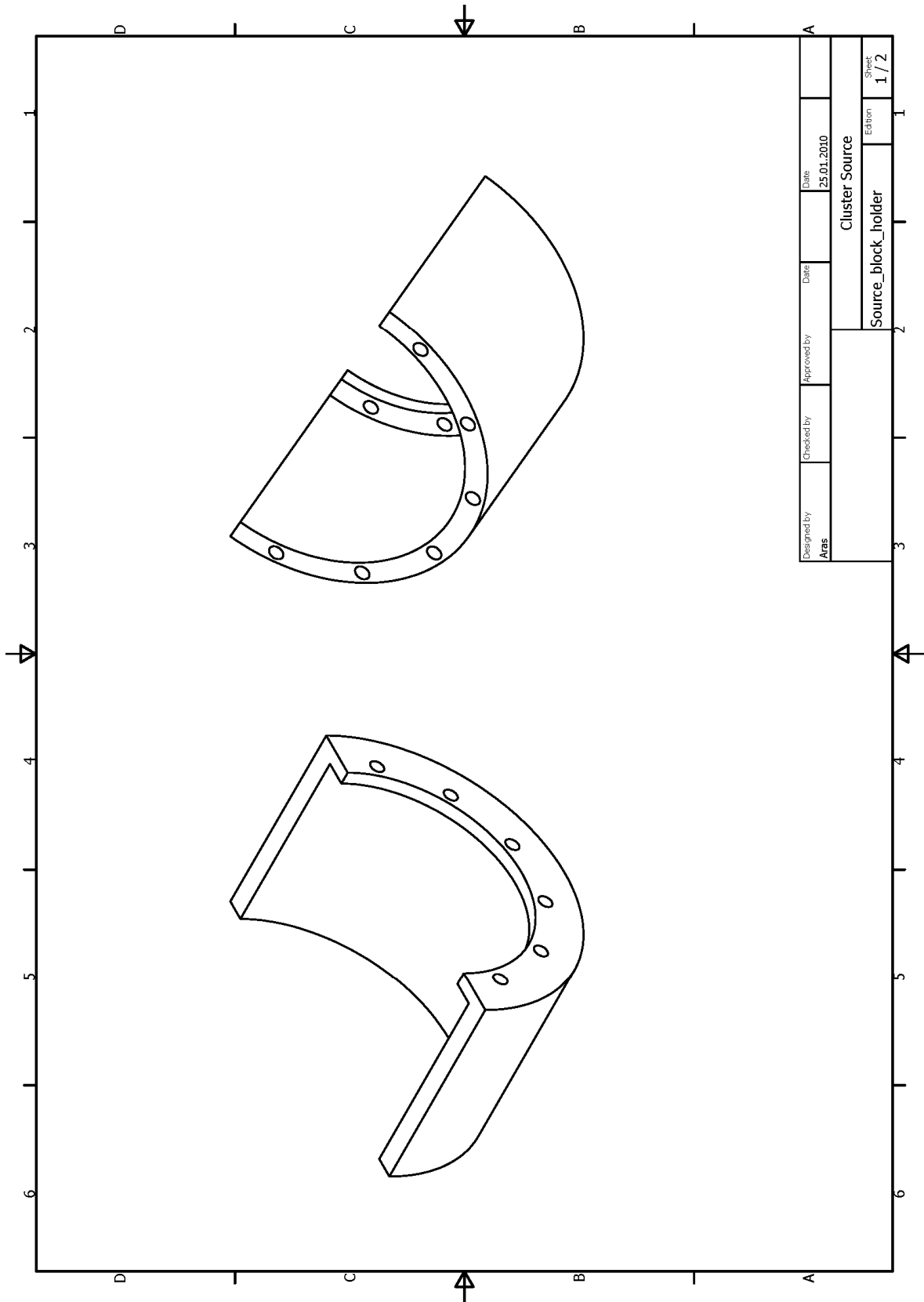


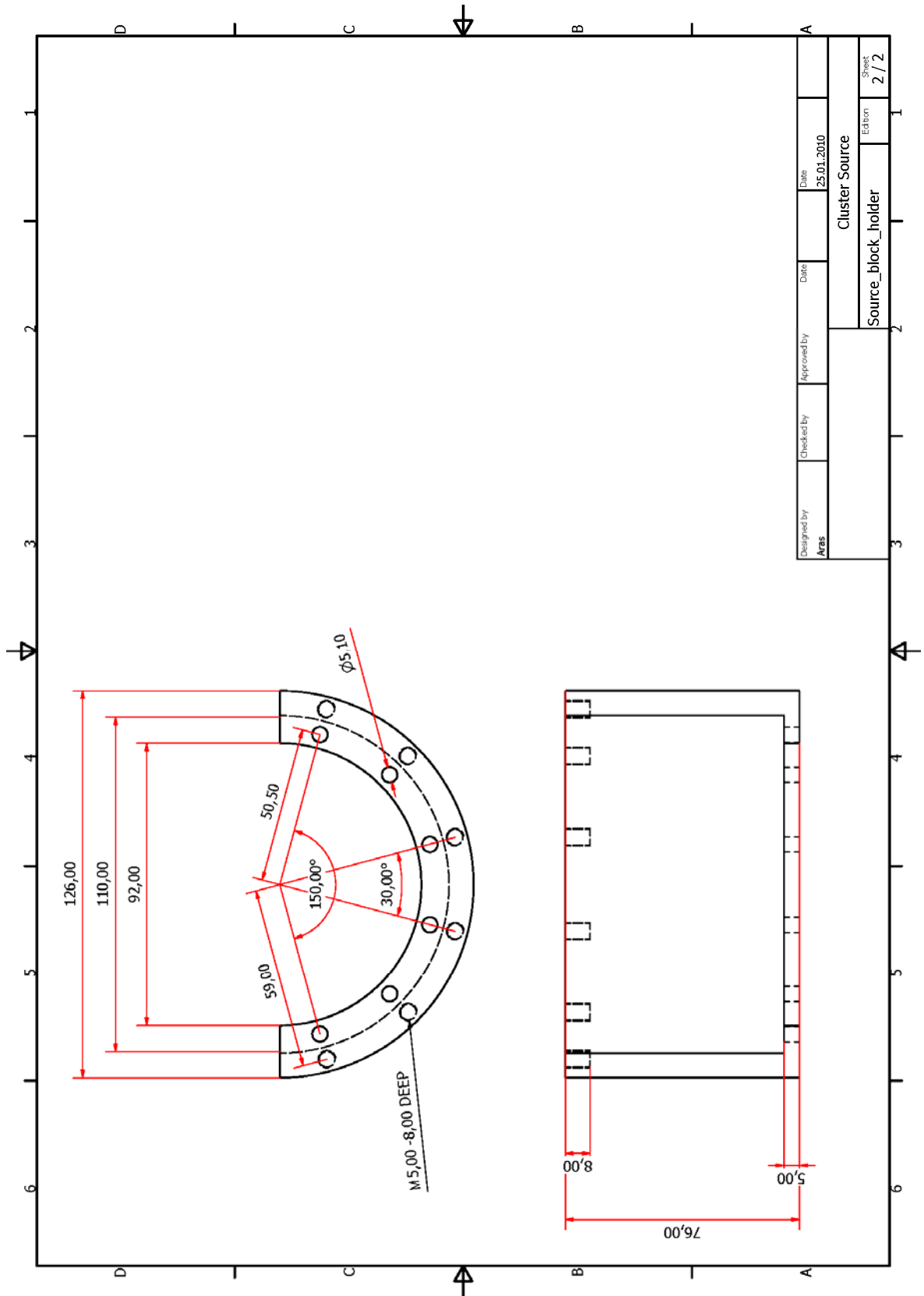
Designed by	Aras	Checked by	Approved by	Date	25.01.2010
Cluster Source				CF_150_Flange	3 / 3

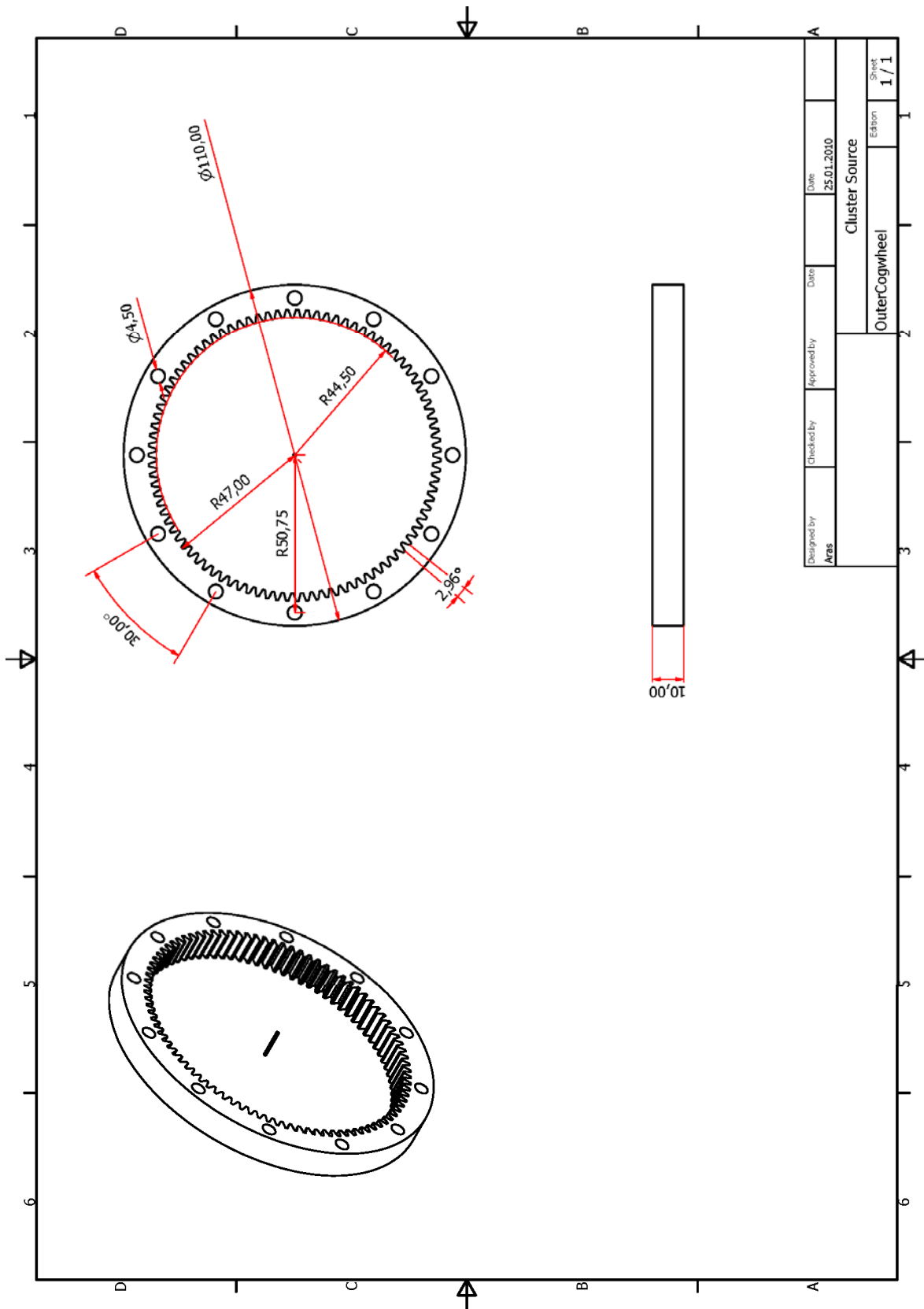


Designed by Anas	Checked by	Approved by	Date	Date	25.01.2010
Cluster Source			Motor_coupling_holder		
			Edition		
			Sheet		
			1 / 2		

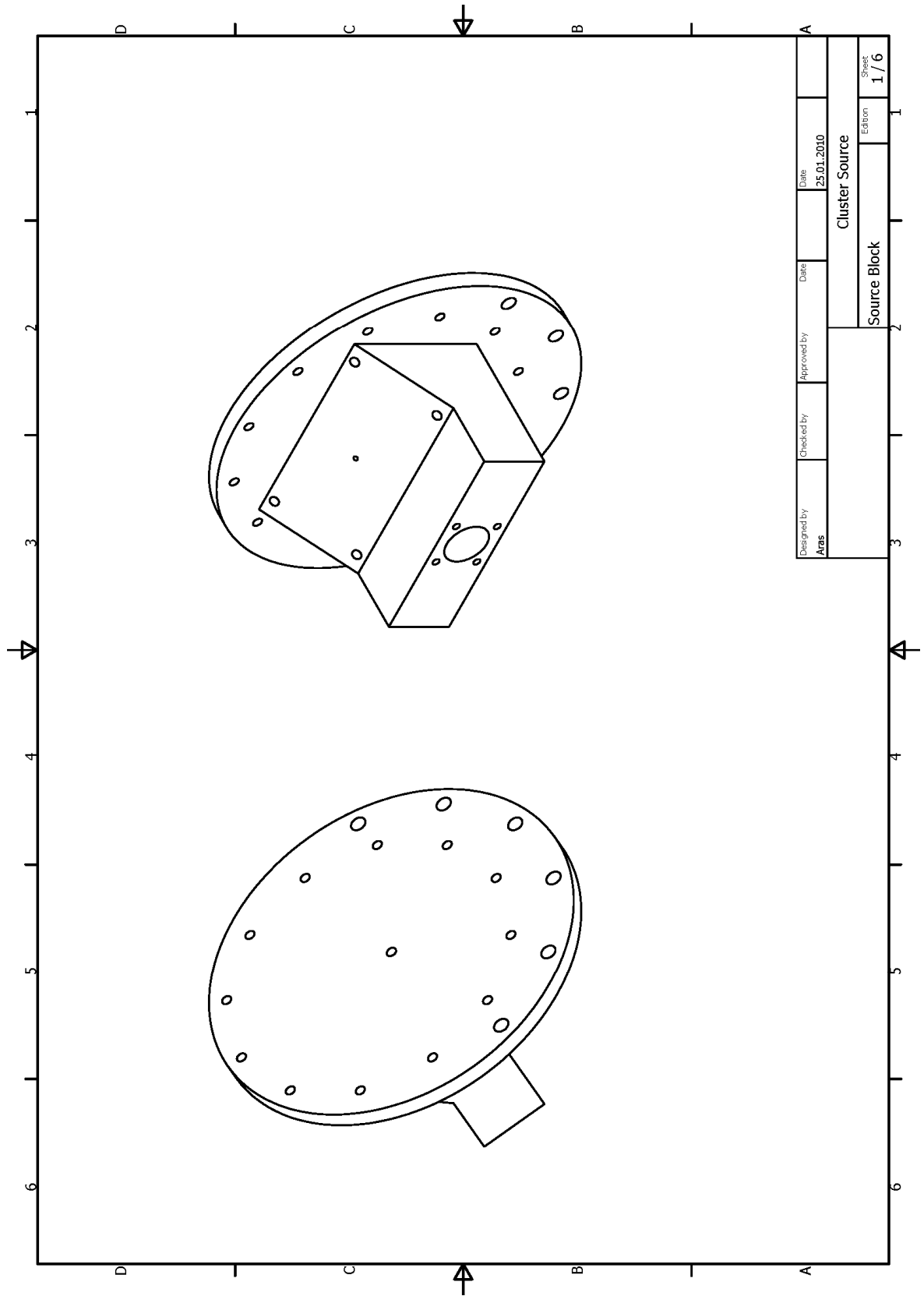


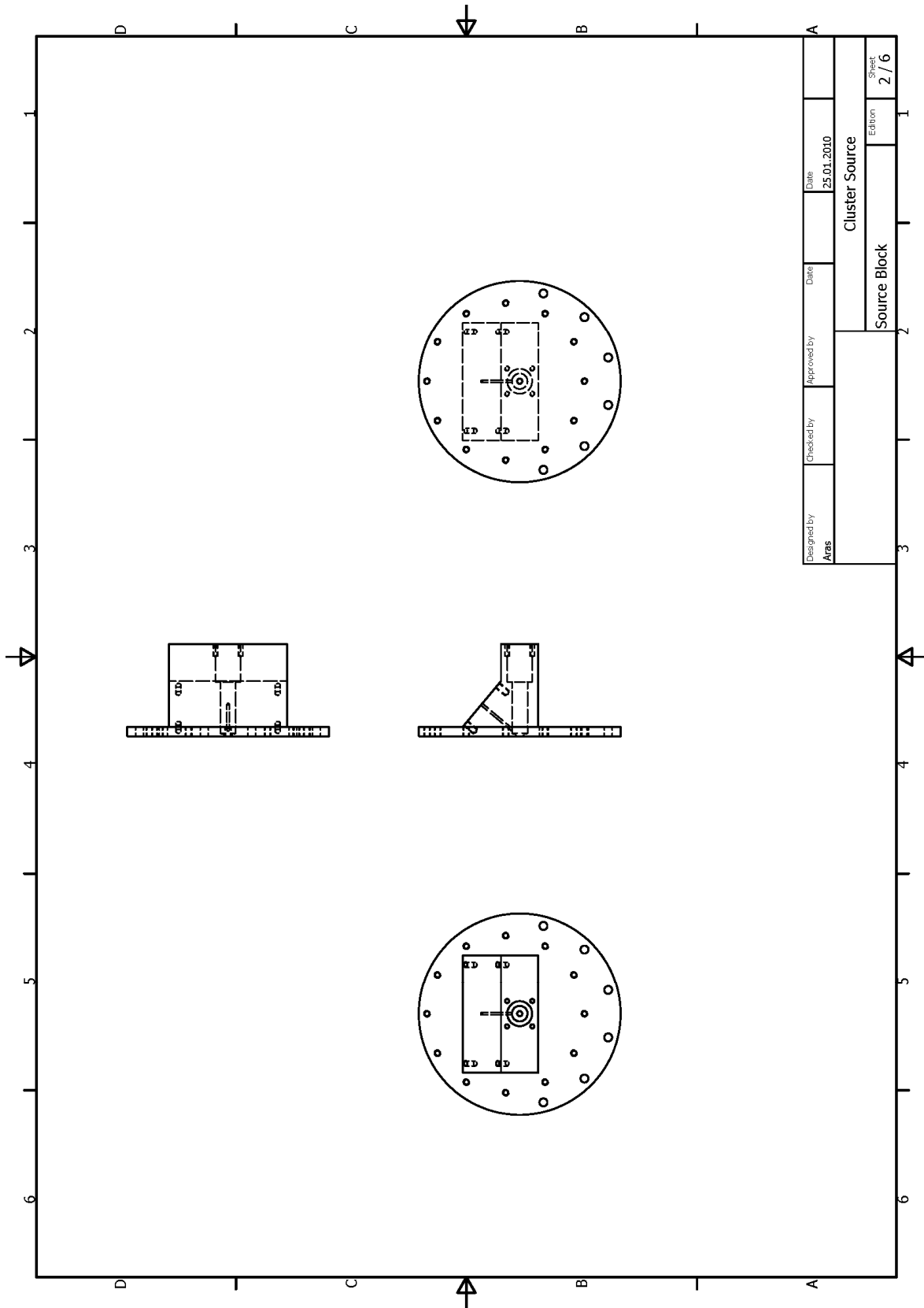




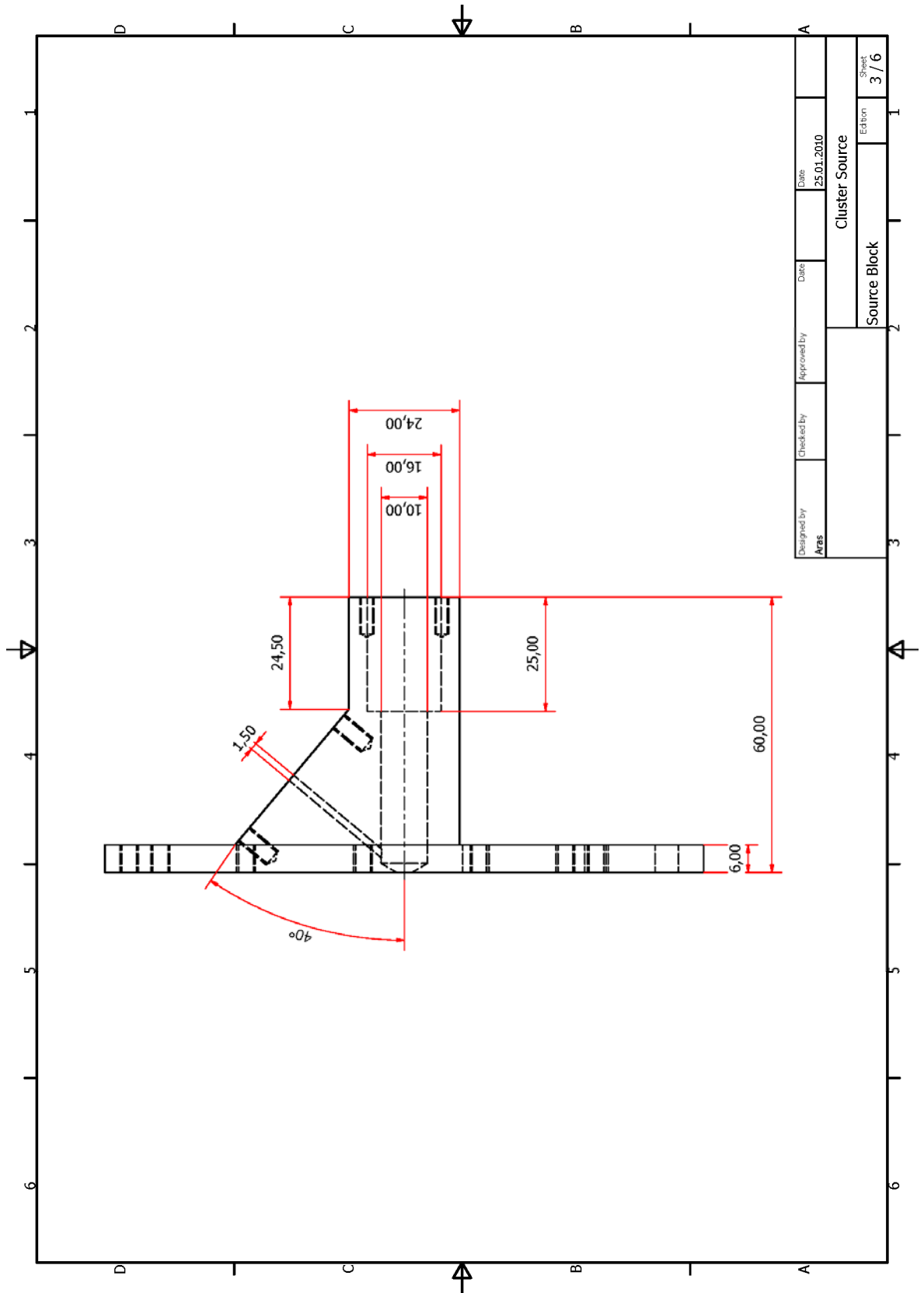


Designed by Aras	Checked by	Approved by	Date 25.01.2010	Sheet 1 / 1
OuterCogwheel			Edition	
Cluster Source				

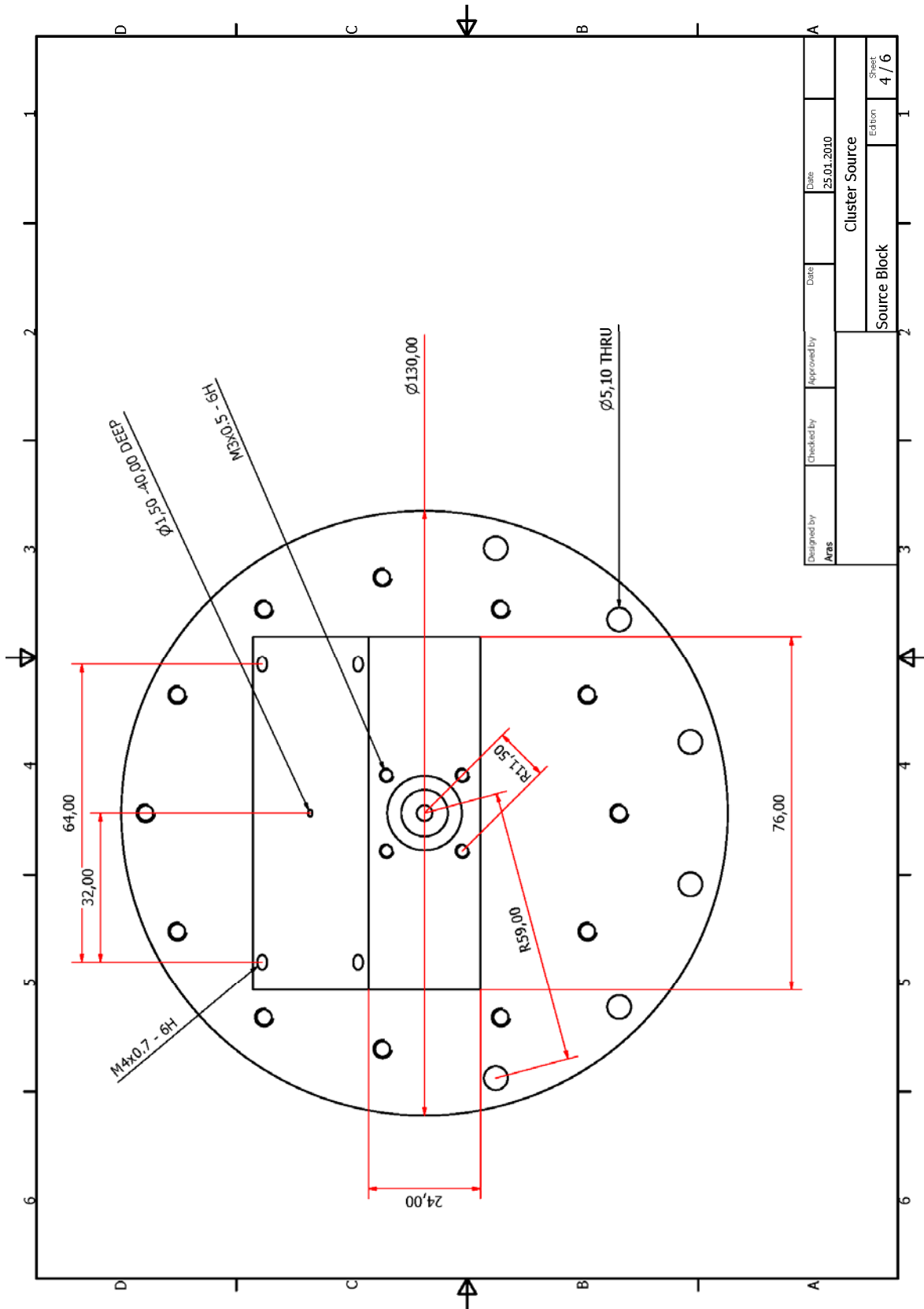




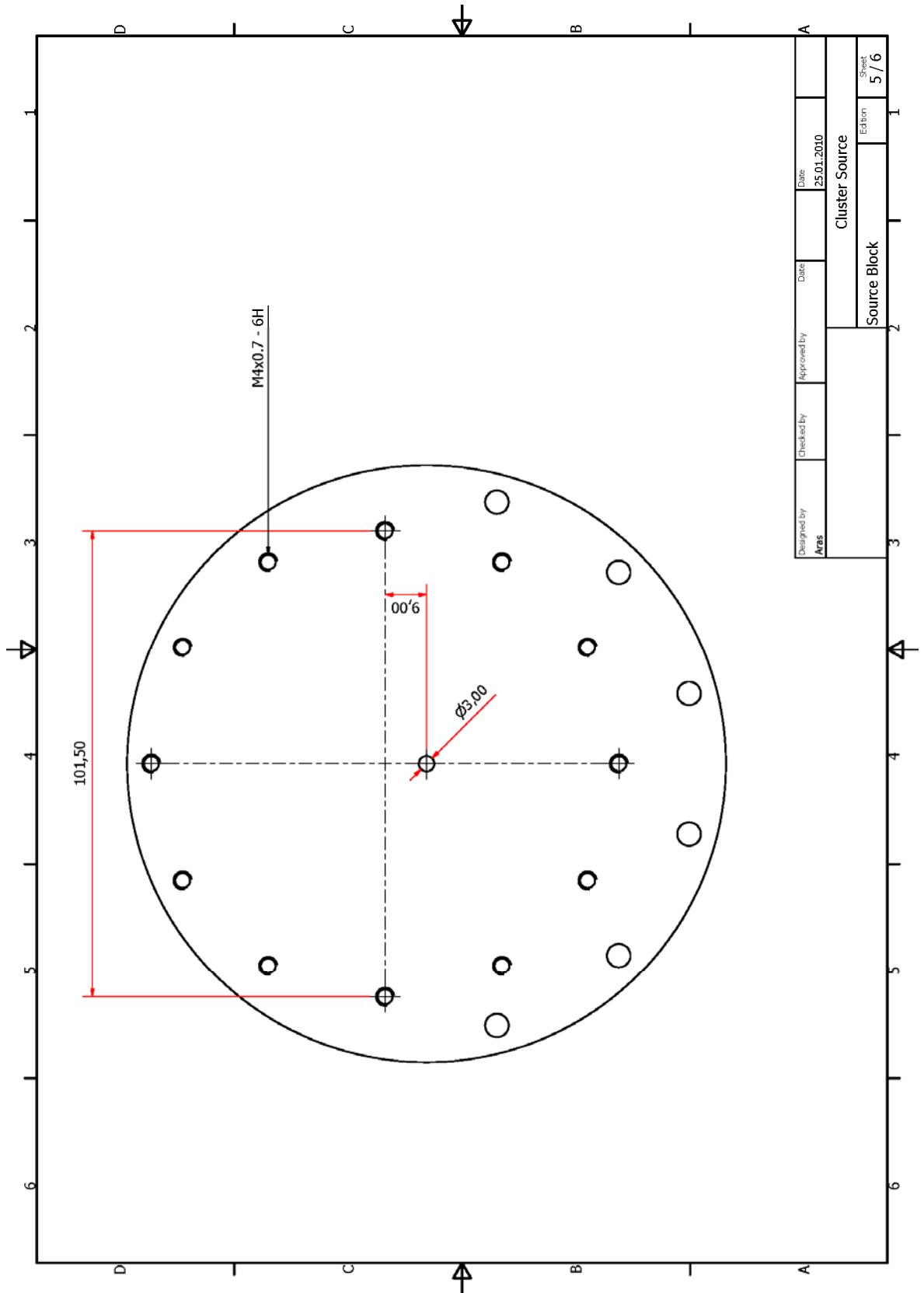




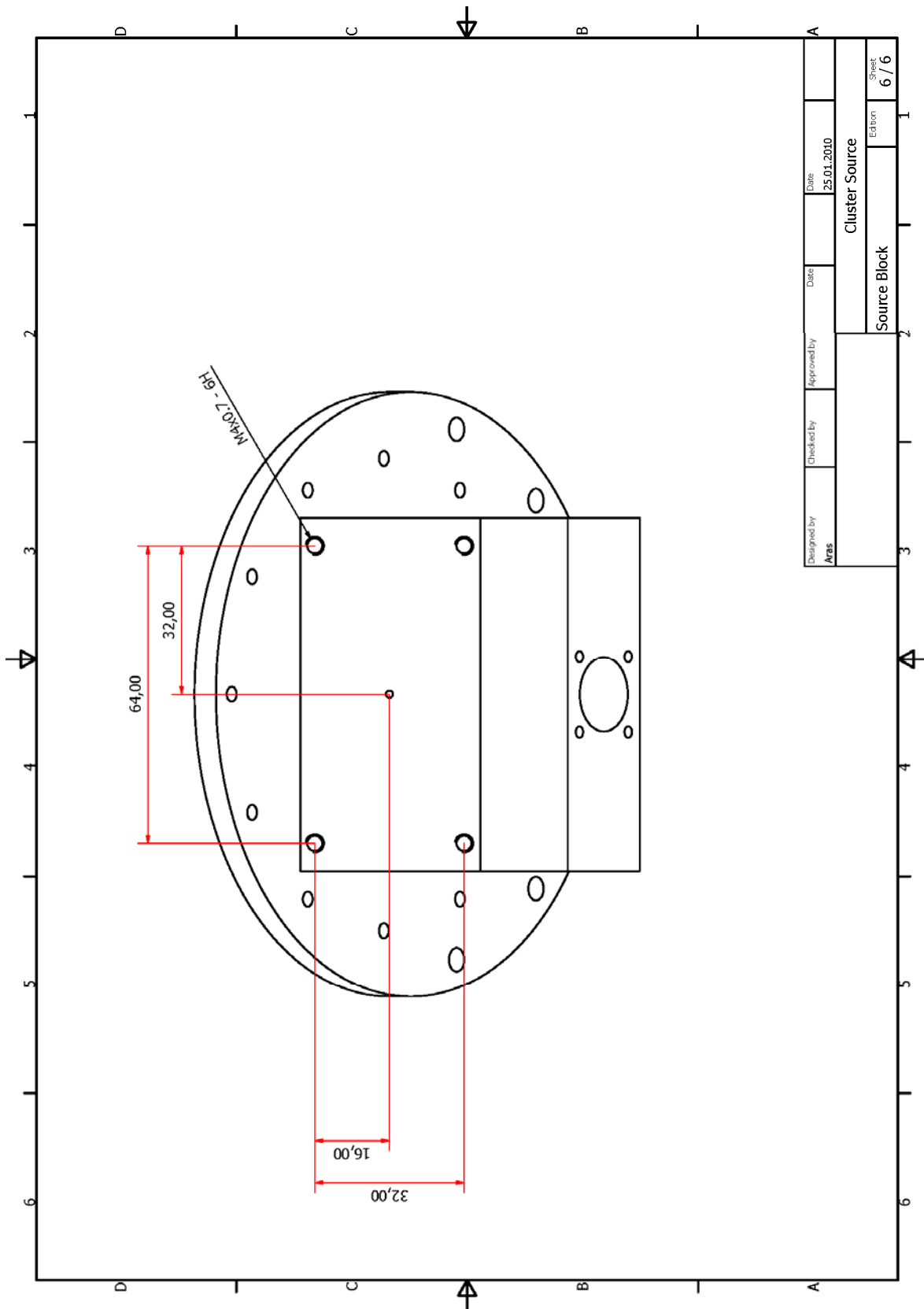
Designed by Aras	Checked by	Approved by	Date 25.01.2010
Source Block			Cluster Source
Edition			Sheet 3 / 6

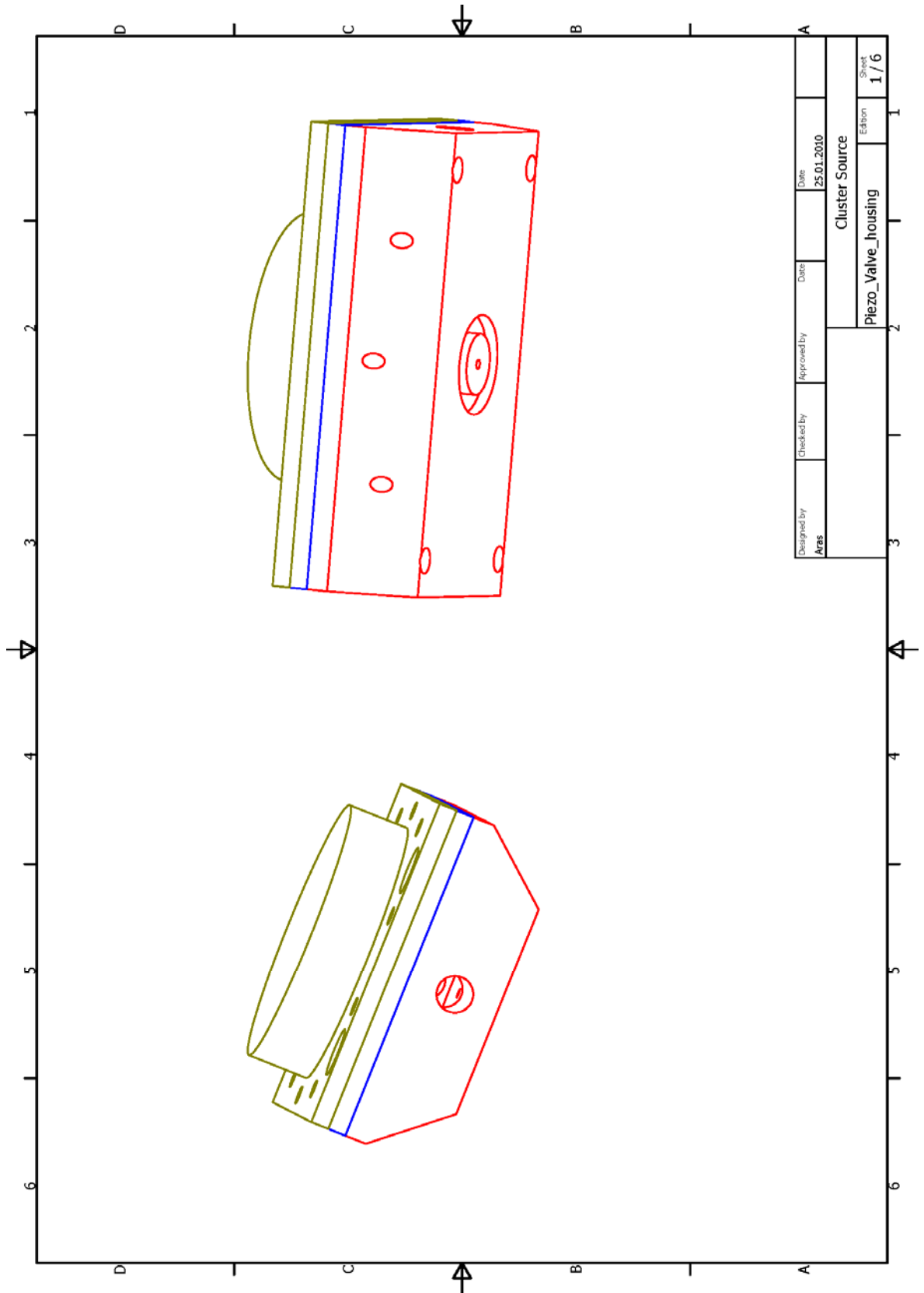


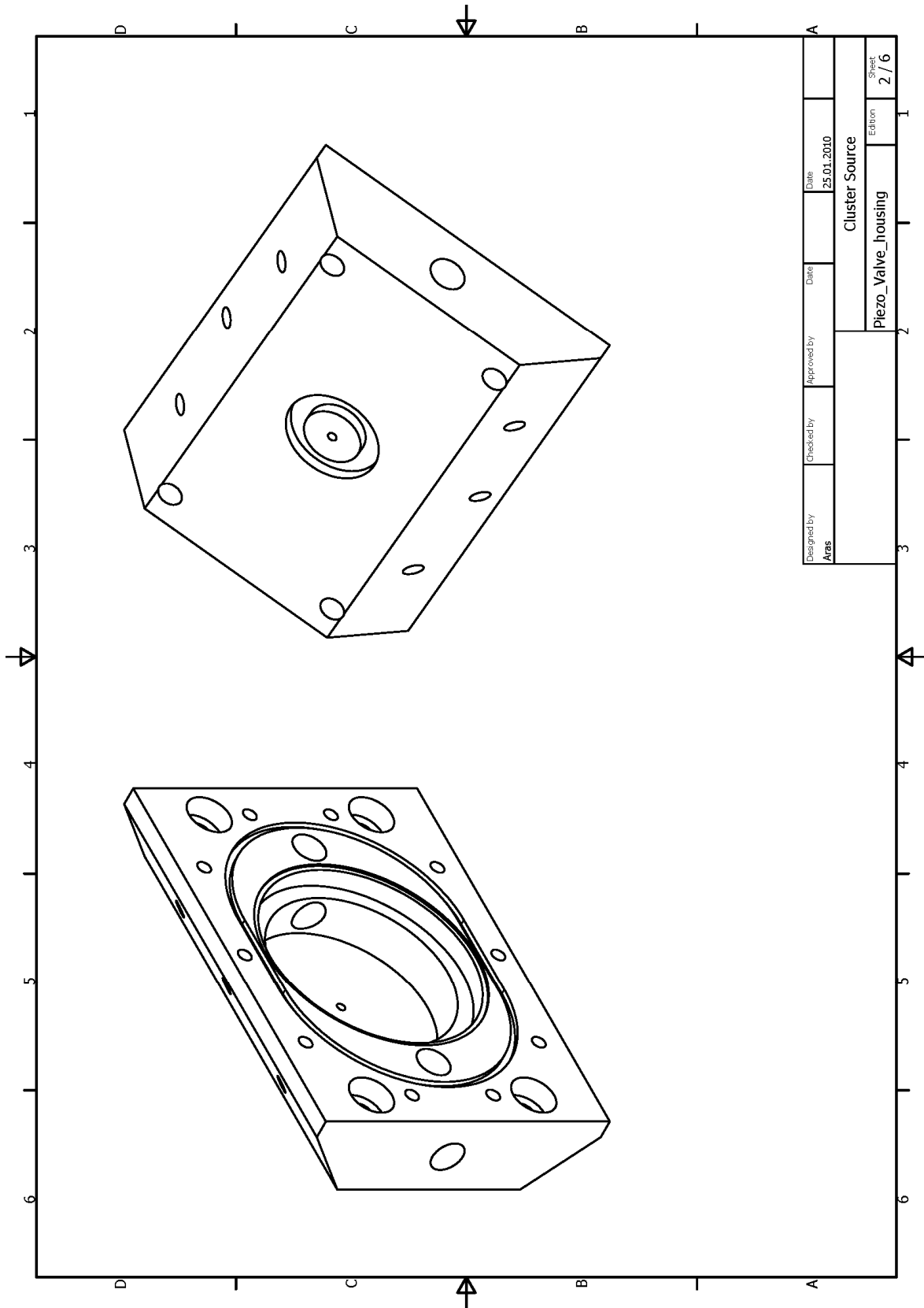
Designed by Aras	Checked by	Approved by	Date	Date	25.01.2010
Source Block			Cluster Source		
Edition			Sheet 4 / 6		

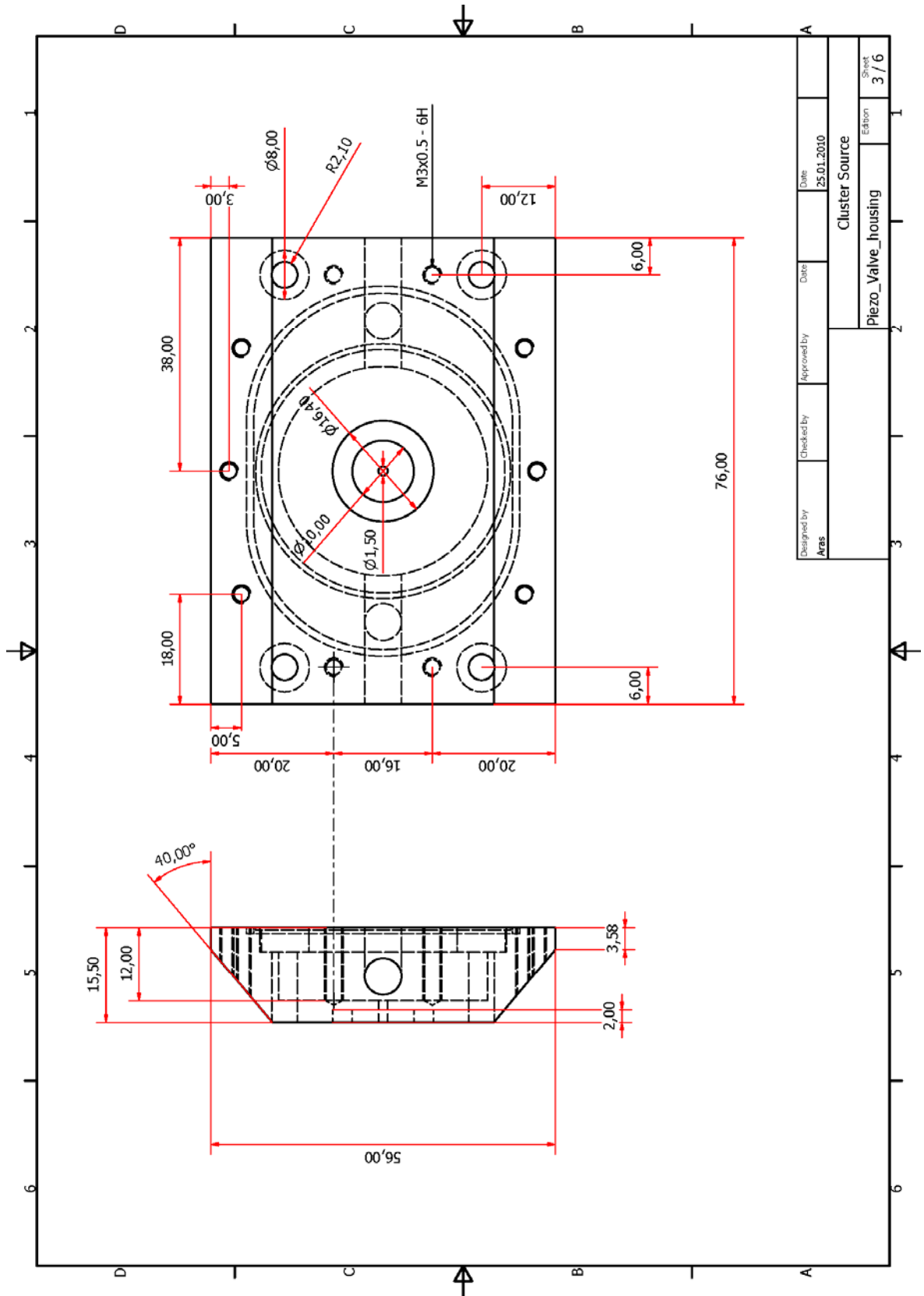


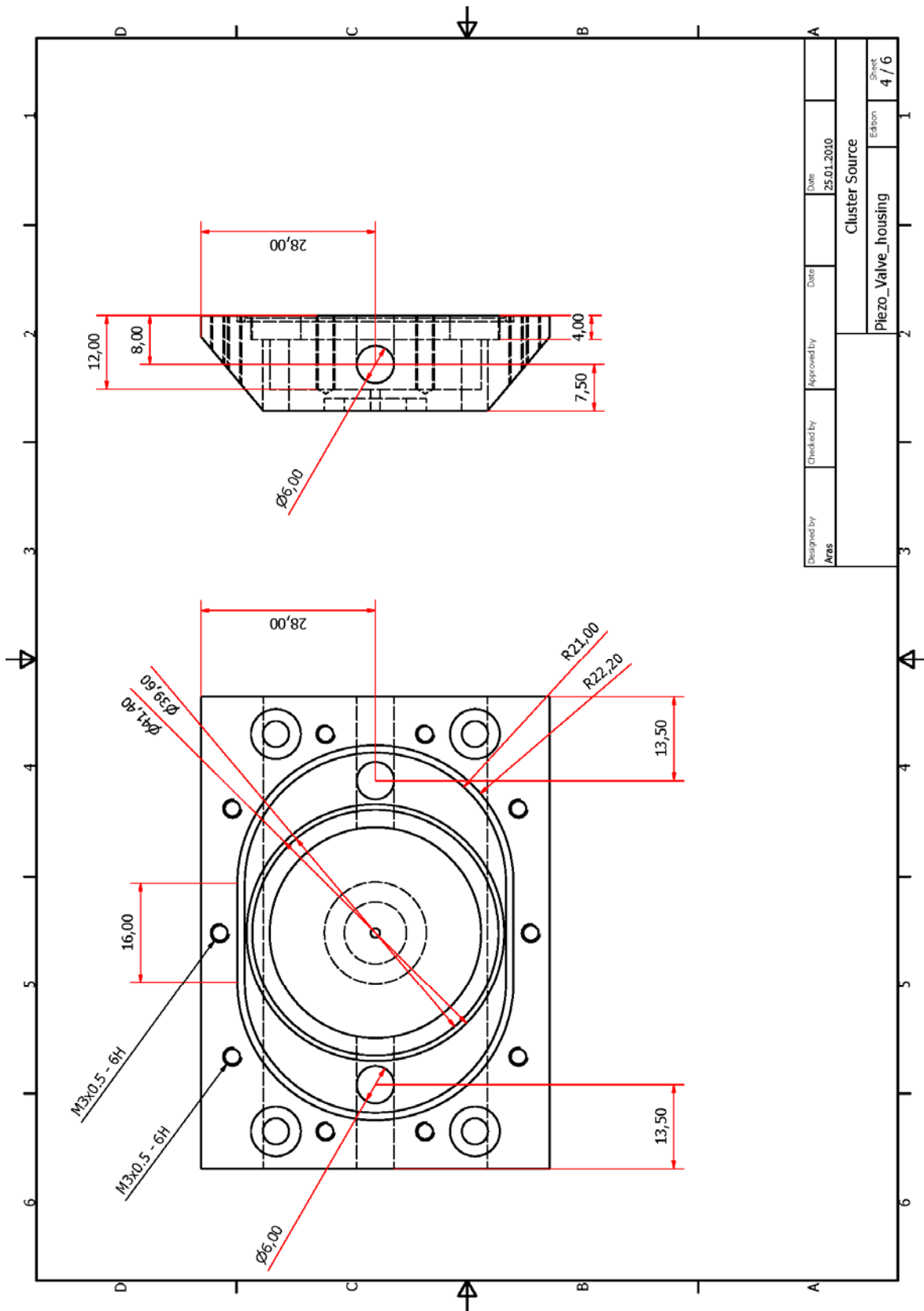
Designed by Aras	Checked by	Approved by	Date 25.01.2010
Source Block			Cluster Source
Edition			Sheet 5 / 6



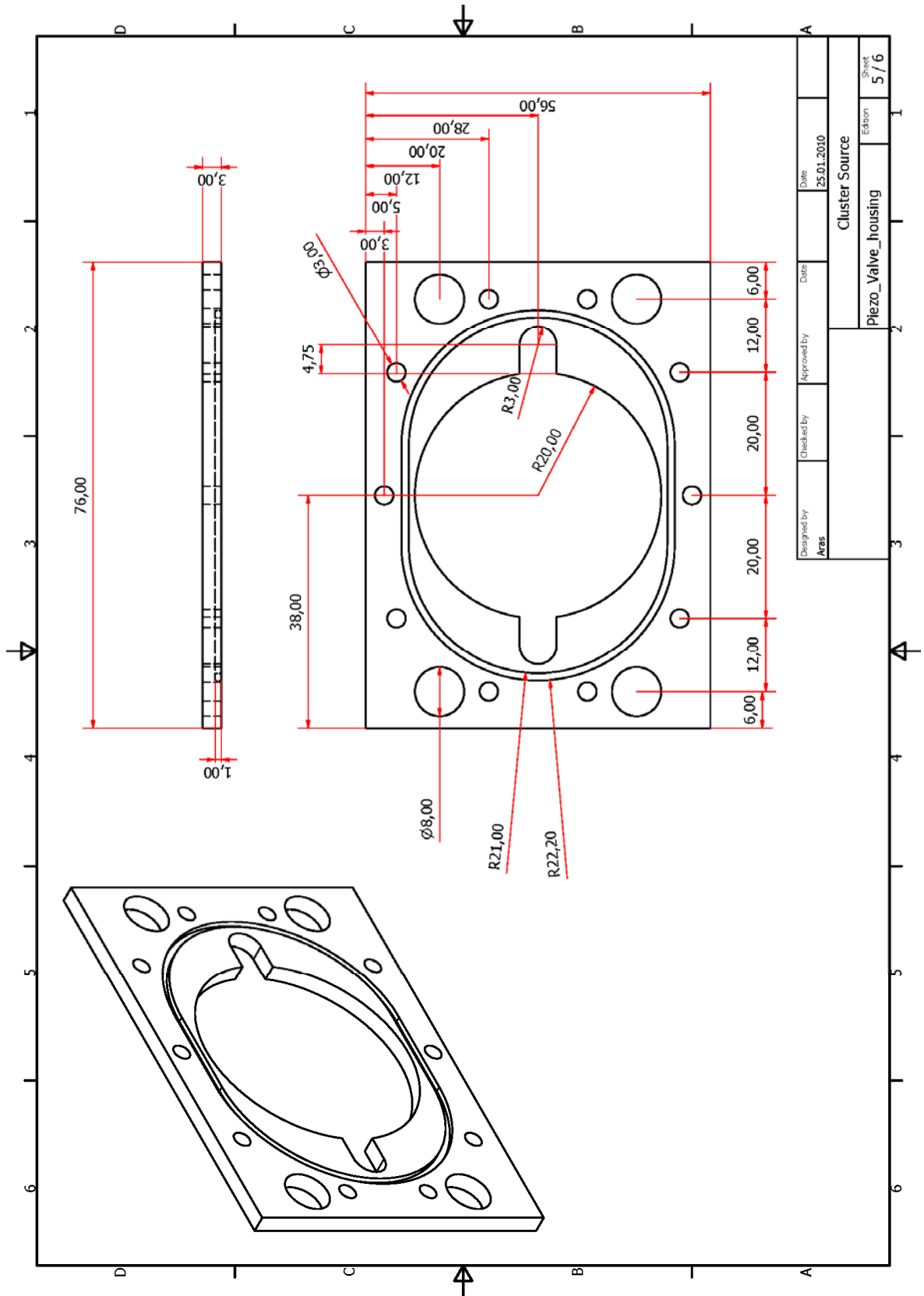


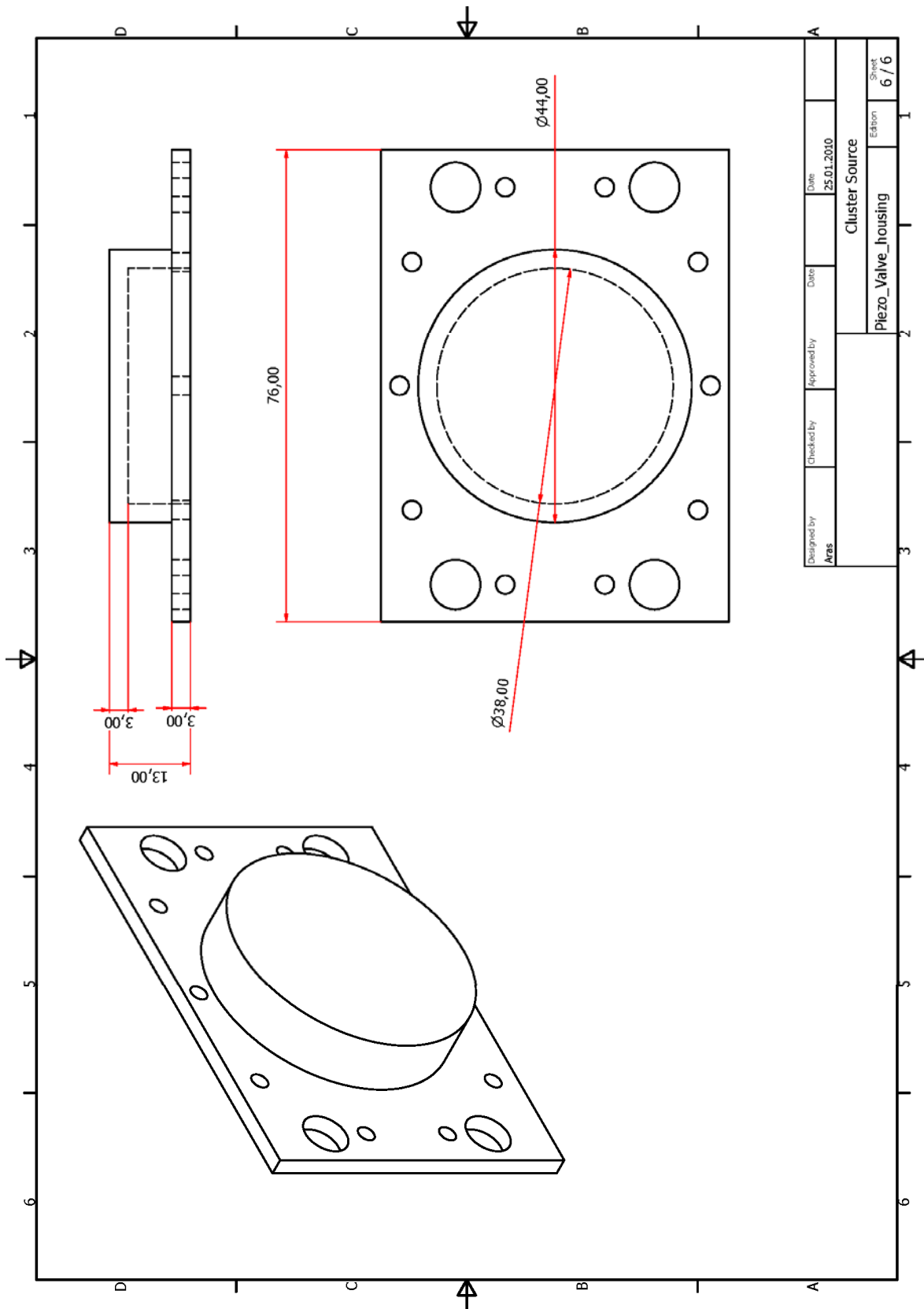




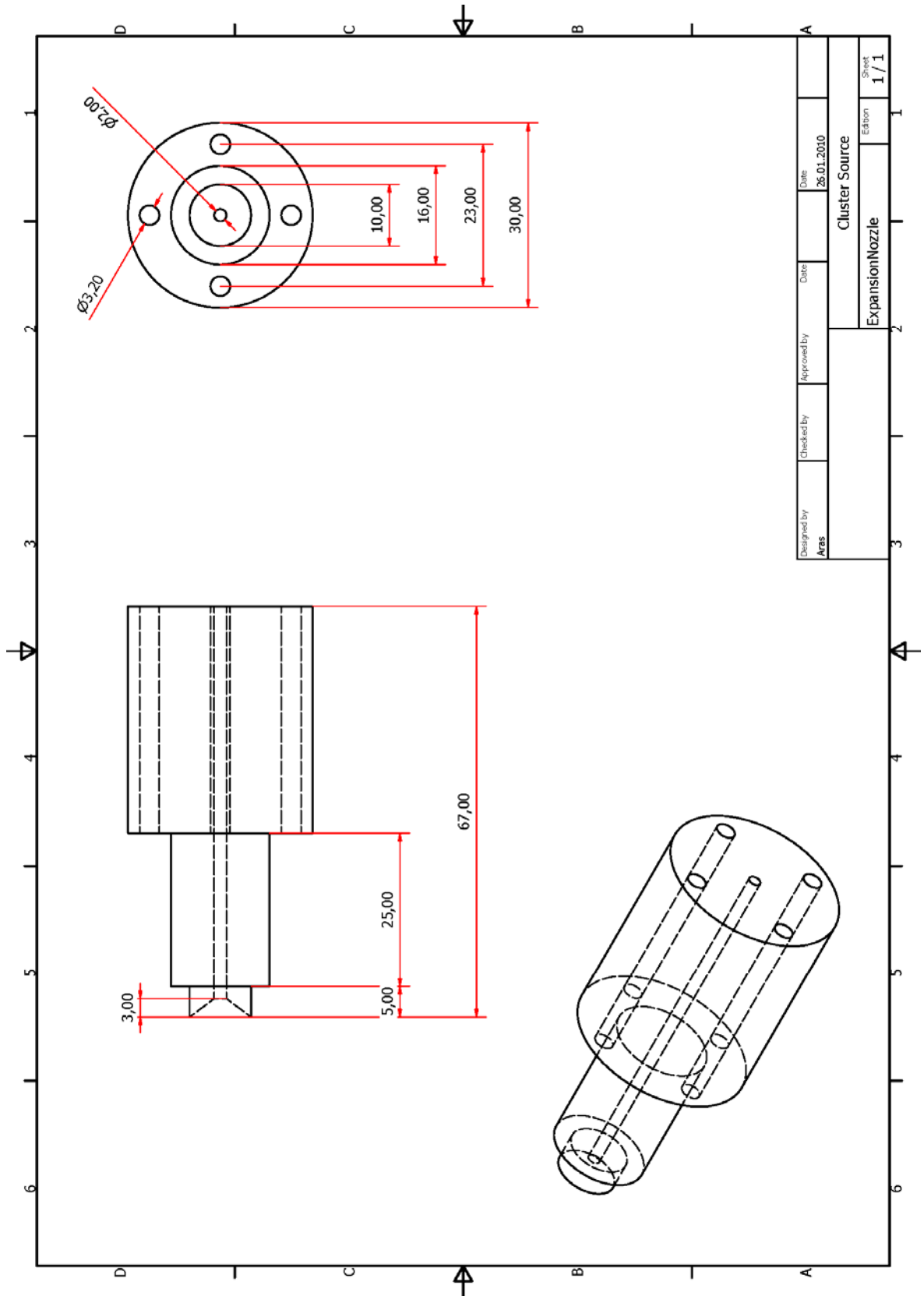




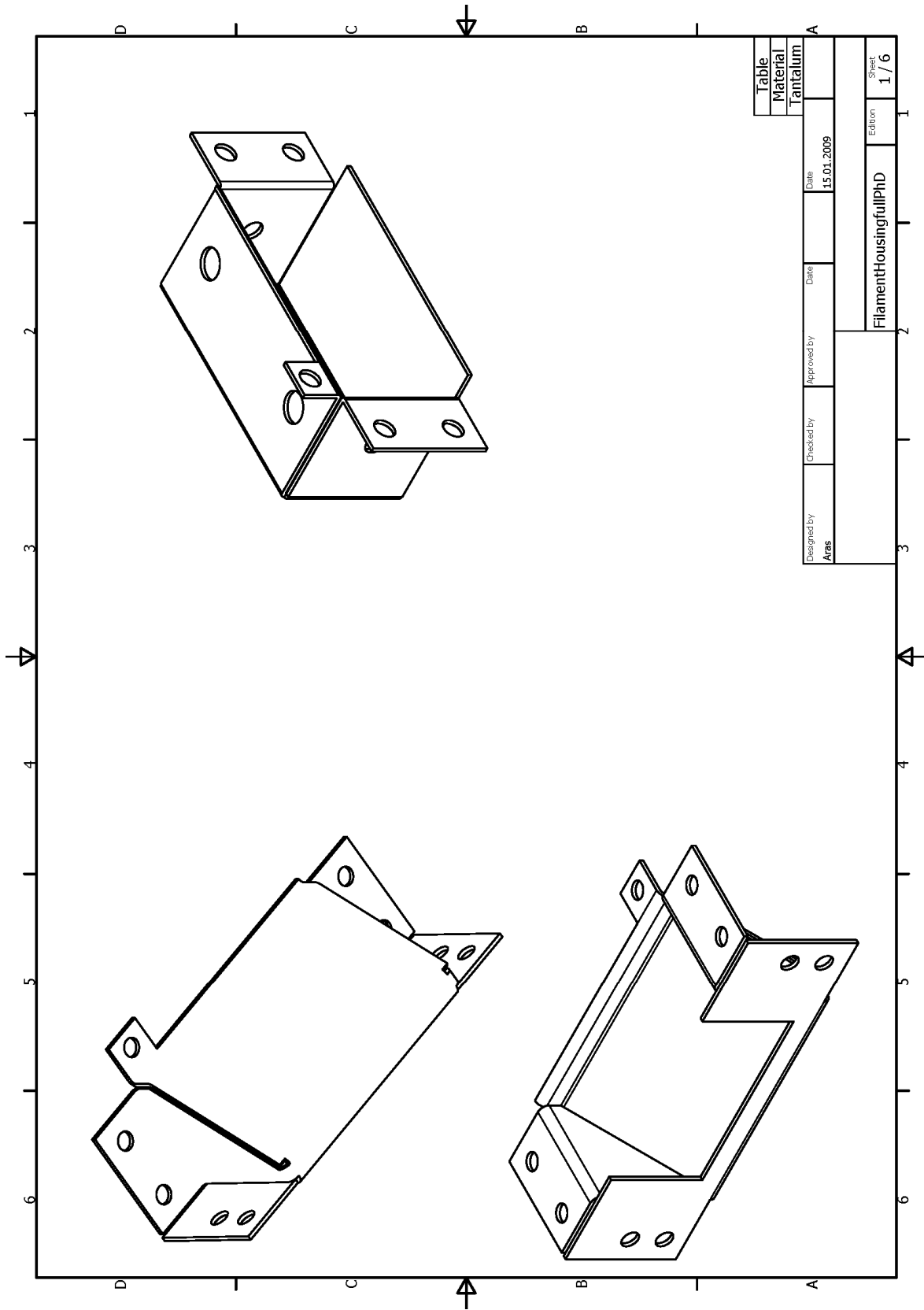


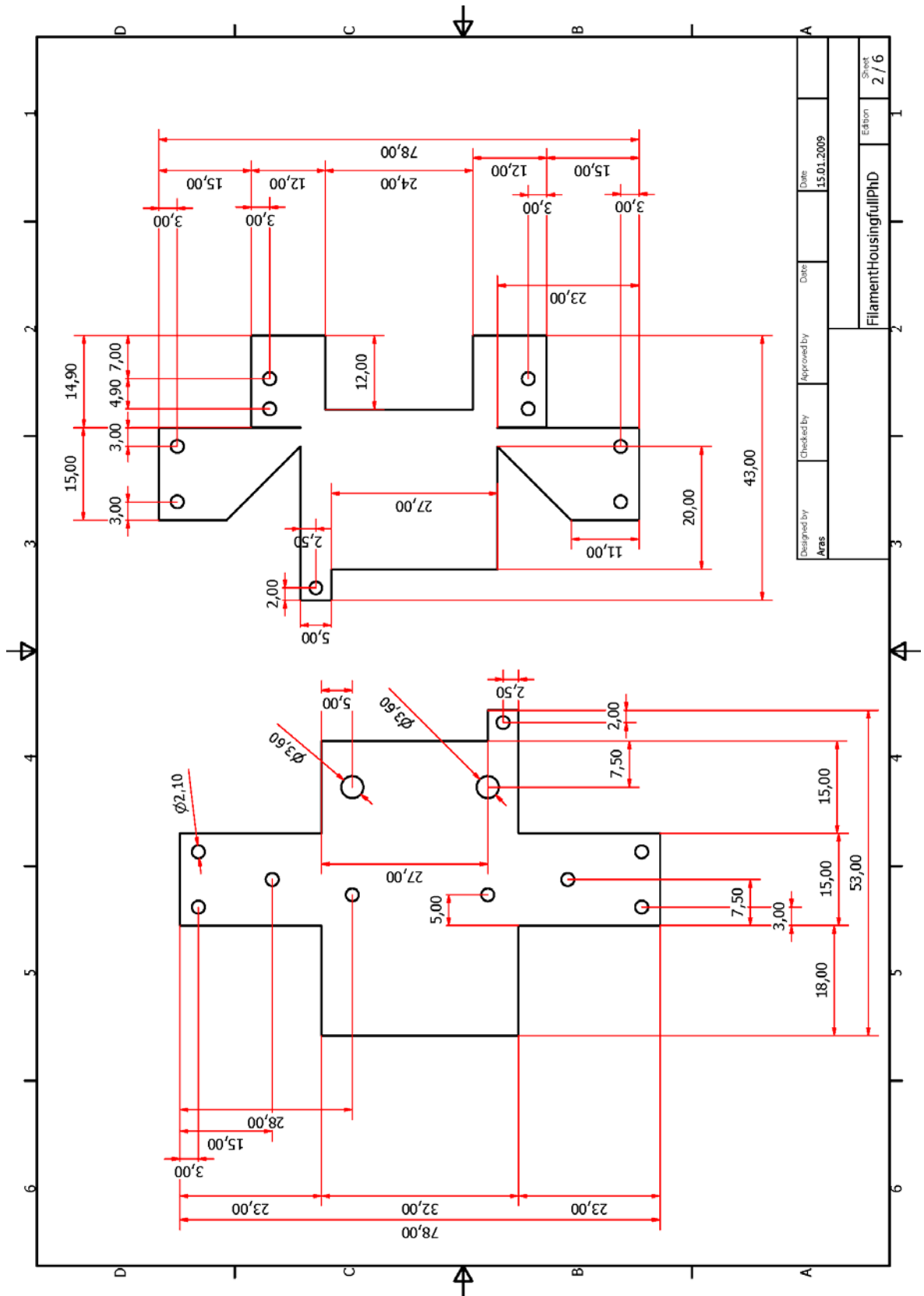


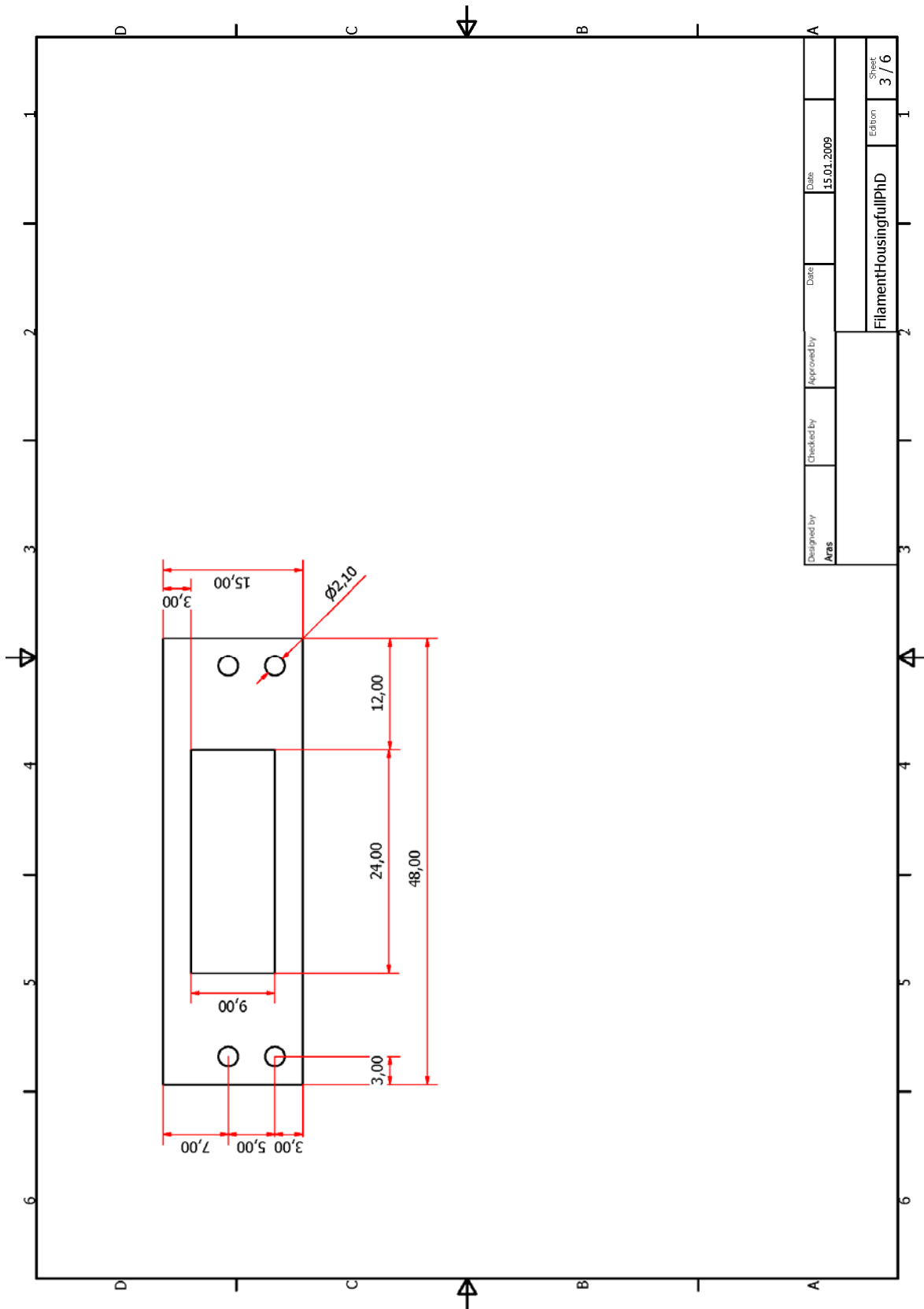
Designed by Aras	Checked by	Approved by	Date 25.01.2010	Sheet 6 / 6
Cluster Source				Edition
Piezo_Valve_housing				6 / 6

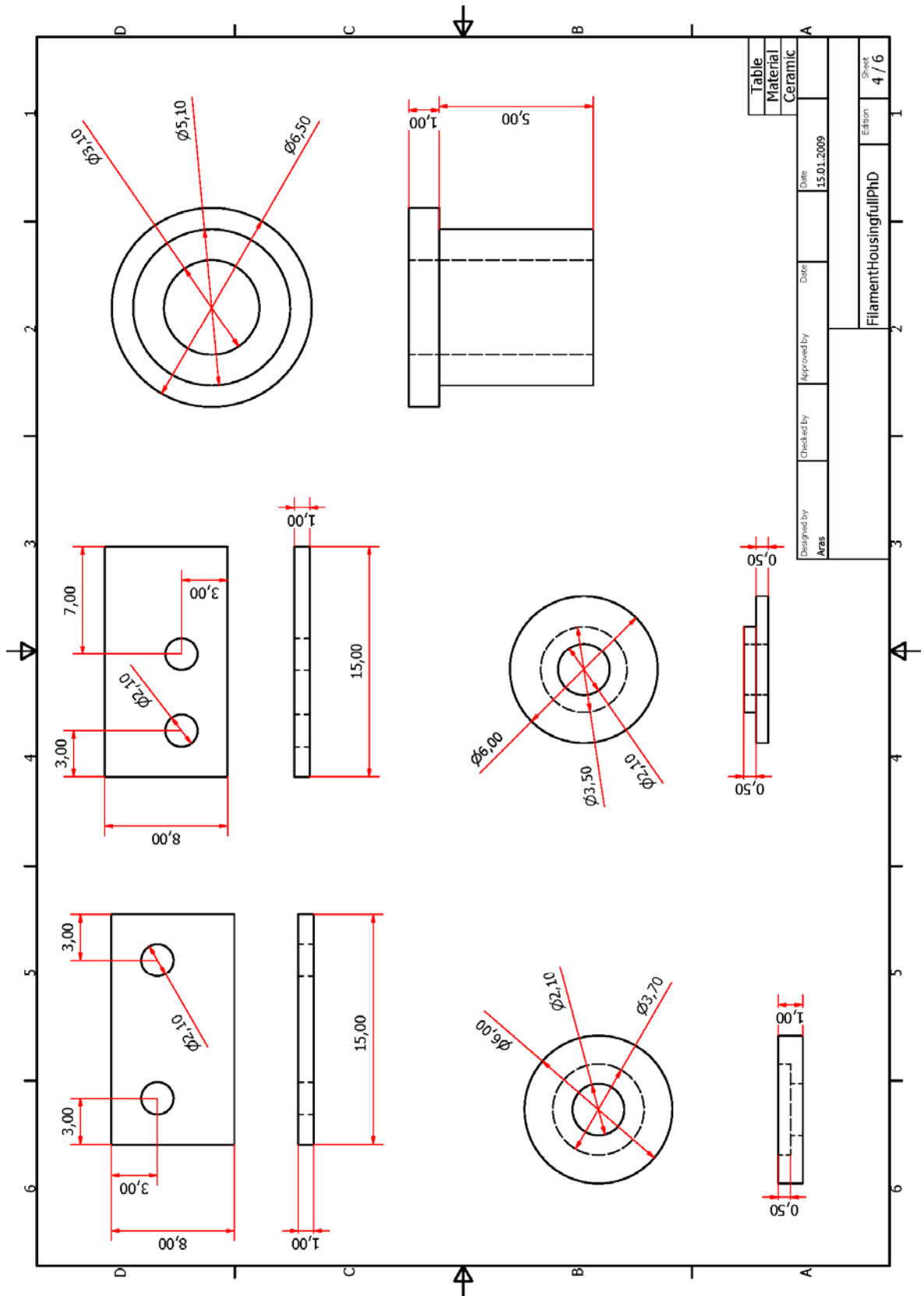


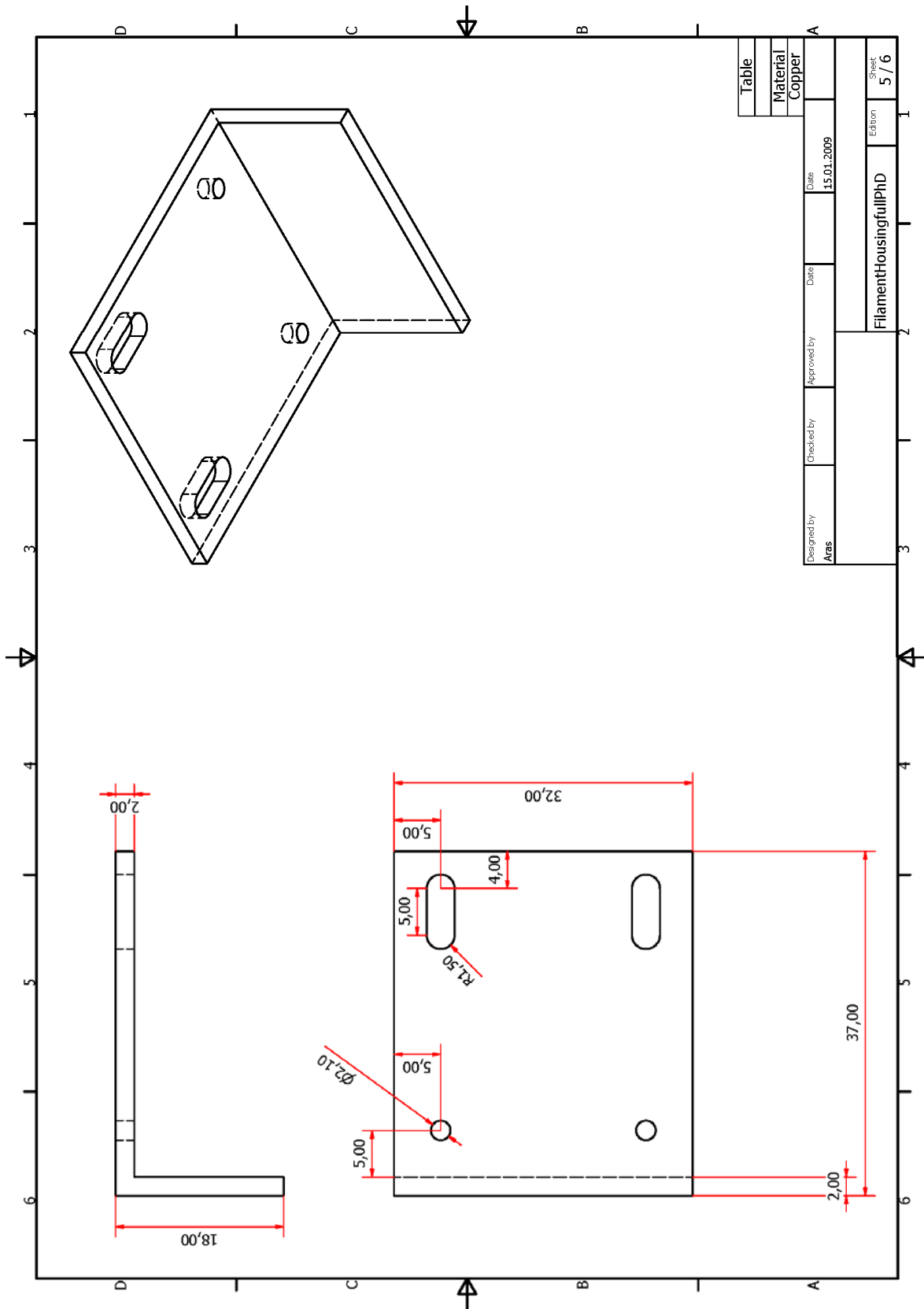
**A3. Electron source**



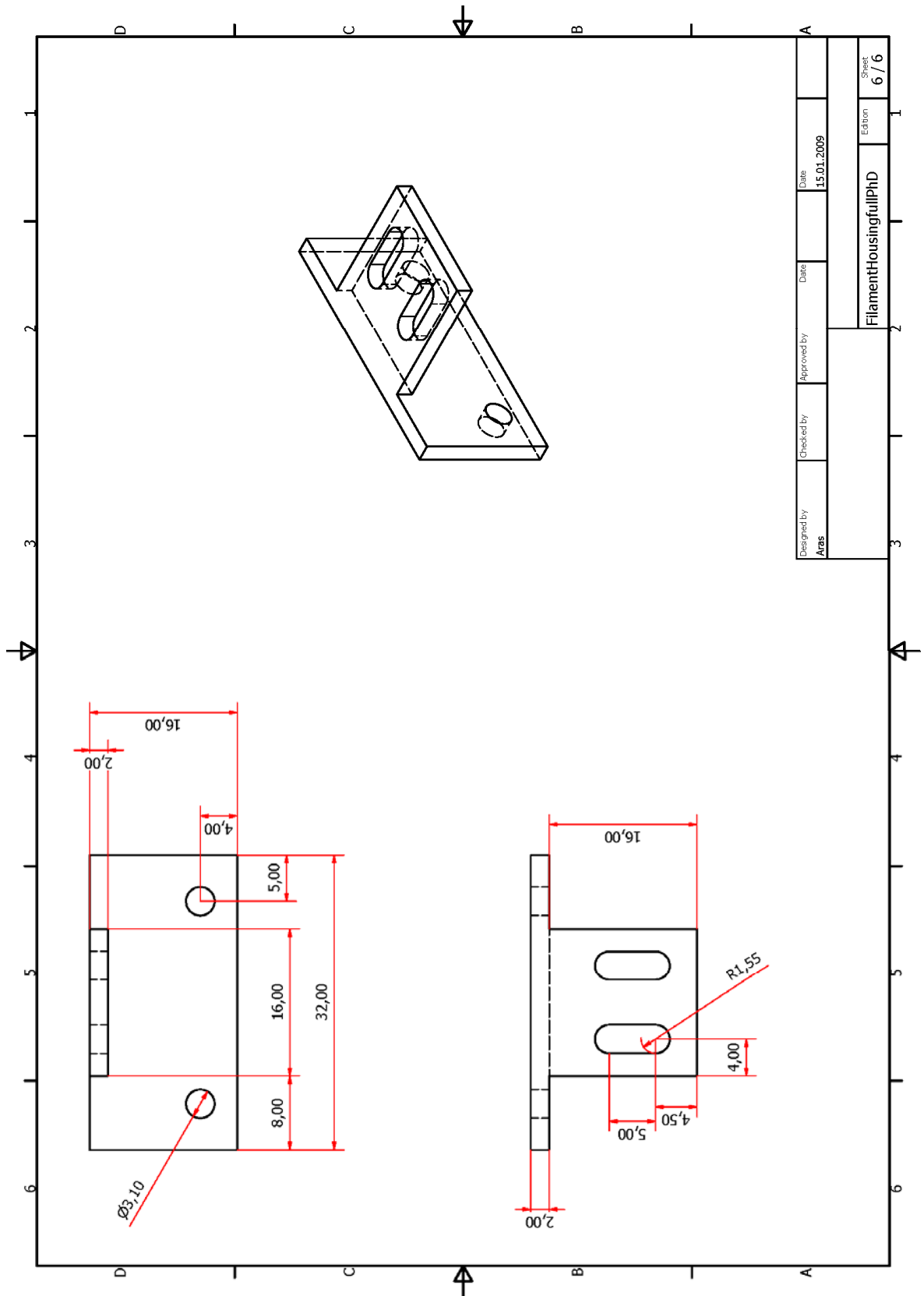












### A4. Sample holder

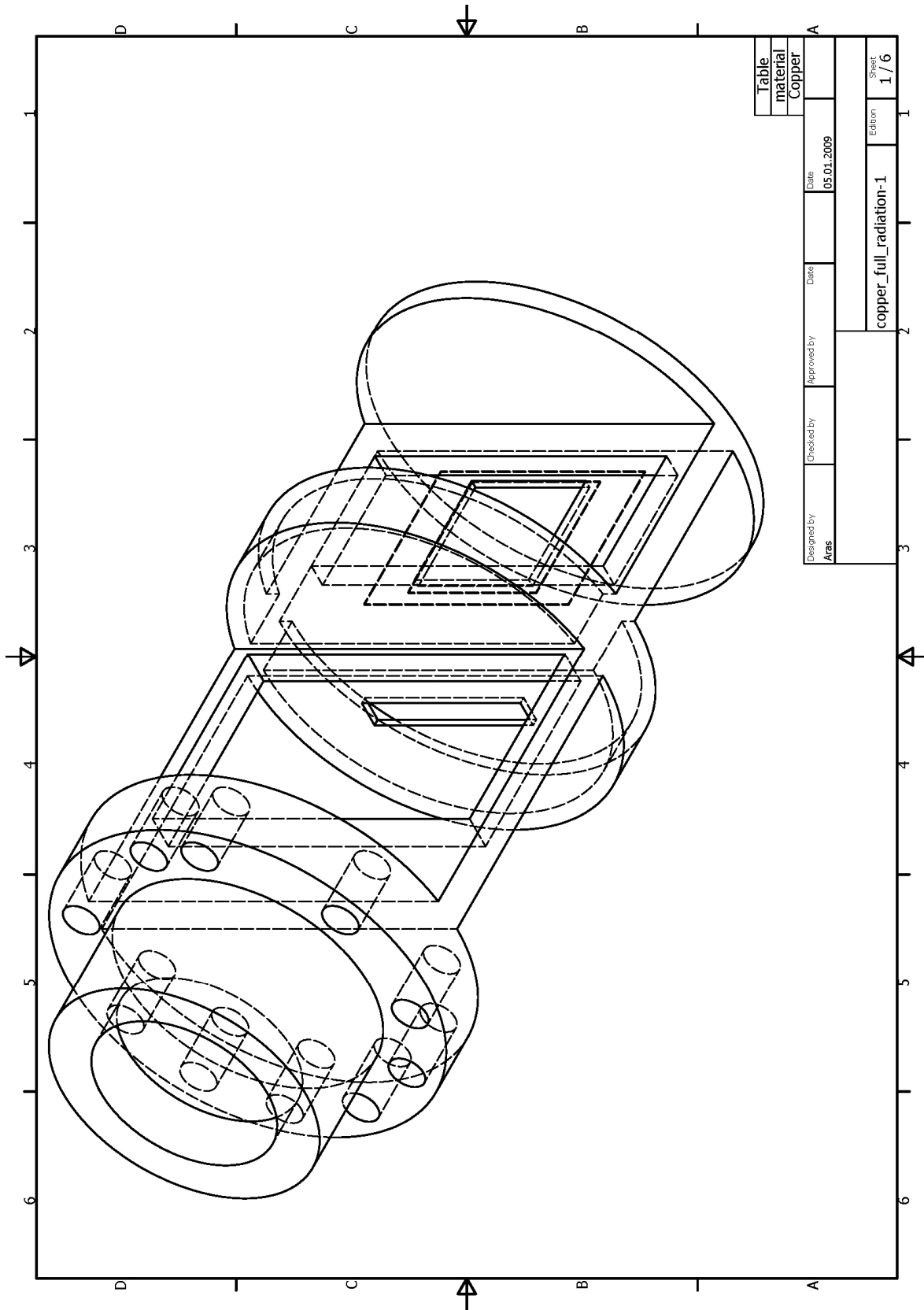
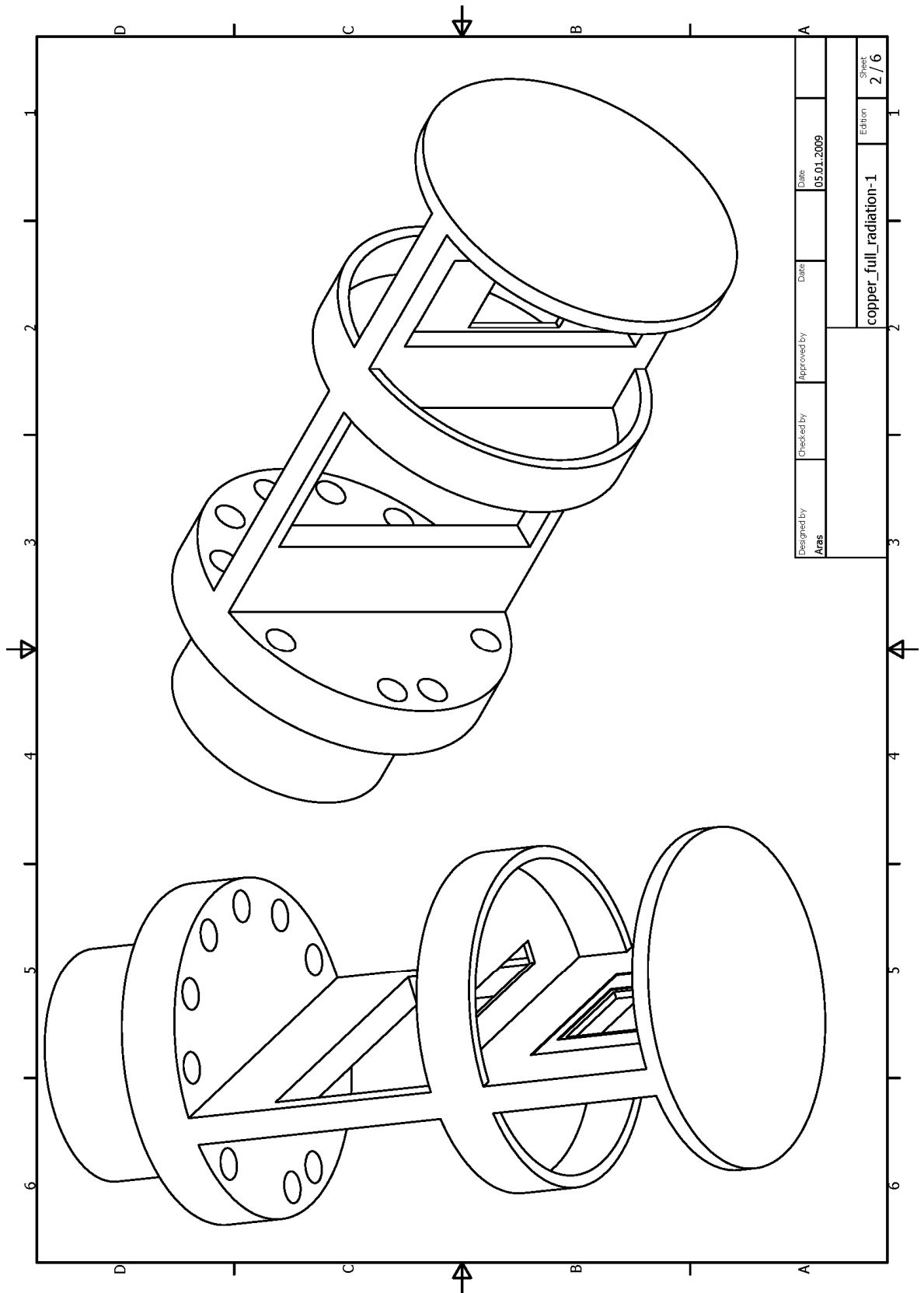
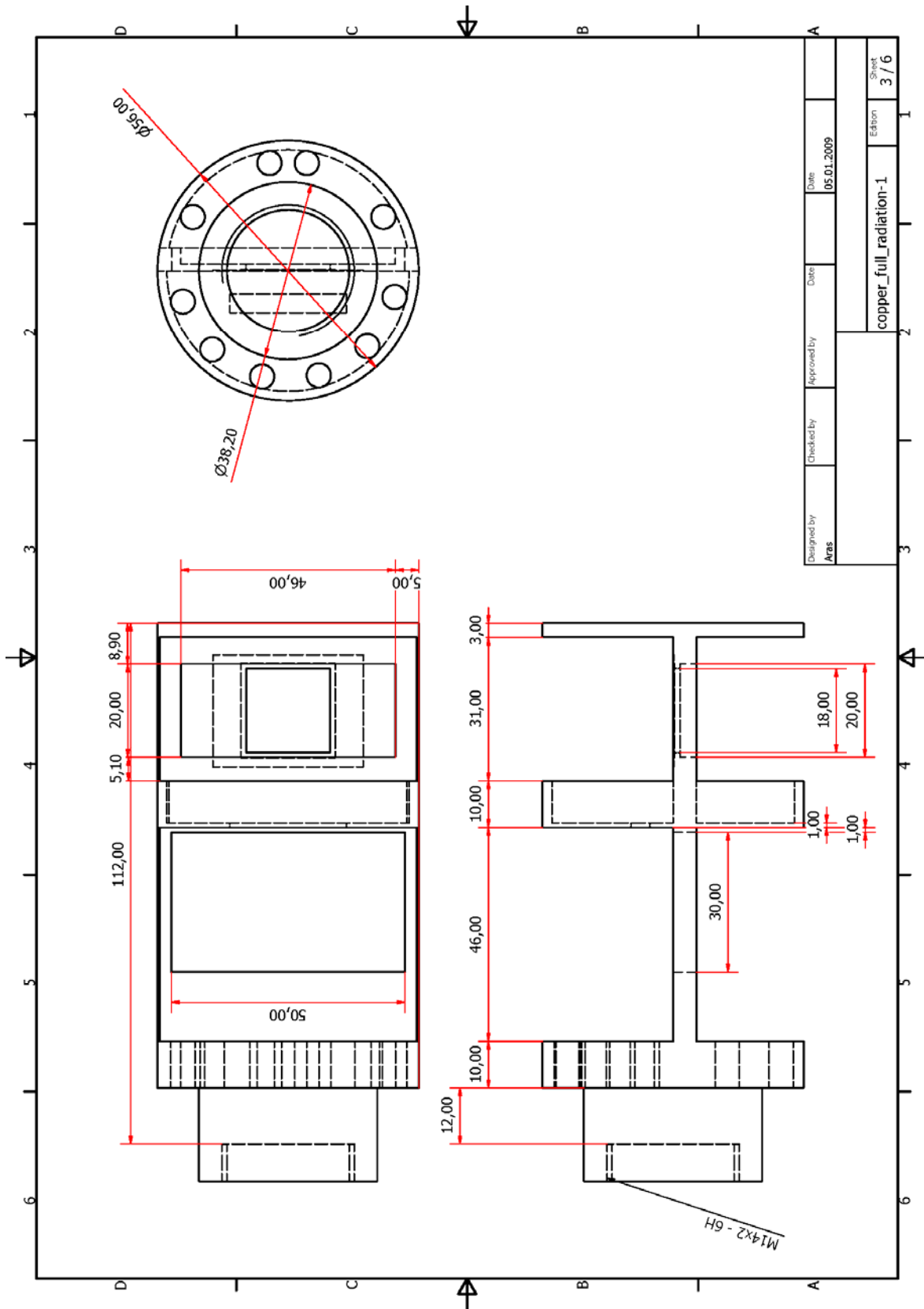
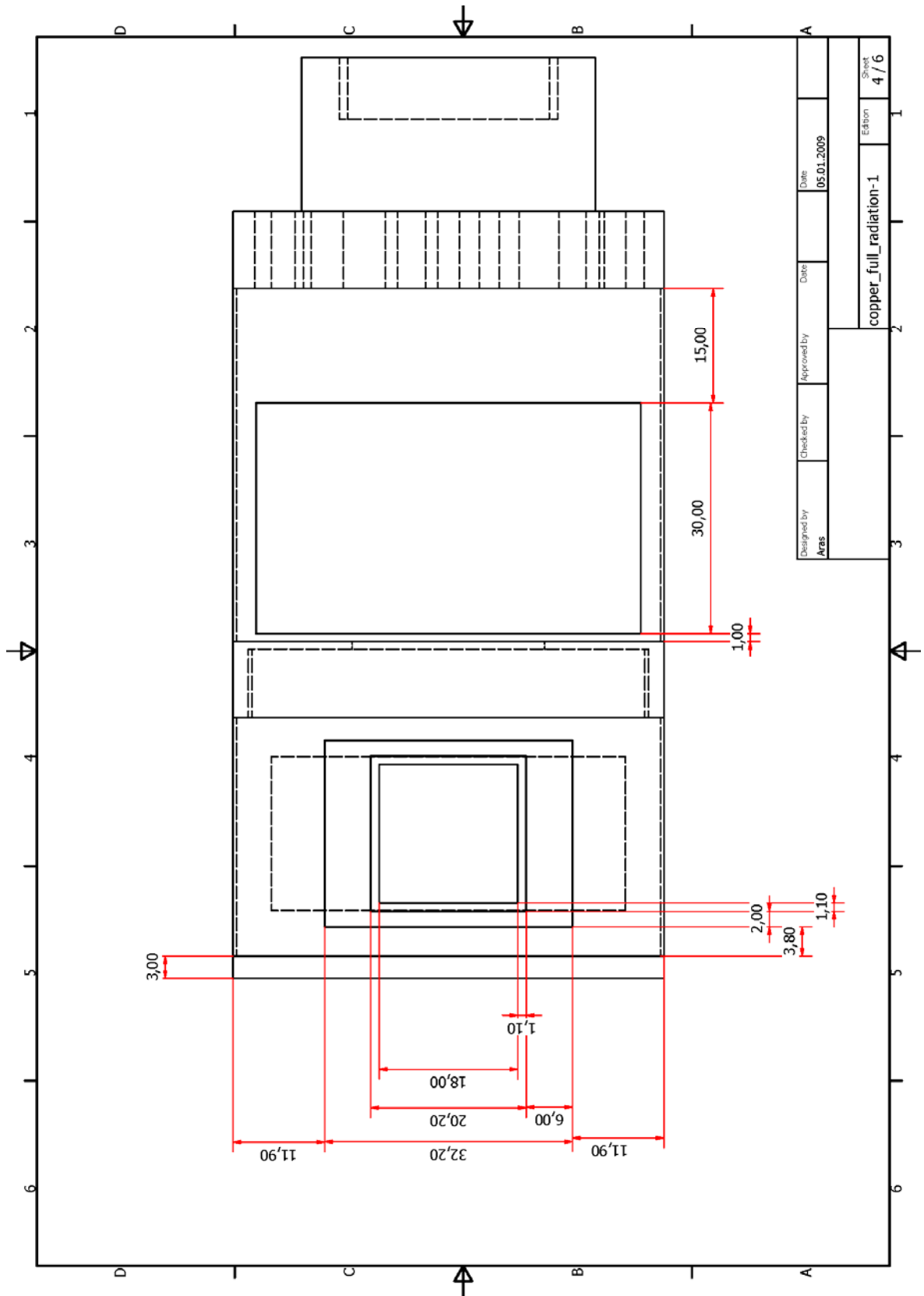
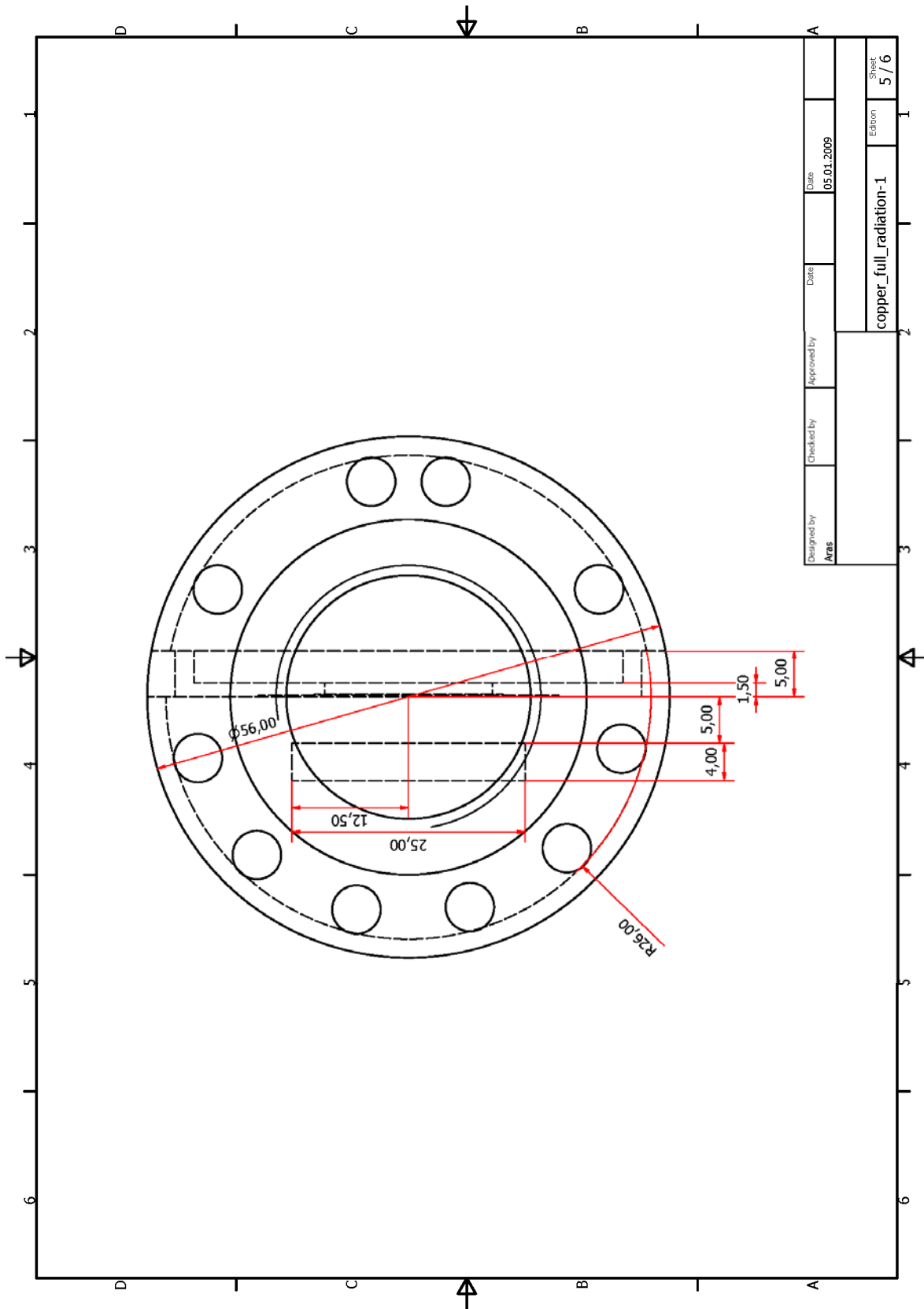


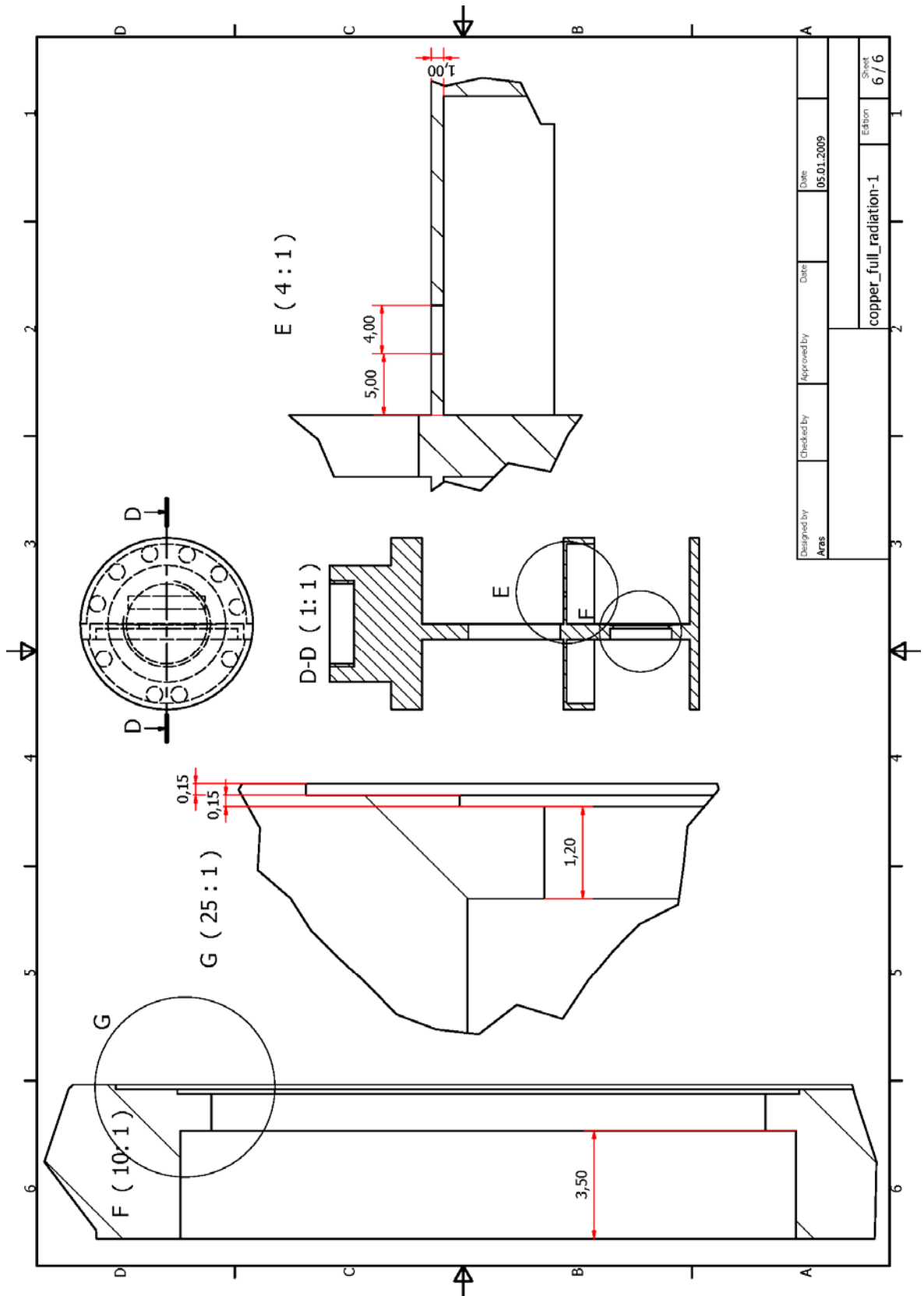
Table	Approved by	Date	05.01.2009
material	Checked by		
Copper	Designed by	Aras	
Echbon		copper_full_radiation-1	
Sheet		1 / 6	



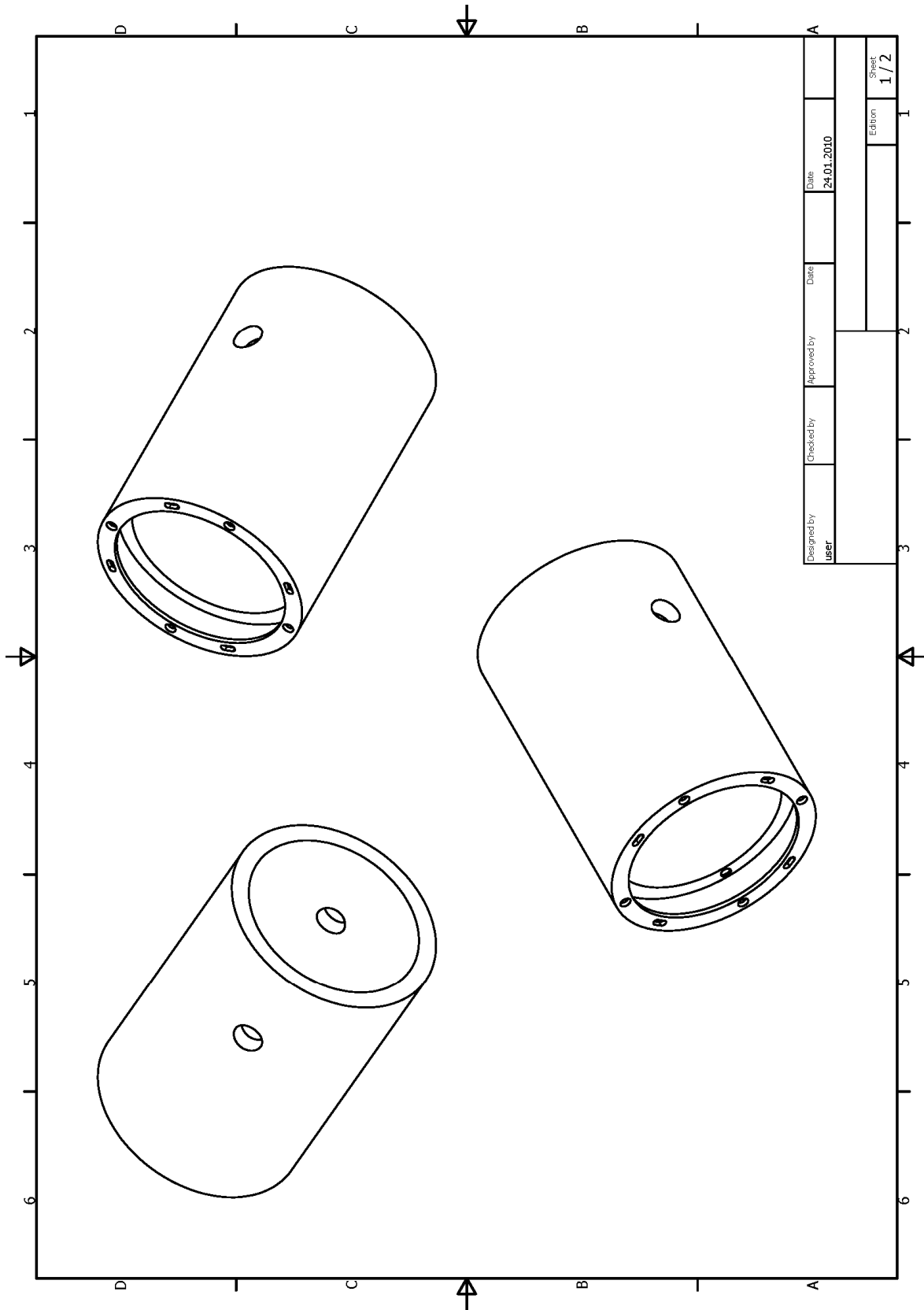




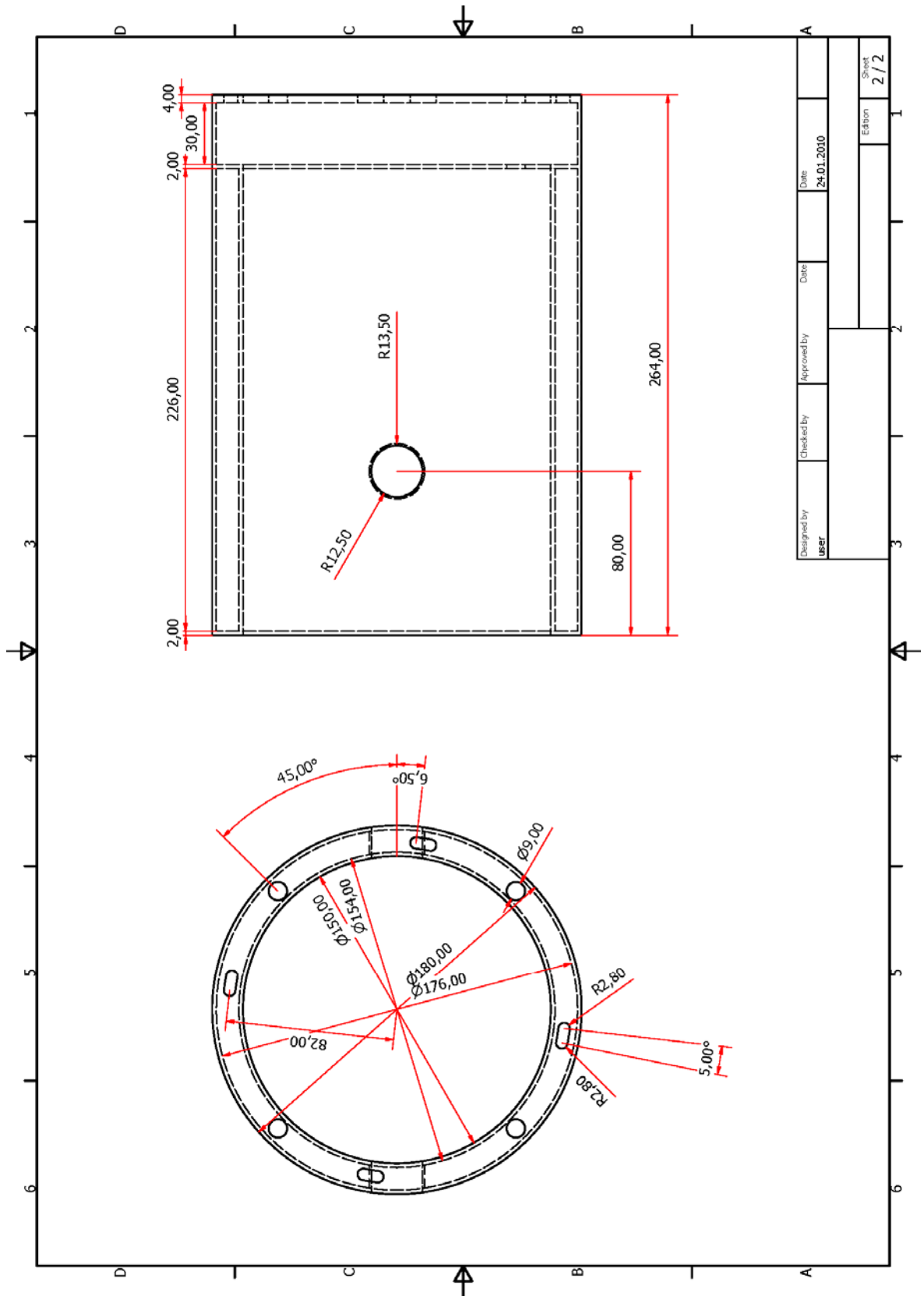




**A5. Second cooling shield**







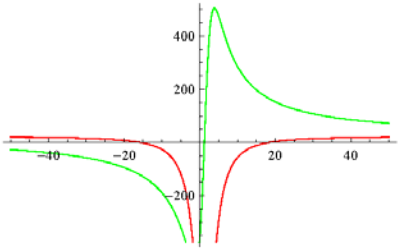
Designed by	Checked by	Approved by	Date
user			24.01.2010
Edition			Sheet
			2 / 2



## Appendix B: Calculations

### B1. Ray transfer matrix analysis

```

In[373]:= MFull =
  TraditionalForm[ $\left(\begin{pmatrix} 1 & 26 \\ 0 & 1 \end{pmatrix} \cdot \begin{pmatrix} 1 & 0 \\ \frac{0.515}{600} & 1.515 \end{pmatrix} \cdot \begin{pmatrix} 1 & 0.66 \\ 0 & 1 \end{pmatrix} \cdot \begin{pmatrix} 1 & 0 \\ 0 & \frac{1}{1.515} \end{pmatrix} \cdot \begin{pmatrix} 1 & 2 \\ 0 & 1 \end{pmatrix} \cdot \begin{pmatrix} 1 & 0 \\ 0 & 1.433 \end{pmatrix} \cdot \begin{pmatrix} 1 & 0.5 \\ 0 & 1 \end{pmatrix} \cdot \begin{pmatrix} 1 & 0 \\ 0 & \frac{1}{1.433} \end{pmatrix} \cdot \begin{pmatrix} 1 & D3 \\ 0 & 1 \end{pmatrix} \cdot \begin{pmatrix} 1 & 0 \\ \frac{-1}{50} & 1 \end{pmatrix} \cdot \begin{pmatrix} 1 & D2 \\ 0 & 1 \end{pmatrix} \cdot \begin{pmatrix} 1 & 0 \\ \frac{-1}{10} & 1 \end{pmatrix} \cdot \begin{pmatrix} 1 & D1 \\ 0 & 1 \end{pmatrix}\right) /. D1 \rightarrow 8.3;$ 
  AF = Part[MFull, 1, 1, 1];
  BF = Part[MFull, 1, 1, 2];
  CF = Part[MFull, 1, 2, 1];
  DF = Part[MFull, 1, 2, 2];
  QP =  $\left(-i \left(\frac{\pi \left(\frac{35 \cdot 10^{-4}}{\pi}\right)^2}{\lambda}\right)^{-1}\right)^{-1} /. \lambda \rightarrow 520 \cdot 10^{-7};$ 
  QM =  $\left(-i \left(\sqrt{\frac{L(L-12)}{4}}\right)^{-1}\right)^{-1} /. L \rightarrow 52;$ 
  Solve[QM ==  $\frac{AF * QP + BF}{CF * QP + DF}, D3]$ 
  ResultD3 = D3 /. %;
  ImD3 = ComplexExpand[Im[ResultD3]];
  ReD3 = ComplexExpand[Re[ResultD3]];
  Plot[{ImD3, ReD3}, {D2, -50, 50}, PlotStyle -> {RGBColor[1, 0, 0], RGBColor[0, 1, 0]}]
  Solve[ImD3 == 0, D2]
  ResultD2 = D2 /. %;
  PositiveD2 = Part[ResultD2, 2];
  ValueD3 = ReD3 /. D2 -> PositiveD2
  Out[380]=  $\left\{\left\{D3 \rightarrow \frac{(-1.77868 \times 10^{40} + 9.25314 \times 10^{38} i) - (1.67345 \times 10^{38} + 1.50511 \times 10^{38} i) D2}{(8.28954 \times 10^{26} - 1.96533 \times 10^{37} i) - (7.35703 \times 10^{36} - 4.65765 \times 10^{35} i) D2}\right\}\right\}$ 
  Out[384]= 
  Out[386]=  $\{(D2 \rightarrow -15.7423), (D2 \rightarrow 18.3237)\}$ 
  Out[388]=  $\{164.823\}$ 

```

## B2. Cooling of the substrate

```

ln[393]:= P11 = NDSolve[{{
  
$$\frac{3263657.092}{0.0004} \int_0^{0.02} \int_0^{0.02} \left(1 - \left(\frac{P[x, y, t]}{295}\right)^4\right) dx dy -$$

  
$$\frac{P^{(0,0,1)}[x, y, t]}{(0.00000087)} + P^{(0,2,0)}[x, y, t] + P^{(2,0,0)}[x, y, t] == 0, P[0.02, y, t] ==$$

  
$$295 - 225 (1 - \text{Exp}[-0.01 t]), P[x, 0, t] == 295 - 225 (1 - \text{Exp}[-0.01 t]),$$

  
$$P[x, 0.02, t] == 295 - 225 (1 - \text{Exp}[-0.01 t]), P[x, y, 0] == 295,$$

  
$$P[0, y, t] == 295 - 225 (1 - \text{Exp}[-0.01 t])},$$

  P, {x, 0, 0.02}, {y, 0, 0.02}, {t, 0, 500000}];

ln[394]:= P31 = NDSolve[{{
  
$$\frac{26933728.33}{0.0004} \int_0^{0.02} \int_0^{0.02} \left(1 - \left(\frac{P[x, y, t]}{500}\right)^4\right) dx dy -$$

  
$$\frac{P^{(0,0,1)}[x, y, t]}{(0.00000087)} + P^{(0,2,0)}[x, y, t] + P^{(2,0,0)}[x, y, t] == 0, P[0.02, y, t] ==$$

  
$$295 - 225 (1 - \text{Exp}[-0.01 t]), P[x, 0, t] == 295 - 225 (1 - \text{Exp}[-0.01 t]),$$

  
$$P[x, 0.02, t] == 295 - 225 (1 - \text{Exp}[-0.01 t]), P[x, y, 0] == 295,$$

  
$$P[0, y, t] == 295 - 225 (1 - \text{Exp}[-0.01 t])},$$

  P, {x, 0, 0.02}, {y, 0, 0.02}, {t, 0, 500000}];

ln[397]:= P12 =
NDSolve[{{
  
$$\frac{3263657.092}{0.0004} \int_0^{0.02} \int_0^{0.02} \left(0.75 - \left(\frac{P[x, y, t]}{295}\right)^4\right) dx dy - \frac{P^{(0,0,1)}[x, y, t]}{(0.00000087)} +$$

  
$$P^{(0,2,0)}[x, y, t] + P^{(2,0,0)}[x, y, t] == 0, P[0.02, y, t] ==$$

  
$$295 - 225 (1 - \text{Exp}[-0.01 t]), P[x, 0, t] == 295 - 225 (1 - \text{Exp}[-0.01 t]),$$

  
$$P[x, 0.02, t] == 295 - 225 (1 - \text{Exp}[-0.01 t]), P[x, y, 0] == 295,$$

  
$$P[0, y, t] == 295 - 225 (1 - \text{Exp}[-0.01 t])},$$

  P, {x, 0, 0.02}, {y, 0, 0.02}, {t, 0, 500000}];

P13 =
NDSolve[{{
  
$$\frac{3263657.092}{0.0004} \int_0^{0.02} \int_0^{0.02} \left(0.70 - \left(\frac{P[x, y, t]}{295}\right)^4\right) dx dy - \frac{P^{(0,0,1)}[x, y, t]}{(0.00000087)} +$$

  
$$P^{(0,2,0)}[x, y, t] + P^{(2,0,0)}[x, y, t] == 0, P[0.02, y, t] ==$$

  
$$295 - 225 (1 - \text{Exp}[-0.01 t]), P[x, 0, t] == 295 - 225 (1 - \text{Exp}[-0.01 t]),$$

  
$$P[x, 0.02, t] == 295 - 225 (1 - \text{Exp}[-0.01 t]), P[x, y, 0] == 295,$$

  
$$P[0, y, t] == 295 - 225 (1 - \text{Exp}[-0.01 t])},$$

  P, {x, 0, 0.02}, {y, 0, 0.02}, {t, 0, 500000}];

ln[399]:= P14 =
NDSolve[{{
  
$$\frac{3263657.092}{0.0004} \int_0^{0.02} \int_0^{0.02} \left(0.50 - \left(\frac{P[x, y, t]}{295}\right)^4\right) dx dy - \frac{P^{(0,0,1)}[x, y, t]}{(0.00000087)} +$$

  
$$P^{(0,2,0)}[x, y, t] + P^{(2,0,0)}[x, y, t] == 0, P[0.02, y, t] ==$$

  
$$295 - 225 (1 - \text{Exp}[-0.01 t]), P[x, 0, t] == 295 - 225 (1 - \text{Exp}[-0.01 t]),$$

  
$$P[x, 0.02, t] == 295 - 225 (1 - \text{Exp}[-0.01 t]), P[x, y, 0] == 295,$$

  
$$P[0, y, t] == 295 - 225 (1 - \text{Exp}[-0.01 t])},$$

  P, {x, 0, 0.02}, {y, 0, 0.02}, {t, 0, 500000}];

ln[400]:= P15 =
NDSolve[{{
  
$$\frac{3263657.092}{0.0004} \int_0^{0.02} \int_0^{0.02} \left(0.30 - \left(\frac{P[x, y, t]}{295}\right)^4\right) dx dy - \frac{P^{(0,0,1)}[x, y, t]}{(0.00000087)} +$$

  
$$P^{(0,2,0)}[x, y, t] + P^{(2,0,0)}[x, y, t] == 0, P[0.02, y, t] ==$$

  
$$295 - 225 (1 - \text{Exp}[-0.01 t]), P[x, 0, t] == 295 - 225 (1 - \text{Exp}[-0.01 t]),$$

  
$$P[x, 0.02, t] == 295 - 225 (1 - \text{Exp}[-0.01 t]), P[x, y, 0] == 295,$$

  
$$P[0, y, t] == 295 - 225 (1 - \text{Exp}[-0.01 t])},$$

  P, {x, 0, 0.02}, {y, 0, 0.02}, {t, 0, 500000}];

```

## Appendix B: Calculations

2 | All-Cooling-PHD.nb

```
In[402]= P32 = NDSolve[{{ $\frac{26933728.33}{0.0004} \int_0^{0.02} \int_0^{0.02} \left(0.5 + 0.5 (295 / 500)^4 - \left(\frac{P[x, y, t]}{500}\right)^4\right) dx dy -$ 
```

$$\frac{P^{(0,0,1)}[x, y, t]}{(0.00000087)} + P^{(0,2,0)}[x, y, t] + P^{(2,0,0)}[x, y, t] = 0, P[0.02, y, t] = 295 - 225 (1 - \text{Exp}[-0.01 t]),$$

$$P[x, 0, t] = 295 - 225 (1 - \text{Exp}[-0.01 t]), P[x, 0.02, t] = 295 - 225 (1 - \text{Exp}[-0.01 t]), P[x, y, 0] = 295,$$

$$P[0, y, t] = 295 - 225 (1 - \text{Exp}[-0.01 t])\}},$$

```
P, {x, 0, 0.02}, {y, 0, 0.02}, {t, 0, 500000}];
```

```
In[403]= P33 = NDSolve[{{ $\frac{26933728.33}{0.0004} \int_0^{0.02} \int_0^{0.02} \left(0.1 + 0.9 (295 / 500)^4 - \left(\frac{P[x, y, t]}{500}\right)^4\right) dx dy -$ 
```

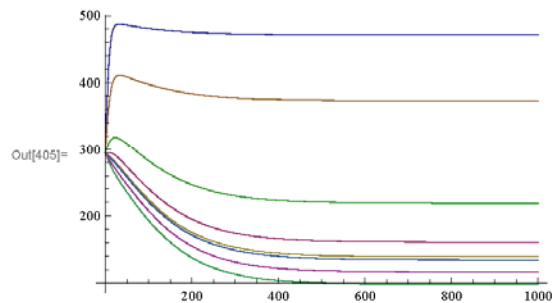
$$\frac{P^{(0,0,1)}[x, y, t]}{(0.00000087)} + P^{(0,2,0)}[x, y, t] + P^{(2,0,0)}[x, y, t] = 0, P[0.02, y, t] = 295 - 225 (1 - \text{Exp}[-0.01 t]),$$

$$P[x, 0, t] = 295 - 225 (1 - \text{Exp}[-0.01 t]), P[x, 0.02, t] = 295 - 225 (1 - \text{Exp}[-0.01 t]), P[x, y, 0] = 295,$$

$$P[0, y, t] = 295 - 225 (1 - \text{Exp}[-0.01 t])\}},$$

```
P, {x, 0, 0.02}, {y, 0, 0.02}, {t, 0, 500000}];
```

```
In[405]= Plot[
  Evaluate[{{P[0.01, 0.01, t] /. P31, P[0.01, 0.01, t] /. P11, P[0.01, 0.01, t] /. P12,
    P[0.01, 0.01, t] /. P15, P[0.01, 0.01, t] /. P13, P[0.01, 0.01, t] /. P14,
    P[0.01, 0.01, t] /. P32, P[0.01, 0.01, t] /. P33}}, {t, 0, 1000}, PlotRange -> All]
```





## **Acknowledgements**

I would like to address my special thanks to Prof. Dr. U. Heiz for his personableness, endless support and advice and all the friendly discussions. Without your help and constant trust in me and my work it would not be possible to finish this work.

My deep thanks also to Prof. U. Boesl-von Grafenstein for his extraordinary active, motivating and highly fruitful discussions on many scientific topics.

Thanks to Dr. F. Esch for his constant enthusiasm which was always stimulating and motivating.

Special thanks to Dr. J.M. Antonietti and Dr. M. Michalski for their friendly support in the early stages of my PhD.

I would like to thank my colleague and friend Martin Thämer for his honest friendship and all the smart and precise questions which led to invaluable discussions. It was always pleasant and efficient to work with you.

Thanks to Sean Aston for not only proof-reading this work but also being a nice fellow.

I'm thankful to all the under graduate students who worked in our lab during these years for the nice time I had and being patient with my German skills. I would like to express my thanks to Thomas Soini for his exceptional contribution during his Bachelor thesis and afterwards.

To all the members of Prof. Dr. U. Heiz group and Prof. U. Boesl group I'm thankful for their cooperativeness and for making a professional working atmosphere.

The invaluable support of the electronic and mechanical workshops is highly appreciated. Only through their high-level skills it was possible to construct this apparatus.

Thanks to my family for all the support and love, for always believing in me and my success and just being so wonderful. The world needs more people like you.

Finally I express my deepest thanks to my wonderful wife for her unconditional love throughout all ups and downs during these years.





## References

- 1 M. Brack, *Reviews of Modern Physics* **65**, 677 (1993).
- 2 W. A. Deheer, *Reviews of Modern Physics* **65**, 611 (1993).
- 3 K. L. Kelly, E. Coronado, L. L. Zhao, et al., *Journal of Physical Chemistry B* **107**, 668 (2003).
- 4 J. P. Wilcoxon and B. L. Abrams, *Chemical Society Reviews* **35**, 1162 (2006).
- 5 J. G. Du, X. Y. Sun, D. Q. Meng, et al., *Journal of Chemical Physics* **131** (2009).
- 6 B. von Issendorff and O. Cheshnovsky, *Annual Review of Physical Chemistry* **56**, 549 (2005).
- 7 E. Schumacher, F. Blatter, M. Frey, et al., *Chimia* **42**, 357 (1988).
- 8 G. Gantefor, C. Y. Cha, H. Handschuh, et al., *Journal of Electron Spectroscopy and Related Phenomena* **76**, 37 (1995).
- 9 A. W. Castleman and K. H. Bowen, *Journal of Physical Chemistry* **100**, 12911 (1996).
- 10 U. Heiz and W. D. Schneider, *Critical Reviews in Solid State and Materials Sciences* **26**, 251 (2001).
- 11 J. J. Scherer, J. B. Paul, C. P. Collier, et al., *Journal of Chemical Physics* **103**, 9187 (1995).
- 12 J. J. Scherer, J. B. Paul, C. P. Collier, et al., *Journal of Chemical Physics* **103**, 113 (1995).
- 13 J. J. Scherer, J. B. Paul, C. P. Collier, et al., *Journal of Chemical Physics* **102**, 5190 (1995).
- 14 J. J. Scherer, J. B. Paul, and R. J. Saykally, *Chemical Physics Letters* **242**, 395 (1995).
- 15 M. H. Schaffner, F. Patthey, U. Heiz, et al., *European Physical Journal D* **2**, 79 (1998).
- 16 J. M. Antonietti, A. Chatelain, and S. Fedrigo, *Journal of Chemical Physics* **114**, 2981 (2001).
- 17 G. Celep, E. Cottancin, J. Lerme, et al., *Physical Review B* **70** (2004).
- 18 F. Fehrer, P. M. Dinh, E. Suraud, et al., *Physical Review B* **75** (2007).
- 19 W. Harbich, S. Fedrigo, and J. Buttet, *Chemical Physics Letters* **195**, 613 (1992).
- 20 W. Harbich, S. Fedrigo, and J. Buttet, *Zeitschrift Fur Physik D-Atoms Molecules and Clusters* **26**, 138 (1993).
- 21 W. Harbich, S. Fedrigo, J. Buttet, et al., *Zeitschrift Fur Physik D-Atoms Molecules and Clusters* **19**, 157 (1991).
- 22 W. Harbich, S. Fedrigo, J. Buttet, et al., *Journal of Chemical Physics* **96**, 8104 (1992).
- 23 W. Harbich, S. Fedrigo, F. Meyer, et al., *Abstracts of Papers of the American Chemical Society* **199**, 103 (1990).
- 24 W. Harbich, S. Fedrigo, F. Meyer, et al., *Journal of Chemical Physics* **93**, 8535 (1990).

## References

---

- 25 B. Palpant, E. Cottancin, M. Pellarin, et al., *Annales De Physique* **23**, 167 (1998).
- 26 B. Palpant, B. Prevel, J. Lerme, et al., *Physical Review B* **57**, 1963 (1998).
- 27 I. Farbman, O. Levi, and S. Efrima, *Journal of Chemical Physics* **96**, 6477 (1992).
- 28 M. Hermann, U. Kreibig, and G. Schmid, *Zeitschrift Fur Physik D-Atoms Molecules and Clusters* **26**, S1 (1993).
- 29 J. J. Mock, M. Barbic, D. R. Smith, et al., *Journal of Chemical Physics* **116**, 6755 (2002).
- 30 P. N. Njoki, I. I. S. Lim, D. Mott, et al., *Journal of Physical Chemistry C* **111**, 14664 (2007).
- 31 K. Kolwas, A. Derkachova, and M. Shopa, *Journal of Quantitative Spectroscopy & Radiative Transfer* **110**, 1490 (2009).
- 32 W. P. Cai, H. Hofmeister, and T. Rainer, *Physica E-Low-Dimensional Systems & Nanostructures* **11**, 339 (2001).
- 33 A. Downes and P. Dumas, *Applied Surface Science* **212**, 770 (2003).
- 34 J. M. Flores-Camacho, L. D. Sun, N. Saucedo-Zeni, et al., *Physical Review B* **78**, 9 (2008).
- 35 U. Kreibig, G. Bour, A. Hilger, et al., *Physica Status Solidi a-Applied Research* **175**, 351 (1999).
- 36 W. D. Knight, K. Clemenger, W. A. Deheer, et al., *Physical Review Letters* **52**, 2141 (1984).
- 37 M. Schmidt, R. Kusche, W. Kronmuller, et al., *Physical Review Letters* **79**, 99 (1997).
- 38 C. L. Cleveland, W. D. Luedtke, and U. Landman, *Physical Review Letters* **81**, 2036 (1998).
- 39 R. L. Whetten, D. M. Cox, D. J. Trevor, et al., *Physical Review Letters* **54**, 1494 (1985).
- 40 I. M. L. Billas, A. Chatelain, and W. A. Deheer, *Science* **265**, 1682 (1994).
- 41 P. Hertz, *Mathematische Annalen* **67**, 387 (1909).
- 42 S. Torquato, B. Lu, and J. Rubinstein, *Physical Review A* **41**, 2059 (1990).
- 43 G. L. Weissler and R. W. Carlson, in *Methods of Experimental Physics* (Academic Press, 1979), Vol. 14.
- 44 D. J. Creasey, P. A. HalfordMaw, D. E. Heard, et al., *Journal of the Chemical Society-Faraday Transactions* **93**, 2907 (1997).
- 45 M. N. R. Ashfold, *Molecular Physics* **58**, 1 (1986).
- 46 M. N. R. Ashfold, S. G. Clement, J. D. Howe, et al., *Journal of the Chemical Society-Faraday Transactions* **89**, 1153 (1993).
- 47 M. N. R. Ashfold and J. D. Howe, *Annual Review of Physical Chemistry* **45**, 57 (1994).
- 48 W. Demtröder, *Laser Spectroscopy* (Springer-Verlag, Berlin Heidelberg Newyork, 2003).
- 49 J. Davidsson, J. H. Gutow, and R. N. Zare, *Journal of Physical Chemistry* **94**, 4069 (1990).
- 50 R. L. Farrow and D. J. Rakestraw, *Science* **257**, 1894 (1992).

## References

---

- 51 M. D. Wheeler, I. R. Lambert, and M. N. R. Ashfold, *Chemical Physics Letters* **229**, 285 (1994).
- 52 G. Hall and B. J. Whitaker, *Journal of the Chemical Society-Faraday Transactions* **90**, 1 (1994).
- 53 S. Williams, D. S. Green, S. Sethuraman, et al., *Journal of the American Chemical Society* **114**, 9122 (1992).
- 54 D. S. Green, T. G. Owano, S. Williams, et al., *Science* **259**, 1726 (1993).
- 55 Y. R. Shen, *The Principles of Nonlinear Optics* (Wiely, New York, 1984).
- 56 D. A. Higgins and R. M. Corn, *Journal of Physical Chemistry* **97**, 489 (1993).
- 57 A. Campargue, F. Stoeckel, and M. Chenevier, *Spectrochimica Acta Reviews* **13**, 69 (1990).
- 58 G. Berden, R. Peeters, and G. Meijer, *International Reviews in Physical Chemistry* **19**, 565 (2000).
- 59 J. M. Herbelin, J. A. McKay, M. A. Kwok, et al., *Appl. Opt.* **19**, 144 (1980).
- 60 D. Z. Anderson, J. C. Frisch, and C. S. Masser, *Applied Optics* **23**, 1238 (1984).
- 61 A. Kastler, *Nouvelle Revue D Optique* **5**, 133 (1974).
- 62 A. Okeefe and D. A. G. Deacon, *Review of Scientific Instruments* **59**, 2544 (1988).
- 63 J. T. Hodges, J. P. Looney, and R. D. vanZee, *Applied Optics* **35**, 4112 (1996).
- 64 E. Hecht, *Optics* (Addison-Wesley Longman, Amsterdam, 2002).
- 65 H. Kogelnik and T. Li, *Applied Optics* **5**, 1550 (1966).
- 66 A. Gerrard and J. M. Bursh, *Introduction to Matrix Methods in Optics* (John Wiely and Sons, New York, 1975).
- 67 W. Brower, *Matrix Methods in Optical Instrument Design* (Benjamin, New York, 1964).
- 68 F. T. Arecchi and E. O. Schulz-Dubois, (NORTH-HOLLAND PUBLISHING COMPANY, Amsterdam, New York, Oxford, 1972), Vol. 1.
- 69 A. C. R. Pipino, J. W. Hudgens, and R. E. Huie, *Review of Scientific Instruments* **68**, 2978 (1997).
- 70 A. C. R. Pipino, *Applied Optics* **39**, 1449 (2000).
- 71 A. C. R. Pipino, J. W. Hudgens, and R. E. Huie, *Chemical Physics Letters* **280**, 104 (1997).
- 72 M. Mazurenka, S. M. Hamilton, P. R. Unwin, et al., *Journal of Physical Chemistry C* **112**, 6462 (2008).
- 73 R. Engeln, G. von Helden, A. J. A. van Roij, et al., *Journal of Chemical Physics* **110**, 2732 (1999).
- 74 S. L. Logunov, *Applied Optics* **40**, 1570 (2001).
- 75 I. M. P. Aarts, B. Hoex, A. H. M. Smets, et al., *Applied Physics Letter* **84**, 3079 (2004).

## References

---

- 76 A. Terasaki, T. Kondow, and K. Egashira, *Journal of Optical Society of America B* **22**, 675 (2005).
- 77 K. Egashira, A. Terasaki, and T. Kondow, *Journal of Chemical Physics* **126**, 221102 (2007).
- 78 S. E. Fiedler, A. Hese, and A. A. Ruth, *Review of Scientific Instruments* **76** (2005).
- 79 W. Henkes, *Zeitschrift Fur Naturforschung Part a-Astrophysik Physik Und Physikalische Chemie* **16**, 842 (1961).
- 80 R. E. Leckenby, P. A. Trevalion, and E. J. Robbins, *Proceedings of the Royal Society of London Series a-Mathematical and Physical Sciences* **280**, 409 (1964).
- 81 E. J. Robbins, R. E. Leckenby, and P. Willis, *Advances in Physics* **16**, 739 (1967).
- 82 R. E. Palmer, S. Pratontep, and H. G. Boyen, *Nature Materials* **2**, 443 (2003).
- 83 V. N. Popok and E. E. B. Campbell, *Reviews on Advanced Materials Science* **11**, 19 (2006).
- 84 K. Wegner, P. Piseri, H. V. Tafreshi, et al., *Journal of Physics D-Applied Physics* **39**, R439 (2006).
- 85 L. Bardotti, B. Prevel, P. Jensen, et al., *Applied Surface Science* **191**, 205 (2002).
- 86 U. Queitsch, E. Mohn, F. Schaffel, et al., *Applied Physics Letters* **90**, 3 (2007).
- 87 K. C. Grabar, R. G. Freeman, M. B. Hommer, et al., *Analytical Chemistry* **67**, 735 (1995).
- 88 J. P. Wilcoxon, J. E. Martin, and P. Provencio, *Journal of Chemical Physics* **115**, 998 (2001).
- 89 R. Bennewitz, J. N. Crain, A. Kirakosian, et al., *Nanotechnology* **13**, 499 (2002).
- 90 O. F. Hagen, *Surface Science* **106**, 101 (1981).
- 91 T. P. Martin and T. Bergmann, *Journal of Chemical Physics* **90**, 6664 (1989).
- 92 K. Sattler, J. Muhlbach, and E. Recknagel, *Physical Review Letters* **45**, 821 (1980).
- 93 I. Katakuse, T. Ichihara, Y. Fujita, et al., *International Journal of Mass Spectrometry and Ion Processes* **67**, 229 (1985).
- 94 W. A. Saunders and S. Fedrigo, *Chemical Physics Letters* **156**, 14 (1989).
- 95 A. Wagner and T. M. Hall, *Journal of Vacuum Science & Technology* **16**, 1871 (1979).
- 96 T. G. Dietz, M. A. Duncan, D. E. Powers, et al., *Journal of Chemical Physics* **74**, 6511 (1981).
- 97 U. Heiz, F. Vanolli, L. Trento, et al., *Review of Scientific Instruments* **68**, 1986 (1997).
- 98 V. E. Bondybey and J. H. English, *Journal of Chemical Physics* **76**, 2165 (1982).
- 99 S. J. Riley, E. K. Parks, C. R. Mao, et al., *Journal of Physical Chemistry* **86**, 3911 (1982).
- 100 P. Milani and W. A. Deheer, *Resonance Ionization Spectroscopy 1990* **114**, 117 (1991).
- 101 P. Gangopadhyay and J. M. Lisy, *Review of Scientific Instruments* **62**, 502 (1991).

## References

---

- 102 R. E. Smalley, L. Wharton, and D. H. Levy, *Accounts of Chemical Research* **10**, 139 (1977).
- 103 R. T. Laaksonen, D. A. Goetsch, D. W. Owens, et al., *Review of Scientific Instruments* **65**, 2267 (1994).
- 104 P. Milani and W. A. Deheer, *Review of Scientific Instruments* **61**, 1835 (1990).
- 105 H. R. Siekmann, C. Luder, J. Faehrmann, et al., *Zeitschrift Fur Physik D-Atoms Molecules and Clusters* **20**, 417 (1991).
- 106 G. Gantefor, H. R. Siekmann, H. O. Lutz, et al., *Chemical Physics Letters* **165**, 293 (1990).
- 107 A. W. Castleman and R. G. Keesee, *Chemical Reviews* **86**, 589 (1986).
- 108 M. A. Rottgen, K. Judai, J. M. Antonietti, et al., *Review of Scientific Instruments* **77** (2006).
- 109 M. Szilagyi, *Electron and Ion Optics* (Plenum, New York, 1988).
- 110 H. D. Zeman, *Review of Scientific Instruments* **48**, 1079 (1977).
- 111 H. D. Baehr and K. Stephan, *Wärme- und Stoffübertragung* (Springer-Verlag, Berlin Heidelberg New York, 2004).
- 112 U. Kreibig and M. Vollmer, *Optical Properties of Metal Clusters* (Springer-Verlag, Berlin Heidelberg New York, 1995).
- 113 M. D. McMahon, R. Lopez, R. F. Haglund, et al., *Physical Review B* **73**, 4 (2006).
- 114 T. Gotz, M. Buck, C. Dressler, et al., *Applied Physics a-Materials Science & Processing* **60**, 607 (1995).
- 115 A. M. Moran, J. H. Sung, E. M. Hicks, et al., *Journal of Physical Chemistry B* **109**, 4501 (2005).
- 116 T. F. Heinz, C. K. Chen, D. Ricard, et al., *Physical Review Letters* **48**, 478 (1982).
- 117 U. Heiz and U. Landman, in *NANOSCIENCE AND TECHNOLOGY* (Springer Verlag, Berlin, 2007).
- 118 R. Casaes, J. B. Paul, R. P. McLaughlin, et al., *J. Phys. Chem. A* **108**, 10989 (2004).
- 119 R. A. Provencal, R. N. Casaes, K. Roth, et al., *J. Phys. Chem. A* **104**, 1423 (2000).
- 120 A. J. Huneycutt, R. N. Casaes, B. J. McCall, et al., *ChemPhysChem* **5**, 321 (2004).
- 121 R. Casaes, R. Provencal, J. Paul, et al., *J. Chem. Phys.* **116**, 6640 (2002).
- 122 J. B. Paul, C. P. Collier, R. J. Saykally, et al., *J. Phys. Chem. A* **101**, 5211 (1997).
- 123 P. Jena and A. W. Castleman, *Proceedings of the National Academy of Sciences of the United States of America* **103**, 10560 (2006).
- 124 D. Harding, M. S. Ford, T. R. Walsh, et al., *Physical Chemistry Chemical Physics* **9**, 2130 (2007).
- 125 P. B. Armentrout, *Annual Review of Physical Chemistry* **52**, 423 (2001).

## References

---

- <sup>126</sup> S. M. Hamilton, W. S. Hopkins, D. Harding, et al., Journal of the American Chemical Society **in press** (2010).